THE UNIVERSITY OF QUEENSLAND

AUSTRALIA

Development of High Capacity Li-rich Layered Cathode Materials for Lithium Ion Batteries

Delai Ye

Bachelor of Science

A thesis submitted for the degree of Doctor of Philosophy at

The University of Queensland in 2014

School of Chemical Engineering

Abstract

Since the launching of the first commercial lithium ion batteries (LIBs) in 1991, LIBs have been widely used to power portable electronic devices such as cell phones and laptop computers due to their high energy density. In the past decade, in response to the finite petroleum supply and the associated serious environmental concerns, low emission or even zero emission electric vehicles (EVs) have attracted increasing research and development interests and LIBs have been considered as one of the most potential power sources. However, the widely used layered $LiCoO_2$ cathode material has very limited chance to meet the demand considering its low capacity, high cost and toxicity. Li_2MnO_3 based layered Li-rich cathode materials as promising cathode candidates of LIBs have attracted much recent attention mainly due to their superior high specific capacity, low cost and high working voltage. To date, although researchers have put much effort to this family of materials, they still face a few serious challenges to overcome in terms of the specific capacity, long-term cycling stability and rate performance. In addition, some fundamental issues are still under debates in the understanding of the crystal structures and the electrochemical reaction mechanisms. This thesis focuses on the development of new high capacity Li-rich cathode materials for LIBs.

The first chapter starts with a general introduction of LIBs, followed by a brief summary of the LIBs component, working principle and three types of the well-developed cathode materials in Chapter 2. A detailed review of the recent development on Li_2MnO_3 based Li-rich cathode materials was also included in Chapter 2. The main objectives and the rationale behind this project are described in Chapter 3. All the experiment details including the material synthesis and characterization, coin cell fabrication and electrochemistry measurement are shown in Chapter 4.

Chapter 5 presents a published work on a series of layered-spinel integrated Li-rich cathode materials with controllable capacity. The Co/Mn mole ratio is fixed while the Li/(Mn+Ni) ratio is varied to adjust the ratio of the layered/spinel phases. They exhibit steadily increased specific capacities upon cycling for several dozen of cycles due to the gradual activation of the initial Li-rich layered phase from the surface of the composite particles. Both experimental and computational results suggest that a small amount of Co dopants plays a critical role in the continuous activation process of these materials. In addition, the structural evaluation mechanism is also discussed. Based on this unique feature, controllable discharge capacities of these cathode materials can be achieved in a broad range from 30 to 240 mAh g^{-1} by deliberately activating the materials at a potential window of 2~4.8 V.

Chapter 6 demonstrates a series of low-Co Li-rich cathode materials showing stepwise capacity increase over a few cycles from less than 50 mAh g^{-1} to around 250 mAh g^{-1}. A systematic analysis on their compositions, crystal structures and the electrochemical performances reveals that the small change of Co content has negligible effect to the crystal structure and morphology, but plays an important role in adjusting the activation rate of the Li_2MnO_3 phase. In addition, optimized cycling potential window and current rate have been demonstrated to significantly ensure the effective Li_2MnO_3 activation and good long-term cycling stability.

Chapter 7 describes a new class of Li-rich materials $Li[Li_{1/3-2x/3}Mn_{2/3-x/3}Ni_x]O_2$ ($0.09 \leq x \leq 0.2$) with a small amount of Ni doping as cathode materials for LIBs. Anomalous gradual capacity growth up to tens of cycles due to the continuous activation of the Li_2MnO_3 phase is observed. Both experimental and computational results indicate that a small amount of Ni doping can promote the stepwise Li_2MnO_3 activation to obtain increased specific capacity and better cycling capability. On the contrary, excessive Ni will overly activate the Li_2MnO_3 and result into a large capacity loss in the first cycle. The $Li_{1.25}Mn_{0.625}Ni_{0.125}O_2$ material with an optimized content of Ni has shown a superior high capacity of ~280 mAh g^{-1} and good cycling stability at room temperature.

Chapter 8 proposes a fundamental understanding on the Li_2MnO_3 activation process. Based on the platform of the low-Ni $Li_{1.87}Mn_{0.94}Ni_{0.19}O_3$ cathode material which exhibits exclusive stepwise capacity increase upon cycling as demonstrated in Chapter 6, the Li_2MnO_3 activation process was artificially retarded significantly and split into quite a few cycles. A combined study including the powerful *in-situ* XRD analysis and HAADF-STEM characterization revealed that the oxygen release sub-reaction is much faster than the TM-diffusion reaction. The latter is the key kinetic step to finalize the Li_2MnO_3 activation and results into the gradual capacity increase.

Finally, conclusions and recommendations are presented in Chapter 9 summarising the key findings and achievements of the present work on Li-rich Mn-based cathode materials and also giving insights into the future research and development on this promising cathode material system.

Declaration by author

This t*hesis* is composed of my original work, and contains no material previously published or written by another person except where due reference has been made in the text. I have clearly stated the contribution by others to jointly-authored works that I have included in my thesis.

I have clearly stated the contribution of others to my thesis as a whole, including statistical assistance, survey design, data analysis, significant technical procedures, professional editorial advice, and any other original research work used or reported in my thesis. The content of my thesis is the result of work I have carried out since the commencement of my research higher degree candidature and does not include a substantial part of work that has been submitted to qualify for the award of any other degree or diploma in any university or other tertiary institution. I have clearly stated which parts of my thesis, if any, have been submitted to qualify for another award.

I acknowledge that an electronic copy of my thesis must be lodged with the University Library and, subject to the General Award Rules of The University of Queensland, immediately made available for research and study in accordance with the *Copyright Act 1968*.

I acknowledge that copyright of all material contained in my thesis resides with the copyright holder(s) of that material. Where appropriate I have obtained copyright permission from the copyright holder to reproduce material in this thesis.

Publications during candidature

Capacity-Controllable Li-rich Cathode Materials for Lithium-Ion Batteries. Delai Ye, Kiyoshi Ozawa, Bei Wang, Denisa Hulicova-Jurcakova, Jin Zou, Chenghua Sun, and Lianzhou Wang, *Nano Energy*, 2014, 6, 92-102, DOI: 10.1016/j.nanoen.2014.03.013.

Understanding the stepwise capacity-increase of high energy low-Co Li-rich cathode materials for lithium ion batteries, Delai Ye, Bei Wang, Yu Chen, Guang Han, Zhi Zhang, Denisa Hulicova-Jurcakova, Jin Zou and Lianzhou Wang, *J. Mater. Chem. A*, 2014, 2, 18767-18774, DOI: 10.1039/C4TA03692A.

Ni-induced stepwise capacity increase in Ni-less Li-rich cathode materials for high performance lithium ion batteries, Delai Ye, Chenghua Sun, Yu Chen, Kiyoshi Ozawa, Denisa Hulicova-Jurcakova, Jin Zou and Lianzhou Wang, *Nano Res.*, 2014, 1-13, DOI: 10.1007/s12274-014-0563-3.

Li_2MnO_3 based Li-rich cathode materials: Towards a better tomorrow of high energy Lithium-Ion batteries, Delai Ye and Lianzhou Wang, *Mater. Tech.*, 2014. DOI: 10.1179/1753555714Y. 0000000166.

Breaking Up of Two-Dimensional MnO_2 Nanosheets Promotes Ultrasensitive PH-Triggered Theranostics of Cancer. Yu Chen[+], Delai Ye[+], Meiying Wu, Hangrong Chen, Linlin Zhang, Jianlin Shi and Lianzhou Wang, [+] These authors contributed equally to this work. *Adv. Mater.*, 2014, 26, 7019-7026, DOI: 10.1002/adma.201402572.

Dual protection of sulfur by carbon nanospheres and graphene sheets for lithium-sulfur batteries, Bei Wang, Yanfen Wen, Delai Ye, Hua Yu, Bing Sun, Guoxiu Wang, Denisa Hulicova-Jurcakova, and Lianzhou Wang,. *CHEM-EUR J*, 2014, 20, 5224-5230, DOI: 10.1002/chem.201400385.

In-Doped Bi_2Se_3 Hierarchical Nanostructures as Anode Materials for Li-Ion Batteries, Guang Han, Zhi-Gang Chen, Delai Ye, Lei Yang, Lianzhou Wang, John Drennanc and Jin Zou, *J. Mater. Chem. A*, 2014, 2, 7109-7116, DOI: 10.1039/C4TA00045E.

Publications included in this thesis

1. Capacity-Controllable Li-rich Cathode Materials for Lithium-Ion Batteries. Delai Ye, Kiyoshi Ozawa, Bei Wang, Denisa Hulicova-Jurcakova, Jin Zou, Chenghua Sun, and Lianzhou Wang, *Nano Energy*, 2014, 6, 92-102, DOI: 10.1016/j.nanoen.2014.03.013. (Incorporated in Chapter 5. Delai Ye is responsible for all of the experimental work and preparation of the manuscript, Kiyoshi Ozawa is responsible for the TEM characterization, Bei Wang is responsible for review of the work, Chenghua Sun is responsible for the simulation work, Denisa Hulicova-Jurcakova, Jin Zou and Lianzhou Wang are responsible for the discussion and review of the work and acted wholly in advisory roles.)

2. Understanding the stepwise capacity-increase of high energy low-Co Li-rich cathode materials for lithium ion batteries, Delai Ye, Bei Wang, Yu Chen, Guang Han, Zhi Zhang, Denisa Hulicova-Jurcakova, Jin Zou and Lianzhou Wang. *J. Mater. Chem. A*, 2014, 2, 18767-18774, DOI: 10.1039/C4TA03692A. (Incorporated in Chapter 6. Delai Ye is responsible for all of the experimental work and preparation of the manuscript, Bei Wang and Yu Chen are responsible for review of the work, Guang Han is responsible for the SEM characterization, Zhi Zhang is responsible for the TEM characterization, Denisa Hulicova-Jurcakova, Jin Zou and Lianzhou Wang are responsible for the discussion and review of the work and acted wholly in advisory roles.)

3. Ni-induced stepwise capacity increase in Ni-less Li-rich cathode materials for high performance lithium ion batteries, Delai Ye, Chenghua Sun, Yu Chen, Kiyoshi Ozawa, Denisa Hulicova-Jurcakova, Jin Zou and Lianzhou Wang. *Nano Res.*, 2014, 1-13, DOI: 10.1007/s12274-014-0563-3. (Incorporated in Chapter 7. Delai Ye is responsible for all of the experimental work and preparation of the manuscript, Chenghua Sun is responsible for the simulation work, Yu Chen and Kiyoshi Ozawa are responsible for review of the work, Denisa Hulicova-Jurcakova, Jin Zou and Lianzhou Wang are responsible for the discussion and review of the work and acted wholly in advisory roles.)

Contributions by others to the thesis

“No contributions by others”

Statement of parts of the thesis submitted to qualify for the award of another degree

None

Acknowledgements

Firstly I would like to express my sincere gratitude to my supervisors Prof. Lianzhou Wang, Prof. Jin Zou and Dr. Denisa Hulicova-Jurcakova for their continuing encouragement, guidance and support throughout this thesis work.

I would also like to thank everyone in the Nanomaterials Centre and all the administration supporting staff in the School of Chemical Engineering for their kind help.

I am very grateful to the University of Queensland International Research Tuition Award (UQIRTA), School of Chemical Engineering and Chinese Scholarship Council (CSC) for providing scholarships.

I would also like to thank all the co-workers in our group for their kind help and the staff in the Centre of Microscopy and Microanalysis who trained and assisted me in using the equipment.

Thanks to Dr. Chenghua Sun for his invaluable help in the simulation work, and Dr. Kiyoshi Ozawa, Mr. Han Guang and Mr. Zhi Zhang for the great help in materials characterization.

In particular, I would like to thank my parents for their consistent encouragement and support during my PhD study.

Keywords

Li-rich, high energy, capacity increase, layered cathode materials, lithium ion batteries

Australian and New Zealand Standard Research Classifications (ANZSRC)

ANZSRC code: 100708, Nanomaterials 40%

ANZSRC code: 091205, Functional Materials 40%

ANZSRC code: 090406, Powder and Particle Technology 20%

Fields of Research (FoR) Classification

FoR code: 0912, Materials Engineering 40%

FoR code: 1007, Nanotechnology 40%

FoR code: 0904, Chemical Engineering 20%

Table of Content

1. Introduction 1

1.1 Background 1

1.2 Development of batteries 1

1.2.1 What are batteries 1

1.2.2 Primary batteries 2

1.2.3 Secondary batteries 2

2. Literature Review 5

2.1 Basic knowledge of LIBs 5

2.1.1 Operation principles of LIBs 5

2.1.2 Basic thermodynamics and kinetics of LIBs 6

2.1.3 Electrochemical evaluation of LIBs 11

2.1.4 Essential components of LIBs 14

2.2 Cathode materials of LIBs 20

2.2.1 Design strategy of cathode materials 20

2.2.2 Traditional cathode materials 22

2.2.3 New generation high capacity Li-rich layered cathode materials 27

2.3 References 42

3. Research Objectives 54

4. Research Methodology 55

4.1 Material synthesis 55

4.2 Material characterizations 55

4.3 Preparation of coin cells 56

4.3.1 Preparation of cathodes 56

4.3.2 Assembly of coin cells 56

4.4 Electrochemical measurements 57

4.4.1 Cycling and rate capability test 57
4.4.2 Cyclic voltammetry 57
4.4.3 Electrochemical impedance spectroscopy 58
5. Capacity-Controllable Li-rich Cathode Materials for Lithium-Ion Batteries 59
5.1 Abstract 59
5.2 Introduction 60
5.3 Experimental section 61
5.4 Results and discussion 63
5.5 Conclusions 76
5.6 References 76
5.7 Supporting Information 82
6. Understanding the stepwise capacity-increase of high energy low-Co Li-rich cathode materials for lithium ion batteries 87
6.1 Abstract 87
6.2 Introduction 88
6.3 Experimental 89
6.4 Results and discussion 90
6.5 Conclusions 105
6.6 References 106
6.7 Supporting Information 110
7. Ni-induced stepwise capacity increase in Ni-less Li-rich cathode materials for high performance lithium ion batteries 112
7.1 Abstract 112
7.2 Introduction 113
7.3 Experimental section 114
7.4 Results and discussion 116
7.5 Conclusions 127

7.6 References 128

7.7 Supporting Information 133

8. Revealing the migration consequence of O and Mn in artificially retarded Li_2MnO_3 activation 136

8.1 Abstract 136

8.2 Introduction 137

8.3 Experimental section 138

8.4 Results and discussion 139

8.5 Conclusions 150

8.6 References 150

9. Conclusions and recommendations 154

9.1 Conclusions 154

9.2 Recommendations 155

List of Tables and Figures

Chapter 1

Table 1.1: Characteristics of major primary battery systems……...2

Table 1.2: Characteristics of the major secondary battery systems……..……3

Figure 1.1: Evolution of the LIBs sale in the electronic and HEV market……..…4

Chapter 2

Table 2.1: Advantages and disadvantages of nanomaterials …….……21

Figure 2.1: Comparison of the different battery technologies in terms of volumetric and gravimetric energy density…….……..……..……5

Figure 2.2: Operation principles of a typical lithium ion battery…….……6

Figure 2.3: Variation of cell voltage with operating current illustrating polarization…….……8

Figure 2.4: Illustration of double layer……...….9

Figure 2.5: Effects of temperature on battery capacity……..……13

Figure 2.6: Crystal structure of graphite before Li intercalation……15

Figure 2.7: Crystal structure of graphite after Li intercalation……...……16

Figure 2.8: α-$NaFeO_2$ layered structure……..22

Figure 2.9: Structure of $LiMn_2O_4$……...……25

Figure 2.10: The crystal structure of olivine $LiFePO_4$……...……26

Figure 2.11: Specific capacities of the major cathode materials for LIBs and the current research focuses on LLLs……...…….……27

Figure 2.12: The entire phase diagram for combinatorial Li−Mn−Ni-O system made in oxygen and quenched from 800 ℃. Red lines: boundaries of single-phase regions; green dashed lines are tie-lines; red dashed lines: tie-lines bounding three-phase regions; blue-dotted line: a phase transition between the cubic and layered rocksalt structures……...29

Figure 2.13: Simulation of the crystal structure of the R-3m $LiTMO_2$ and the C2/m Li_2MnO_3 phases viewed along the [100] direction……...……30

Figure 2.14: (a) and (b) HAADF and ABF STEM images of the R-3m $LiTMO_2$ structure projected along the $[100]_{rh}$ direction. (c) and (d) HAADF and ABF STEM images of the

monoclinic Li_2MnO_3-like structure projected along the $[100]_{mon}$ direction. Insets: simulated HAADF, ABF STEM and crystal structure images of the $LiTMO_2$ and Li_2MnO_3-like structures, respectively…….……32

Figure 2.15: Schematic illustrating the different structure-transition routes of the layered R-3m and C2/m phases to spinel grains with different features ……..……33

Figure 2.16: Proposed surface reaction mechanisms and oxygen-activation related products of $Li[Ni_xLi_{(1-2x)/3}Mn_{(2-x)/3}]O_2$ during different charging and discharging stages ……34

Figure 2.17: Electron distribution of the highest occupied orbit in $Li[Li_{1/3}Ti_{2/3}]O_2$ with oxygen vacancies. Green spheres: Li; red: O; blue: Ti; and black: O vacancy……35

Figure 2.18: Schematic illustration of the formation mechanisms for Mn and Ni segregation and densification during electrochemical reactions. Bulk and edge of the crystal are on the left and the right, respectively. Gray parts: shrinkage of the crystal……...…36

Figure 2.19: Left: 3D XEDS tomography map of segregated Mn and Ni distribution on a $Li_{1.2}Ni_{0.2}Mn_{0.6}O_2$ nanoparticle; middle: atomic resolution Z-contrast STEM image of the nanoparticle in surface layers; right: simulated [010] zone projection Z-contrast image based on $LiNi_{0.5}Mn_{0.5}O_2$ crystal model with 20% Ni/Li disorder and [0−10] with 10% Ni/Li disorder corresponding to the region labelled with blue and white rectangle in the middle STEM image ……..…….……38

Figure 2.20: a) 3D magnitude of the Fourier transformed Mn K-edge spectra of $Li_{1.2}Ni_{0.15}Co_{0.1}Mn_{0.55}O_2$ collected during constant 5 V charging; b) Projection view of the corresponding Ni–O, Co–O, and Mn–O spectra as functions of charging time……39

Figure 2.21: HRTEM of (A) un-coated and (B) coated $Li_{1.2}Ni_{0.2}Mn_{0.6}O_2$ materials, inset of (B) is the 2.5 × magnified view of the black rectangle area; (C) HRTEM of the nanostructure of the surface coating layer; (D) schematic diagram of the spinel/layered heterostructured material…….……...……41

Chapter 4

Figure 4.1: Schematic representation of coin cell assembly……..…57

Chapter 5

Table 5.1： ICP-AES analysis results and weight percentage of the layered and spinel phases of the $xLi_2[Mn_{0.857}Co_{0.143}]O_3$-(1-x)$Li[Mn_{1.714}Co_{0.286}]O_4$ (x = 0.95, 0.85, 0.75 and 0.65) composites……...…64

Table S5.1: Weigh percentage of the layered phase in the $xLi_2[Mn_{0.857}Co_{0.143}]O_3$-(1-x)$Li[Mn_{1.714}Co_{0.286}]O_4$ (x = 0.95, 0.75 and 0.65) composite cathodes after different cycles…….……..……86

Figure 5.1： Powder X-ray diffraction patterns of the (a) original compounds and (b) enlarged main peaks…….……...……65

Figure 5.2: Electrochemical cycling performance of the integrated composite cathode materials at 30 mA g^{-1} between 2-4.6 V and 2-4.8 V, respectively for the first 100 cycles……...…66

Figure 5.3: Electrochemical and XRD characterization of the x = 0.85 sample; (a) Charge/discharge profiles at 2-4.8 V for the 1^{st}, 5^{th}, 10^{th}, 40^{th}, 70^{th} and 100^{th} cycles. (b) Cyclic voltammogram loops of the 1^{st}, 2^{nd}, 5^{th}, 10^{th}, 20th and 30th cycles at 2-4.8V, the inset shows the cyclic voltammogram loops of the same cycles at 2-4.6 V. (c) XRD patterns of the electrodes before cycling and after the 1^{st}, 10^{th} and 100^{th} cycles at 2-4.8 V…….68

Figure 5.4: High resolution STEM-HAADF images of the x = 0.95 sample taken along the [100] zone axis. (a) Before cycling; (b) After 20 cycles at 2-4.8 V; (c) Surface area after 50 cycles at 2-4.8 V; and (d) Internal area after 50 cycles at 2-4.8 V. The right top inset in a) is the corresponding SAED pattern of the monoclinic structure projected along the [100] direction; the middle inset in (a) is a schematic simulation of the Li (green) and Mn/Co (purple/red) ordering in the pristine material. The red dotted lines in (b) separate the bulk area from the surface area where bright spots in the TM layers can be seen……..70

Figure 5.5: (a) Schematic figure of TM ions diffusion and oxygen removal in the layered crystal structure of $Li_2Mn_{1-x}Co_xO_3$. The arrows with dotted tails indicate OV generated by oxygen removal can promote the diffusion of neighboring TM, which will in return facilitate the OV generation. (b) Comparison of discharge capacities between the x = 0.95 sample and the Li_2MnO_3 sample at 2-4.6 V and 2-4.8 V……72

Figure 5.6: Discharge capacities of the x = 0.85 sample: (a) alternatively activated at 2-4.6 V and 2-4.8 V in the step of 10 cycles each for the first 140 cycles; (b) firstly activated at 2-4.8 V for 10, 15 or 20 (named as a10, a15 and a20) cycles respectively, and then at 2-4.6 V for another 50 cycles. The current density for all the tests was 30 mA g^{-1}…….74

Figure 5.7: Schematic illustration of the activating behaviour of the Li-rich layered phase at different potential ranges. The gradient from orange to red means the level up of the activation. Note (N+M) is no more than the cycles when these composite materials reach their maximum capacities……..……75

Figure S5.1: SEM images of the $xLi_2[Mn_{0.857}Co_{0.143}]O_3$-(1-x)$Li[Mn_{1.714}Co_{0.286}]O_4$ (x = 0.95, 0.85, 0.75 and 0.65) compounds. ……..…82

Figure S5.2: Charge/discharge profiles of the $xLi_2[Mn_{0.857}Co_{0.143}]O_3$-(1-x)$Li[Mn_{1.714}Co_{0.286}]O_4$ (x = 0.95, 0.75 and 0.65) composite cathodes in the 1st, 5th, 10th, 40th, 70th and 100th cycles measured in the potential range of 2-4.8 V at the current density of 30 mA g^{-1}…….83

Figure S5.3: Cyclic voltammogram loops of the $xLi_2[Mn_{0.857}Co_{0.143}]O_3$-(1-x)$Li[Mn_{1.714}Co_{0.286}]O_4$ (x = 0.95, 0.75 and 0.65) composite cathodes at the 1st, 2nd, 5th, 10th, 20th and 30th cycles at a scan rate of 0.2 mV s^{-1} within 2-4.8 V or 2-4.6 V……...…….……84

Figure S5.4: XRD patterns of the $xLi_2[Mn_{0.857}Co_{0.143}]O_3$-(1-x)$Li[Mn_{1.714}Co_{0.286}]O_4$ (x = 0.95, 0.75 and 0.65) composite cathodes before cycling and after the 1st, 20th and 100th cycle at 2-4.8 V……...…….……85

Chapter 6

Table 6.1: ICP-AES analysis results of the $Li[Co_xLi_{1/3-x/3}Mn_{2/3-2x/3}]O_2$ (x = 0.087, 0.1 and 0.118) composites…….……..……90

Table 6.2: Full-width at half maximum (FWHM) of the typical XRD diffraction peaks of the $Li[Co_xLi_{1/3-x/3}Mn_{2/3-2x/3}]O_2$ (x=0.087, 0.1, 0.118) composites…….…91

Table S6.1: Resistance values of the $Li[Co_xLi_{1/3-x/3}Mn_{2/3-2x/3}]O_2$ (x=0.087, 0.1, 0.118) composites before cycling and after the 1st and 5th cycle…….....….…111

Figure 6.1: Powder X-ray diffraction patterns of the original $Li[Co_xLi_{1/3-x/3}Mn_{2/3-2x/3}]O_2$(x = 0, 0.087, 0.1 and 0.118) compounds……..…….……91

Figure 6.2: (a) to (d) SEM images of the $Li[Co_xLi_{1/3-x/3}Mn_{2/3-2x/3}]O_2$ (x=0, 0.087, 0.1, 0.118) compounds; (e) and (f) high-resolution SEM images of the typical x=0.087 and 0.1 samples…..……..……93

Figure 6.3: (a) TEM images of the x=0.087 sample; (b) Enlargement of the yellow frame in (a); (c, d) HRTEM images of the yellow frame area in (b) along two different zone axis of $[1\text{-}10]_{mon}$ and $[010]_{mon}$. Right-top inset images in (c) and (d) are the corresponding SAED patterns…….94

Figure 6.4: The XPS patterns of (a): Mn and (b): Co elements in the original $Li[Co_xLi_{1/3-x/3}Mn_{2/3-2x/3}]O_2$(x = 0.087, 0.1, and 0.118) compounds…….……..……...……95

Figure 6.5: Specific discharge capacities of the $Li[Co_xLi_{1/3-x/3}Mn_{2/3-2x/3}]O_2$ (x = 0, 0.087, 0.1 and 0.118) composites in the first 120 cycles at three potential windows of 2-4.6 V, 2-4.8 V and 2-5 V. The current density is 30 mA g^{-1}……...……96

Figure 6.6: Columbic efficiencies of the $Li[Co_xLi_{1/3-x/3}Mn_{2/3-2x/3}]O_2$ (x=0, 0.087, 0.1, 0.118) composites between 2-4.8 V potential window in the first 120 charging-discharging cycles…….……..……98

Figure 6.7: Charge/discharge curves of the $Li[Co_xLi_{1/3-x/3}Mn_{2/3-2x/3}]O_2$ (x = 0, 0.087, 0.1 and 0.118) composites at different cycles between 2-4.8 V…….…….……99

Figure 6.8: CV curves of the $Li[Co_xLi_{1/3-x/3}Mn_{2/3-2x/3}]O_2$ (x = 0.087, 0.1 and 0.118) composites at 2-4.8 V in the first 10 cycles…….100

Figure 6.9: Cycling performance of the $Li[Co_xLi_{1/3-x/3}Mn_{2/3-2x/3}]O_2$ (x = 0.087, 0.1 and 0.118) composites at three current densities of 30, 60 and 150 mA g^{-1} between 2-4.8 V…...102

Figure 6.10: Typical Nyquist plots of the Co-doped samples (a) before and after (b) 1 and (c) 5 charging-discharging cycles…….…….……...104

Figure 6.11: *Ex-situ* X-ray diffraction patterns of the x = 0.087, x = 0.1 and x = 0.118 electrodes after 120 cycles at 0.1C between 2-4.8 V……..…105

Figure S6.1: Comparison of the cycling performance of the $Li[Co_xLi_{1/3-x/3}Mn_{2/3-2x/3}]O_2$ (x=0, 0.087, 0.1, 0.118) composites between 2-4.8 V potential window in the first 120 charging-discharging cycles……..…110

Figure S6.2: Cycling performance of the x=0.143 and 0.182 samples at 30 mA g^{-1} between 2-4.8 V……..……..…110

Chapter 7

Table S7.1： The nominal and experimental mole ratios of Mn/Ni and Li/(Mn+Ni) of the $Li[Ni_xLi_{1/3-2x/3}Mn_{2/3-x/3}]O_2$ materials…….…….……133

Figure 7.1: (a) XRD patterns of pristine cathode materials with different Ni-doping content; (b) Cycling performance of the cathode materials in the first 150 cycles at 30 mA g^{-1} between 2-4.8 V; (c) The relevant 1st charge and discharge curves of Ni-doped cathode materials at 30 mA g^{-1} between 2-4.8 V; d) XRD patterns of the electrodes after the 1st cycle……...……...……...……...…...116

Figure 7.2: Schematic illustration of TM diffusion and formation of oxygen vacancies in Li-rich materials and the relevant energy barriers as the function of different TM ions……...119

Figure 7.3: (a) SEM image and corresponding EDS- mapping of Mn and Ni; (b) and the related EDS spectra of the Ni/5 sample……..……120

Figure 7.4: (a, c) HR-TEM images of the pristine Ni/5 sample and Ni/5 electrode after 100 electrochemical cycles; (b, d) the corresponding electron diffraction patterns along the $[010]_{mon}$ axis……..……121

Figure 7.5: (a) Charge/discharge curves of Ni/5 in typical cycles tested at 30 mA g^{-1} between 2-4.8 V; (b) CV curves of Ni/5 in different cycles at a scan rate of 0.02 mV s^{-1}; (c) XRD patterns of the Ni/5 electrodes after different cycles…….……123

Figure 7.6: (a) Cycling performance and (b) first charge/discharge curves of the Ni/5 electrode and its (c) XRD patterns after the first cycle without or with extended 4, 7 or 10h of 4.8 V constant-voltage charging in the first cycle, respectively…….……125

Figure 7.7: Effect of over activation, optimized activation and under activation of the Li_2MnO_3 phase on the structure evolution and electrochemical behaviours of layered Li-rich materials depending on the content of Ni……..……127

Figure S7.1: FE-SEM of all the Ni-doped cathode materials……...……133

Figure S7.2: Columbic efficiencies of all the Ni-doped samples in the first 150 cycles…….134

Figure S7.3: Rate performance of the Ni/5 sample after activation at 30 mA g^{-1} for 100 cycles…135

Figure S7.4: (a) Nyquist plots of the Ni/5 sample and (b) its enlargement before and after different activation cycles at the charge state of 4.5 V…….135

Chapter 8

Figure 8.1: Powder X-ray diffraction pattern of the pristine $Li_{1.87}Mn_{0.94}Ni_{0.19}O_3$ composite…….……..……140

Figure 8.2: FESEM images of the (a) carbonate precursor (b) 500 ℃ pre-heated oxide precursor and (c, d) final $Li_{1.87}Mn_{0.94}Ni_{0.19}O_3$ composite……..……140

Figure 8.3: The XPS spectra of (a) Mn_{2p} and (b) Ni_{2p} for the pristine $Li_{1.87}Mn_{0.94}Ni_{0.19}O_3$ composite powder…….....141

Figure 8.4: Charge and discharge capacities and the corresponding columbic efficiency of the $Li_{1.87}Mn_{0.94}Ni_{0.19}O_3$ material in the first 100 cycles at 30 mA g^{-1} between 2V and 4.8 V. Inset are the detailed charge/discharge curves of this material in some typical cycles.143

Figure 8.5: (a) Net specific charge capacities of the $Li_{1.87}Mn_{0.94}Ni_{0.19}O_3$ cathode material in the voltage ranges of 2-3.8 V, 3.8-4.6 V and 4.6-4.8 V in the first 100 cycle; (b) net discharge capacities in the voltage ranges of 4.8-3.5 V, 3.5-2.8 V and 2.8-2 V in the first 100 cycle……144

Figure 8.6: Selected area *in-situ* XRD patterns and corresponding first cycle charge/discharge profile versus time of the $Li_{1.87}Mn_{0.94}Ni_{0.19}O_3$ composite. (a) is the stacked *in-situ* XRD patterns and (b) is the colourful time resolved intensity distribution plots with reference colour bar underneath……145

Figure 8.7: Change of the Rietveld refined a- and c-lattice parameters and corresponding unit cell volume during the first cycle……146

Figure 8.8: HAADF-STEM images and the corresponding SAED of the (a) pristine (b) 10 time cycled and (c, d) 50 time cycled $Li_{1.87}Mn_{0.94}Ni_{0.19}O_3$ material……148

LIST OF ABBREVIATIONS

LIB	lithium ion battery
HEV	hybrid electric vehicle
EV	electric vehicle
NMP	N-2-methyl pyrrolidone
PVDF	poly-vinylidene fluoride
CV	cyclic Voltammetry
EIS	electrochemical Impedance Spectroscopy
OCV	open circuit voltage
EC	ethylene carbonate
DC	diethyl carbonate
DMC	dimethyl carbonate
SEI	solid Electrolyte Interface
TGA	thermo gravimetric analysis
SEM	scanning electron microscopy
FESEM	field-emission scanning electron microscopy
TEM	transmission electron microscopy
HRTEM	high resolution transmission electron microscopy
TM	transition metal
TMO	transition metal oxide
STEM	scanning transmission electron microscopy
HAADF-STEM	high-angle annular-dark-field scanning transmission electron microscopy
SAED	selected area electron diffraction
XRD	X-ray diffraction

1. Introduction

1.1 Background

The shortage of fossil energy sources and increasing environmental problems trigger the development of viable alternative energy technologies that can make profound impact in world economy and ecology. Electrochemical power sources are attractive alternative energy technologies as they provide clean energy with high efficiency. An electrochemical power source is a device that can convert the energy generated in a chemical reaction directly into electricity. There are three significant types of electrochemical power sources: electrochemical capacitors, batteries, and fuel cells. Generally, batteries store electrical energy chemically in a material, which can then transfer the chemical energy directly into electrical energy by electrochemical redox reactions [1].

1.2 Development of batteries

1.2.1 What are batteries

Scientifically, batteries are referred as electrochemical or galvanic cells, because they store electrical energy in the form of chemical energy. The relative electrochemical reactions that take place are also termed galvanic [2]. Galvanic reactions are thermodynamically favourable because their free energy difference ΔG is negative. They occur spontaneously when two materials of different positive standard reduction potentials are connected by an electronic load (which means a voltage is derived). The material with the lower potential undergoes an oxidation reaction providing electrons by the external circuit to the other material with the higher potential, which undergoes a reduction reaction. These half reactions occur concurrently and allow for the conversion of chemical energy to electrical energy by electron transfer through the external circuit. The material with the lower potential is generally defined as the negative electrode or anode on discharge (provide electrons), while the material with the higher potential is the positive electrode or cathode on discharge (accept electrons). In addition to the electrodes, the two other constituents required for such reactions to take place are the electrolyte and separator. Electrolyte is an ion conducting media which can be in the form of aqueous, molten, or solid solution. Separator is a membrane that physically prevents a direct contact between the two electrodes and allows ions but not electrons to pass through; therefore it ensures electrical insulation for charge neutralization in both electrodes once the reaction is completed. Two other essential parts to constitute a commercial galvanic cell are the terminals. They are specifically

designed and shaped to fit electrical appliances with specific holder designs in order to prevent short-circuits by battery reverse installation. For example, in cylindrical batteries, the negative terminal is either flat, or to protrude out of the battery end, while the positive terminal extends as a pip at the opposite end. There are two categories of batteries based on their ability to recharge: primary and secondary batteries. In primary batteries, electrode materials undergo irreversible chemical reactions while in secondary batteries, the electrode materials exhibit reversible chemical reactions.

1.2.2 Primary batteries

Primary batteries can't be recharged. The electrochemical reactions that occur are not reversible and the cell is operated until the active component in one or both the electrodes is exhausted. Therefore, primary batteries are normally designed to operate at low currents with long lifetime and widely used in portable devices, toys, watches, hearing aids, and medical implants. Some major primary battery systems are shown in **Table 1.1**.

Table 1.1 Characteristics of major primary battery systems [3, 4]

	Leclanché	**Alkaline MnO_2**	**Zinc-HgO**	**Zinc-air**	**Li-MnO_2**
Anode	Zn	Zn	Zn	Zn	Li
Cathode	MnO_2	MnO_2	HgO	O_2	MnO_2
Electrolyte	NH_4Cl and $ZnCl_2$ (aq)	KOH (aq)	KOH (aq)	KOH (aq)	Organic solvent + Li salt
Cell Voltage(V)	1.6	1.5	1.34	1.65	3.5
Capacity(mAh g^{-1})	220	220	190	660	290

1.2.3 Secondary batteries

A secondary battery can be effectively reused many times after discharging by applying electrical energy to recharge the cell via reverse electrochemical reactions. When a secondary cell is fully charged, the electrodes return back to their original state, allowing the discharge reactions to occur again, thus, the cell can be reused to power an electric appliance/device. This charge-discharge

process is referred as an electrochemical "cycle". There are several types of rechargeable batteries including traditional ones such as lead-acid battery, nickel-cadmium battery, nickel metal hydride battery and zinc-air battery, and new member of lithium ion battery as shown in **Table 1.2**.

Table 1.2 Characteristics of the major secondary battery systems[3]

	Lead-acid	**Ni-Cd**	**Ni-MH**	**Li-ion**
Anode	Pb	Cd	Metal Hydride	C
Cathode	PbO_2	NiOOH	NiOOH	$LiCoO_2$
Electrolyte	H_2SO_4 (aq)	KOH (aq)	KOH (aq)	Organic solvent+ Li salt
Cell Voltage (V)	2.0	1.35	1.35	3.6
Capacity (mAh g^{-1})	120	180	210	140
Wh kg^{-1}	35	40	90	200
Wh L^{-1}	70	100	245	440

As the first type of practical rechargeable battery, lead-acid battery has many advantages such as relatively low cost, large availability of raw materials (lead and sulphur), ease of manufacture and long cycle life. Ni-Cd and Ni-MH batteries are the representatives of alkaline rechargeable batteries [4, 5]. Ni-Cd batteries are characterized by long life, relatively high power rates of discharge and charge, almost constant discharge voltage and the capability to operate at low temperatures. But Ni-Cd batteries are expensive and harmful to the environment as Cd is employed in negative electrode. Ni-MH battery is a more recent cell technology than nickel-cadmium. The replacement of cadmium not only increases the energy density, but also produces a more environment friendly power source. However, the Ni-MH battery has lower rate capability, poorer charge retention and less tolerance to overcharge than the Ni-Cd batteries.

Rechargeable LIBs were first successfully commercialized by Sony in 1991[6] using $LiCoO_2$ as the cathode material and carbon as the anode material. Since then, LIBs have been widely used for the portable electronic devices due to their high energy density and design flexibility compared with the other existing battery systems as listed in **Table 1.2**. Indeed, LIBs are produced by billions of units

per year as shown in **Figure 1.1**. In addition to the portable applications, LIBs are also drawing much attention for their potential use in large-scale applications such as HEV.

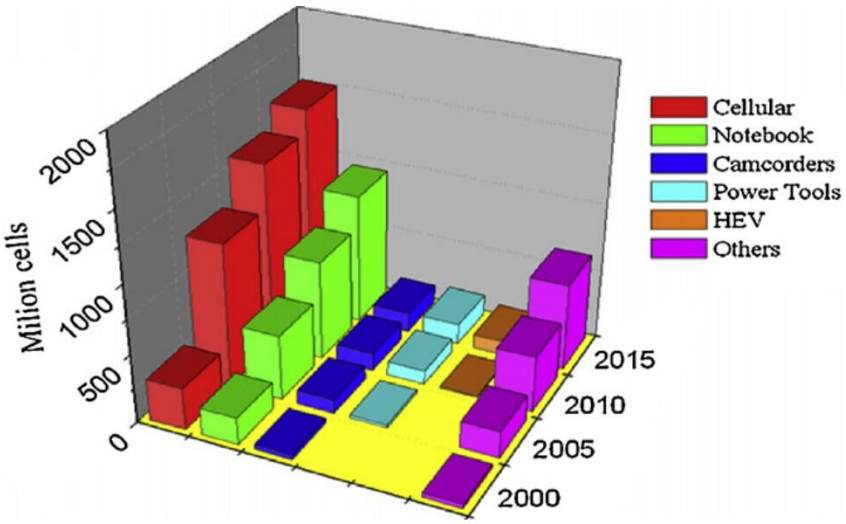

Figure 1.1 Evolution of the LIBs sale in the electronic and HEV market[7]

2. Literature Review

2.1 Basic knowledge of LIBs

LIBs technology has been tremendously developed in the past two decades, leading to the booming of the portable electronics market. Because of the high electronegativity and low molecular weight of lithium (6.94 g mol^{-1}), LIBs favor a high energy density and high power density that is far beyond the lead acid, Ni-Cd and Ni-MH battery systems.

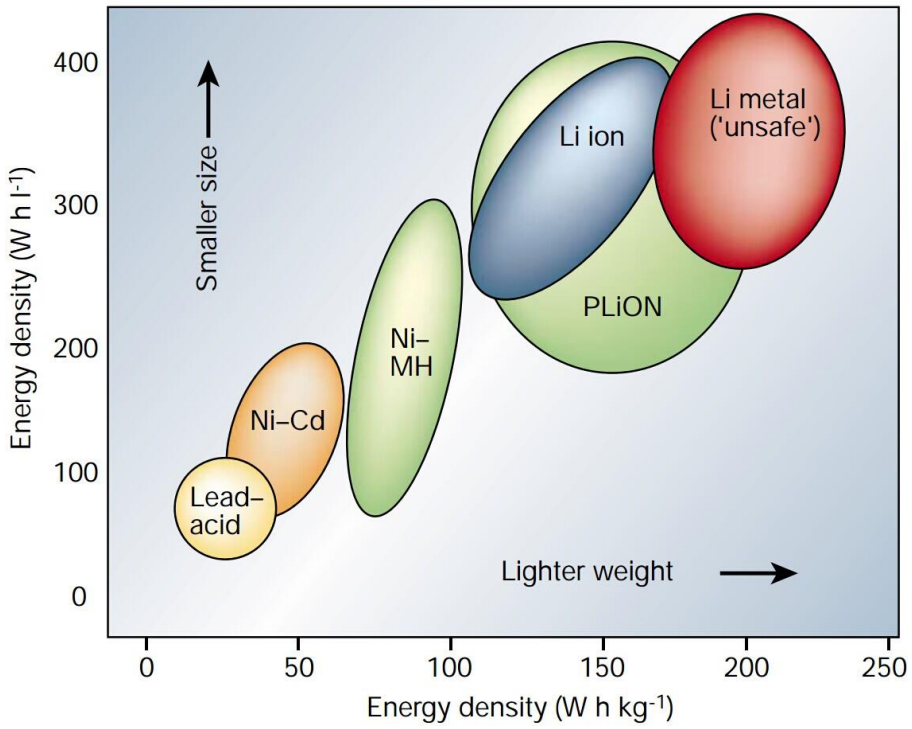

Figure 2.1 Comparison of the different battery technologies in terms of volumetric and gravimetric energy density [7]

2.1.1 Operation principles of LIBs

In LIBs, both electrodes are composed of insertion materials which can insert and de-insert lithium ions and electrons reversibly over many cycles. There are numerous cathode and anode materials that have been developed for LIBs over the past two decades; however, the working principle remains the same as shown in **Figure 2.2**. $LiCoO_2$ and carbon based materials, specifically, graphite are used here as the cathode and anode, separately, and both of them possess layered structures which facilitate the reverse insertion and extraction of Li^+.

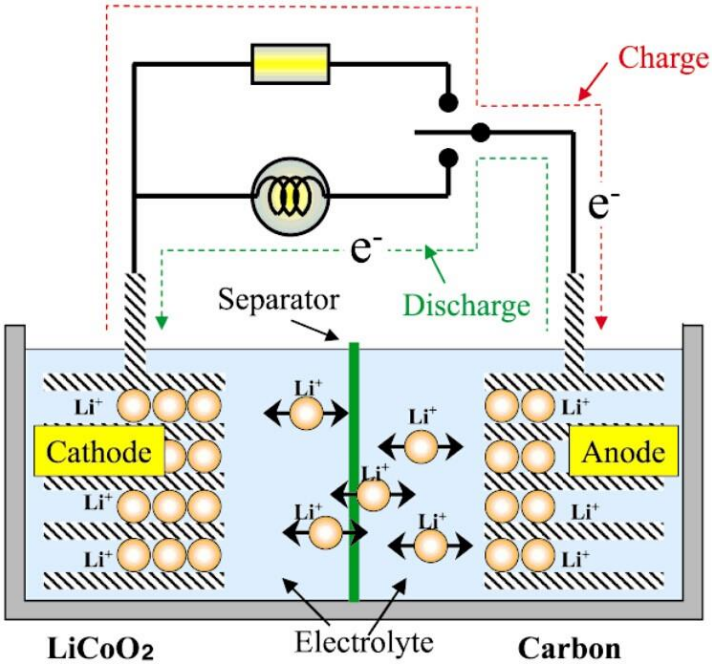

Figure 2.2 Operation principles of a typical lithium ion battery [8].

During the charging process, lithium ions are extracted by electrochemical oxidation from the cathode, migrate through the electrolyte, and then get intercalated into the layers of the graphite anode by electrochemical reduction, while the electron flow travels from the cathode to the anode through the external circuit at the same time. Conversely, during the discharge process, lithium ions are extracted from the anode by electrochemical oxidation, and then inserted into the cathode by electrochemical reduction, accompanied by electron flow from the anode to the cathode through the external circuit again. All lithium species are in the ionic state in both anodes and cathodes. This is why this battery system is named “lithium ion battery”.

2.1.2 Basic thermodynamics and kinetics of LIBs

LIBs thermodynamics in terms of the electrode potentials can tell us the theoretical and open circuit cell voltage of the cell and also how feasible it is for a cell reaction to occur. On the other side, it is also necessary to consider the LIBs kinetics in order to obtain a better understanding of what the actual cell voltage may be, because the charge transfer and the rates of the reactions at the electrodes can usually play the limiting roles. Therefore, the main thermodynamic and kinetic issues that affect battery performance are summarized in the following section.

The characteristics of a LIB follow the rules of thermodynamics and kinetics for electrochemical reactions. [9] The driving force for an electrochemical cell to deliver electrical energy to an external

circuit is the decrease of the standard free energy ΔG^0. Assuming the process occurs under isothermal and isobaric conditions where the system is an ideal cell with no volumetric work and the process is well reversible, the standard cell potential is then related to the Gibbs free energy of the system as

$$E^0 = - \Delta G^0/nF \qquad \text{Equation 2.1}$$

where n is the number of electrons transferred per mole of the reactants and F is the Faraday constant. In particular, from a view of the LIBs, E^0 can also be determined by the difference between the standard electrode potential at the cathode, E^0 (cathode), and the standard electrode potential at the anode, E^0 (anode) as

$$E^0 = E^0(\text{cathode}) - E^0(\text{anode}) \qquad \text{Equation 2.2}$$

The standard electrode potential, E^0 is the potential generated by that reaction under the condition that the reactants and the products are in their standard state in relation to a reference electrode. (A reactant or product is defined to be in its standard state when the component in a condensed phase is at unit activity and any component in the gas phase is at a partial pressure of 1 atmosphere.) In aqueous systems, the standard hydrogen potential is taken as the universal reference electrode, whose potential is defined as zero.

In order to obtain a true estimate of the actual open circuit cell voltage in the fully charged, the theoretical cell voltage is modified by the Nernst equation, which takes into account the nonstandard state of the reacting component as

$$E = E^0 - RT\ln Q \qquad \text{Equation 2.3}$$

where $Q = a_{products}/a_{reactants}$ is the chemical quotient for the overall cell reaction and R is the gas constant (R = 8.31 J/kmol). Q is represented in the same way as the equilibrium constant K, except that the activities and partial pressures in Eq. 2.3 reflect the actual nonstandard values prevailing in the system. The Nernst potential in Eq. 2.3 will change with time due to the self-discharge by which the activity (or concentration) of the electroactive component in the cell is changed. Thus, the nominal voltage is determined by the cell chemistry at any given point of time.

The operating voltage will always be lower than the theoretical voltage due to polarization and the resistance loss (IR drop) of the battery. And the practical voltage is dependent on the current (I) drawn by an external load and the cell resistance, R, in the path of the current. Thus, not all of the theoretically energy stored in the electrodes can be fully converted into electrical energy, and part of

it is given off as waste heat. **Figure 2.3** shows the relationship between cell polarization and discharge current, and there are three types of polarization losses:

(1) Activation polarization loss η_a, which is related to the kinetics of electrode reactions;

(2) Concentration polarization η_c, which is due to mass transport limitations during cell operation; and

(3) Ohmic polarization IR_i, which is related to the internal impedance of the cell.

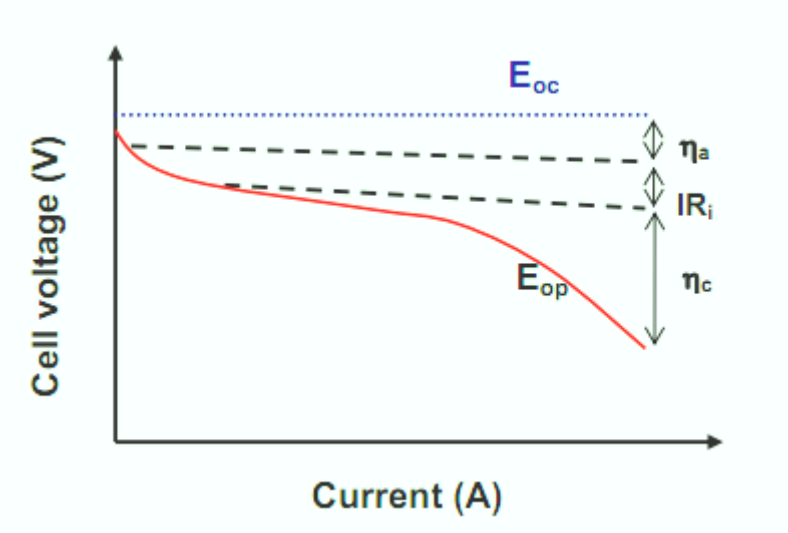

Figure 2.3 Variation of cell voltage with operating current illustrating polarization

Polarization rises in order to overcome any activation energy for the electrode reaction and/or concentration gradients near the electrode. These factors are dependent upon electrode kinetics and vary with temperature, state of charge and the age of the cell.

When connected to an external load R, the cell voltage E_{op} can be described as

$$E_{op} = E_{oc} - (\eta_a + \eta_c + IR_i) \qquad \text{Equation 2.4}$$

Only when operating at a very low current, the cell voltage will be close to the open circuit voltage E_{oc} and the cell will deliver most of the theoretically energy.

When an electrode is in contact with the electrolyte, the charge on the electrode will attract ions of opposite charge in the electrolyte to the electrode surface, and the dipoles in the solvent will align to form a solid electrolyte interphase (SEI) film on electrode surfaces. As the SEI films reach a certain thickness, they become electronic insulators. Hence, any possible electrical conductance can be due to either anionic or cationic migration, through the films under the electrical field. Meanwhile, a thin layer with double layers of charges between the electrode and the electrolyte, which is called the

electrical double layer as shown in **Figure 2.4,** is formed as well. The electrochemical reactions take place in this layer, where all atoms or ions that are reduced or oxidized must pass through. Thus, the ability of ions to pass through this layer controls the kinetics, and is therefore the limiting factor in controlling the electrode reaction rate. The energy barrier toward the electrode reaction, described as the activation energy of the electrochemical reaction, lies across this electrical double layer.

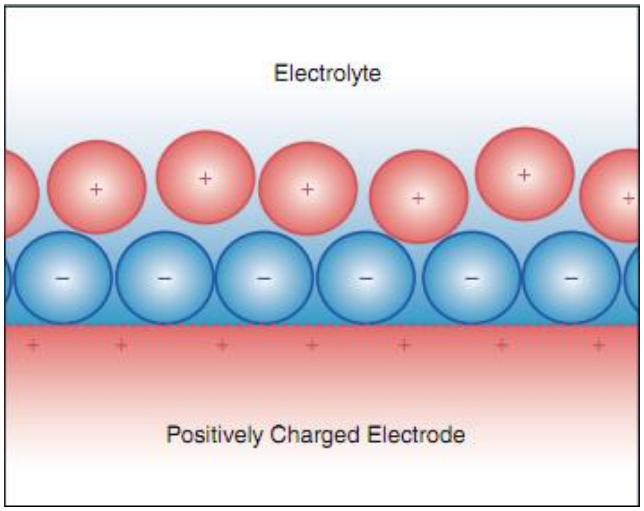

Figure 2.4 Illustration of the electrical double layer [2]

Specifically, the rates of the electrochemical reactions can be determined by the Arrhenius relationship,

$$k \propto \exp (- Q/RT) \qquad \text{Equation 2.5}$$

where k is the activation energy for the reaction, T is the temperature in Kelvin, and R is the universal gas constant. In this case, the rate of the reaction can be measured by the current. Because the current is the amount of charge produced per unit of time, it is in proportional to the number of electrons, in other words, proportional to the rate of the reaction.

When an electrode is not at equilibrium state, an overpotential exists, given by

$$\eta = E - E_0 \qquad \text{Equation 2.6}$$

where η is the overpotential, E is the actual potential, and E_0 is the equilibrium potential. Overpotential is synonymous with polarization. The relationship between the current and the overpotential during the oxidation or reduction reaction of an electrode can be evaluated by the Tafel equation as

$$i_a = i_{0,a} \cdot \exp(\alpha z F \eta_a / RT) \qquad \text{Equation 2.7}$$

where i_a is the electrode current density, $i_{0,a}$ is the exchange current density at the electrode, α is the "symmetry factor" of the electrical double layer, nominally 0.5, and η_a is the electrode overpotential. According to Eq. 2.7, the greater the operating current density is, the lower the electrode potential is. The overpotential contributes to the reduction in the cell potential during discharge, signifying the energy barrier for the electron transfer reaction. On the other hand, during charging, the electrode potential increases with the applied current, thus, increasing the potential required for charging the cell back to its original state (by electrochemical reduction in this example). For a faster charging rate, a higher current density is desirable, but this may also require a higher applied voltage (higher energy) to overcome the increasing overpotential.

In summary, in order to maximize power density, it is important to achieve the most optimum value of cell potential at the lowest overpotential and internal resistance. Normally, at low current densities, overpotential derived from an activation energy barrier is related to electron transfer reactions, while at a higher current density, the transport of ions becomes rate limiting, thus giving rise to a current limit. Ohmic losses increase with increasing current as well, and can be further enhanced by the increased formation of insulating phases during the progress of charging.

Currently, the application of LIBs for high power devices such as EVs are under intensive research, however, the required high power density, or high rate performance of LIBs, is still a big challenge. There are many factors affecting the high rate performance of LIBs. Li^+ transport/diffusion on the cathode side, sometimes as well as the electrical conduction of the cathode (when the cathode materials are poor electrical conductors) is believed to be the key rate limiting step in a LIB system. To improve the powder density of the LIBs, various approaches have been explored and briefly summarized below:

1) Increase the surface area of electrode by synthesizing the electrode materials in nanoparticles [10, 11], nanowires [12, 13], or other nanostructures [14, 15]. This can effectively increase the charge/discharge rate of LIBs.

2) Increase the intrinsic Li^+ diffusion. The Li^+ diffusion in the solid frameworks is determined by the Li^+ diffusion length and the site activation energy. Besides, it is also closely related to the type and density of defects. Therefore, decreasing the particle size of the cathode materials can effectively shorten the Li^+ diffusion length and increase the Li^+ diffusion rate. Moreover,

cation or anion doping may modify the site activation energy or produce more defect sites which also can facilitate the Li^+ diffusion.

3) Enhance the electrical conductivity of the cathode. In commercial LIBs, it has been a routine to add small amount (3-8 wt %) of carbon black in the cathode to facilitate the electrical conductivity. Other materials of good electrical conductivities, such as carbon nanotubes [16, 17] and metal nanowires [18], have also been used as conductive additives instead of carbon blacks in order to form a better conductive 3-D network with much less volume and weight percentages of the overall electrode. Besides, carbon or metal coatings on the particle surface of cathode materials have been extensively studied, especially for the cathode materials with poor electrical conductivities, such as $LiFePO_4$. In very recent work, Kang and Ceder [19] applied a phase-segregation induced coating layer on non-stoichiometry $LiFePO_4$ and greatly improved the rate capability of $LiFePO_4$. A cycling rate as high as 600C was achieved, but only when using high carbon content.

2.1.3 Electrochemical evaluation of LIBs

2.1.3.1 Capacity

The theoretical molar capacity of a LIB is the quantity of electricity involved in the electrochemical reaction. It is denoted as Q_{charge} and is given by

$$Q_{charge} = xnF \qquad \text{Equation 2.8}$$

where x is the number of moles of a chosen electroactive component that take place in the reaction, and n is the number of electrons transferred per mole of reaction. The mass of the electroactive component can be calculated as

$$M = xM_r \qquad \text{Equation 2.9}$$

where M denotes the mass of the electroactive component in the cell and M_r the molecular mass of the same component. The capacity is conventionally expressed as Ah kg^{-1} or mAh g^{-1} in terms of mass, thus often called specific capacity, $C_{specific}$

$$C_{specific} = nF/M_r \qquad \text{Equation 2.10}$$

It is important to note that, in a LIB, the mass may refer to the final cell mass including packaging or the mass of the electroactive components alone.

In practice, the full battery capacity could never be realized, as there is a significant mass contribution from nonreactive components including binders, conducting particles, separators, electrolytes, current collectors, substrates and packaging staff. Additionally, the chemical reactions can't be 100% completed either due to unavailability of reactive components, inaccessibility of active materials or poor reactivity at the electrode/electrolyte interface. The capacity is strongly dependent on the load and may decrease rapidly at high current rates due to increased overpotential losses and ohmic losses. And this problem can get worse as the electrochemical reactions moving on. At higher operating currents, a battery will be discharged faster.

2.1.3.2 Cycle life

The cycle life of a rechargeable LIB is generally expressed in terms of the number of discharge/charge cycles it can undergo before its capacity falls to 80% of the initial value.

2.1.3.3 Energy density

The energy density is the energy that can be derived per unit volume of the cell and is often quoted as Wh lt^{-1}, where lt stands for liter. This value is dependent upon the density of the components and the design by which the various materials are interfaced together. In many applications, availability of space for placing a battery must be minimized and thus, the energy density should be as high as possible without greatly increasing the volume of the battery to reach a given energy level.

2.1.3.4 Specific energy density

The specific energy density (Wh kg^{-1}) is the energy that can be derived per unit mass of the cell (or sometimes per unit mass of the active electrode material). It is the product of the specific capacity and the operating voltage in one full discharge cycle. Both the current and the voltage may vary within a discharge cycle and, therefore, the specific energy, E, is calculated by integrating the product of the current and the voltage over time

$$E = \int V \cdot I dt \qquad \text{Equation 2.11}$$

The discharge time is related to the maximum and minimum voltage thresholds and is dependent upon the state of availability of the active materials. The maximum voltage threshold may be related to an irreversible drop of voltage in the first cycle, after which that part of cycle is not available. The minimum threshold voltage may be determined by a lower limit, below which the voltage is deemed to be too low for practical use due to the irreversible energy loss and inadequate energy and power supply of the system. Since batteries are used mainly as energy storage devices, the amount of

energy (Wh) per unit mass (kg) is the most important property for a battery. It must be noted that the quoted values only apply for the typical rates at which a particular type of battery is discharged.

2.1.3.5 Power density

The power density is the power that can be derived per unit mass of the cell (W kg^{-1}). At higher current density, a higher power density can be expected; however, the specific energy tends to fall off rapidly due to decrease of the capacity. In order to derive the maximum amount of energy, the current or the power drain must be at the lowest practical level. For a given cell, increasing the surface area of the electrodes can increase the cell current at a given current density, thus, delivering higher power. The most efficient way to deliver a higher power density is to increase the effective surface area of an electrode while keeping the nominal area constant.

2.1.3.6 Temperature dependence

The rate of the electrochemical reactions in LIBs is temperature dependent according to kinetics theories (**Figure 2.5**). The internal resistance also varies with temperature. A low temperature will give a higher internal resistance. At very low temperatures, the electrolyte may freeze, giving a lower voltage with ion movement impeded. At very high temperatures, the chemicals may decompose, or there may be enough energy to activate irreversible side reactions and lead to the capacity loss. The rate of voltage decrease during discharge will also be higher at lower temperatures.

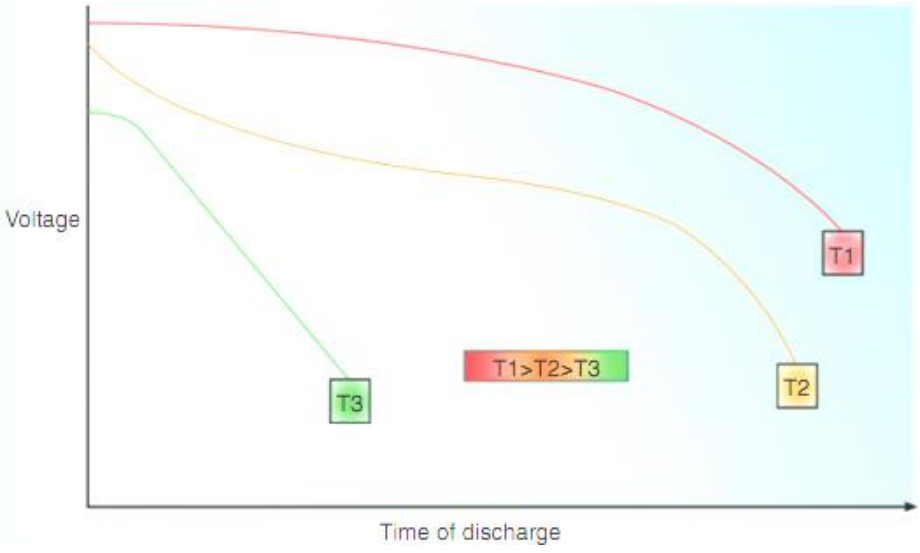

Figure 2.5 Effects of temperature on battery capacity [2]

2.1.4 Essential components of LIBs

A battery is a device that converts chemical energy into electrical energy and vice versa [20]. It contains three key parts: an anode, a cathode, and an electrolyte. In the case of LIBs, the anode acts as the source of Li^+ while the cathode is the sink for Li^+ during the discharging process, and then they swap their roles in the charging process. The electrolyte serves to separate the ionic transport and electronic transport. In a perfect battery, the transport number of Li^+ will be unity in the electrolyte. In addition, a separator located between the two electrodes is always essential to prevent electrical short circuit of the batteries.

2.1.4.1 Cathodes

There are several factors affecting the performance of LIBs including the characteristics of anode, cathode, electrolyte and separator as well as the cell fabrication process. Among them, cathode performance plays the key role.

Sony introduced the commercial LIBs successfully into the market in 1991 using $LiCoO_2$ as the cathode [6], and more than two decades later; this is still a popular cathode of choice. Nonetheless, the research on cathode materials has been more intense than ever and remarkable success has been met at both the practical and the theoretical level. Improvement of the $LiCoO_2$ synthesis technology has doubled the specific energy of the current commercial batteries from 80 to 165 Wh kg^{-1}. More importantly, numerous new cathodes have been introduced and developed and showed great potential as future cathodes in the market.

In terms of the cathodes, a wealth of knowledge has been acquired including: synthesis techniques, reaction mechanisms, effect of particle size, interfaces, structural modifications, effect of doping, electrochemical and thermal stability. This knowledge allows revisiting the criteria of choice of an efficient cathode and will be discussed in detail in a following section.

2.1.4.2 Anodes

Lithium metal with a specific capacity of 3860 mAh g^{-1} was the first choice of anode material for a lithium battery. However, lithium dendrites formed on the anode surface will inevitably grow through the separator during cycling, causing cell failure and even fires due to the short circuit [21, 22]. Because of the poor safety, lithium metal anode was abandoned soon after its birth. Currently, most of the commercialized anode materials are based on carbon materials which typically have a stable layered structure to host Li^+ as well as a relatively high theoretical capacity. Besides, a large

number of alternative anode materials are also being studied to overcome the disadvantages of graphite anode.

(a) carbon-based anode materials

The major criteria of selecting a carbon-based anode lie in the capacity and electrochemical potential. A large number of carbons including graphite, carbon black, active carbons, carbon fibers and etc. have been used as anode materials. Graphite is of particular interest due to its high gravimetric specific capacity of 372 mAh g^{-1} with a lithium intercalation mechanism of LiC_6 [23].

Figure 2.6 shows the layered structure of graphite with an ABAB stacking sequence and many six carbon rings in each layer. The interlayer distance is 3.35Å larger than the ionic radius of Li^+ and thus provides a wide path for Li^+ intercalation. After the Li^+ insertion, the stacking sequence evolves to AAA as shown in **Figure 2.7**. At the first Li^+ intercalation stage, a solid electrolyte interface (SEI) film unavoidably appears on the surface of the graphite because of the decomposition of the organic solvent at this negative potential. This film can prevent further co-intercalation and decomposition of the solvent molecules and therefore allows only Li^+ to migrate between the electrode and electrolyte [24].

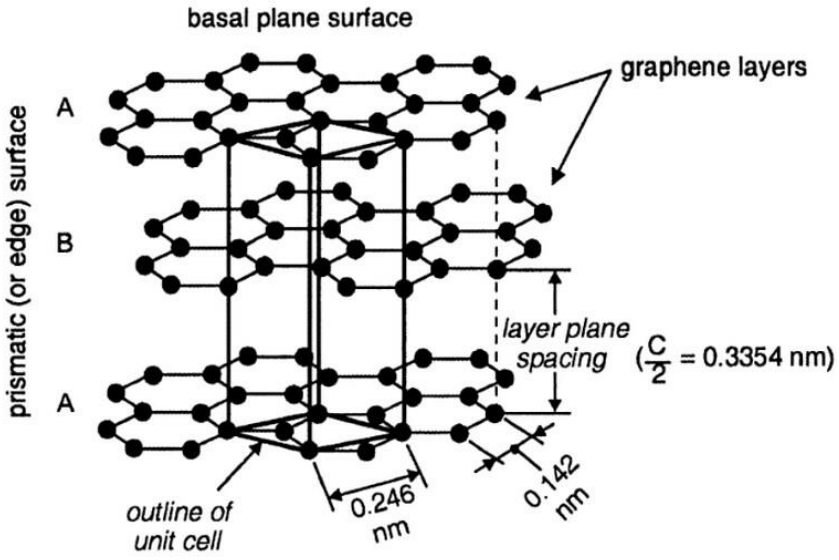

Figure 2.6 Crystal structure of graphite before Li^+ intercalation [25]

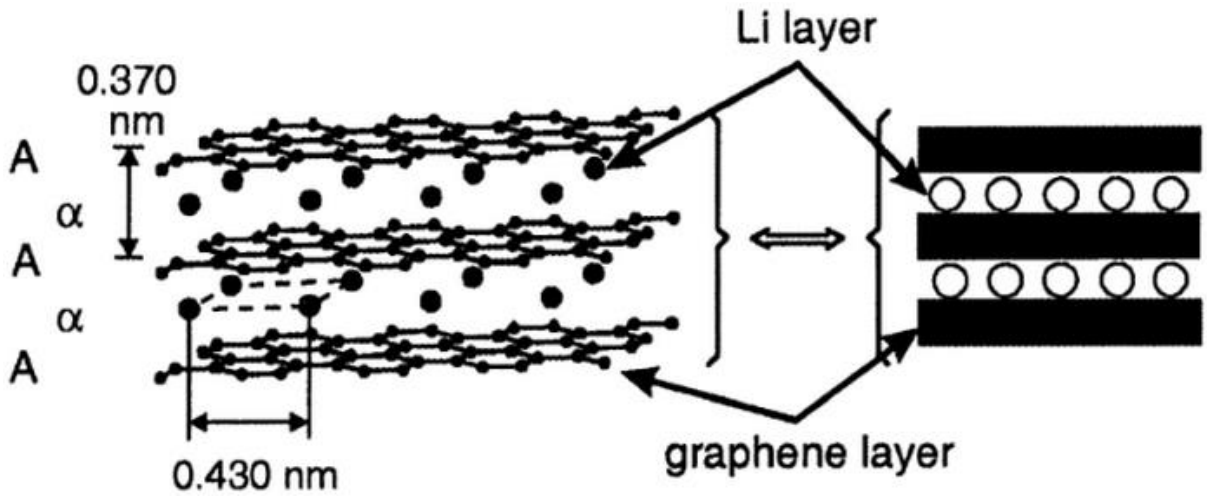

Figure 2.7 Crystal structure of graphite after Li^+ intercalation [25]

Currently, nanotechnology has also been applied in the energy materials area. Many researchers have been exploring the use of nano-sized carbons including nano-porous graphitized carbons, carbon nanotubes [26, 27] and graphene as anode for LIBs.

Both single and multi-wall nanotubes have been investigated. Typically, the reported Li^+ storage capacity exceeds the values of graphite [28-31]. By ball-milling, the carbon nanotubes can generate a higher capacity which is ascribed to the increased defect density and the reduced nanotube length that can facilitate Li^+ diffusion [32]. However, regarding the Li^+ storage sites in the carbon nanotubes, no convinced results have been reported and much structural and electronic work has been performed to elucidate the Li^+ storage mechanisms in carbon nanotubes.

Graphene, a single layer of carbon atoms in a two-dimensional honeycomb lattice, was found to be an exciting alternative of carbon anodes for LIBs due to its superior electrical conductivity, high surface areas, chemical tolerance and broad electrochemical windows [33]. Theoretically, the specific capacity of graphene should exceed that of graphite due to the fact that both sides of the graphene can store Li^+. Besides, multilayer adsorption at a high chemical potential of Li^+ can give rise to the Li^+ storage capacities [34]. Some graphene materials such as graphene nanosheets and graphene paper [35] have been studied as high capacity anode materials. For example, an anode consisting of chemical-reduced graphene nanosheets delivered a reversible capacity of 650 mAh g^{-1} in the first cycle and kept more than 500 mAh g^{-1} in the first 100 cycles [36]. Another anode made by highly disordered graphene nanosheets also displayed high reversible capacity (794-1054 mAh g^{-1}) and good cyclic stability. The greatly enhanced capacity is suggested to be mainly ascribed to the additional Li^+ storage sites such as edges and defects of the highly disordered structure [37].

(b) Other anode materials

Some main-group elements (e.g., Si, Ge, Sn, Al, Bi, Zn, and Sb) can alloy with Li^+ at a low potential [38]. Representatively, Si and Sn can accommodate Li^+ up to $Li_{4.4}M$, generating theoretical specific capacities as high as 4200 and 993 mAh g^{-1}, respectively. Their volumetric capacities also exceed that of graphite. However, their large volume changes on alloying and de-alloying, as much as 300%, inevitably leads to severe stress fracturing, loss of contact between particles and therefore, fast and significant capacity fade during cycling [39]. Besides, the poor electronic conductivity of Si impedes fast lithiation [40]. To overcome these drawbacks, substantial efforts have been employed on the synthesis of nano-scale materials and dispersing the active component in a rigid matrix to form composite structures [41].

There is also an interest in developing titanate anodes. They can be operated at relatively high potentials to provide inherent overcharge protection instead of relying on careful electronic control of charging. This would benefit for large-scale batteries such as those for HEV. Taking $Li_4Ti_5O_{12}$ for example, its theoretical capacity is about 160 mAh g^{-1} and the Li^+ intercalation potential is around 1.5 V providing inherent overcharge protection [42, 43]. Specifically, it has zero-strain Li^+ insertion host, implying an unlimited cycle life. Besides, the absence of SEI film on its surface allows high rate and low temperature operations [44].

TMOs (TM = Co, Ni, Cu, Fe) with interstice-free rock-salt structure are capable of incorporating more than one Li^+ per 3d metal, hence giving much higher electrochemical capacities than those of graphite anodes [45]. TMOs are reduced to metal nanoparticles through a conversion reaction:

$$M_xO_y + 2yLi^+ + 2ye^- \leftrightarrow yLi_2O + xM \qquad \text{Equation 2.12}$$

Meanwhile, Li_2O matrix is formed *in situ* during the first reduction of the metal oxide and hosts the highly reactive metallic nanodomains that enable the feasibility of the reverse reaction [46]. The reversible electrochemical Li^+ storage proceeds more easily in a nano-sized electrode. Therefore, research on TMOs has focused on nano-scale such as reducing particle size or using nanocomposites as the anode materials. Self-supported Co_3O_4 mesoporous nanowire arrays on a Ti substrate delivered a first discharge capacity of 1124 mAh g^{-1} and maintained a stable capacity of 700 mAh g^{-1} after 20 cycles. Even at 20C, a capacity of 450 mAh g^{-1} could still be retained due to the novel hierarchical and mesoporous structure [47]. In the case of Cu_xO_y electrodes, a urchin-like CuO nanoparticles produced from the oxidation of Cu_2O nanocubes achieved a capacity above 560 mAh g^{-1} for up to 50 cycles. Such an impressive performance was believed to come from the advantageous

electrode configuration with structural robustness [48]. Iron oxide is another type of attractive anode material with low cost, low toxicity and high abundance. An anode fabricated with Fe_3O_4 nanorods and carbon nanotubes reached the theoretical reversible capacity of 1000 mAh g^{-1} at 1C rate and a stable capacity of 600 mAh g^{-1} at 10C [49].

Apart from the prominent virtues of low cost and high capacity, the TMO anode suffers from two main hurdles. One is volume variation caused by the conversion reaction upon cycling. And the current nano technology is an efficient approach to relieve this issue. Another problem is the poor energy efficiency which is related to the large voltage separation between the charge and discharge profiles. To overcome this limitation, temperature considerations and electrode concepts involving only two solid phases have been proposed [50].

Another type of high-capacity anode materials attracting much attention in the past a few years are the graphene-based hybrid nanocomposites (such as TiO_2/graphene [37], SnO_2/graphene [51, 52], Mn_3O_4/graphene [53], Co_3O_4/graphene [54]). Graphene provides not only a buffer to relieve the cracking of metal oxides, but also a good ion and/or electron transport medium for the electrode. Representatively, a Co_3O_4/graphene composite produced by solid state pyrolysis of structurally-defined organic-cobalt precursors was developed recently. Its initial reversible capacity reached 920 mAh g^{-1}, and even after 20 cycles, the capacity was almost the same as the first cycle. Another example is the hybrid materials of Mn_3O_4 nanoparticles on reduced graphene oxide sheets. Graphene connected the Mn_3O_4 nanoparticles with the current collector, thus enabled the highly electrically insulating Mn_3O_4 to deliver a high specific capacity up to 900 mAh g^{-1} (near its theoretical capacity) with good rate capability and cycling stability [53].

2.1.4.3 Electrolytes

Besides the two electrodes, the electrolyte is the third essential component of a battery. A lithium electrolyte is usually a solution of one salt in mixtures of two or more solvents. A single-solvent formula is rarely used because of the diverse or even contradicting requirements of the battery application [55]. The basic requirements of liquid electrolytes for lithium batteries are listed below:[25]

- High ionic conductivity to minimize the cell resistance and resistive heating of the device.
- High chemical stability to prevent decomposition of electrolyte on the surface of a highly reducing anode material, e.g. metallic lithium or lithiated graphite, LiC_6, and a highly

oxidizing cathode material such as a delithiated $Li_{1-x}MO_2$ electrode, where M = Co, Ni, Mn or their mixture.

- Electrochemical stability to tolerate the high voltage difference between anode and cathode (>4 V). Not many organic solvents can tolerate such a wide voltage range without being reduced or oxidized.
- Low melting point to provide sufficient conductivity at sub-ambient temperatures and preventing solidification and phase separation.
- High boiling point to ensure safety and prevent explosions resulting from high pressure build-up in the cell.
- Low toxicity to be environmentally accepted for ease of handling, mass production, and waste treatment.
- Low cost to be affordable and compete with existing power sources using aqueous electrolytes.

Based on the required characteristics for lithium battery electrolytes, any solvents consisting of active protons have to be ignored in spite of their excellent power in solvating salts. A wide range of solvents has been studied such as propylene carbonate (PC), diethyl carbonate (DEC), Ethylene Carbonate (EC), dimethyl carbonate (DMC) and ethylmethyl carbonate (EMC). To date, the mixture of EC and DEC solvents at a ratio of 1:1 attracts the most interests. EC has almost equal viscosity and slightly higher dielectric constant than PC but a high melting point (36 ℃). So EC is widely used as an additive to electrolyte solutions to enhance the ion conductivity. DMC can form homogeneous mixtures with EC at any ratio. The benefits from the mixed electrolyte include the suppression of the melting-temperature of EC and higher ion conductivity of DMC. Moreover, even up to 5.0 V, it still stays stable [25]. Other common linear carbonates such as DEC and EMC have the similar advantages as DMC.

Compared to the types of organic electrolyte solvent, the available choice of lithium salts is limited in a narrower range because the small ionic radius of Li^+ leads to a low solubility of the lithium salts in low dielectric media. Most qualified lithium salts are based on complex anions due to the lower melting point and better solubility in low dielectric media than their parent anions [25]. Lithium hexafluorophosphate ($LiPF_6$), which can be considered as F^- complexed by the Lewis acid PF_5, is dominantly used in LIBs. Other lithium salts based on milder Lewis acids e.g. lithium perchlorate ($LiClO_4$) and various lithium borates, arsenates, phosphates and antimonates ($LiMX_n$, M = B. As, P

or Sb, n = 4 or 6) can also keep stable with organic solvents at ambient temperature and attract broad interest from researchers [56].

2.1.4.4 Separators

The separator is located between the cathode and anode. Its main function is to keep the two electrodes apart to prevent electrical short circuits and at the same time allow rapid ionic transport between them [57]. Currently, the most popular LIBs separators are polyolefin membranes, which are made of polyethylene (PE), polypropylene (PP) or laminates of PE and PP. These separators provide excellent mechanical properties and chemical stability with acceptable cost. Additionally, they function as a safety device. When the cell temperature increases above the separators' melting point (about 130 ℃), they will shut down their pores, thus effectively stopping Li^+ transport and preventing further overcharging of the battery.

2.2 Cathode materials of LIBs

Compared with the high specific capacity of anode materials, the cathode is probably the most limiting component to determine its performance. The following section will introduce the fundamental requirements of a suitable cathode material and then make a brief summary of the cathode materials with three different crystal structures that are of particular interests to researchers in the last two decades.

2.2.1 Design strategy of cathode materials

Based on thermodynamic and kinetic considerations, the key requirements for a good cathode material in rechargeable LIBs are as follows:[20]

- The material contains a readily reducible/oxidizable ion, for example, a TM ion;
- The material reacts with Li^+ in a reversible manner which dictates an intercalation reaction in which the host structure essentially does not change as Li^+ are added;
- The material reacts with Li^+ with a high reaction free energy:
  - High capacity, preferably at least one Li^+ per TM ion
  - High voltage, preferably around 4 V for high-energy storage
  - The material reacts with Li^+ rapidly both on insertion and extraction for high power density, which can then replace the Ni/Cd battery or be recharged using HEV regenerative braking

- The material is a good electronic conductor, which:
  - allows for the easy addition or removal of electrons during the electrochemical reaction
  - allows for reaction at all contact points between the cathode material and the electrolyte
  - minimizes the need for inactive conductive agents that reduce the overall energy density.
- The material is stable without serious structure change or degradation over long-term cycling

From the view of practical applications, some other factors have to be considered as well [25].

- A favourable interface formed by contacting with the electrolyte
- A simple and reproducible synthesis procedure for material with desired particle size and morphology
- The material has to be easily processed into a practical electrode

As the particle size distribution and morphology will make significant impact on the cathodes performance, this project aims to design cathodes in the nano-scale. Nanomaterials have the genuine potential to enhance the LIBs performance, while some of their disadvantages can't be ignored. A brief summary of the pros and cons of nanomaterials is given in Table 2.1 as shown below:[58]

Table 2.1 Advantages and disadvantages of nanomaterials

Advantages	disadvantages
Reduced Li^+ diffusion paths	Complicated synthesis process
Enable bulk-impossible reactions occur in nano-sized particles[59]	Significant side reactions with electrolyte on the surface
Enhanced electron transport[60]	Reduced volumetric energy density
Increased surface area for more electrode-electrolyte contact	
Modified chemical potentials for lithium ions and electrons	
Better accommodation of the lattice strain over cycling	

2.2.2 Traditional cathode materials

During the past three decades, tremendous research efforts have been devoted to investigating the electrochemical performance of a wide variety of cathode materials. In the early era of lithium cells, metal chalcogenides (e.g., TiS_2 and MoS_2) and manganese or vanadium oxides were used as the positive electrodes to pair with the metallic Li or the graphite anode and led to the commercial success of rechargeable LIBs. Afterwards, with decades of study, the research focus on the cathode materials for LIBs has been shifted to hexagonal layered $LiCoO_2$, spinel $LiMn_2O_4$, olivine $LiFePO_4$ and their derivatives, which are the most promising candidates for LIBs to power portable electronics. The following section will make an introduction of typical cathode materials in these three structures in terms of their basic crystal structure, electrochemical and thermal stability, reaction mechanisms, effect of doping and etc.

2.2.2.1 Cathodes with layered structure

$LiCoO_2$ has been the most widely used cathode material in commercialized LIBs. The crystal structure of $LiCoO_2$ is shown in **Figure 2.8** [63]. $LiCoO_2$ has a layered α-$NaFeO_2$ structure with the oxygen in a cubic close-packed arrangement. In a unit cell of $LiCoO_2$, three CoO_2 layers co-exist with an oxygen stacking sequence of ABCABC along the c axis, and the Li^+ ions occupy the octahedral interstitial sites between them. Hence, it is designated as an O3 type layered structure (O represents the coordination environment for the alkali-metal ions and the number 3 represents the number of MO_2 sheets per unit cell).

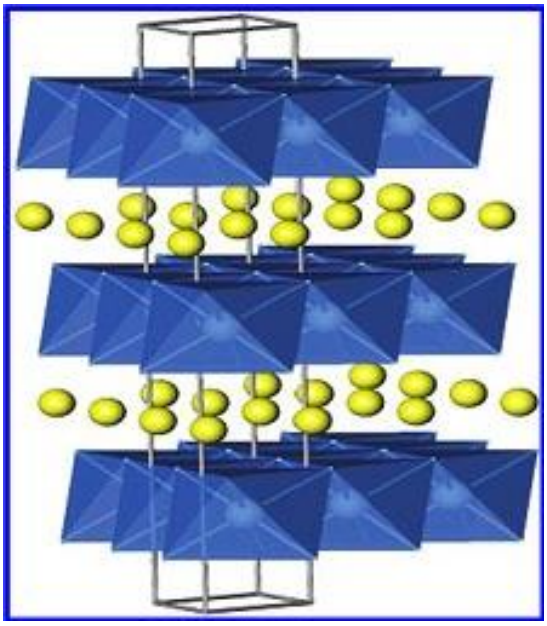

Figure 2.8 α-$NaFeO_2$ layered structure [20]

$LiCoO_2$ has the ideal layered structure due to the large difference in the ionic radius between Li^+ and Co^{3+}, and such a structure provides fast two-dimensional diffusion channel for Li^+. The edge-shared CoO_6 octahedral arrangement provides direct Co-Co interaction and good electronic conductivity for high rate performance. The highly oxidized $Co^{3+/4+}$ redox couple provides a relatively high cell voltage of around 4 V vs. lithium anode, and $LiCoO_2$ is easily synthesized by solid state reactions under 1000 ℃ in a few hours [64]. All these advantageous features have made $LiCoO_2$ an attractive cathode for a long time. However, layered $LiCoO_2$ shows a reversible capacity of only 140 mAh g^{-1}, which is half of its theoretical capacity value, and also, cobalt is toxic and expensive (only about 10 million tons of cobalt deposits are available in the world). Therefore, many other TMs were used to dope or to replace Co in the layered structure. Many $LiTMO_2$ compounds isostructural to $LiCoO_2$ or with similar layered structures have been studied, e.g., $LiNiO_2$, $LiMnO_2$ and $Li(Ni_{1/3}Co_{1/3}Mn_{1/3})O_2$.

$LiNiO_2$ has the same layered structure as $LiCoO_2$, but it is cheaper, less toxic and shows a higher capacity than $LiCoO_2$ [65]. Due to the configuration of low spin Ni^{3+}:$t_{2g}^6e_g^1$, electrons are removed only from the e_g band that barely touches the top of the O^{2-}:2p band, thus most of the lithium can be extracted from $LiNiO_2$ prior to the oxygen loss and a high capacity of around 200 mAh g^{-1} is generated [66-68]. However, $LiNiO_2$ is not an ideal candidate for cathode material due to its intrinsic drawbacks. Firstly, it is difficult to avoid the occupancy of nickel ions to the lithium sites which significantly blocks the diffusion path of Li^+ [69, 70]. Secondly, the low spin Ni^{3+}:d^7 configuration could lead to Jahn-Teller distortion [71] and irreversible phase transitions [72] during cycling which leads to severe capacity fade. Besides, it is not safe at elevated temperatures because of the release of oxygen.

Generally, there are two structures of $LiMnO_2$, the layered structure and the orthorhombic structure. Thermodynamically, the latter is more stable. However, the difference in stability is rather small and the layered phase can be synthesized through soft chemical routes such as ion exchange from the sodium analog $NaMnO_2$ [73] or hydrothermal treatment. Layered $LiMnO_2$ is of great interest due to the low cost and toxicity of manganese and high initial charge capacities of about 270 mAh g^{-1} below 4.3V, although a rapid capacity fade is observed as the structure converts to a pseude-spinel structure during cycling [74]. First principle calculations indicate that the structure transformation to spinel is associated with the charge-disproportionation reaction of Mn^{3+}, which may be effectively depressed by substitution with low valent cations [75]. Another layered $LiMnO_2$ based on manganese oxide nanosheets is also worth mentioning. Flocculation between manganese oxide nanosheets and Li^+ produces the $Li_{0.36}MnO_2$ $0.7H_2O$ [76]. This material exhibited a continuous slope without a plateau

and an initial large capacity over 193 mAh g^{-1}. And the capacity decline was rather limited upon cycling. All these features are in sharp contrast to that of $NaMnO_2$-derived $LiMnO_2$, which suffers from severe capacity fading due to the structure change into spinel upon cycling [73]. In contrast, $Li_{0.36}MnO_2$ prepared by flocculation has a turbostratic layer structure which differs the oxygen atom packing to $LiMnO_2$ and does not change into spinel upon cycling. Besides, electrode materials prepared by this route also show promise for discharging at large current. For example, a large capacity of 79 mAh g^{-1} at a current density of 2 A g^{-1} or 151 mAh g^{-1} at 50 mA g^{-1} was measured for flocculated manganese oxide nanosheets, respectively [77].

The ternary oxides $LiNi_{1-y-z}Co_yMn_zO_2$ created from the solid solution of $LiNi_{0.5}Mn_{0.5}O_2$ and $LiCoO_2$ have been examined by a wide number of research groups. These materials show improved capacities, rate capacities and thermal characteristics over the single metal oxides discussed previously [20]. In particular, the cathode materials with the compositions of $LiNi_{1/3}Co_{1/3}Mn_{1/3}O_2$ [78-82] and $LiNi_{0.4}Co_{0.2}Mn_{0.4}O_2$ [83-85] have been demonstrated to be very promising due to the combined benefits of the structural stability of Mn^{4+} and improved lamellar structure from the high content of Co. However, as these materials do suffer from around 6% anti-site mixing, the rate performance could be further optimized under proper conditions.

The class of layered oxide cathode materials has been the mainstay for high-energy commercial LIBs for small portable applications for the last twenty years. Subsequent research activities have led to the discovery of numerous novel cathode compositions crystallizing in the α-$NaFeO_2$ structure that are pushing forward the boundaries of energy density, rate performance and safety. Future improvements and insights are still required to fully realize the ultimate performance of these materials, especially if they are to be utilized in large-scale vehicular applications.

2.2.2.2 Cathodes with spinel structure

The electrochemical charge/discharge of spinel $LiMn_2O_4$ was firstly reported by Thackeray et al. [86] and was firstly introduced into the commercial cells in as early as 1996 [87]. It has been extensively studied because of its lower cost, lower toxicity and higher rate capability over $LiCoO_2$.

$LiMn_2O_4$ crystallizes in the space group of Fd3m with Li^+ and $Mn^{3+/4+}$ ions occupying the 8a tetrahedral sites and the 16d octahedral sites of the cubic close-packed oxygen array as shown in **Figure 2.9**. In this framework, MnO_6 octahedral shares edges with direct Mn-Mn interaction, providing good electrical conductivity, while the three-dimensional network provides good Li^+ mobility along the 8a-16c-8a channel. All these features result in high rate capability for $LiMn_2O_4$.

However, spinel $LiMn_2O_4$ suffers from severe capacity fade, especially at elevated temperatures, and delivers a slightly lower capacity of around 120 mAh g^{-1} [88]. Several mechanisms have been proposed to explain the capacity fade of $LiMn_2O_4$. The most important factor is the dissolution of manganese from the material lattice into the electrolyte due to a disproportionation reaction of Mn^{3+} into Mn^{2+} and Mn^{4+}. Trace amount of HF generated in the electrolyte can intensify the manganese dissolution [81, 83]. Furthermore, the dissolved manganese ions can get reduced at the anode surface and result in higher impedance in LIB cells. The Jahn-Teller distortion has been identified as a main factor to account for the capacity fade in spinel $LiMn_2O_4$. It will lead to a huge volume change and consequent loss of structural integrity and inter-particle contact [85]. Another important reason for capacity fade in $Li_{1-x}Mn_2O_4$ is the formation of two cubic phases during the charge-discharge process, which results in micro-strain in the lattice due to the differences in the lattice parameters of the two cubic phases [89-93].

A solution to the room-temperature capacity fade is substituting TMs into the Mn sites in the form of $LiTM_xMn_{2-x}O_4$ [94-97]. Solid solutions in which TMs replace the Mn cations increase the average Mn oxidation state. Consequently, the unstable Mn^{3+} cations will be reduced and the material will be less susceptible to the disproportionation reaction. Another effective way to improve the structure stability is to block Mn dissolution by completely encapsulating the spinel particles with oxides that are resistant to acidic HF, and solution-based techniques, such as sol-gel and solution precipitation have been used to enhance the high temperature cycling of the spinels [98-103].

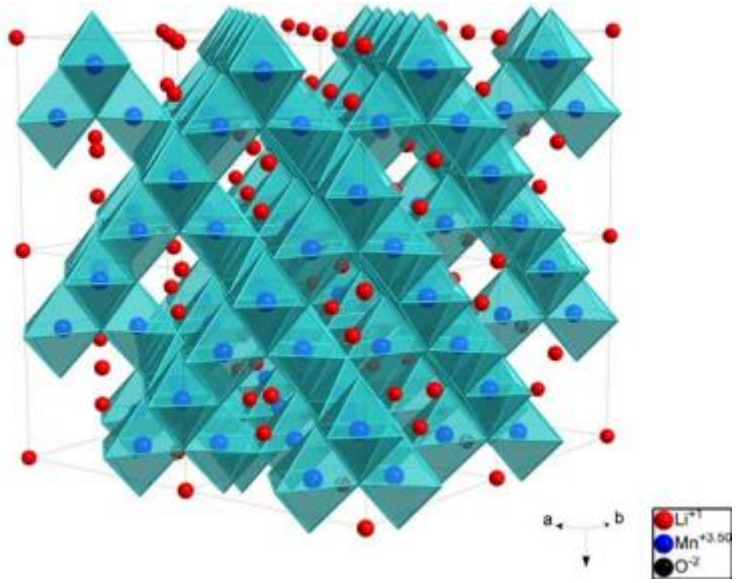

Figure 2.9 Structure of $LiMn_2O_4$ [91]

2.2.2.3 Cathodes with olivine structure

Another promising class of cathode materials is phosphates ($LiMPO_4$) with the olivine structure (Pnma), in which phosphorous occupies tetrahedral sites, TM occupies octahedral sites and Li^+ forms one-dimensional chains along the [010] direction [104].

The most popular phosphate cathode is $LiFePO_4$, which has the ordered-olivine structure as shown in **Figure 2.10**. The framework of the unit cell is constructed by FeO_6 octahedral and PO_4 tetrahedral with Li and Fe ordered into alternate (001) planes [105, 106]. During Li^+ removal, the $FePO_4$ phase is formed but retains essentially the same structure as $LiFePO_4$. The two phase formation gives a flat voltage curve at around 3.4 V, independent of the Li^+ content x in Li_xFePO_4 and a good theoretical capacity of 170 mAh g^{-1} with good structural and chemical stability during cycling.

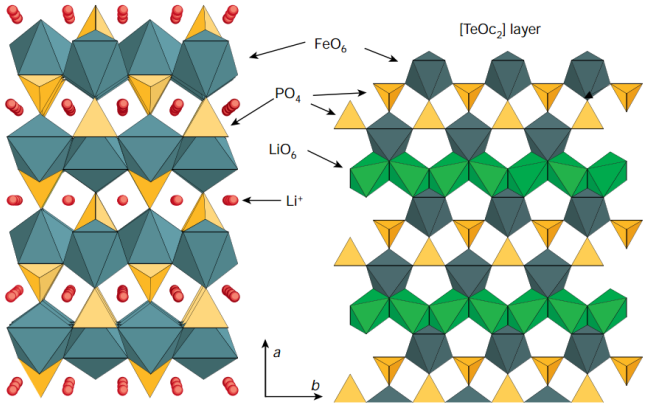

Figure 2.10 The crystal structure of olivine $LiFePO_4$ [7]

However, this material has very low electronic conductivity (10^{-9} S cm^{-1}) at room temperature due to the insulating PO_4 groups and localized $Fe^{2+/3+}$ couple and poor Li^+ conductivity due to the one-dimensional Li^+ diffusion channel. Many studies have focused on improving the electronic and ionic conductivities of $LiFePO_4$. Commonly, carbon coating is considered the most efficient way to improve the electronic conductivity since carbon is always deposited *in situ* on the surface of $LiFePO_4$ particles during synthesis in a reducing atmosphere. Armand et al. carried out the pioneering work and found that $LiFePO_4$ with a carbon coating could achieve almost the theoretical capacity [107, 108]. In addition, carbon can also act as a nucleating agent to decrease the particle size of the final product as well as a reductant to avoid formation of undesirable ferric impurities [109, 110]. Decreasing the particle size is another promising way that can provide shorter diffusion lengths of Li^+ and larger electrolyte/electrode contact interface for Li^+ insertion and extraction. The particles mentioned above are generally less than 200 nm, some even less than 40 nm [111]. Besides, low-level doping of $LiFePO_4$ with some super-valent cations has also drawn a lot of attention since

Chiang and his colleagues [112] claimed they raised the electronic conductivity of bulk $LiFePO_4$ by 8 orders of magnitude to 10^{-2} S cm^{-1} by this route. However, the origin of the increased conductivity is still under debates.

2.2.3 New generation high capacity Li-rich layered cathode materials

Li_2MnO_3 based layered Li-rich cathode materials (LLLs) have become a prevalent candidate in recent years to replace the traditional cathode materials due to their superior specific capacities (up to *ca.* 280 mAh g^{-1}) and high working voltage [113-117]. However, the materials still face some significant challenges that block their way from the laboratory-scale to practical application. Firstly, a systematic understanding of the reaction mechanism on the first and following electrochemical cycles is still retarded for LLLs; in addition, there are also serious debates on the compositions and crystal structures of LLLs before and after electrochemical reactions; finally, the electrochemical performance of LLLs in terms of the rate capability, first cycle charge/discharge efficiency and working voltage stability is desired to be enhanced by advanced material technologies to satisfy the market. The following part will focus on the recent research development of LLLs from these aspects as displayed in **Figure 2.11**.

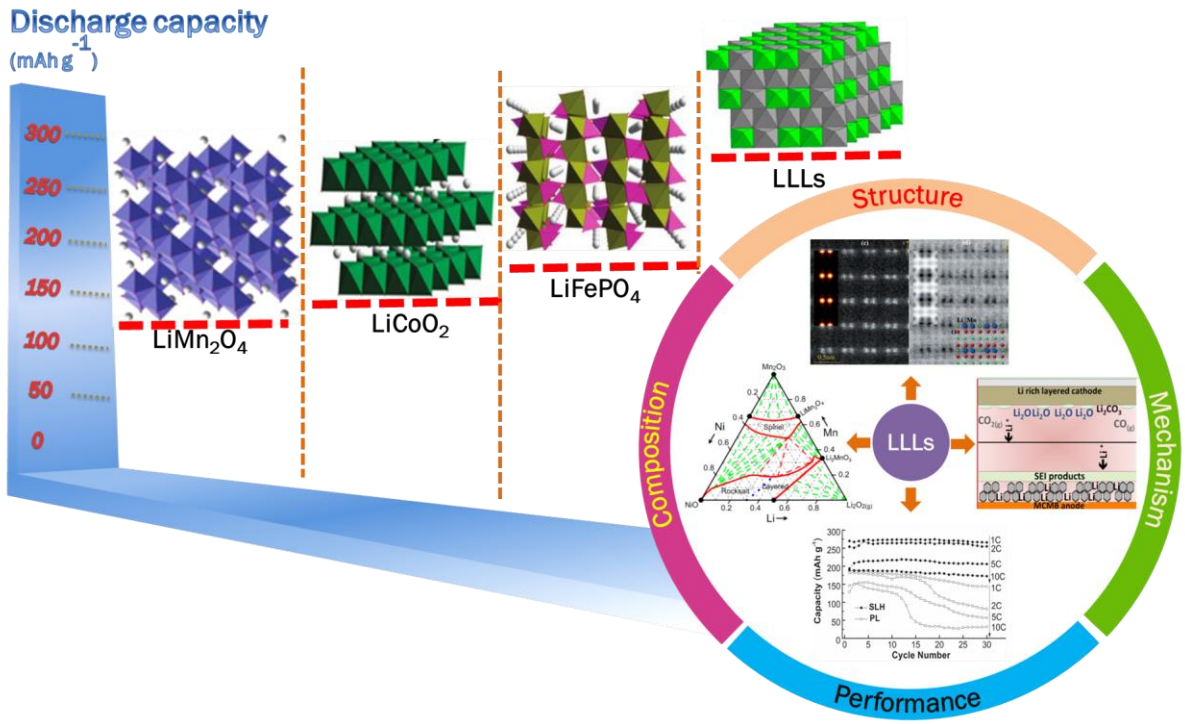

Figure 2.11 Specific capacities of the major cathode materials for LIBs and the current research focuses on LLLs[118-123]

2.2.3.1 Strategy of notation and composition design

LLLs are generally notated in literature either as $xLi_2MnO_3 \cdot (1-x)LiMO_2$ or standard layered formula of $Li_{1+x}M_{1-x}O_2$ (M = Mn, Co, Ni or their mixture) [113]. The first notation represents the co-existence of the Li-rich monoclinic phase (C2/m space group) and the other rhombohedral phase ($R\bar{3}m$ space group) with their ratio of x/(1-x). The other simple one directly shows the composition of the compounds and indicates the excess of Li in comparison to normal layered cathode materials. This is also why they are named as Li-rich materials. Both notations can unambiguously describe the same Li-rich material and will be interchangeably used in this review. For example, as one of the typical LLLs, $Li_{1.2}Mn_{0.6}Ni_{0.2}O_2$ can also be written as $0.5Li_2MnO_3 \cdot 0.5Li[Mn_{0.5}Ni_{0.5}]O_2$ where the ratio of Li/Mn/Ni remains the same.

One of the advantages of the two-phase notation is that researchers are able to draw phase diagrams to illustrate the relationships among the composition, the crystal structure and the electrochemical reaction of a certain LLLs system [113, 120, 124, 125]. In 2007, Thackeray et al. reported the representative triangle phase diagram to reveal the possible reaction pathways of $xLi_2MnO_3 \cdot (1-x)LiMO_2$ composites as the function of the composition [113]. They proposed the Li_2MnO_3 could stabilize the structure at low charging voltage and provide extra lithium in the high voltage region. Concurrently, the original composition will be changed to $xLi_2MnO_3 \cdot (1-x)MO_2$ at the first stage and then end as $(x-y)Li_2MnO_3 \cdot yMnO_2 \cdot (1-x)MO_2$. Such a compositional phase diagram could be very helpful to offer straightforward information of the complex LLLs systems and has been further developed by other senior researchers. Dahn et al. applied a new triangle phase diagram very recently to study the metal site vacancies in Li-Mn-Ni-O systems with less or more lithium than normal LLLs [120]. By detailed analysis of the sharp "bump" of the red boundary region in **Figure 2.12**, it was found that the single layered phase in this "bump"' region contained a high concentration of Li^+ vacancies, which may allow the Ni^{3+} rather than Ni^{2+} and Li^+ to replace the Mn^{4+} in the local superlattice. A most lithium deficient composition of $Li[Ni_{1/6}\square_{1/6}Mn_{2/3}]O_2$ was thus synthesized. Interestingly, although the Li stoichiometry in this case was not "rich", it still electrochemically behaved as a lithium rich layered material.

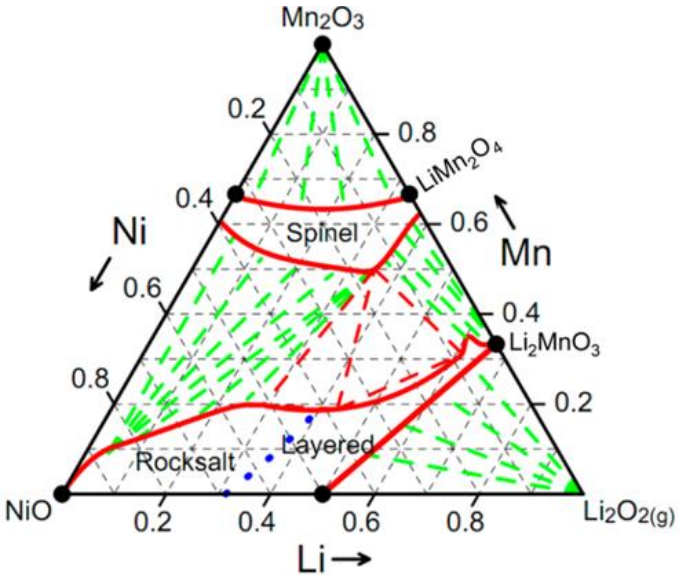

Figure 2.12 The entire phase diagram for combinatorial Li−Mn−Ni-O system made in oxygen and quenched from 800 ℃. Red lines: boundaries of single-phase regions; green dashed lines are tie-lines; red dashed lines: tie-lines bounding three-phase regions; blue-dotted line: a phase transition between the cubic and layered rocksalt structures [120]

To design a high performance LLLs material, one major concern is the composition. It is well accepted that the superior high capacities of LLLs are from the activation of Li_2MnO_3 phase [126-129], therefore, if one considers to maximum the specific capacity, it would be better to increase the percentage of Li_2MnO_3 or even use pure Li_2MnO_3 material. However, a few attempts demonstrated that it is not practical to use pure Li_2MnO_3 as the cathode material in terms of the columbic efficiency, cycling stability and the rate capability [126-128]. In aim to enhance the electrochemical performance, some other TMs such as Ni and Co that can co-exist with Mn in the TM slabs are generally applied to replace part of the Mn and form the highly integrated two-phase structure. Lu et al. conducted a systematic study on the Ni-doped LLLs with the composition of $Li[Ni_xLi_{1/3-2x/3}Mn_{2/3-x/3}]O_2$ (x = 1/6, 1/4, 1/3, and 5/12) [116, 129, 130]. Distinguished electrochemical performances were observed in their samples with different amount of Ni doping. Although an irreversible plateau occurred in the first charge up to 4.8 V due to the simultaneous removal of Li and O from the Li_2MnO_3 phase, the cycling stability was significantly enhanced in samples with x>1/4. Similar Co-doped LLLs are also very attractive as the candidates of high energy cathode materials [131, 132]. Park et al. reported a series of Li-Mn-Co-O materials formulated as $Li[Co_xLi_{(1/3-x/3)}Mn_{(2/3-2x/3)}]O_2$ (x = 0.1, 0.17, 0.20, 0.25, 0.33, and 0.5) in 2004 [131]. They confirmed the 4+ and 3+ oxidation state of Mn and Co respectively in the pristine compounds by XANES and concluded that the high content of Co could suppress the structure change from layered to the spinel and enhance the cycling

performance. More recently, Manthiram et al. reported the influence of several cations doping including Ti, Co and Ni on the electrochemical reactions of LLLs [133]. With combined experimental and theoretical results, they suggested that Ti could suppress the oxygen loss in Li_2MnO_3 phase while Co and Ni played a positive role for the O^{2-} ions oxidation to O_2, which was further supported by their later work using density functional theory to predict the oxygen stability in LLLs with Ti or Co bonded [134].

2.2.3.2 Understanding of the structures

It has been proposed that the LLLs consist of two phases, the monoclinic Li_2MnO_3 (C2/m) and the rhombohedral $LiMO_2$ ($R\bar{3}m$) as shown in **Figure 2.13**. They share the rock-salt structure and close-packed cubic oxygen array, which allow high compatibility of them with a close interlayer distance ($(001)_{mon}$ and $(003)_{tri}$) of about 0.47 nm. Specifically, the Li_2MnO_3 can be considered as one of the $LiMO_2$ structures when it is formulated as $Li[Li_{1/3}Mn_{2/3}]O_2$ with the M layers replaced by periodic $LiMn_2$ ordering.

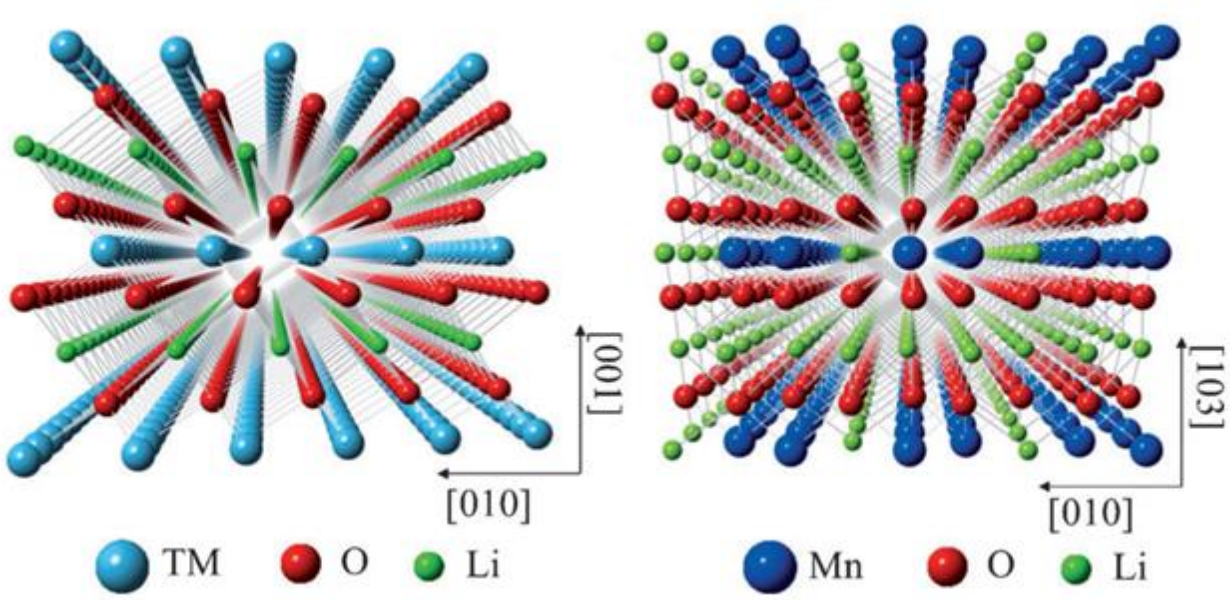

Figure 2.13 Simulation of the crystal structure of the R-3m $LiTMO_2$ and the C2/m Li_2MnO_3 phases viewed along the [100] direction [121]

To date, there are still debates on the atomic structures of whether the two structures co-exist as a solid solution or reside in different local regions as separate phases. In the early stage, X-ray diffraction (XRD) and electron diffraction (ED) have been used to investigate the structure of LLLs; however, the results are explained contradictorily by different groups. Some believe the broad and small diffraction peaks between 20-25 ° are related to the $LiMn_6$ cation ordering in the Li_2MnO_3

domains while others consider these weak peaks are characteristics of long rang Li-ordering in the TM layers. Also in terms of the ED patterns, debates arise on the extra spots and streaks [135-138], which Boulineau et al. considered to be the results of stacking faults rather than the widely reported superstructures of Li_2MnO_3. Very recently, more advanced techniques including high-angle annular dark-field (HAADF) STEM and annular bright-field (ABF) STEM have been applied to directly visualize the local atomic arrangement. In HAADF images, pixel intensity is in proportion to the atomic number Z, therefore, only TM can be seen as a white spot while light Li atom is invisible as a black spot. When seen along the [100] direction, vertical row distance of ~0.47 nm can be detected in both Li_2MnO_3 and $LiMnO_2$ phases corresponding to the TM layer spacing. However, in each row, the white spots are located in different manners. For $R\bar{3}m$ $LiMO_2$, white spots appear with equal in-row distance, but for Li_2MnO_3, periodic two bright spots and one dark spot are displayed denoting the $LiMn_2$ projection within the ab hexagonal plane of Li_2MnO_3. With the help of HAADF-STEM, Jarvis et al. suggested that the thin planar defects along the (001) planes of the $Li[Li_{0.2}Ni_{0.2}Mn_{0.6}]O_2$ compound lead to the streaks on [001] ED pattern and widen the small XRD peaks within 20-25 ° [139]. In addition, no separate regions of Li_2MnO_3 and $LiMO_2$ were found in their $Li[Li_{0.2}Ni_{0.2}Mn_{0.6}]O_2$ material, indicating the formation of a solid solution. However, as reported by Yu et al. using combined ABF and HAADF STEM to directly observe the nano structure of LLLs, two phases inter-grown in the $Li_{1.2}Mn_{0.567}Ni_{0.166}Co_{0.067}O_2$ material and their hetero-interface in grains are clearly revealed as can be seen from **Figure 2.14**, strongly evidencing the co-existence of two separate phases [121]. In addition, some researchers found that the composition, particularly the content of Li excess, may be the key factor to determine the microstructure of LLLs [140, 141]. A high content of Li favours the formation of a homogeneous solid solution. When the ratio of Li and TM declines, insufficient Li will break the periodic LiM_2 ordering and lead to local two-phase regions.

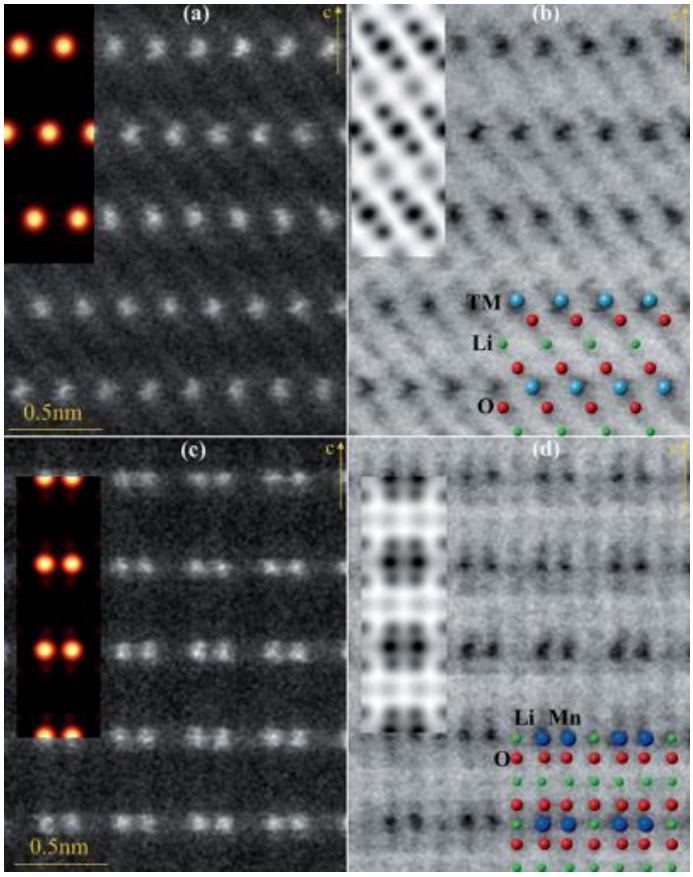

Figure 2.14 (a) and (b) HAADF and ABF STEM images of the R-3m $LiTMO_2$ structure projected along the [100]rh direction. (c) and (d) HAADF and ABF STEM images of the monoclinic Li_2MnO_3-like structure projected along the [100]mon direction. Insets: simulated HAADF, ABF STEM and crystal-structure images of the $LiTMO_2$ and Li_2MnO_3-like structures, respectively [121]

Due to the close relationship between the electrochemical performance and crystal structure of the LLLs, it is important to not only investigate their pristine structure, but also to understand the structure evolution during electrochemical reactions. Based on the observation results from XRD, HR-TEM and Raman spectroscopy as well as a first principle calculation, Hong et al. reported that a new spinel phase was generated and embedded locally in the parent layered framework of their $Li_{1.2}Ni_{0.2}Mn_{0.6}O_2$ compound during electrochemical cycling [142]. Soon later, Xu et al. revealed, from the atomic level, that the diffusion of TM ions to the Li layers can facilitate the formation of a spinel phase in the surface area according to their Z-contrast HAADF STEM image analysis [143]. Consequently, a two-phase boundary near the surface was suggested to explain the remarkably increased resistance, which, together with the low Li mobility in the TM-rich Li layers, led to poor rate performance of their $Li_{1.2}Ni_{0.2}Mn_{0.6}O_2$ material. Such a layered-to-spinel structure change during long term cycling was further confirmed by Song et al. with solid evidence from their detailed

analysis of the XPS, TEM and ICP results [144]. They found the cubic $LiMn_2O_4$ and tetragonal $Li_2Mn_2O_4$ spinels co-existed in the cycled materials and traded off the high working voltage with better rate capability. However, the structures of the LLLs are considered as a whole in these studies during the structure evolution. In fact, the $LiMO_2$ and Li_2MnO_3 phases may experience different manners of structure change. Gu et al. found in their $Li_{1.2}Ni_{0.2}Mn_{0.6}O_2$ material that the $R\bar{3}m$ $LiMO_2$ partially transformed to a mosaic spinel that was induced by the TM diffusing to the Li layers [145]. And no lattice breakage was detected during this process. On the other side, Li^+ and O^{2-} were extracted from the C2/m Li_2MnO_3 at high voltage charging, leading to serious lattice strain and distortion that broke the parent lattice down and yielded cracks and pores to the layered nanoparticles as shown in **Figure 2.15**. The structure evolution to the spinel phase is well believed to account for the gradual capacity decay and low rate capability of LLLs. Therefore, some advanced nano-techniques, for example, AlF_3-coating, have been developed to restrain the spinel formation and improve the electrochemical performance, and they will be discussed in a following section.

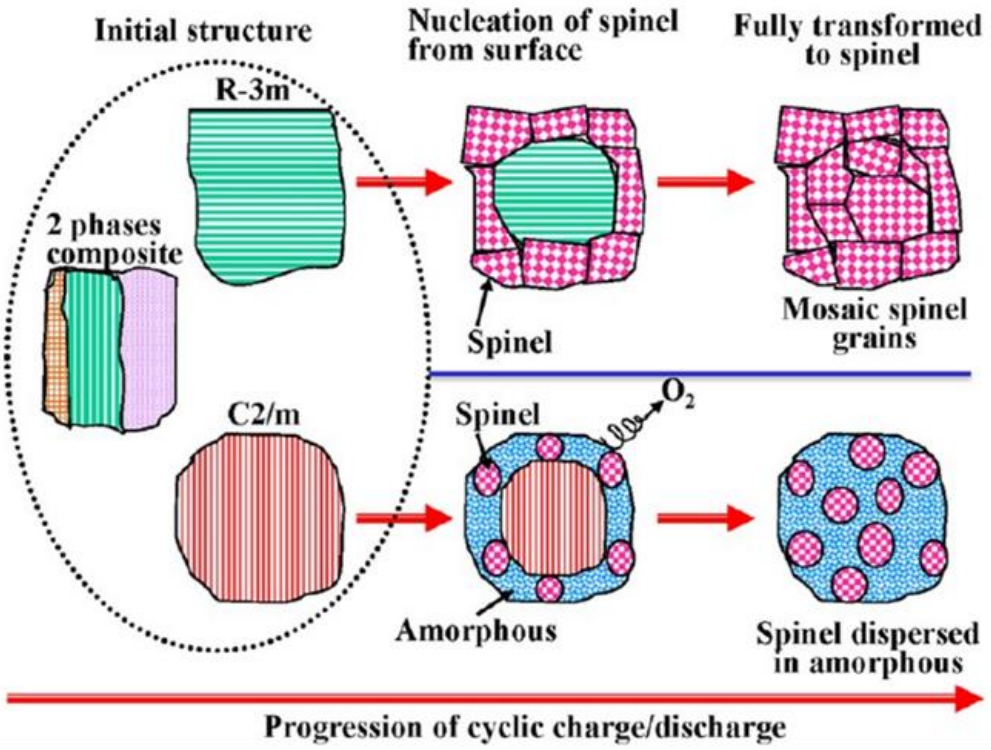

Figure 2.15 Schematic illustrating the different structure-transition routes of the layered R-3m and C2/m phases to spinel grains with different features [145]

2.2.3.3 Reaction mechanisms

Although LLLs are highly attractive in respect to their superior high capacity, the electrochemical reaction mechanisms of them are very complex and not fully revealed due to the complicated crystal structure and variable multi-element composition. In the past decade, many efforts have been committed to the fundamental understanding of the reaction mechanisms and some reasonable reaction models and mechanisms have been built on the basis of experimental and computational results.

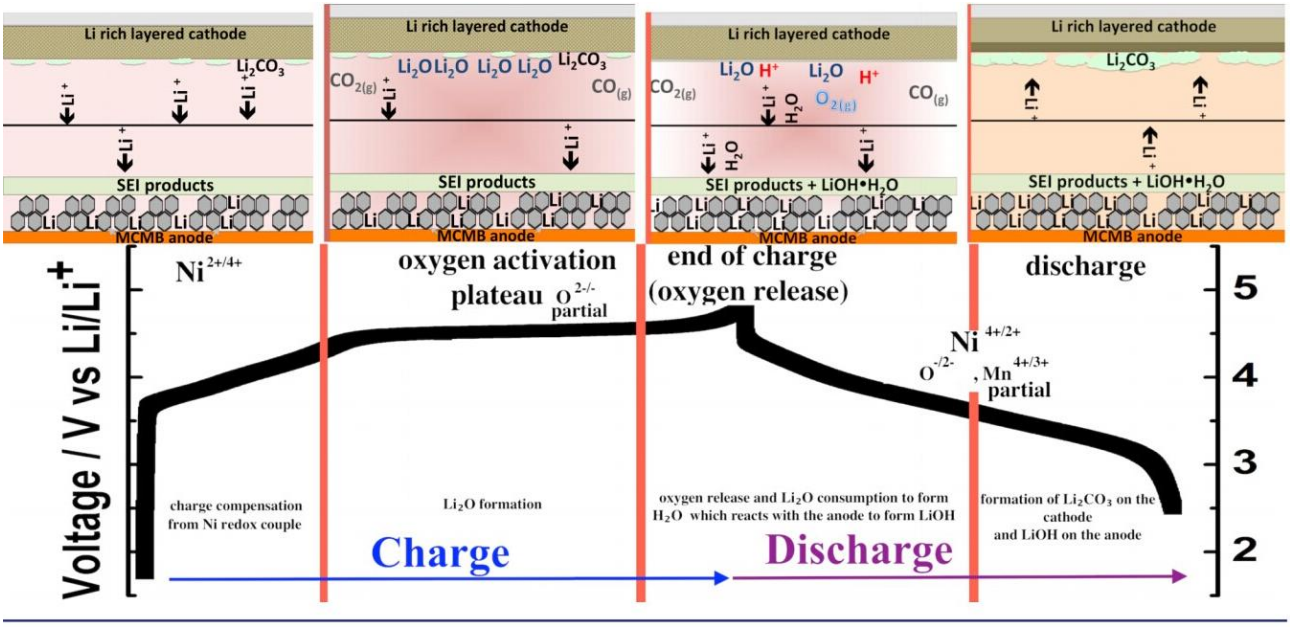

Figure 2.16 Proposed surface reaction mechanisms and oxygen-activation related products of $Li[Ni_xLi_{(1-2x)/3}Mn_{(2-x)/3}]O_2$ during different charging and discharging stages [122]

Most of the research interests have focused on the investigation of the first cycle, particularly the behaviours of the different elements including Li^+, TM and O^{2-} during the first charge process to a high voltage of 4.6 V or higher and the associated reactions and products. Typically, the first charge curve of LLLs, taking the $Li_{1.2}Ni_{0.2}Mn_{0.6}O_2$ for instance, is composed of two parts as shown in **Figure 2.16** [122]. A steep slope is observed in the beginning corresponding to the Ni^{2+} oxidation to Ni^{4+}. When the charging voltage reaches 4.5 V where all the Ni^{2+} has been oxidized, a long and flat plateau appears and extends to the end of the charging, leading to a superior high specific capacity of the material.

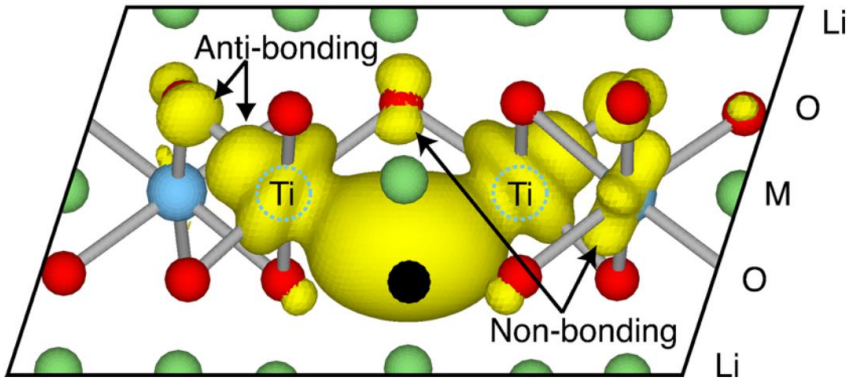

Figure 2.17 Electron distribution of the highest occupied orbit in $Li[Li_{1/3}Ti_{2/3}]O_2$ with oxygen vacancies. Green spheres: Li; red: O; blue: Ti; and black: O vacancy [134]

Based on the results of *in-situ* XRD and differential capacity measurements, Lu et al. inferred oxygen loss from their LLLs compounds and diffusion of TMs to the Li layers in the first charge to 4.8 V. [129] The oxygen evolution in the first charging above 4.5 V was solidly confirmed later by Armstrong et al. in the $Li[Ni_{0.2}Li_{0.2}Mn_{0.6}]O_2$ compound using *in situ* differential electrochemical mass spectrometry to monitor the mass fluctuation of gases during charging [146]. In addition, from the powder neutron diffraction analysis, they proposed that the TM ions diffused from the surface to the bulk and occupied the Li vacancies to end the oxygen generation. Moreover, Manthiram et al. found the formation of oxygen in LLLs during the first charge was significantly influenced by cationic doping [133, 134]. Co can narrow the band gap of the compound and promote the oxygen release while Ti, as shown in **Figure 2.17** may lift the nonbonding band and bundle O^{2-} to restrain the oxygen formation.

It is important to note that different TMs may behave differently during the electrochemical reactions. In another study, Lu et al. concluded that Ni atoms instead of Mn moved to the Li layers in their LLLs by refining the XRD and neutron diffraction patterns [130]. With combined HAADF-STEM observation and comparison of the XRD pattern refinement between pristine and cycled $Li_{1.2}Ni_{0.2}Mn_{0.6}O_2$ samples, Xu et al. indicated a higher concentration of Ni in the Li layers after 10 electrochemical cycles [143]. In addition, from the simulation results, they proposed a mechanism of Ni migration through a tetrahedral Li vacancy to the Li layers. Boulineau et al. recently reported that Mn and Ni were actually segregated on the surface of the $Li_{1.2}Mn_{0.6}1Ni_{0.18}Mg_{0.01}O_2$ nanoparticle after 50 electrochemical cycles according to HAADF-STEM observation and associated STEM EELS analysis [119]. The Mn was inferred to migrate into the bulk material and occupy the Li vacancies in the TM layers, leaving a Ni-rich and Mn-poor surface. The proposed mechanism is shown in **Figure 2.18**. This distinguished diffusion behaviours of Mn and Ni in the material could

explain the loss of superstructure peaks in the XRD patterns and account for the voltage decay and capacity degradation. Interestingly, Wang et al. concluded from the spherical aberration-corrected STEM results that Mn could also move to the Li layers in the Li_2MnO_3 compound during electrochemical delithiation and move back to the TM layers reversibly when Li is reinserted [147].

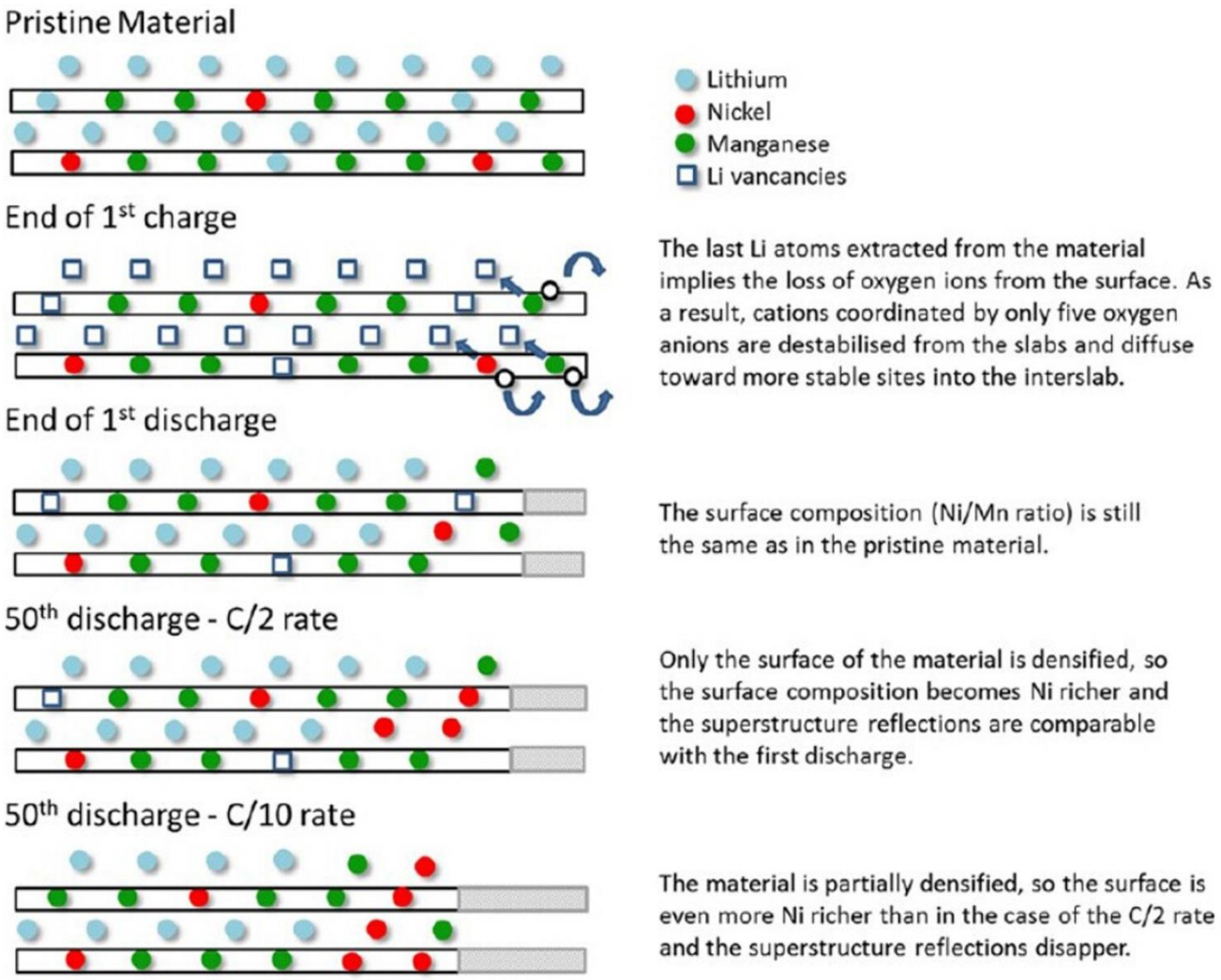

Figure 2.18 Schematic illustration of the formation mechanisms for Mn and Ni segregation and densification during electrochemical reactions. Bulk and edge of the crystal are on the left and the right, respectively. Grey parts: shrinkage of the crystal [119]

To understand the origin of the high specific capacity of LLLs, it is essential to investigate the associated side reactions and by-products. Yabuuchi et al. conducted detailed study using synchrotron XRD, X-ray photoelectron spectroscopy (XPS), X-ray absorption spectroscopy (XAS) and time-of-flight secondary ion mass spectroscopy (SIMS)) to reveal the reaction mechanism of the $Li_{1.2}Ni_{0.13}Co_{0.13}Mn_{0.54}O_2$ material in the first cycle [148]. The released oxygen in the first charge has been demonstrated to be electrochemically reduced and deposited at the electrode surface in the form

of mainly Li_2CO_3 in the first discharge, leading to the decay of the reversible specific capacity of the material. Based on these results, they suggested that the formation of Li_2CO_3 in the surface should be suppressed to improve the cycling stability of the surface redox reactions. Very recently, Hy et el developed the advanced *in situ* surfaced-enhanced Raman spectroscopy (SERS) to observe the instant surface redox reactions of $Li_{1.2}Ni_{0.2}Mn_{0.6}O_2$ during electrochemical cycling [122]. Combined with other electrochemical and structural characterizations, they proposed a detailed surface reaction mechanism of the material as illustrated in **Figure 2.16**. In addition to Li_2CO_3, the formation of Li_2O on the cathode and $LiOH \cdot H_2O$ on the anode were directly evidenced during electrochemical reactions. Hydrolysis of the electrolyte was detected due to the H_2O generated by the subsequent reactions of Li_2O. Therefore, it is necessary to not only protect the surface of both cathode and anode, but also improve the stability of the electrolyte.

2.2.3.4 Challenges to achieving high performance LIBs

LLLs have shown very promising high specific-capacity and energy-density; however, to meet the requirement of practical applications, they still face critical challenges to overcome as follows:

- low initial Columbic efficiency
- low rate performance
- poor long-term cycling stability
- working voltage decline over cycles
- absence of fundamental understanding of the electrochemical reaction mechanisms and the associated crystal structure evolution.

In spite of the common solid electrolyte interface (SEI) layer formation, the main reason for low initial Coulombic efficiency of LLLs (generally less than 80%) is the activation process of the Li_2MnO_3 component, which involves partially irreversible oxygen release and associated Li^+ extraction in the first charge. Some methods like pre-treating the materials with acid [149] or substitution of Mn with Ru [150] have been demonstrated to improve the first cycle efficiency of LLLs. However, in these cases, the Li_2MnO_3 content was reduced, which may sacrifice the specific capacity of the material. To concurrently improve the initial cycle efficiency and discharge capacity, Ito et al. activated their $Li[Li_{0.2}Ni_{0.13}Mn_{0.54}Co_{0.13}]O_2$ material with stepwise increased upper voltage and achieved a much enhanced discharge capacity (275 mAh g^{-1}) and efficiency (more than 90%) in the first cycle [151].

Due to the complexity in composition and crystal structure, it is difficult to find a simple and versatile reason for the poor rate capability of LLLs. Xu et al. proposed that a spinel phase formed on the surface of the parent layered material during electrochemical cycling might be responsible for the retarded rate performance because the TMs transformed into Li layers could block the way of Li diffusion [143].

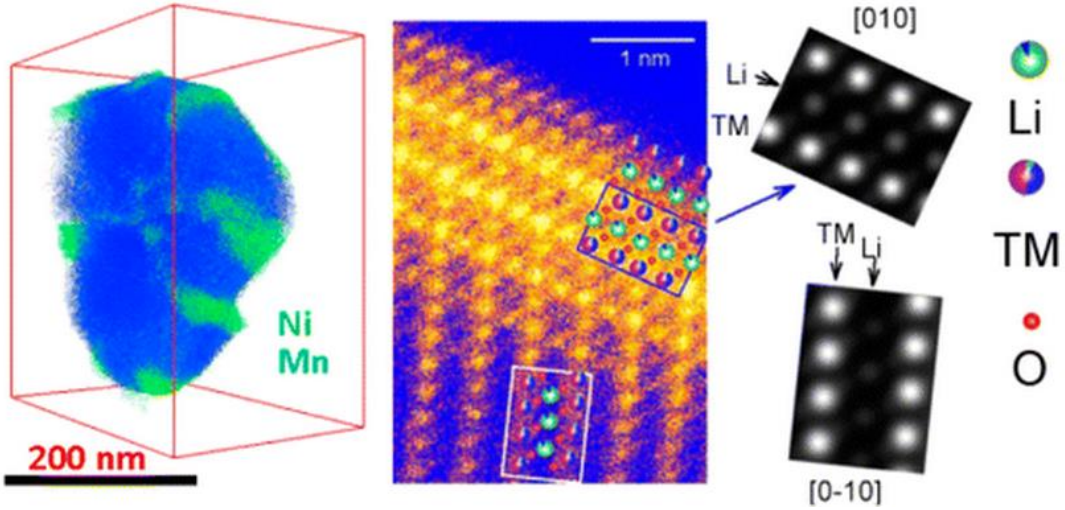

Figure 2.19 Left: 3D XEDS tomography map of segregated Mn and Ni distribution on a $Li_{1.2}Ni_{0.2}Mn_{0.6}O_2$ nanoparticle; middle: atomic resolution Z-contrast STEM image of the nanoparticle in surface layers; right: simulated [010] zone projection Z-contrast image based on $LiNi_{0.5}Mn_{0.5}O_2$ crystal model with 20% Ni/Li disorder and [0−10] with 10% Ni/Li disorder corresponding to the region labelled with blue and white rectangle in the middle STEM image [152]

In fact, the rate performance of LLLs may also depend on the synthesis condition. Gu et al. found that the Ni was selectively segregated at the surface facets of the $Li_{1.2}Ni_{0.2}Mn_{0.6}O_2$ material as shown in **Figure 2.19** rather than homogeneously distributed over the whole particle surface [152]. The Z-contrast image and associated simulations clearly show that the bulk Li diffusion channels are blocked by large TMs on the surface due to the preferential segregation of Ni. As a result, the Li diffusion energy barrier was increased, leading to poor rate capability. Because the calcination temperature and dwelling time at high temperature are critical to the cation distribution in the crystal structure, a better synthesis approach with optimized parameters are suggested to suppress or even avoid the TM segregation. To structurally understand the origin of the rate capability of LLLs, Yu et al. conducted detailed investigation on the $Li_{1.2}Ni_{0.15}Co_{0.1}Mn_{0.55}O_2$ material with *in situ* XRD and time-resolved XAS [153]. Based on the time-resolved XAS data, a beautiful 3D Fourier transformed map of Mn K-edge EXAFS spectra and the projection view of Ni-O, Co-O and Mn-O were drawn

(**Figure 2.20**). This provided direct evidence of poor delithiation kinetics in Mn site and indicated that Li_2MnO_3 is possibly the limiting component of the rate capability of the LLLs.

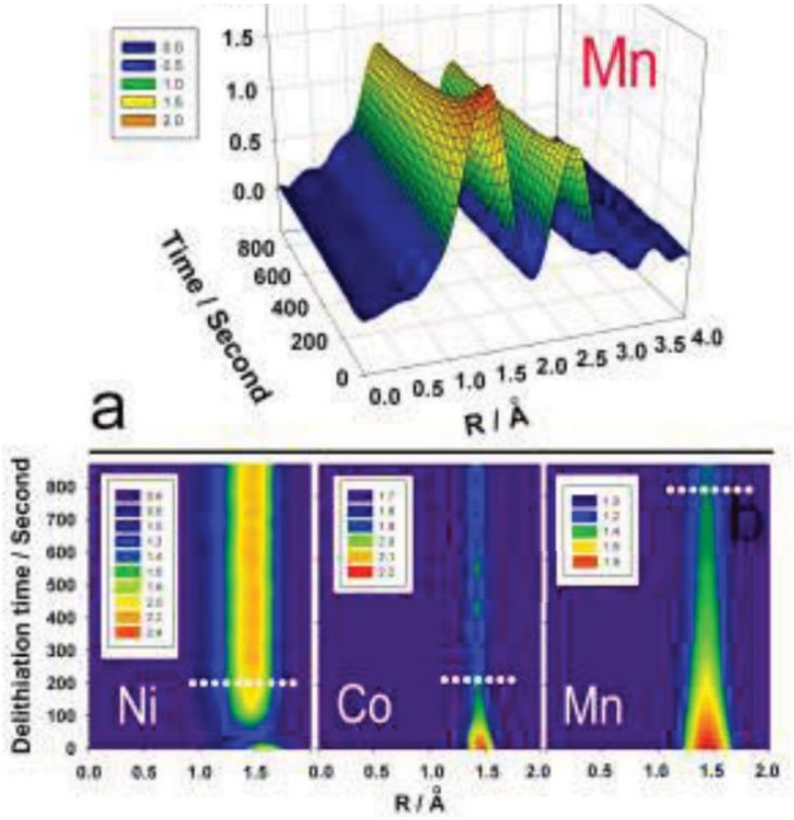

Figure 2.20 (a) 3D magnitude of the Fourier transformed Mn K-edge spectra of $Li_{1.2}Ni_{0.15}Co_{0.1}Mn_{0.55}O_2$ collected during constant 5 V charging; (b) Projection view of the corresponding Ni–O, Co–O, and Mn–O spectra as functions of charging time [153]

Cycling stability is another significant concern of the LLLs. After long period electrochemical cycling, both the specific capacity and working voltage of LLLs tend to decay, leading to large decrease of the energy density and low efficiency. Generally, the poor cycling performance can be attributed to two aspects: the structure evolution of the layered phase and the side reaction with electrolyte on the electrode surface. As proposed by Reed et al., the $R\bar{3}m$ layered phase and the cubic spinel phase share the oxygen framework and only differ in the arrangement of one-fourth of the TM ions [75]. According to the previously discussion, TMs have been well demonstrated to diffuse into the Li layers during electrochemical cycling and facilitate the formation of a spinel structure, which shows a lower working voltage than the original layered structure. On the other side, the Mn^{4+} in the pristine LLLs will be activated and reduced to Mn^{2+} and Mn^{3+} in the discharging process. The Mn^{3+}, which is the main form of Mn element in the spinel structure, is known to suffer from Jahn-Teller

distortion and easy dissolution in the electrolyte [86, 154]. As the distortion accumulated during the cycling, the crystal lattice may break down and lead to specific capacity decline.

Surface coating has been verified as one of the effective ways to improve the electrochemical performance of LLLs. As discussed previously, the released oxygen in the first charge due to the Li_2MnO_3 activation may lead to the formation of H_2O, which can then react with the electrolyte and produce HF [155]. Because HF would etch the electrode surface and deteriorate the electrochemical performance, the primary concern of surface coating is to passivate the electrode surface to avoid the direct contact with HF. Some inorganic materials such as Al_2O_3, ZnO, $AlPO_4$ and AlF_3 that are inert to HF have been investigated as the surface coating layer of LLLs [156-160]. Sun et al. suggested that AlF_3 was the most promising candidate that would not react with HF while other candidates may partially peel off by HF fluoration [160]. The cycling stability, rate performance and thermal stability of their $Li[Li_{0.19}Ni_{0.16}Co_{0.08}Mn_{0.57}]O_2$ composite was improved by AlF_3 coating, which was believed to induce the Li chemical leaching effect and facilitate the structure transformation of the surface Li_2MnO_3 layer to a more stable spinal phase.

Although HF-resistant surface layer can enhance the cycling stability of LLLs, it is still challenging to achieve a high power density [161, 162]. To promote the rate capability, Wu et al. recently developed a very smart design of spinel/layered hetero-structured material as shown in **Figure 2.21** [123]. The high-capacity layered Li-rich $Li_{1.2}Mn_{0.6}Ni_{0.2}O_2$ core was encapsulated by a nanospinel ($LiNi_xMn_{2-x}O_4$) layer with the thickness of about 10 nm as clearly revealed by the HR-TEM image. Taking advantages of the highly conductive spinel surface and high capacity layered core, the spinel/layered composite exhibited excellent rate performance (274.6 mAh g^{-1} at 1C) and superior high specific capacity. Another good example to enhance the rate performance of LLLs was demonstrated by Song et al. using graphene oxide (GO) to wrap their $Li(Li_{0.2}Mn_{0.54}Ni_{0.13}Co_{0.13})O_2$ material [163]. In addition to the highly conductive cubic spinels transformed from the layered phase in the surface during electrochemical cycling [164], the GO was also reduced to provide extraordinary rate performance of 201 mAh g^{-1} at an extremely high current density of 2500 mA g^{-1} for their material.

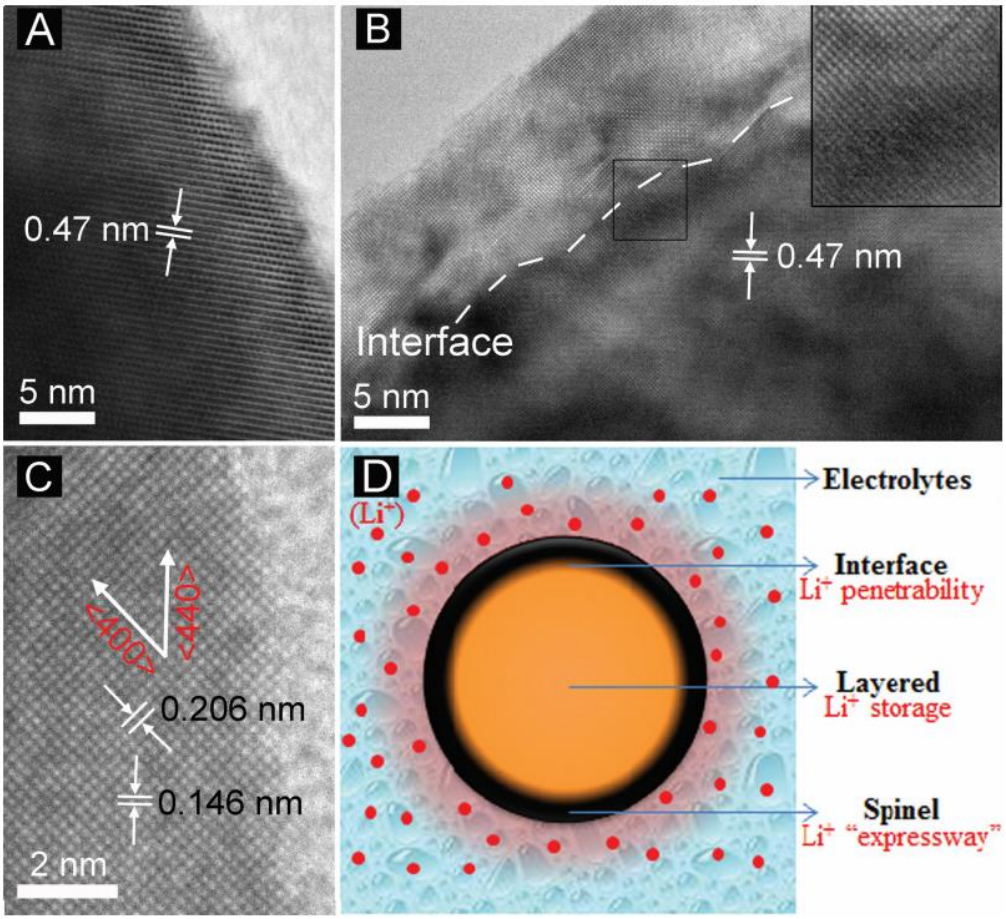

Figure 2.21 HRTEM of (A) un-coated and B) coated $Li_{1.2}Ni_{0.2}Mn_{0.6}O_2$ materials, inset of (B) is the 2.5 × magnified view of the black rectangle area; (C) HRTEM of the nanostructure of the surface coating layer; (D) schematic diagram of the spinel/layered heterostructured material [123]

For the problematic voltage decay of LLLs during cycling, a comprehensive understanding in terms of the structural, composition and electrochemically testing conditions is still on the way. Thackeray et al. demonstrated that the reversible migration of TMs to metastable tetrahedral sites in the Li layer during electrochemical cycling will lead to 1 V hysteresis in site energy [165]. Once the TMs further move to irreversible cubic environments with lower energy, the voltage fade will occur in LLLs. This TM relocation mechanism for voltage decay was also supported by Bettge et al [166]. But more interestingly, they developed a methodology to quantify the voltage fade and the related impact on the energy density of LLLs. In addition, they effectively mitigated the voltage fade with lower upper cut-off voltage and lower temperatures, however, at the expense of energy and power densities. Bloom et al. investigated the effect of surface coating of a few metal oxides and phosphate and electrolyte additives on the electrochemical performance of the $0.5Li_2MnO_3{\cdot}0.5LiNi_{0.375}Mn_{0.375}Co_{0.25}O_2$ material. The specific capacity loss of the material was

decreased; however, no prominent improvement was detected on voltage decay, implying the intrinsic bulk structure evolution could be the reason for the phenomenon of voltage decay. Croy et al. developed a simple and versatile method to synthesize LLLs using Li_2MnO_3 as a template [167]. Other TM cations were introduced by acid treatment and a post annealing process. The as-prepared materials exhibited lighter voltage decay and less capacity loss due to the stabilized cations and anions at the electrode surface. In addition, Lee et al. found that another important factor that impacted the voltage decay was the length of the high voltage plateau in the first charge [168]. A series of intentionally designed LLLs in the composition of $Li_{1.2-x}Mn_{0.54}Ni_{0.13+2x}Co_{0.13-x}O_2$ demonstrated much limited voltage decay during long term cycling mainly due to the minimized first charge capacity.

2.3 References

1. Vincent, C.A. and B. Scrosati, *Modern batteries: an introduction to electrochemical power sources*. 1997: Butterworth-Heinemann.
2. Ozawa, K., *Lithium Ion Rechargeable Batteries*. 2009: Wiley Online Library.
3. Linden, D. and T.B. Reddy, *Handbook of batteries*. New York.
4. Barak, M. *Electrochemical power sources: primary and secondary batteries*. 1980. Institution of Electrical Engineers.
5. Beck, F. and P. Rüetschi, *Rechargeable batteries with aqueous electrolytes*. Electrochim. Acta, 2000. **45**(15-16): p. 2467-2482.
6. Nagaura, T. and K. Tozawa, *Lithium ion rechargeable battery*. Progress in batteries and solar cells, 1990. **9**: p. 209-217.
7. Tarascon, J.M. and M. Armand, *Issues and challenges facing rechargeable lithium batteries*. Nature, 2001. **414**(6861): p. 359-367.
8. Nishi, Y., *The development of lithium ion secondary batteries*. Chem. Rec., 2001. **1**(5): p. 406-413.
9. Linden, D. and T.B. Reddy, *Basic concepts*. Handbook of batteries. 3rd ed. New York: McGraw-Hill, 2001: p. 1.3-18.
10. Sun, Y.K., et al., *Synthesis and characterization of $Li[(Ni_{0.8}Co_{0.1}Mn_{0.1})_{0.8}(Ni_{0.5}Mn_{0.5})_{0.2}]O_2$ with the microscale core-shell structure as the positive electrode material for lithium batteries*. J. Am. Chem. Soc., 2005. **127**(38): p. 13411-13418.
11. Hwang, B., R. Santhanam, and D. Liu, *Characterization of nanoparticles of $LiMn_2O_4$ synthesized by citric acid sol-gel method*. J. Power Sources, 2001. **97**: p. 443-446.

12. Park, D.H., et al., *Non-Hydrothermal Synthesis of 1D Nanostructured Manganese-Based Oxides: Effect of Cation Substitution on the Electrochemical Performance of Nanowires*. Adv. Funct. Mater., 2007. **17**(15): p. 2949-2956.
13. Hosono, E., et al., *Synthesis of single crystalline spinel $LiMn_2O_4$ nanowires for a lithium ion battery with high power density*. Nano lett., 2009. **9**(3): p. 1045-1051.
14. Li, N., et al., *Rate Capabilities of Nanostructured $LiMnO_2$ Electrodes in Aqueous Electrolyte*. J. Electrochem. Soc., 2000. **147**: p. 2044.
15. Sides, C.R. and C.R. Martin, *Nanostructured Electrodes and the Low-Temperature Performance of Li-Ion Batteries*. Adv. Mater., 2005. **17**(1): p. 125-128.
16. Li, X., et al., *A novel network composite cathode of $LiFePO_4$/multiwalled carbon nanotubes with high rate capability for lithium ion batteries*. Electrochem. Commun., 2007. **9**(4): p. 663-666.
17. Li, X., F. Kang, and W. Shen, *Multiwalled carbon nanotubes as a conducting additive in a $LiNi_{0.7}Co_{0.3}O_2$ cathode for rechargeable lithium batteries*. Letters to the Editor, 2006. **44**: p. 1298-1352.
18. Yang, X., et al., *Electrochemical performances of silicon electrode with silver additives*. Solid State Ionics, 2006. **177**(26-32): p. 2807-2810.
19. Kang, B. and G. Ceder, *Battery materials for ultrafast charging and discharging*. Nature, 2009. **458**(7235): p. 190-193.
20. Whittingham, M.S., *Lithium batteries and cathode materials*. Chem. Rev., 2004. **104**(10): p. 4271-4302.
21. Orsini, F., et al., *In situ Scanning Electron Microscopy (SEM) observation of interfaces within plastic lithium batteries*. J. Power Sources, 1998. **76**(1): p. 19-29.
22. Wakihara, M. and O. Yamamoto, *Lithium ion batteries, fundamentals and performance*. Vol. 135. 1998: Kodansha (Tokyo and Weinheim and New York).
23. Dahn, J., et al., *Mechanisms for lithium insertion in carbonaceous materials*. Science, 1995. **270**(5236): p. 590.
24. Besenhard, J.O., *Handbook of battery materials*. 1999: LibreDigital.
25. Nazri, G.A. and G. Pistoia, *Lithium batteries: science and technology*. 2009: Springer Verlag.
26. Ajayan, P., et al., *Opening carbon nanotubes with oxygen and implications for filling*. Nature, 1993. **362**(6420): p. 522-525.
27. Chen, W.X., J.Y. Lee, and Z. Liu, *Electrochemical lithiation and de-lithiation of carbon nanotube-Sn_2Sb nanocomposites*. Electrochem. Commun., 2002. **4**(3): p. 260-265.

28. Che, G., et al., *Carbon nanotubule membranes for electrochemical energy storage and production*. Nature, 1998. **393**(6683): p. 346-349.
29. Chen, J., et al., *Flexible, aligned carbon nanotube/conducting polymer electrodes for a lithium-ion battery*. Chem. Mater., 2007. **19**(15): p. 3595-3597.
30. Frackowiak, E., et al., *Electrochemical storage of lithium in multiwalled carbon nanotubes*. Carbon, 1999. **37**(1): p. 61-69.
31. Zhang, J., et al., *CNFs@CNTs: Superior Carbon for Electrochemical Energy Storage*. Adv. Mater., 2008. **20**(8): p. 1450-1455.
32. Gao, B., et al., *Enhanced saturation lithium composition in ball-milled single-walled carbon nanotubes*. Chem. Phys. Lett., 2000. **327**(1-2): p. 69-75.
33. Geim, A.K. and K.S. Novoselov, *The rise of graphene*. Nat. Mater., 2007. **6**(3): p. 183-191.
34. Deschamps, M. and R. Yazami, *Great reversible capacity of carbon lithium electrode in solid polymer electrolyte*. J. Power Sources, 1997. **68**(2): p. 236-238.
35. Wang, C., et al., *Electrochemical properties of graphene paper electrodes used in lithium batteries*. Chem. Mater., 2009. **21**(13): p. 2604-2606.
36. Wang, G., et al., *Graphene nanosheets for enhanced lithium storage in lithium ion batteries*. Carbon, 2009. **47**(8): p. 2049-2053.
37. Pan, D., et al., *Li storage properties of disordered graphene nanosheets*. Chem. Mater., 2009. **21**(14): p. 3136-3142.
38. Park, C.M. and H.J. Sohn, *Quasi Intercalation and Facile Amorphization in Layered ZnSb for Li Ion Batteries*. Adv. Mater., 2010. **22**(1): p. 47-52.
39. Bruce, P.G., *Energy storage beyond the horizon: Rechargeable lithium batteries*. Solid State Ionics, 2008. **179**(21-26): p. 752-760.
40. Teki, R., et al., *Nanostructured silicon anodes for lithium ion rechargeable batteries*. small, 2009. **5**(20): p. 2236-2242.
41. Kasavajjula, U., C. Wang, and A.J. Appleby, *Nano-and bulk-silicon-based insertion anodes for lithium-ion secondary cells*. J. Power Sources, 2007. **163**(2): p. 1003-1039.
42. Ferg, E., et al., *Spinal Anodes for Lithium-Ion Batteries*. 1994.
43. Jansen, A., et al., *Development of a high-power lithium-ion battery*. J. Power Sources, 1999. **81**: p. 902-905.
44. Allen, J., T. Jow, and J. Wolfenstine, *Low temperature performance of nanophase $Li_4Ti_5O_{12}$*. J. Power Sources, 2006. **159**(2): p. 1340-1345.

45. Cabana, J., et al., *Beyond Intercalation Based Li Ion Batteries: The State of the Art and Challenges of Electrode Materials Reacting Through Conversion Reactions*. Adv. Mater., 2010.
46. Poizot, P., et al., *Nano-sized transition-metal oxides as negative-electrode materials for lithium-ion batteries*. Nature, 2000. **407**(6803): p. 496-499.
47. Li, Y., B. Tan, and Y. Wu, *Mesoporous Co_3O_4 nanowire arrays for lithium ion batteries with high capacity and rate capability*. Nano lett., 2008. **8**(1): p. 265-270.
48. Park, J.C., et al., *Gram Scale Synthesis of Cu_2O Nanocubes and Subsequent Oxidation to CuO Hollow Nanostructures for Lithium Ion Battery Anode Materials*. Adv. Mater., 2009. **21**(7): p. 803-807.
49. Ban, C., et al., *Nanostructured Fe_3O_4/SWNT Electrode: Binder Free and High Rate Li Ion Anode*. Adv. Mater., 2010. **22**(20): p. E145-E149.
50. Taberna, P.L., et al., *High rate capabilities Fe_3O_4-based Cu nano-architectured electrodes for lithium-ion battery applications*. Nat. Mater., 2006. **5**: p. 567-573.
51. Yao, J., et al., *In situ chemical synthesis of SnO_2-graphene nanocomposite as anode materials for lithium-ion batteries*. Electrochem. Commun., 2009. **11**(10): p. 1849-1852.
52. Yoo, E.J., et al., *Large reversible Li storage of graphene nanosheet families for use in rechargeable lithium ion batteries*. Nano lett., 2008. **8**(8): p. 2277-2282.
53. Wang, H., et al., *Mn_3O_4-Graphene Hybrid as a High-Capacity Anode Material for Lithium Ion Batteries*. J. Am. Chem. Soc., 2010.
54. Zhi, L., et al., *Precursor Controlled Formation of Novel Carbon/Metal and Carbon/Metal Oxide Nanocomposites*. Adv. Mater., 2008. **20**(9): p. 1727-1731.
55. Xu, K., *Nonaqueous liquid electrolytes for lithium-based rechargeable batteries*. Chem. Rev., 2004. **104**(10): p. 4303-4418.
56. Schmidt, M., et al., *Lithium fluoroalkylphosphates: a new class of conducting salts for electrolytes for high energy lithium-ion batteries*. J. Power Sources, 2001. **97**: p. 557-560.
57. Arora, P. and Z. Zhang, *Battery separators*. Chem. Rev., 2004. **104**(10): p. 4419-4462.
58. Bruce, P.G., B. Scrosati, and J.M. Tarascon, *Nanomaterials for rechargeable lithium batteries*. Angew. Chem., Int. Ed., 2008. **47**(16): p. 2930-2946.
59. Jiao, F. and P.G. Bruce, *Mesoporous Crystalline β-MnO_2 a Reversible Positive Electrode for Rechargeable Lithium Batteries*. Adv. Mater., 2007. **19**(5): p. 657-660.
60. Arico, A.S., et al., *Nanostructured materials for advanced energy conversion and storage devices*. Nat. Mater., 2005. **4**(5): p. 366-377.

61. Balaya, P., et al., *Nano-ionics in the context of lithium batteries*. J. Power Sources, 2006. **159**(1): p. 171-178.
62. Meethong, N., et al., *Size-Dependent Lithium Miscibility Gap in Nanoscale $LiFePO_4$*. Electrochem. Solid-State Lett., 2007. **10**: p. A134.
63. Delmas, C., C. Fouassier, and P. Hagenmuller, *Structural classification and properties of the layered oxides*. Phys. B+ C, 1980. **99**(1-4): p. 81-85.
64. Antolini, E., *$LiCoO_2$: formation, structure, lithium and oxygen nonstoichiometry, electrochemical behaviour and transport properties*. Solid State Ionics, 2004. **170**(3-4): p. 159-171.
65. Dahn, J., et al., *Rechargeable $LiNiO_2$/Carbon Cells*. J. Electrochem. Soc., 1991. **138**: p. 2207.
66. Chebiam, R., F. Prado, and A. Manthiram, *Soft Chemistry Synthesis and Characterization of Layered $Li_{1-x}Ni_{1-y}Co_yO_{2-\delta}$ ($0 \leq x \leq 1$ and $0 \leq y \leq 1$)*. Chem. Mater., 2001. **13**(9): p. 2951-2957.
67. Chebiam, R., F. Prado, and A. Manthiram, *Comparison of the chemical stability of $Li_{1-x}CoO_2$ and $Li_{1-x}Ni_{0.85}Co_{0.15}O_2$ cathodes*. J. Solid State Chem., 2002. **163**(1): p. 5-9.
68. Venkatraman, S. and A. Manthiram, *Synthesis and characterization of P3-Type CoO_2*. Chem. Mater., 2002. **14**(9): p. 3907-3912.
69. Arai, H., et al., *Characterization and cathode performance of $Li_{1-x}Ni_{1+x}O_2$ prepared with the excess lithium method*. Solid State Ionics, 1995. **80**(3-4): p. 261-269.
70. Dutta, G., et al., *Chemical synthesis and properties of $Li_{1-\delta-x}Ni_{1+\delta}O_2$ and $LiNi_2O_4$*. J. Solid State Chem., 1992. **96**(1): p. 123-131.
71. Nakai, I., et al., *Study of the Jahn-Teller Distortion in $LiNiO_2$, a Cathode Material in a Rechargeable Lithium Battery, byin SituX-Ray Absorption Fine Structure Analysis* 1*. J. Solid State Chem., 1998. **140**(1): p. 145-148.
72. Ohzuku, T., et al., *Comparative study of $LiCoO_2$, $LiNiCoO_2$ and $LiNiO_2$ for 4 volt secondary lithium cells*. Electrochim. Acta, 1993. **38**(9): p. 1159-1167.
73. Armstrong, A.R. and P.G. Bruce, *Synthesis of layered $LiMnO_2$ as an electrode for rechargeable lithium batteries*. Nature, 1996. **381**(6582): p. 499-500.
74. Armstrong, A.R., et al., *Nonstoichiometric Layered $Li_xMn_yO_2$ with a High Capacity for Lithium Intercalation/Deintercalation*. Chem. Mater., 2002. **14**(2): p. 710-719.
75. Reed, J., G. Ceder, and A. Van Der Ven, *Layered-to-Spinel Phase Transition in Li_xMnO_2*. Electrochem. Solid-State Lett., 2001. **4**: p. A78.

76. Wang, L., et al., *Synthesis of a Li-Mn-oxide with disordered layer stacking through flocculation of exfoliated MnO_2 nanosheets, and its electrochemical properties*. Chem. Mater., 2003. **15**(23): p. 4508-4514.
77. Suzuki, S., et al., *High-Rate Electrode Properties of Li-Mn-oxide Synthesized by Reassembly of MnO_2 Nanosheets for Li-Ion Battery*. Key Eng. Mater., 2006. **320**: p. 223-226.
78. Ohzuku, T. and Y. Makimura, *Layered lithium insertion material of $LiCo_{1/3}Ni_{1/3}Mn_{1/3}O_2$ for lithium-ion batteries*. Chem. Lett., 2001. **30**(7): p. 642-643.
79. Shaju, K., G. Subba Rao, and B. Chowdari, *Performance of layered $Li(Ni_{1/3}Co_{1/3}Mn_{1/3})O_2$ as cathode for Li-ion batteries*. Electrochim. Acta, 2002. **48**(2): p. 145-151.
80. Belharouak, I., et al., *$Li(Ni_{1/3}Co_{1/3}Mn_{1/3})O_2$ as a suitable cathode for high power applications*. J. Power Sources, 2003. **123**(2): p. 247-252.
81. Koyama, Y., et al., *Solid-State Chemistry and Electrochemistry of $LiCo_{1/3}Ni_{1/3}Mn_{1/3}O_2$ for Advanced Lithium-Ion Batteries*. J. Electrochem. Soc., 2004. **151**: p. A1545.
82. Cho, T.H., Y. Shiosaki, and H. Noguchi, *Preparation and characterization of layered $LiMn_{1/3}Ni_{1/3}Co_{1/3}O_2$ as a cathode material by an oxalate co-precipitation method*. J. Power Sources, 2006. **159**(2): p. 1322-1327.
83. Ngala, J.K., et al., *The synthesis, characterization and electrochemical behavior of the layered $LiNi_{0.4}Mn_{0.4}Co_{0.2}O_2$ compound*. J. Mater. Chem., 2003. **14**(2): p. 214-220.
84. Li, J., J. Zheng, and Y. Yang, *Studies on Storage Characteristics of $LiNi_{0.4}Co_{0.2}Mn_{0.4}O_2$ as Cathode Materials in Lithium-Ion Batteries*. J. Electrochem. Soc., 2007. **154**: p. A427.
85. Ma, M., et al., *Structural and electrochemical behavior of $LiMn_{0.4}Ni_{0.4}Co_{0.2}O_2$*. J. Power Sources, 2007. **165**(2): p. 517-534.
86. Thackeray, M., et al., *Lithium insertion into manganese spinels*. Mater. Res. Bull., 1983. **18**(4): p. 461-472.
87. Japan Electronics, March 6th,, 1996.
88. Jang, D.H., Y.J. Shin, and S.M. Oh, *Dissolution of Spinel Oxides and Capacity Losses in 4 V $Li/Li_xMn_2O_4$ Cells*. J. Electrochem. Soc., 1996. **143**(7): p. 2204-2211.
89. Shin, Y. and A. Manthiram, *Influence of the lattice parameter difference between the two cubic phases formed in the 4 V region on the capacity fading of spinel manganese oxides*. Chem. Mater., 2003. **15**(15): p. 2954-2961.
90. Shin, Y. and A. Manthiram, *Factors influencing the capacity fade of spinel lithium manganese oxides*. J. Electrochem. Soc., 2004. **151**: p. A204.

91. Xia, Y. and M. Yoshio, *An Investigation of Lithium Ion Insertion into Spinel Structure Li-Mn-O Compounds*. J. Electrochem. Soc., 1996. **143**: p. 825.
92. Shin, Y. and A. Manthiram, *High Rate, Superior Capacity Retention $LiMn_{2-2y}Li_yNi_yO_4$ Spinel Cathodes for Lithium-Ion Batteries*. Electrochem. Solid-State Lett., 2003. **6**: p. A34.
93. Shin, Y. and A. Manthiram, *Microstrain and capacity fade in spinel manganese oxides*. Electrochem. Solid-State Lett., 2002. **5**: p. A55.
94. Sigala, C., et al., *Positive electrode materials with high operating voltage for lithium batteries: $LiCr_yMn_{2-y}O_4$ $(0\leq y\leq 1)$*. Solid State Ionics, 1995. **81**(3-4): p. 167-170.
95. Kawai, H., et al., *5 V lithium cathodes based on spinel solid solutions $Li_2Co_{1+X}Mn_{3-X}O_8$: $-1\leq X\leq 1$*. Electrochim. Acta, 1999. **45**(1-2): p. 315-327.
96. Shigemura, H., et al., *Structure and Electrochemical Properties of $LiFe_xMn_{2-x}O_4$ $(0\leq x\leq 0.5)$ Spinel as 5 V Electrode Material for Lithium Batteries*. J. Electrochem. Soc., 2001. **148**: p. A730.
97. Jo, M., et al., *Nanoparticle-Nanorod Core-Shell $LiNi_{0.5}Mn_{1.5}O_4$ Spinel Cathodes with High Energy Density for Li-Ion Batteries*. J. Electrochem. Soc., 2010. **157**: p. A841.
98. Liu, Z., et al., *Improving the high-temperature performance of $LiMn_2O_4$ spinel by micro-emulsion coating of $LiCoO_2$*. J. Power Sources, 2002. **104**(1): p. 101-107.
99. Zheng, Z., et al., *Surface modification of $Li_{1.03}Mn_{1.97}O_4$ spinels for improved capacity retention*. Solid State Ionics, 2002. **148**(3-4): p. 317-321.
100. Xiong, L., A. Kannan, and A. Manthiram, *Pt-M (M = Fe, Co, Ni and Cu) electrocatalysts synthesized by an aqueous route for proton exchange membrane fuel cells*. Electrochem. Commun., 2002. **4**(11): p. 898-903.
101. Cho, J., et al., *Improvement of Structural Stability of $LiMn_2O_4$ Cathode Material on 55 ℃ Cycling by Sol-Gel Coating of $LiCoO_2$*. Electrochem. Solid-State Lett., 1999. **2**: p. 607.
102. Amatucci, G., et al., *Surface treatments of $Li_{1+x}Mn_{2-x}O_4$ spinels for improved elevated temperature performance*. Solid State Ionics, 1997. **104**(1-2): p. 13-25.
103. Cho, J., et al., *Complete blocking of Mn^{3+} ion dissolution from a $LiMn_2O_4$ spinel intercalation compound by Co_3O_4 coating*. Chem. Commun., 2001(12): p. 1074-1075.
104. Padhi, A., K. Nanjundaswamy, and J. Goodenough, *Phospho olivines as Positive Electrode Materials for Rechargeable Lithium Batteries*. J. Electrochem. Soc., 1997. **144**: p. 1188.
105. Padhi, A., et al., *Effect of Structure on the Fe^{3+}/Fe^{2+} Redox Couple in Iron Phosphates*. J. Electrochem. Soc., 1997. **144**: p. 1609.

106. Huang, H., S.C. Yin, and L. Nazar, *Approaching Theoretical Capacity of $LiFePO_4$ at Room Temperature at High Rates*. Electrochem. Solid-State Lett., 2001. **4**: p. A170.
107. Ravet, N., et al. *Electrochem. Soc*. 1999.
108. Ravet, N., et al., *Electroactivity of natural and synthetic triphylite*. J. Power Sources, 2001. **97**: p. 503-507.
109. Julien, C., et al., *Nanoscopic scale studies of $LiFePO_4$ as cathode material in lithium-ion batteries for HEV application*. Ionics, 2007. **13**(6): p. 395-411.
110. Salah, A.A., et al., *Nano-sized impurity phases in relation to the mode of preparation of $LiFePO_4$*. Mater. Sci. Eng. B, 2006. **129**(1-3): p. 232-244.
111. Wang, Y., et al., *The design of a $LiFePO_4$/carbon nanocomposite with a core-shell structure and its synthesis by an in situ polymerization restriction method*. Angew. Chem., Int. Ed., 2008. **47**(39): p. 7461-7465.
112. Chung, S.Y., J.T. Bloking, and Y.M. Chiang, *Electronically conductive phospho-olivines as lithium storage electrodes*. Nat. Mater., 2002. **1**(2): p. 123-128.
113. Thackeray, M.M., et al., *Li_2MnO_3-stabilized $LiMO_2$(M = Mn, Ni, Co) electrodes for lithium-ion batteries*. J. Mater. Chem., 2007. **17**(30): p. 3112-3125.
114. Yu, H. and H. Zhou, *High-Energy Cathode Materials (Li_2MnO_3-$LiMO_2$) for Lithium-Ion Batteries*. J. Phys. Chem. Lett., 2013. **4**(8): p. 1268-1280.
115. Kang, S.-H., et al., *Interpreting the structural and electrochemical complexity of $0.5Li_2MnO_3$ $0.5LiMO_2$ electrodes for lithium batteries ($M = Mn_{0.5-x}Ni_{0.5-x}Co_{2x}, 0 \le x \le 0.5$)*. J.Mater.Chem., 2007.**17**(20):p. 2069-2077.
116. Lu, Z., D. MacNeil, and J. Dahn, *Layered cathode materials $Li[Ni_xLi_{(1/3-2x/3)}Mn_{(2/3-x/3)}]O_2$ for lithium-ion batteries*. Electrochemical and Solid-State Letters, 2001. **4**(11): p. A191-A194.
117. Johnson, C., et al., *The significance of the Li_2MnO_3 component in composite xLi_2MnO_3-$(1-x)LiMn_{0.5}Ni_{0.5}O_2$ electrodes*. Electrochem. Commun., 2004. **6**(10): p. 1085-1091.
118. Yang, Z., et al., *Electrochemical energy storage for green grid*. Chem. Rev., 2011. **111**(5): p. 3577-3613.
119. Boulineau, A., et al., *First Evidence of Manganese-Nickel Segregation and Densification upon Cycling in Li-Rich Layered Oxides for Lithium Batteries*. Nano lett., 2013. **13**(8): p. 3857-3863.
120. McCalla, E., et al., *The Role of Metal Site Vacancies in Promoting Li-Mn-Ni-O Layered Solid Solutions*. Chem. Mater., 2013. **25**(13): p. 2716-2721.

121. Yu, H., et al., *Direct Atomic-Resolution Observation of Two Phases in the $Li_{1.2}Mn_{0.567}Ni_{0.166}Co_{0.067}O_2$ Cathode Material for Lithium-Ion Batteries*. Angew. Chem., Int. Ed., 2013. **52**(23): p. 5969-5973.
122. Hy, S., et al., *Direct In situ Observation of Li_2O Evolution on Li Rich High Capacity Cathode Material, $Li[Ni_xLi_{(1-2x)/3}Mn_{(2-x)/3}]O_2$ ($0 \leq x \leq 0.5$)*. J. Am. Chem. Soc., 2013.
123. Wu, F., et al., *Spinel/Layered Heterostructured Cathode Material for High-Capacity and High-Rate Li-Ion Batteries*. Adv. Mater., 2013. **25**(27): p. 3722-3726.
124. Yu, H., et al., *High-energy 'composite' layered manganese-rich cathode materials via controlling Li_2MnO_3 phase activation for lithium-ion batteries*. Phys. Chem. Chem. Phys., 2012. **14**(18): p. 6584-6595.
125. Rowe, A.W. and J. Dahn, *Positive Electrode Materials in the Li-Mn-Ni-O System Exhibiting Anomalous Capacity Growth during Extended Cycling*. J. Electrochem. Soc., 2014. **161**(3): p. A308-A317.
126. Kalyani, P., et al., *Lithium metal rechargeable cells using Li_2MnO_3 as the positive electrode*. J. Power Sources, 1999. **80**(1): p. 103-106.
127. Robertson, A.D. and P.G. Bruce, *Mechanism of electrochemical activity in Li_2MnO_3*. Chem. Mater., 2003. **15**(10): p. 1984-1992.
128. Denis, Y., et al., *Electrochemical activities in Li_2MnO_3*. J. Electrochem. Soc., 2009. **156**(6): p. A417-A424.
129. Lu, Z. and J. Dahn, *Understanding the Anomalous Capacity of $Li/Li[Ni_xLi_{(1/3-2x/3)}Mn_{(2/3-x/3)}]O_2$ Cells Using In Situ X-Ray Diffraction and Electrochemical Studies*. J. Electrochem. Soc., 2002. **149**(7): p. A815-A822.
130. Lu, Z., et al., *Synthesis, Structure, and Electrochemical Behavior of $Li[Ni_xLi_{1/3-2x/3}Mn_{2/3-x/3}]O_2$*. J. Electrochem. Soc., 2002. **149**(6): p. A778-A791.
131. Park, Y.J., et al., *Synthesis and Electrochemical Characteristics of $Li[Co_xLi_{(1/3-x/3)}Mn_{(2/3-2x/3)}]O_2$ Compounds*. J. Electrochem. Soc., 2004. **151**(5): p. A720-A727.
132. Kim, J.M., S. Tsuruta, and N. Kumagai, *Electrochemical properties of $Li(Li_{(1-x)/3}Co_xMn_{(2-2x)/3})O_2$ ($0 \leq x \leq 1$) solid solutions prepared by poly-vinyl alcohol (PVA) method*. Electrochem. Commun., 2007. **9**(1): p. 103-108.
133. Deng, Z. and A. Manthiram, *Influence of cationic substitutions on the oxygen loss and reversible capacity of lithium-rich layered oxide cathodes*. J. Phys. Chem. C, 2011. **115**(14): p. 7097-7103.

134. Xiao, P., et al., *Calculations of Oxygen Stability in Lithium-Rich Layered Cathodes*. J. Phys. Chem. C, 2012. **116**(44): p. 23201-23204.
135. Boulineau, A., et al., *Structure of Li_2MnO_3 with different degrees of defects*. Solid State Ionics, 2010. **180**(40): p. 1652-1659.
136. Kim, D., et al., *Synthesis of xLi_2MnO_3 $(1-x)LiMO_2$ (M = Cr, Mn, Co, Ni) nanocomposites and their electrochemical properties*. Mater. Res. Bull., 2010. **45**(3): p. 252-255.
137. Thackeray, M., et al., *Comments on the structural complexity of lithium-rich $Li_{1+x}M_{1-x}O_2$ electrodes (M = Mn, Ni, Co) for lithium batteries*. Electrochem. Commun., 2006. **8**(9): p. 1531-1538.
138. Meng, Y., et al., *Cation Ordering in Layered O_3 $Li[Ni_xLi_{1/3-2x/3}Mn_{2/3-x/3}]O_2$ $(0\leq x\leq 1/2)$ Compounds*. Chem. Mater., 2005. **17**(9): p. 2386-2394.
139. Jarvis, K.A., et al., *Atomic structure of a lithium-rich layered oxide material for lithium-ion batteries: evidence of a solid solution*. Chem. Mater., 2011. **23**(16): p. 3614-3621.
140. Rossen, E., C. Jones, and J. Dahn, *Structure and electrochemistry of $Li_xMn_yNi_{1-y}O_2$*. Solid State Ionics, 1992. **57**(3): p. 311-318.
141. Liu, Y., Y. Gao, and A. Dou, *Influence of Li content on the structure and electrochemical performance of $Li_{1+x}Ni_{0.25}Mn_{0.75}O_{2.25+x/2}$ cathode for Li-ion battery*. J. Power Sources, 2014. **248**: p. 679-684.
142. Hong, J., et al., *Structural evolution of layered $Li_{1.2}Ni_{0.2}Mn_{0.6}O_2$ upon electrochemical cycling in a Li rechargeable battery*. J. Mater. Chem., 2010. **20**(45): p. 10179-10186.
143. Xu, B., et al., *Identifying surface structural changes in layered Li-excess nickel manganese oxides in high voltage lithium ion batteries: A joint experimental and theoretical study*. Energy Environ. Sci., 2011. **4**(6): p. 2223-2233.
144. Song, B., et al., *Structural evolution and the capacity fade mechanism upon long-term cycling in Li-rich cathode material*. Phys. Chem. Chem. Phys., 2012. **14**(37): p. 12875-12883.
145. Gu, M., et al., *Formation of the spinel phase in the layered composite cathode used in Li-ion batteries*. Acs Nano, 2012. **7**(1): p. 760-767.
146. Armstrong, A.R., et al., *Demonstrating oxygen loss and associated structural reorganization in the lithium battery cathode $Li[Ni_{0.2}Li_{0.2}Mn_{0.6}]O_2$*. J. Am. Chem. Soc., 2006. **128**(26): p. 8694-8698.
147. Wang, R., et al., *Atomic Structure of Li_2MnO_3 after Partial Delithiation and Re-Lithiation*. Adv. Energy Mater., 2013. **3**(10): p. 1358-1367.

148. Yabuuchi, N., et al., *Detailed Studies of a High-Capacity Electrode Material for Rechargeable Batteries, Li_2MnO_3-$LiCo_{1/3}Ni_{1/3}Mn_{1/3}O_2$*. J. Am. Chem. Soc., 2011. **133**(12): p. 4404-4419.
149. Kang, S.-H., et al., *The Effects of Acid Treatment on the Electrochemical Properties of $0.5Li_2MnO_3{\cdot}0.5LiNi_{0.44}Co_{0.25}Mn_{0.31}O_2$ Electrodes in Lithium Cells*. J. Electrochem. Soc., 2006. **153**(6): p. A1186-A1192.
150. Kang, Y.-M., et al., *Improvement of Initial Coulombic Efficiency of Co_3O_4 by Ballmilling Using Ni as an Additive*. J. Electrochem. Soc., 2003. **150**(11): p. A1538-A1543.
151. Ito, A., et al., *Cyclic deterioration and its improvement for Li-rich layered cathode material $Li[Ni_{0.17}Li_{0.2}Co_{0.07}Mn_{0.56}]O_2$*. J. Power Sources, 2010. **195**(2): p. 567-573.
152. Gu, M., et al., *Conflicting roles of nickel in controlling cathode performance in lithium ion batteries*. Nano lett., 2012. **12**(10): p. 5186-5191.
153. Yu, X., et al., *Understanding the Rate Capability of High-Energy-Density Li-Rich Layered $Li_{1.2}Ni_{0.15}Co_{0.1}Mn_{0.55}O_2$ Cathode Materials*. Adv. Energy Mater., 2013.
154. Yamada, A. and M. Tanaka, *Jahn-Teller structural phase transition around 280K in $LiMn_2O_4$*. Mater. Res. Bull., 1995. **30**(6): p. 715-721.
155. Deng, H., et al., *High Temperature Performance of Surface-Treated $Li_{1.1}(Ni_{0.15}Co_{0.1}Mn_{0.55})O_{1.95}$ Layered Oxide*. J. Electrochem. Soc., 2010. **157**(10): p. A1035-A1039.
156. Wu, Y. and A. Manthiram, *High Capacity, Surface-Modified Layered $Li[Li_{(1-x)/3}Mn_{(2-x)/3}Ni_{x/3}Co_{x/3}]O_2$ Cathodes with Low Irreversible Capacity Loss*. Electrochem. Solid-State Lett., 2006. **9**(5): p. A221-A224.
157. Liu, J., B. Reeja-Jayan, and A. Manthiram, *Conductive surface modification with aluminum of high capacity layered $Li[Li_{0.2}Mn_{0.54}Ni_{0.13}Co_{0.13}]O_2$ cathodes*. J. Phys. Chem. C, 2010. **114**(20): p. 9528-9533.
158. Sun, Y.-K., et al., *Synthesis and Electrochemical Properties of ZnO-Coated $LiNi_{0.5}Mn_{1.5}O_4$ Spinel as 5 V Cathode Material for Lithium Secondary Batteries*. Electrochem. Solid-State Lett., 2002. **5**(5): p. A99-A102.
159. Cho, J., et al., *Synthesis, Thermal, and Electrochemical Properties of $AlPO_4$-Coated $LiNi_{0.8}Co_{0.1}Mn_{0.1}O_2$ Cathode Materials for a Li-Ion Cell*. J. Electrochem. Soc., 2004. **151**(11): p. A1899-A1904.
160. Sun, Y.K., et al., *The Role of AlF_3 Coatings in Improving Electrochemical Cycling of Li-Enriched Nickel-Manganese Oxide Electrodes for Li-Ion Batteries*. Adv. Mater., 2012. **24**(9): p. 1192-1196.

161. Kang, S.-H. and M.M. Thackeray, *Enhancing the rate capability of high capacity xLi_2MnO_3 (1-x)$LiMO_2$ (M = Mn, Ni, Co) electrodes by $LiNiPO_4$ treatment*. Electrochem. Commun., 2009. **11**(4): p. 748-751.
162. Croy, J.R., et al., *Designing high-capacity, lithium-ion cathodes using X-ray absorption spectroscopy*. Chem. Mater., 2011. **23**(24): p. 5415-5424.
163. Song, B., et al., *Graphene-based surface modification on layered Li-rich cathode for high-performance Li-ion batteries*. J. Mater. Chem. A, 2013. **1**(34): p. 9954-9965.
164. Song, B., et al., *High rate capability caused by surface cubic spinels in Li-rich layer-structured cathodes for Li-ion batteries*. Sci. Rep., 2013. **3**.
165. Gallagher, K.G., et al., *Correlating hysteresis and voltage fade in lithium-and manganese-rich layered transition-metal oxide electrodes*. Electrochem. Commun., 2013. **33**: p. 96-98.
166. Bettge, M., et al., *Voltage Fade of Layered Oxides: Its Measurement and Impact on Energy Density*. J. Electrochem. Soc., 2013. **160**(11): p. A2046-A2055.
167. Croy, J.R., et al., *Countering the Voltage Decay in High Capacity xLi_2MnO_3 (1-x)$LiMO_2$ Electrodes (M = Mn,Ni, Co) for Li^+ Ion Batteries*. J. Electrochem. Soc., 2012. **159**(6): p. A781-A790.
168. Lee, E.-S. and A. Manthiram, *Smart Design of Lithium-rich Layered Oxide Cathode Compositions with Suppressed Voltage Decay*. J. Mater. Chem. A, 2014.

3. Research Objectives

Currently, one of the most challenging issues for EVs to replace the traditional car is the cost, which is mainly determined by the car batteries. Cathode is the key component that plays the main role in determining the energy density and prices for batteries. Some of the popular cathode materials such as layered $LiCoO_2$, spinel $LiMn_2O_4$ and olivine $LiFePO_4$ have been successfully commercialized in portable electronics; however, their limited specific capacities seriously restrict their way to the EVs.

Li_2MnO_3 based layered Li-rich materials have attracted much recent attention as the most promising cathode candidates for EVs. They feature a superior high specific capacity that is almost two times of the traditional cathode materials and also a high working voltage. Currently, there are still some challenges for Li-rich cathode materials to overcome before practical application. On one hand, a fundamental understanding of the electrochemical reaction mechanisms and the corresponding crystal structure evolution is still not available. On the other hand, there is still much room to improve the electrochemical performance in terms of the energy density, long term cycling stability and rate capability.

This thesis aims to develop high energy Li-rich cathode materials for LIBs and investigate the electrochemistry reaction mechanisms. Specifically, the objectives of the work in the thesis focus on two aspects:

1) Composition and crystal structure control of the Li-rich Mn-based layered cathode materials to obtain new generation high capacity cathode materials for LIBs. (Chapter 4, 5 and 6)

2) Better understanding the electrochemistry reactions and the corresponding crystal structure evolution in Li-rich cathode materials to guide the design and development of new high energy Li-rich cathode materials (Chapter 4, 5, 6 and 7).

4. Research Methodology

4.1 Material synthesis

All the chemicals are purchased from Aldrich Sigma. The Ni or Co doped Li-rich composites were synthesized by two steps. Firstly, stoichiometric amount of manganese nitrate and cobalt nitrate/ nickel nitrate were dissolved in distilled water and then slowly dropped to equal volume of 0.2 M sodium carbonate solution under vigorous stirring. After 20 h aging at room temperature, the metal ions were fully co-precipitated as carbonates. In the second step, the collected carbonates were pre-treated at 500 ℃ for 5 h in air and then calcined with stoichiometric amount of LiOH·H_2O at 900 ℃ for another 12 h in air to produce the final cathode materials. A 3 wt % excess of LiOH·H_2O was applied for the calcination process to compensate for Li volatilization at elevated temperature.

4.2 Material characterizations

A variety of advanced characterization techniques will be employed to comprehensively study the cathode materials, including:

- Inductively Coupled Plasma Atomic Emission Spectroscopy (ICP-AES, Varian 725-ES)
- Scanning electron microscopy (SEM, JEOL 6610)
- Transmission electron microscopy (TEM, JEOL 1010 at 100 kV)
- Scanning transmission electron microscopy (STEM, Philips FEI Tecnai F20 at 200 kV)
- Scanning transmission electron microscopy with high angle annular dark field detector (STEM, JEM-ARM200F at 200kV with HAADF)
- X-ray powder diffraction (XRD, Bruker Advanced X-Ray Diffractometer (40 kV, 30 mA) with Cu Kα (λ= 1.5406 Å) radiation)
- High-resolution synchrotron *in-situ* X-ray diffraction (synchrotron *in-situ* XRD, in transmission mode on beamline 10-BM-1 of Australian Synchrotron using the MY THEN micro-strip detector and a Si(111) monochromator with the wavelength of 0.8265 Å)
- X-ray photoelectron spectroscopy (XPS, Kratos Axis Ultra X-ray Photoelectron Spectrometer with AlKα (1253.6 eV) X-ray)
- Energy dispersive X-ray spectroscopy (EDS, on Philips XL30)

- Thermogravimetric analysis (TGA, Mettler Toledo)

ICP-AES and XPS analysis were employed to determine elemental compositions. Morphology and local crystal structure of the cathode materials were observed using SEM and TEM. EDS was carried out together with the SEM in order to confirm the existing elements in confined local areas. STEM-HAADF was performed to directly visualize the local atom arrangement of the cathode materials. Crystal structure of the bulk materials was identified by XRD. In-situ XRD with synchrotron radiation was applied to detect the crystal structure evolution of the cathode materials during electrochemical reactions. Thermal stability of the materials was investigated by TGA under nitrogen atmosphere.

4.3 Preparation of coin cells

4.3.1 Preparation of cathodes

Circular cathodes with a diameter of 15 mm and mass loading of around 3 mg/cm^2 were prepared by a popular doctor-blade method. Firstly, the active material was mixed with acetylene black and PVDF binder with the weight ratio of 7:2:1 in a mortar. After that, the mixture was dissolved by a few drops of NMP and then further grounded to make slurry, which was coated on aluminium current collector by doctor-blade method. Afterwards, the electrodes were dried under vacuum at 110℃ for 12h. Finally, the whole electrode sheet was punched into a few circular electrodes by a small puncher with the diameter of 15mm and each electrode was weighed to get the exact mass loading on each electrode. Note all the electrodes are in the same lateral size and basically the same mass loading with only marginal deviation.

4.3.2 Assembly of coin cells

The CR2032 coin cells were assembled in an argon-filled glove box (MBraun, German) with the configuration as shown in **Figure 4.1**. A circular Li metal foil (99.9% purity, 200um thick, 15mm diameter) was used as the anode and 1 M LiPF6 in Ethylene carbonate : Diethyl carbonate : Dimethyl carbonate 1:1:1 w/w was used as the electrolyte. To separate the two electrodes, two pieces of circular Celgard 3501 membrane with a diameter that slightly larger than the cathode were placed between the two electrodes. To ensure the close contact of each part, a space and/or a wave spring was set between the anode and the negative cell shell.

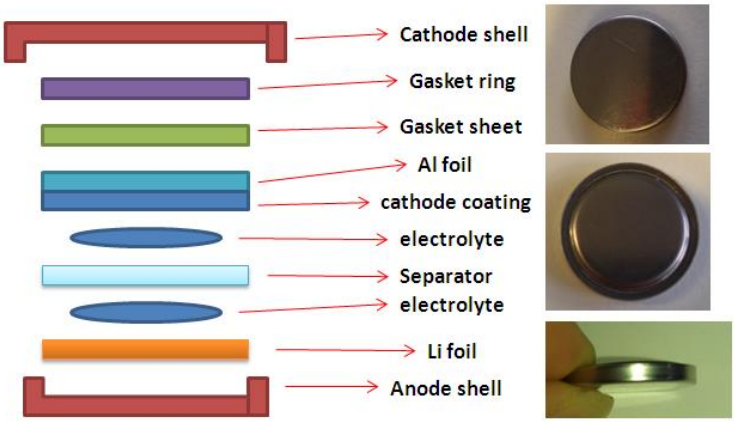

Figure 4.1 Schematic representation of coin cell assembly

4.4 Electrochemical measurements

To test the electrochemical properties of the cathode materials, some measurements were conducted including the charge-discharge test, cyclic voltammetry (CV) and electrochemical impedance spectroscopy (EIS). Note all the electrochemical measurements were performed on the CR 2032 coin cell.

4.4.1 Cycling and rate capability test

Cycling performance was evaluated by a multi-channel battery tester (Land CT2001A). Specifically, three cycling potential windows including 2-4.6 V, 2-4.8 V and 2-5 V were investigated in our Li-rich cathode material systems, and a standard current density of 30 mA g^{-1} (0.1 C) was applied for all the materials to test their specific capacity. To measure the rate performance, after a few activation cycles at 0.1 C, the electrodes were then cycled at different current densities of 60 mA g^{-1}, 150 mA g^{-1}, 300 mA g^{-1}, 600 mA g^{-1}, 1500 mA g^{-1} and 3000 mA g^{-1} with 10 cycles in each current density.

4.4.2 Cyclic voltammetry

All the cyclic voltammetry tests were conducted in a CHI660E electrochemical workstation. Three cycling potential windows including 2-4.6 V, 2-4.8 V and 2-5 V and a standard scan rate of 0.2 mV/s were applied for all the materials. Note that the lithium metal was used in the coin cell as the counter and reference electrodes.

4.4.3 Electrochemical impedance spectroscopy

Electrochemical impedance spectroscopy (EIS) measurements were performed at room temperature using the same CHI660E electrochemical workstation. And all the tests were conducted on the coin cells with metallic lithium as the counter and reference electrodes. A frequency range of 100 kHz to 10 mHz was selected as a standard testing range at either the open circuit voltage or 4.5 V after a few stabilizing cycles and then charged to 4.5 V.

5. Capacity-Controllable Li-rich Cathode Materials for Lithium-Ion Batteries

5.1 Abstract

In this study, we report a new type of Li-rich layered-spinel materials with a general composition formula of $xLi_2[Mn_{0.857}Co_{0.143}]O_3$-$(1-x)Li[Mn_{1.714}Co_{0.286}]O_4$ (x = 0.95, 0.85, 0.75 and 0.65) for use as cathode materials in Li-ion batteries. These materials exhibit steadily increased specific capacities upon cycling for up to several dozen of cycles, depending on the charge-discharge potential windows. Various characterizations reveal that the specific capacity increase is due to the gradual activation of the initial Li-rich layered phase from the surface of the composite particles. Both experimental and computational results suggest that a small amount of Co dopants plays a critical role in the continuous activation process of these materials and the structural evaluation mechanism is also discussed. Based on this unique feature, controllable discharge capacities of these cathode materials can be achieved in a broad range from 30 to 240 mAh g^{-1} by deliberately activating the materials at a potential window of 2~4.8 V.

5.2 Introduction

Rechargeable lithium-ion batteries (LIBs) have become a dominant power source for portable electronics [1]. In recent years, due to the global warming and shortage of fossil fuel, low-emission EVs have attracted much interest and lithium-ion batteries have been considered as one of the most promising candidates as the EV power source [2-4]. However, low energy density of conventional LIBs remains as the bottleneck mainly due to inadequate capacity of the cathode materials, for instance $LiCoO_2$ (*ca.*150 mAh g^{-1}) or $LiFePO_4$ (170 mAh g^{-1}) [5, 6]. In this respect, extensive studies have been devoted to developing new cathode materials with potentially higher specific capacities.

Early studies have revealed that Li-rich Mn-based oxides with a general chemical composition of xLi_2MnO_3-(1-x)$LiMO_2$ (M = Mn, Co or Ni) are presumed to be promising cathode materials mainly because of their high specific capacities over 250 mAh g^{-1} [7-11]. In this type of materials, C2/m Li-rich Li_2MnO_3 phase can be highly integrated with a $R\bar{3}m$ $LiMO_2$; and Co/Ni doping with a (Co+Ni)/Mn molar ratio of 1/3 or higher is usually applied to improve the structure stability during cycling [9, 11]. Typically, this Li-rich Li_2MnO_3 component is fully activated in the first cycle with a long charging plateau above 4.5V, followed by a high discharge capacity in the first discharge process [9, 11-14]. Currently, Li-rich layered cathode materials still face some challenges such as poor long-term cycling stability and low power density mainly due to the drastic activation and structure evolution of the Li-rich layered phase in the first cycle and following deterioration upon further cycling [12, 14, 15]. Fortunately, the cycling stability and rate performance have been effectively improved by some novel methods such smart microstructure design and efficient surface coating in recent progress [16-18]. However, due to the complicated composition and crystal structures, the fundamental mechanisms of the origin of the ultrahigh reversible capacity and the related structure evolution during cycling have not been fully revealed and remain the most challenging issue for Li-rich cathode material [19, 20].

Considering the relatively high content of toxic and relatively expensive Co dopants in these previously reported Li-rich compounds, we recently studied layered Li-rich cathode materials with much lower Co/Mn molar ratio of 1/6 [21]. Interestingly, unlike most Li-rich cathode materials with continuous capacity decrease upon cycling, this low-Co Li-rich material exhibited quite different electrochemistry behaviour. Its discharge capacity increased anomalously from around 40 mAh g^{-1} to more than 200 mAh g^{-1} in the first several cycles. This phenomenon of capacity increase upon cycling (CIUC) has been observed in some other materials systems like CoO [22] and Fe_3O_4 [23],

however, the intrinsic reasons seem to be different from the Li-rich materials. In fact, this CIUC phenomenon in Li-rich materials has been reported by a few senior groups recently [24-27]. For example, in a recent paper by Kang et al., the overall capacity of their Ni-doped Li-rich material gradually increased in the first 40 cycles, and the large particle size is suggested to be the cause [25]. Another more recent study by Sung *et al.* reported specific capacity increase in their materials in the first 20 cycles from 187 mAh g^{-1} to 194 mAh g^{-1} and proposed the increase is related to the continuous activation of the remaining Li_2MnO_3 structure [28]. However, the increment of capacity in those reported was very limited and the information about the systematic understanding of this CIUC phenomenon in Li-rich cathode materials is still not available. The key questions of why the Li_2MnO_3 is activated continuously in a few cycles rather than fully in the first cycle only and what's the main factor that can affect the rate of activation are still not well-answered.

In this study, we report a detailed study on the understanding of CIUC behaviour based on a series of low-Co containing Li-rich cathode materials with a modified layered-spinel structure. By a simple co-precipitation and solid-state reaction, we were able to alter the chemical composition of $xLi_2[Mn_{0.857}Co_{0.143}]O_3$-(1-x)$Li[Mn_{1.714}Co_{0.286}]O_4$ (x = 0.95, 0.85, 0.75 and 0.65) to introduce a slightly variable amount of spinel phase into the layered structure. A very prominent CIUC behaviour up to several dozens of charge-discharge cycles in these materials was observed by applying a potential window of 2-4.8 V. Interestingly, such phenomenon can be effectively suppressed when the upper cut-off potential was reduced to 4.6 V. Detailed electrochemical and structural characterizations reveal that the increment in specific capacity is attributable to the gradual activation of the surface Li-rich layered phase. In addition, further computational study along with experimental results indicates that Co-doping plays a significant role in promoting the activation process of the Li-rich layered phase by energetically facilitating the diffusion of TMs and the formation of oxygen vacancies (OVs), both of which are directly involved in the activation of Li-rich phase. As a result, we can rationally control the reversible capacity in a broad range from around 30 to 240 mAh g^{-1} by deliberately activating the pristine materials at 2-4.8 V for certain cycles. The findings herein may shed light not only on the mechanism understanding of the CIUC behaviour in Li-rich compounds but also on the design of some "smart" capacity-controllable battery systems which have been rarely reported before.

5.3 Experimental section

Materials synthesis: The $xLi_2[Mn_{0.857}Co_{0.143}]O_3$-(1-x)$Li[Mn_{1.714}Co_{0.286}]O_4$ (x = 0.95, 0.85, 0.75 and 0.65) composites materials were synthesized via a high-temperature calcination process using

LiOH·H_2O and manganese-cobalt carbonate as starting materials [14, 21]. In a typical synthesis, a 0.2 M aqueous solution of $MnSO_4 \cdot 5H_2O$ and $CoSO_4 \cdot 7H_2O$ with the Mn/Co molar ratio of 6:1 was added to an equal volume of 0.2M sodium carbonate aqueous solution, yielding a light pink precipitate. After being aged for 20 h under continuous stirring at room temperature, the obtained precipitate was filtered, washed thoroughly with distilled water for three times, dried at 100 ℃ and then heated at 500 ℃ in air for 5 h. The resultant black powders were then mixed with LiOH·H_2O with different Li:(Mn+Co) molar ratios of 1.85, 1.61, 1.4, and 1.22, for the samples with x = 0.95, 0.85, 0.75, and 0.65 respectively. A 3 wt % excess of LiOH·H_2O was added to the starting materials to compensate Li insufficiency due to the Li volatilization at elevated temperature. The mixtures were calcined at 900 ℃ in air for 12 h to produce the layered-spinel composites.

Materials characterization: The Li, Mn and Co molar ratios in all the composites were measured by a Varian 725-ES Inductively Coupled Plasma Atomic Emission Spectroscopy – (ICP-AES). Crystalline structures of powder samples, electrodes before and after different charge/discharge cycles were identified by X-ray diffraction (XRD) on a Bruker Advanced X-Ray Diffractometer (40 kV, 30 mA) with Cu Kα (λ= 0.15406 nm) radiation at a scanning rate of 1^o min^{-1} from 15º to 75º (2θ). The morphological characteristics of synthesized samples were investigated using a scanning electron microscope (SEM, JEOL 7800). Scanning transmission electron microscopy (STEM) investigations were acquired on a JEM-ARM200F transmission electron microscope (TEM), operated at 200kV with a high angle annular dark field (HAADF) detector.

Electrochemical test: To prepare the working electrodes, a mixed slurry containing 70 wt % of the active materials, 20 wt % of acetylene black and 10 wt % of polyvinylidene fluoride (dissolved in N-methyl-2-pyrrolidone with a concentration of 5 wt %) was spread onto aluminium foils (0.7 cm^2) by doctor blade process and then dried in an oven under vacuum at 120 °C for 12 h. These working electrodes were then assembled with lithium metal as the negative electrode and 1 M $LiPF_6$ in a mixture of ethylene carbonate (EC) and dimethyl carbonate (DMC) (1:1) as the electrolyte to fabricate CR2032-type coin cells in an argon-filled glove box. The galvanostatic charge/discharge test was conducted on a multi-channel battery tester (Land CT2001A) with the voltage range of 2.0−4.6 V and 2.0−4.8 V at room temperature, respectively. Cyclic voltammetry (CV) measurements of the cells were performed by using a CHI660E Electrochemical Workstation with a scan rate of 0.2 mV s^{-1} in the same voltage windows.

Computational Method: In this study, periodic density functional theory (DFT) calculations were carried out using the Perdew–Burke–Ernzerhof functional, as embedded in the Vienna ab initio

simulation package (VASP), and the electron-ion interaction was described by the projector augmented wave method with a cut-off energy of 380 eV [29-31]. The k-space was sampled by the gamma point. Since OV was involved, the on-site electron correlation was particularly necessary; therefore DFT plus Hubbard model (DFT +U) was employed in the calculations [32]. The U values for Mn and Co atoms were set as 5.0 eV, based on references [33, 34]. Li_2MnO_3 was modelled by the 2×1×2 supercell, with a dimension size of 9.87 Å×8.53 Å ×10.06 Å and a formula of $Li_{32}Mn_{16}O_{48}$. Co-doping was modelled with one Mn-atom replaced by Co-atom and OV was modelled by removing one O-atom from the lattice. The OV formation energy was calculated by $E_f = E(Li_xMn_{16-\delta}Co_\delta O_{48})-E(Li_xMn_{16-\delta}Co_\delta O_{47})-1/2E(O_2)$. Negative value of E_f indicates the formation of OV is endothermic.

5.4 Results and discussion

Chemical composition and crystal structure

ICP-AES analysis results of $xLi_2[Mn_{0.857}Co_{0.143}]O_3$-(1-x)$Li[Mn_{1.714}Co_{0.286}]O_4$ (x = 0.95, 0.85, 0.75 and 0.65) composites are shown in **Table 5.1**. The experimental data of Mn:Co and Li:(Mn+Co) ratios in all samples are in good agreement with the nominal values. Spherical micrometer-sized particles (1~2μm) consisting of 100~200 nm sized primary nanoparticles aggregates were obtained for all samples (**Figure S5.1**). This hierarchical particle structure can be of advantage in terms of electrolyte diffusion and Li ions insertion/extraction. **Figure 5.1a** shows XRD patterns of pristine $xLi_2[Mn_{0.857}Co_{0.143}]O_3$-(1-x)$Li[Mn_{1.714}Co_{0.286}]O_4$ (x = 0.95, 0.85, 0.75 and 0.65) samples.

For the x = 0.95 sample, all strong diffraction peaks can be well indexed to $R\bar{3}m$ space group of layered hexagonal α-$NaFeO_2$ phase. In addition, weak diffraction peaks between 20° and 25° can be indexed as the $LiMn_6$ superstructures existing in the TM layers of the Li_2MnO_3-like regions [8, 15, 35, 36], suggesting that the crystal structure of this sample corresponds to a monoclinic unit cell with C2/m symmetry rather than the $R\bar{3}m$ (JCPDS No. 84-1634). The well split of (-112)/(200) and (-133)/(-331) peaks and the relatively high peak intensity ratio (I(001)/I(131) = 1.36 (>1.2)) indicate a highly-crystalline layered structure with low degree of cation mixing in the Li layers and the absence of spinel phase [37, 38]. For other three samples (x = 0.85, 0.75, 0.65), additional diffraction peaks corresponding to a cubic spinel structure with a space group of $Fd\bar{3}m$ (JCPDS No. 38-0789) are gradually developed while the reflections of the layered phase become weakened with decreasing x value. As clearly illustrated in **Figure 5.1b**, main peak (~19.2°) of the spinel phase grows steadily when x decreases and reaches almost the same intensity as the neighbouring main one (~18.8°) of

the layered phase in the x = 0.65 sample. In addition, the (-133) and (-331) peaks become broader and eventually overlap with a new (440) spinel peak intercalated in between, attributing to partial phase transition from layered to cubic spinel [39, 40]. Note that even the intensity of the spinel peaks is intensified, a high and sharp (001) peak and other small peaks between 20 ° and 25 ° are still well detected in all composite samples, indicating that the layered Li-rich phase is dominant in the structures. In addition, no cubic spinel phase can be detected in the XRD pattern for the x = 0.95 sample, suggesting negligible cubic spinel phase in this material. Based on the XRD results, it is clear that both the layered and spinel phase are highly crystalline, weight percentage of different phases was estimated semi-quantitatively by the reference intensity ratio (RIR) method [41] and listed in **Table 5.1**. It can be clearly seen that the weight percentage of the layered phase is suppressed with decreasing x value. All these XRD features suggest that spinel phase can be introduced into the original layered structure by adjusting the ratio of Li source in the precursor.

Table 5.1 ICP-AES analysis results and weight percentage of the layered and spinel phases of the $xLi_2[Mn_{0.857}Co_{0.143}]O_3$-(1-x)$Li[Mn_{1.714}Co_{0.286}]O_4$ (x = 0.95, 0.85, 0.75 and 0.65) composites.

		Li : (Mn+Co)		Weight %	
X	Mn : Co	Nominal	Experimental	layered (C2/m)	spinel ($Fd\bar{3}m$)
0.95	5.89	1.86	1.88	100	0
0.85	6.14	1.61	1.62	93.8	6.2
0.75	5.95	1.40	1.38	78.8	21.2
0.65	5.95	1.22	1.22	69.1	30.9

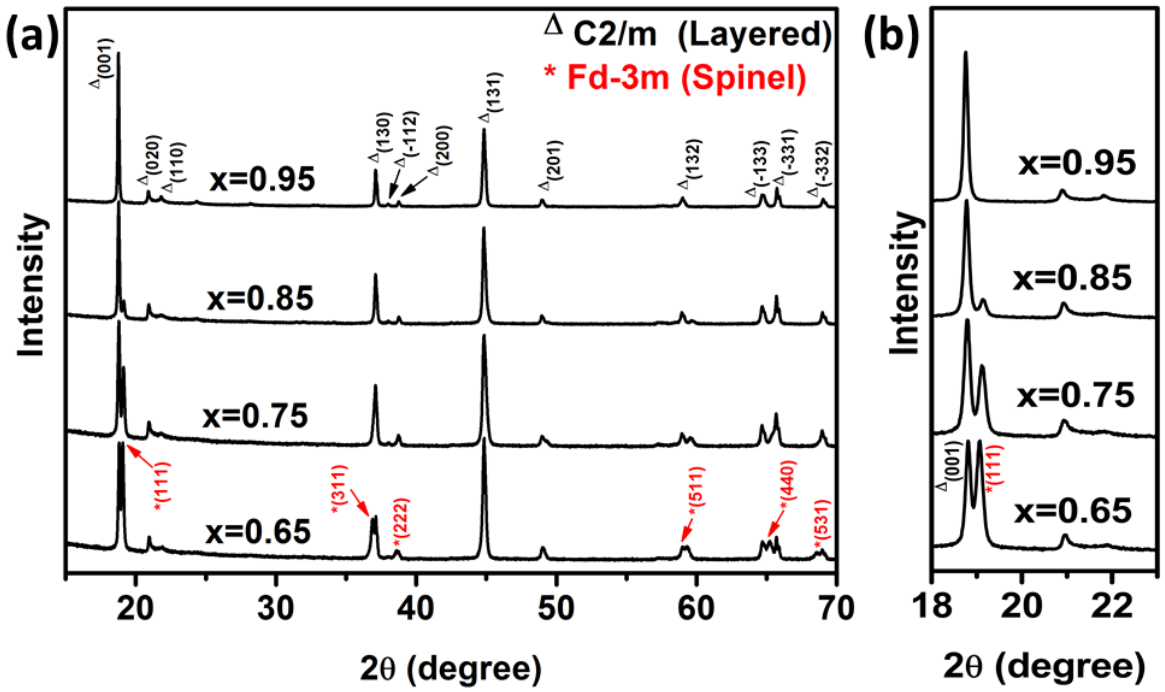

Figure 5.1 Powder X-ray diffraction patterns of the original compounds and b) enlarged main peaks.

Electrochemistry performance

The cycling performances of the $xLi_2[Mn_{0.857}Co_{0.143}]O_3$-(1-x)$Li[Mn_{1.714}Co_{0.286}]O_4$ (x = 0.95, 0.85, 0.75 and 0.65) composite materials at a current density of 30 mA g^{-1} (~0.1 C) under 2-4.8 V and 2-4.6 V for the first 100 cycles are shown in **Figure 5.2**. All the samples tested at 2-4.8 V exhibited interesting CIUP features in the initial tens of cycles from a very low initial capacity to over 250 mAh g^{-1}, and the increment was maintained upon cycling. This is in strong contrast to that of conventional Li-rich cathode materials in which gradual discharge capacity loss is normally observed upon cycling from an initial capacity value of ~200 mAh g^{-1} [11, 13, 42]. Interestingly, considering the largest capacity in the first 100 cycles at 2-4.8 V, the x = 0.85 sample displayed the highest value (255.8 mAh g^{-1}), while the other samples basically followed the trend that the less the Li-rich layered phase was, the smaller the fully-activated capacity became [24, 40]. The reason for such a superior capacity of the x = 0.85 sample will be discussed later with the charge/discharge profiles. It should be noted that, for the x = 0.85 sample, the discharge capacity reached the highest value between the 40-50th cycle and still retained ~90% of the capacity after 100 cycles. Due to the good cycling stability of the original spinel phase as demonstrated in a following section, this 10% loss in capacity (actually the greatest loss among all prepared samples) may be accounted for by the decay of the activated layered phase. Taking the imposed high cycling potential window (2-4.8 V) and the

relatively low current density (30 mA g^{-1}) into account, such a loss is understandable for the layered-spinel composites without any surface modification.

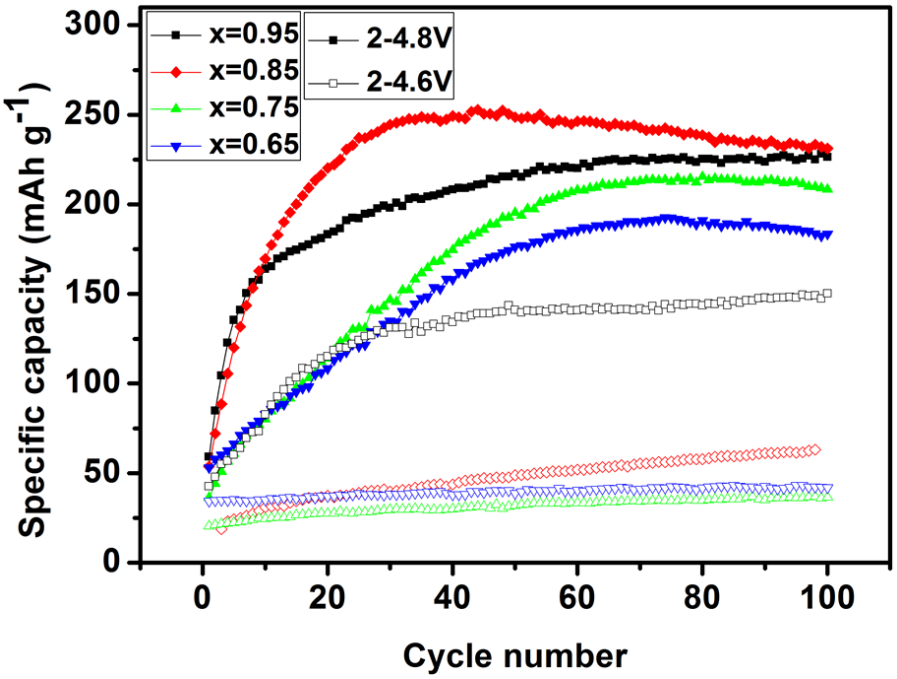

Figure 5.2 Electrochemical cycling performance of the integrated composite cathode materials at 30 mA g^{-1} between 2-4.6 V and 2-4.8 V, respectively for the first 100 cycles.

On the other hand, with upper cut-off potential of 4.6 V, the CIUP behaviour was dramatically suppressed in the first 100 cycles or even disappeared for most samples. This behaviour change clearly indicates that the required potential for effective CIUP phenomenon to occur should be slightly higher than 4.6 V in these Li-rich samples. This can be partially explained by a recent study on the high voltage charge plateau difference (0.2-0.3V) between layered and layered-spinel composite structures [16]. An exception is the x = 0.95 sample, which still exhibited noticeable capacity increase to 150 mAh g^{-1}.

To understand such unique CIUP behaviour, detailed electrochemical and structural analysis of these materials at different charge/discharge stages was conducted. **Figure 5.3a** shows the Galvanostatic charge-discharge profiles of the typical x = 0.85 sample at the 1^{st}, 5^{th}, 10^{th}, 40^{th}, 70^{th} and 100^{th} cycles within 2-4.8 V at 30 mA g^{-1}. For the charge curve, it is mainly composed of two regions: a short and steep slope from around 4 V to 4.6 V, followed by a long plateau extending up to 4.8 V. The first short region is most likely due to the oxidation of the TM ions including Co^{3+} and minimal Mn^{3+} residual to the 4+ state when around 0.083 Li^{+} units per 0.857 Mn in the formula of the layered

phase (assuming all the charge capacity at 4-4.6 V is contributed from the layered phase only) were extracted from the composite [21, 43]. The long plateau started at 4.6 V corresponds to a complicated electrochemical process involving further extraction of around 0.22 Li^+ unit per 0.857 Mn from both the TM layer and Li layer. This process simultaneously releases O_2 from the oxidation of O^{2-} in the lattice, leading to possible localized structure transition and activation of the layered phase [9, 14, 44, 45]. In contrast, the first discharge curve showed only a steep slope during the whole potential window with a capacity slightly larger than 50 mAh g^{-1}. In the following cycles, the charge and discharge capacities were almost the same and a short ~4 V and a long ~3 V discharge plateaus were gradually developed, which could be related to a new spinel phase transferred from the original layered phase [11, 24]. This suggests that the CIUP behaviour could be attributed to the activating and transferring of the original Li-rich layered phase during cycling. For the x = 0.95 sample (**Figu**re S5.2), the charge/discharge curves are similar to that of the x = 0.85 sample except for the first cycle where the capacity loss (40 mAh g^{-1}) is much larger than that of the x = 0.85 sample (14.2 mAh g^{-1}). The strategy of introducing an appropriate ratio of compatible spinel phase into the Li-rich layered materials has been reported to suppress the large irreversible capacity loss in the first cycle of the Li-rich materials [40], therefore, it can be assumed that the original spinel phase in the x = 0.85 sample alleviated the rapid structure transformation of the layered phase in the first cycle, thus large capacity loss from drastic structure change and lattice strain has been constrained. Comparing x = 0.95 and 0.85 samples, the difference (25.8 mAh g^{-1}) of the first-cycle capacity loss between two samples is almost the same as the difference (24.6 mAh g^{-1}) of their maximum discharge capacity in the first 100 cycles within 2-4.8 V. Since the Coulombic efficiency of these two samples were both close to 100% from the second cycle, the large first-cycle capacity fade of the x = 0.95 sample could be a good explanation to the aforementioned fact that the x = 0.85 sample showed a higher maximum discharge capacity than that of the x = 0.95 sample in the first 100 cycles between 2-4.8 V.

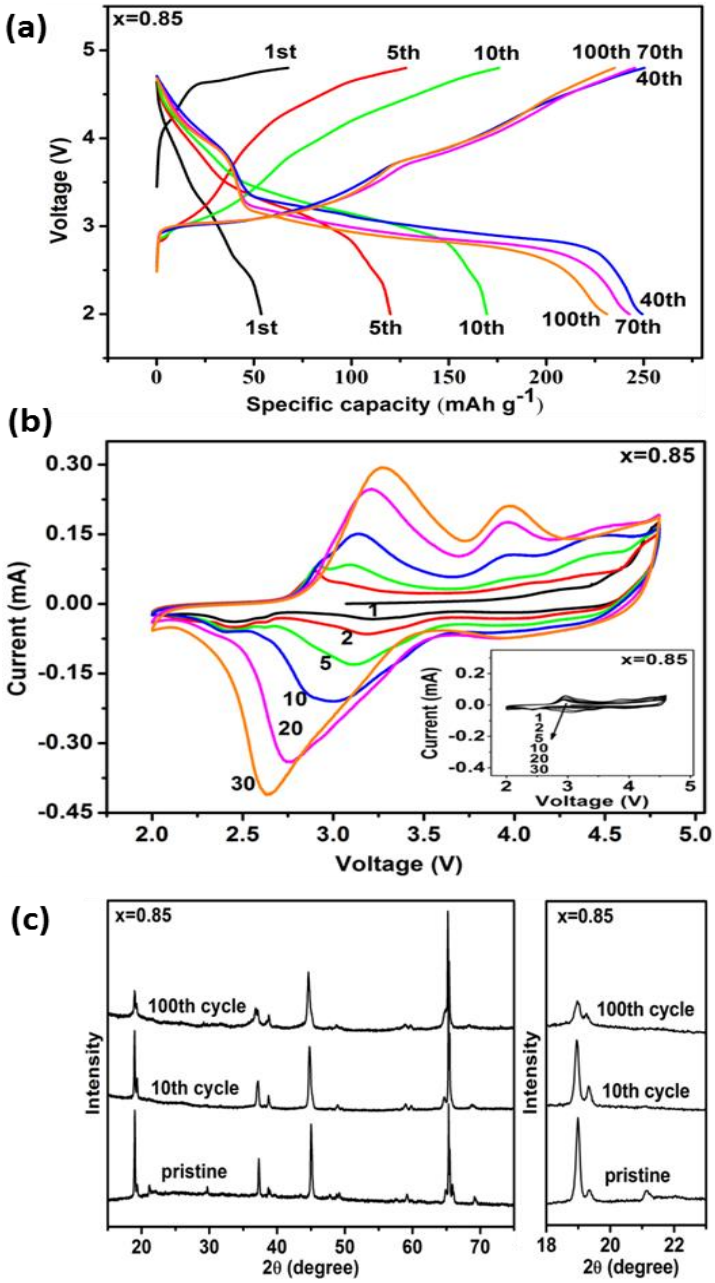

Figure 5.3 Electrochemical and XRD characterization of the x = 0.85 sample; a) Charge/discharge profiles at 2-4.8 V for the 1st, 5th, 10th, 40th, 70th and 100th cycles. b) Cyclic voltammogram loops of the 1st, 2nd, 5th, 10th, 20th and 30th cycles at 2-4.8V, the inset shows the cyclic voltammogram loops of the same cycles at 2-4.6 V. c) XRD patterns of the electrodes before cycling and after the 1st, 10th and 100th cycles at 2-4.8 V.

For the x = 0.75 and x = 0.65 samples, the charge/discharge curves (**Figure S5.2**) are similar to that of the x = 0.85 sample except a clear discharge plateau between 2.4-2.6 V. This short plateau is associated with the Li-ion intercalation into the 16c octahedral sites of the initial spinel structure [11,

24, 26]. In good fit with the XRD results, this plateau appeared in the x = 0.85 sample and was further developed in the x = 0.75 and 0.65 samples, confirming that the initial spinel phase is developed in the samples. Note that this distinctive plateau could still be clearly observed without noticeable change in the x = 0.75 and 0.65 samples even after 100 cycles, implying the good stability of the initial spinel phase upon cycling. **Figure 5.3b** presents the cyclic voltammogram (CV) loops of the x = 0.85 sample at different cycles. Clearly these loops develop gradually during cycling at 2-4.8 V but merely keep almost the same at 2-4.6 V. As the area of the CV loops is in direct proportion to the amount of Li^+ intercalation/deintercalation during charge/discharge, or in other words, the charge/discharge capacity, it indicates that the electrochemistry performance of this sample highly depends on the potential window. Another impressive feature is the evolution of the characteristic redox peaks at around 3V during cycling within 2-4.8 V. This broad 3V redox pair was rather small in the first cycle, but became dominant at the 30^{th} cycle. In accordance to the long 3V plateau in the charge/discharge profiles, it can also be ascribed to the activation process of the initial Li-rich layered phase [21, 24, 46, 47]. In addition, a small reduction peak from the initial spinel phase can be observed at around 2.6 V in the x = 0.85 sample and steadily grew in the x = 0.75 and x = 0.65 samples (**Figure S5.3**). Apparently, the size and shape of this peak in the x = 0.75 and x = 0.65 samples were almost the same during the entire 30 cycles, further confirming the good cycling stability of the initial spinel phase.

Figure 5.3c shows the *ex-situ* XRD patterns of the x = 0.85 composite electrodes before cycling and after 10 and 100 cycles. A noticeable change is that the superlattice peaks between 20 and 25 ° became wider and weaker after 10 cycles and totally disappeared after 100 cycles. This phenomenon suggests the atomic rearrangement and resultant loss of Li-Mn ordering in the TM layer of the Li-rich layered phase [14, 24, 25]. In addition, the intensity ratio of the main peaks at 18.75 ° and 19.2 °, denoting the layered Li-rich and the original spinel phases, respectively, decreased gradually during cycling. Considering the relatively good stability of the initial spinel phase, if the content of this phase is set to be fixed, the weight percentage of the layered phase after different cycles can be roughly estimated by the RIR method. As shown in **Figure S5.4** and **Table S5.1**, (The x = 0.95 sample can't be calculated by this method due to the absence of the pristine spinel phase for reference) the weight percentage of the layered phase was significantly reduced from 94.2% to 26.4% in the x = 0.85 sample and less than 30% in the other x = 0.75 and x = 0.65 samples after 100 cycles, providing solid evidence of the continuous crystal structure evolution of the layered Li-rich phase upon cycling.

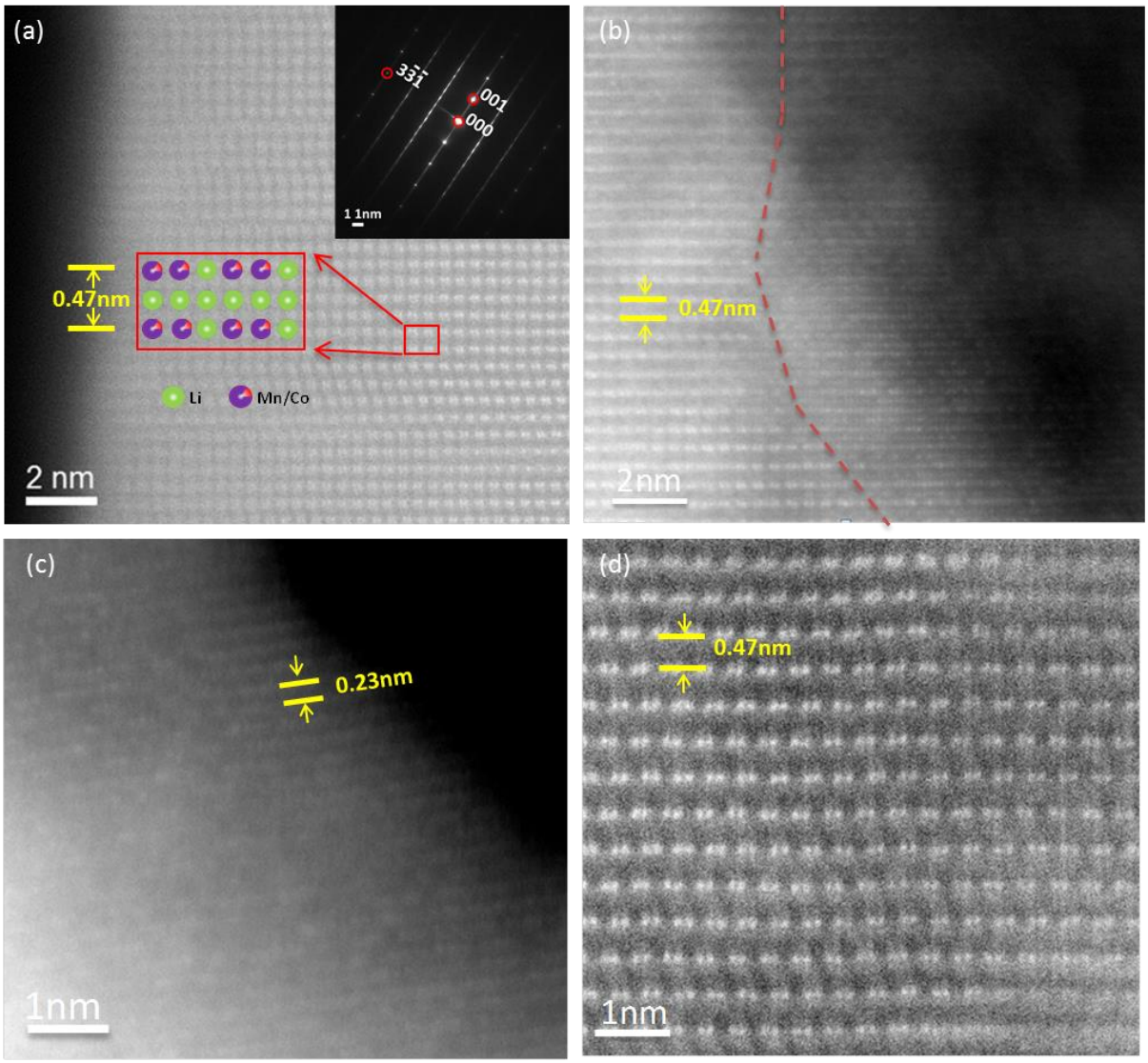

Figure 5.4 High resolution STEM-HAADF images of the x = 0.95 sample taken along the [100] zone axis. a) Before cycling; b) After 20 cycles at 2-4.8 V; c) Surface area after 50 cycles at 2-4.8 V; and d) Internal area after 50 cycles at 2-4.8 V. The right top inset in a) is the corresponding SAED pattern of the monoclinic structure projected along the [100] direction; the middle inset in a) is a schematic simulation of the Li (green) and Mn/Co (purple/red) ordering in the pristine material. The red dotted lines in b) separate the bulk area from the surface area where bright spots in the TM layers can be seen.

To fundamentally understand the activation process of the Li-rich layered phase in the local structure, the x = 0.95 sample (only pure layered phase present as confirmed by XRD) at different stages was investigated using high resolution STEM-HAADF (**Figure 5.4**). It should be noted that the contrast of the atomic columns depends mainly on the atomic mass, thus only Mn and Co are visible in this

case [48]. For the pristine material, well crystallized layered structure was homogeneously formed even in the surface area with some stacking faults of the $LiMn_2$ planes along the c-axis, which are commonly seen in doped Li-rich layered materials [45, 48]. As represented by the atomic model in **Figure 5.4a**, the typical two Mn (Co) columns (bright dumbbell-like spots) and one Li column (dark spots between two bright dumbbells) ordering in the TM layers with a layer distance of 0.47 nm are clearly identified. On the other hand, no contrast in Li layers is visible, indicating the absence of TM ions in the Li layers. In the inset selected area electron diffraction (SAED) pattern, in spite of the sharp spots reflection from the parent α-$NaFeO_2$ structure, spotted streaks along the c-axis can be clearly observed, which strongly indicated the $LiMn_6$ ordering in the TM planes and the existence of thin platelets resulted from the stacking faults along the [100] orientation [48, 49]. However, after 20 cycles, the contrast of the Li layers at the surface area (right side of the dotted red lines in **Figure 5.4b**) is changed and some bright columns can be easily observed, although not as bright as those in the neighbouring TM layers. This change suggests the transition of the original layered structure to a defect spinel phase facilitated by the migration of the TM ions from TM layers to the Li layers [50-52]. After 50 cycles, although the STEM images became a little blurry due to the decreased crystallinity of the sample after long time contact with electrolyte, it is still clear enough to see that all the layers in the surface area, no matter TM layers or Li layers, have the same contrast with the layer distance (0.23 nm) of only half of the original one (0.47 nm). This means that more TM ions had moved into the Li layers on the surface area after 50 cycles, making the concentrations of the TM layers and Li layers too close to be distinguished. Interestingly, in contrast to the surface area, the structure in the internal area was relatively stable. Consistent dark columns in the Li layers with a layer distance of 0.47 nm were well maintained even after 50 cycles. All these observations suggest that the Li-rich layered phase was gradually activated and probably converted into a new defect spinel structure in the surface area during cycling at 2-4.8 V.

Mechanism of the CIUP behaviour

Activation of the Li-rich phase may be affected by a few factors like the charge and discharge rate and the testing temperature [13, 53]. In this study, all the electrochemistry tests were conducted with a constant current density of 30 mA g^{-1} (0.1C) at room temperature. This testing condition is commonly applied in Li-rich cathode materials without any CIUP behaviour [42, 54]. Therefore, this interesting phenomenon is considered to be caused by another issue. As mentioned before, much lower Co/Mn molar ratios were used in these materials than that of the conventional Li-rich cathode materials, which may play a vital role for the observed new electrochemistry behaviours. To verify

this speculation, it is important to firstly understand the role of Co played in the activation process of the Li-rich layered phase. Theoretical calculations focusing on the energy variation of TM ions diffusion and oxygen vacancy (OV) formation with different Li-ion occupancies in the Li layers were performed (**Figure 5.5a**). It is found that TM ions diffusion to the Li-layer is very difficult when the Li-layer is fully occupied by Li ions. For instance, the reaction energy for Mn- and Co-diffusion is up to 2.70 eV and 3.96 eV respectively, which is not surprising since TM ions need to overcome the strong repulsive interaction of the positively charged Li ions in the Li-layer. With more Li ions diffusing out of the Li-layers during the charge process, the reaction energy for TM ions diffusion decreases dramatically and finally reaches 1.21 eV and 0.74 eV for Mn and Co, respectively when all Li ions in the Li-layers move out.

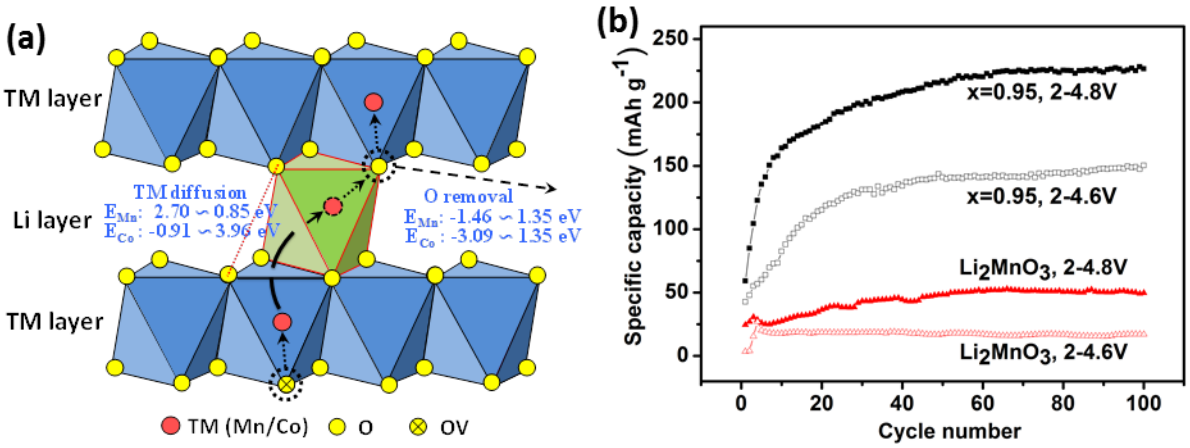

Figure 5.5 a) Schematic figure of TM ions diffusion and oxygen removal in the layered crystal structure of $Li_2Mn_{1-x}Co_xO_3$. The arrows with dotted tails indicate OV generated by oxygen removal can promote the diffusion of neighboring TM, which will in return facilitate the OV generation. b) Comparison of discharge capacities between the x = 0.95 sample and the Li_2MnO_3 sample at 2-4.6 V and 2-4.8 V.

In practice, to maintain the structure stability, only ~ 1/3 of the Li ions in the Li layers can be removed at maximum [44, 55, 56], and thus the energy required for TM ions diffusion is between 1.21-2.70 eV for Mn and 0.74-3.96 eV for Co, respectively. From these calculated values, it is reasonable to state that the TM ions diffusion is not favourable even the Li layers are completely empty. However, the above calculations were carried out without the consideration of OVs. In fact, the oxygen loss has been demonstrated both theoretically and experimentally [14, 57]. In the calculations, if one OV is introduced, the reaction energy for neighbouring Mn- and Co-diffusion will decrease to 0.85 eV and -0.91 eV (Li-layer is empty), respectively, indicating that the oxygen

loss can promote the TM ions diffusion and Co is much easier than Mn to diffuse into the Li layers when OVs exist. As a consequence, it is necessary to examine whether the above OV generation is energetically possible. In this regard, we started with a fully occupied Li-layer and found that the OV formation energy is ~ 1.35 eV, regardless of Co doped or not. Moving Co or Mn to the Li-layer can slightly reduce the formation energy to 1.17 eV and 1.29 eV, respectively, indicating that the formation of OVs is also not favourable in this case. However, if the Li-layer becomes empty and no TM ions diffuse to the Li-layer, the OV formation energy decreases to -1.10 eV and -1.44 eV, and this energy can be further reduced to -1.46 eV and -3.09 eV if Mn or Co ions diffuse into the Li-layer. All these results can also be supported by a recent study [58] in which it is demonstrated that Co-doping can lower the non-bonding band and thus effectively promote the generation of OVs. To confirm the effect of Co-doping, pure layered Li_2MnO_3 without Co doping was synthesized via the same procedure and tested as a cathode material under the same condition, as shown in **Figure 5.5b**. In comparison to the x = 0.95 sample with Co-doping, the Li_2MnO_3 material exhibited very limited capacity increase upon cycling, merely less than 50 mAh g^{-1} in the first 100 cycles at 2-4.8 V. This result provides solid experimental support to the conclusion that Co-doping plays a critical role in promoting the activation process of the Li-rich phase.

In previous studies on Li-rich layered materials with variable Co content [27, 47], the CIUP phenomenon in the first several cycles was also observed, usually the more the Co was, the faster the capacity increased. Thus Co doping is important to promote the phase transformation of the Li-rich layered phase from two aspects. On one side, the $Co^{3+/4+}$ e_g band is partially overlapped with the top of the O^{2-} 2p band [39, 59, 60], resulting into stronger metal-oxide covalence and easier oxidation of O^{2-} in the layered lattice into O_2, thus enhanced phase transformation of the Li-rich layered phase. On the other side, the TM ions can diffuse into the Li layer during the charge process. According to the first-principle calculation results reported by Xu *et al.* [50], when most of the Li are extracted in the high potential region, the TM ions in the Li layers enable the formation of a spinel-like phase with extremely low energy. However, checking the composition of those Li-rich cathode materials which are fully activated in the first charging process, the molar ratio of Co/Mn was often between 1/3 and 1/2, sometimes even 1/1, much higher than that in these materials (only 1/6) [61-64]. As a result, we anticipate that the limited content of Co doping was insufficient to fully activate the Li-rich layered phase in the first cycle and thus led to the unusual CIUP behaviour.

As discussed above, these cathodes materials had distinct electrochemical performances at the two marginally changed cycling potential windows. Then we were inspired to think about the possible

capacity control by simply altering the activation potential windows. For example, partial activation at 2-4.8 V for certain cycles before reaching full activation, what the capacities of these cathode materials would deliver at 2-4.6 V? Will the increment of the capacity still be continued at 2-4.8V or not? To answer these questions, a deliberately designed charge/discharge procedure was conducted: Each sample was charged and discharged for 140 cycles alternately between 2-4.6 V for 10 cycles and 2-4.8 V for another 10 cycles. The results are shown in **Figure 5.6a**. In general, as the potential range periodically changed between 2-4.6 V and 2-4.8 V after every 10 cycles, the discharge capacity of all the composites experienced alternating stages of stabilizing and increasing for the first ~100 cycles. After that, the capacity became steady at both potential windows. Specifically, for each 10 cycles at 2-4.8 V, all samples showed a gradual increase in capacity until the maximum values were reached, which is consistent with the behaviour observed before (**Figure 5.2**); on the other side, when the potential window was changed to 2-4.6 V, the capacity of each sample behaved somewhat like being "frozen", stopped increasing and kept stable.

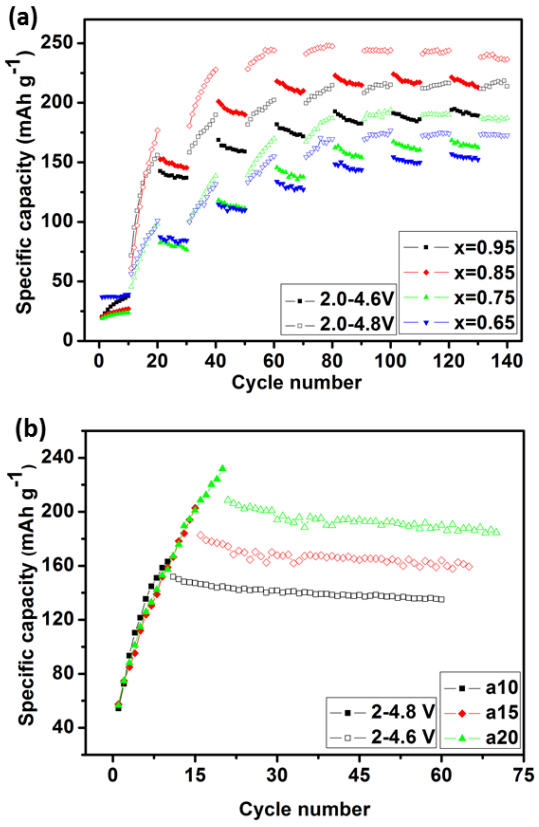

Figure 5.6 Discharge capacities of the x = 0.85 sample: a) alternatively activated at 2-4.6 V and 2-4.8 V in the step of 10 cycles each for the first 140 cycles; b) firstly activated at 2-4.8 V for 10, 15 or 20 (named as a10, a15 and a20) cycles respectively, and then at 2-4.6 V for another 50 cycles. The current density for all the tests was 30 mA g^{-1}.

Based on these results, it is suggested that the discharge capacities of these cathode materials could be controllable. More specifically, these cathode materials could obtain a certain reversible discharge capacity at 2-4.6 V after a selected number of pre-cycles at 2-4.8 V. To confirm this, three cells with the discharge capacities of 140, 160 or 180 mAh g^{-1} respectively at 2-4.6 V were designed based on the x = 0.85 composite sample. The key point to realize such a specified discharge capacity at 2-4.6 V is to determine exactly how many activation cycles at 2-4.8 V are required. Taking the 140 mAh g^{-1} for instance, according to **Figure 5.6a**, the discharge capacity of the x = 0.85 sample dropped from around 175 mAh g^{-1} at the 20th cycle to ~ 150 mAh g^{-1} at the 21th cycle when the potential window was lowered to 4.6 V. This small capacity loss is associated with the reversible Li insertion/extraction within the narrow 0.2 V region between 4.6-4.8 V. In addition, another 10% percent of capacity decay upon cycling for this sample as shown in **Figure 5.2** should be considered as well. As a result, 10 pre-cycles at 2-4.8 V were applied to achieve a consequently stable and reversible discharge capacity of around 140 mAh g^{-1} at 2-4.6 V. Similarly, 15 and 20 pre-cycles at 2-4.8 V were conducted for 160 and 180 mAh g^{-1}, respectively. The experimental results were in good agreement with the expected values (**Figure 5.6b**). In the following 50 cycles between 2-4.6 V, the discharge capacities of the x = 0.85 sample experienced a slight capacity decline in the early stage, and then became stable and finally ended up steadily at the predicted values within the error range of 5 mAh g^{-1}.

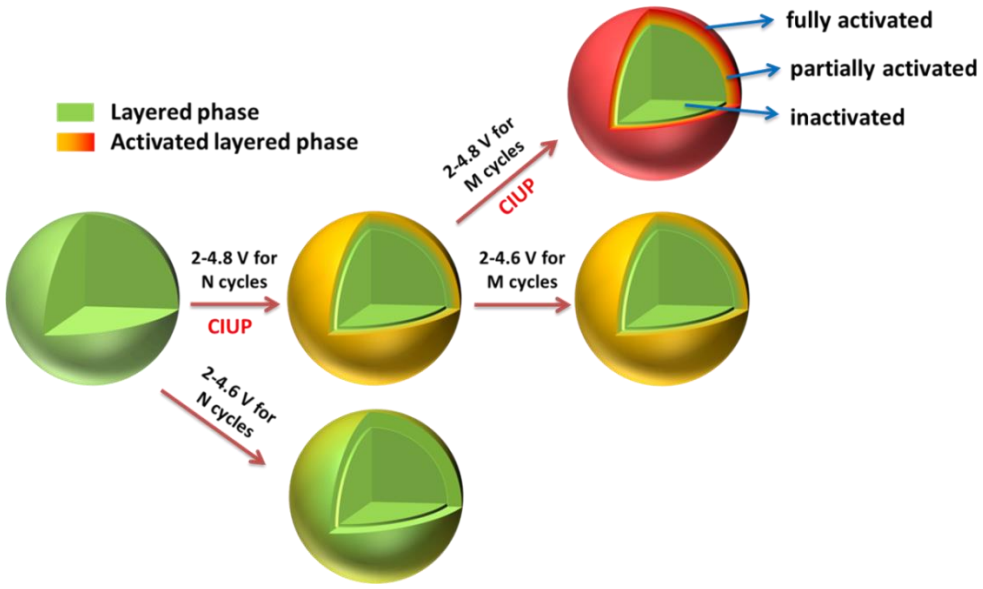

Figure 5.7 Schematic illustration of the activating behaviour of the Li-rich layered phase at different potential ranges. The gradient from orange to red means the level up of the activation. Note (N+M) is no more than the cycles when these composite materials reach their maximum capacities.

On the ground of the structural and electrochemical studies together with calculation analysis, the structure changes of the original layered phase evolved at different potential windows are illustrated in **Figure 5.7**. Based on the discussion outlined above, the Li-rich layered phase was negligibly or not activated at 2-4.6 V, but continuously activated at 2-4.8 V on the surface of particles during cycling. Interestingly, after a few cycles of partial activation at 2-4.8 V, the activated and intact regions could electrochemically stay active and inert, respectively, if the samples were subject to 2-4.6 V potential windows again. In battery research and development fields, it is commonly accepted that the higher the capacity can be achieved, the better the electrode material is. On the other hand, the study presented herein not only provides some better understanding on the Li-rich cathode materials, but may also be useful for possible "smart" capacity-control concept in battery design.

5.5 Conclusions

The composition, structure and electrochemistry performance of a series of Li-rich layered-spinel integrated cathode materials: $xLi_2[Mn_{0.857}Co_{0.143}]O_3$-$(1-x)Li[Mn_{1.714}Co_{0.286}]O_4$ (x = 0.95, 0.85, 0.75 and 0.65) have been studied systematically. Unlike the conventional Li-rich cathode materials, the Li-rich composite materials in this work exhibited continuous capacity increase in the first tens of cycles at potential window of 2-4.8 V, but limited or no capacity increase at 2-4.6 V. With a combined computation and experimental study, it was demonstrated that the regular capacity increase upon cycles at 2-4.8 V was due to the continuous activation of the initial Li-rich layered phase, and the limited content of Co doping was revealed to play a vital role in leading to the unique CIUP behaviour. Based on the electrochemistry behaviours of these materials at different potential windows, cathode materials with controllable specific discharge capacity were designed by deliberately partially activating the composite materials to certain degrees.

5.6 References

1. Nishi, Y., *The development of lithium ion secondary batteries*. Chem. Rec., 2001. **1**(5): p. 406-413.
2. Goodenough, J.B. and K.-S. Park, *The Li-ion Rechargeable Battery: A Perspective*. J. Am. Chem. Soc., 2013.
3. Xu, B., et al., *Recent progress in cathode materials research for advanced lithium ion batteries*. Mater. Sci. Eng. R Rep., 2012.
4. Xu, J., et al., *Cathode materials for next generation lithium ion batteries*. Nano Energy, 2013. **2**(4): p. 439-442.

5. Whittingham, M.S., *Lithium batteries and cathode materials*. Chem. Rev., 2004. **104**(10): p. 4271-4302.
6. Goodenough, J.B. and K.-S. Park, *The Li-ion rechargeable battery: a perspective*. Journal of the American Chemical Society, 2013. **135**(4): p. 1167-1176.
7. Lu, Z., D. MacNeil, and J. Dahn, *Layered cathode materials $Li[Ni_xLi_{(1/3-2x/3)}Mn_{(2/3-x/3)}]O_2$ for lithium-ion batteries*. Electrochem. Solid-State Lett., 2001. **4**(11): p. A191-A194.
8. Lu, Z., et al., *Synthesis, Structure, and Electrochemical Behavior of $Li[Ni_xLi_{(1/3-2x/3)}Mn_{(2/3-x/3)}]O_2$*. Journal of the Electrochemical Society, 2002. **149**(6): p. A778-A791.
9. Thackeray, M.M., et al., *Li_2MnO_3-stabilized $LiMO_2$ (M = Mn, Ni, Co) electrodes for lithium-ion batteries*. J. Mater. Chem., 2007. **17**(30): p. 3112-3125.
10. Ellis, B.L., K.T. Lee, and L.F. Nazar, *Positive Electrode Materials for Li-Ion and Li-Batteries†*. Chem. Mater., 2010. **22**(3): p. 691-714.
11. Thackeray, M.M., et al., *Advances in manganese-oxide 'composite' electrodes for lithium-ion batteries*. J. Mater. Chem., 2005. **15**(23): p. 2257-2267.
12. Lu, Z. and J.R. Dahn, *Understanding the anomalous capacity of $Li/Li[Ni_xLi_{(1/3-2x/3)}Mn_{(2/3-x/3)}]O_2$ cells using in situ X-ray diffraction and electrochemical studies*. Journal of The Electrochemical Society, 2002. **149**(7): p. A815-A822.
13. Robertson, A.D. and P.G. Bruce, *Mechanism of electrochemical activity in Li2MnO3*. Chem. Mater., 2003. **15**(10): p. 1984-1992.
14. Armstrong, A.R., et al., *Demonstrating oxygen loss and associated structural reorganization in the lithium battery cathode $Li[Ni_{0.2}Li_{0.2}Mn_{0.6}]O_2$*. J. Am. Chem. Soc., 2006. **128**(26): p. 8694-8698.
15. Kang, S.-H., et al., *Interpreting the structural and electrochemical complexity of 0.5 Li_2MnO_3 0.5$LiMO_2$ electrodes for lithium batteries (M = $Mn_{0.5-x}Ni_{0.5-x}Co_{2x}$, $0 \leq x \leq 0.5$)*. Journal of Materials Chemistry, 2007. **17**(20): p. 2069-2077.
16. Jiang, Y., et al., *Hollow 0.3Li_2MnO_3 0.7$LiNi_{0.5}Mn_{0.5}O_2$ microspheres as a high-performance cathode material for lithium–ion batteries*. Phys. Chem. Chem. Phys., 2013. **15**(8): p. 2954-2960.
17. Wu, F., et al., *Spinel/Layered Heterostructured Cathode Material for High-Capacity and High-Rate Li-Ion Batteries*. Adv. Mater., 2013. **25**(27): p. 3722-3726.
18. Mukherjee, R., et al., *Nanostructured electrodes for high-power lithium ion batteries*. Nano Energy, 2012. **1**(4): p. 518-533.

19. Wang, R., et al., *Atomic Structure of Li_2MnO_3 after Partial Delithiation and Re-Lithiation*. Adv. Energy Mater., 2013. **3**(10): p. 1358-1367.
20. Yu, H. and H. Zhou, *High-Energy Cathode Materials (Li_2MnO_3-$LiMO_2$) for Lithium-Ion Batteries*. The Journal of Physical Chemistry Letters, 2013. **4**(8): p. 1268-1280.
21. Ozawa, K., et al., *Electrochemical characteristics of layered $Li_{1.95}Mn_{0.9}Co_{0.15}O_3$ (C2/m) as a lithium-battery cathode*. Journal of the Electrochemical Society, 2012. **159**(3): p. A300-A304.
22. Laruelle, S., et al., *On the origin of the extra electrochemical capacity displayed by MO/Li cells at low potential*. J. Electrochem. Soc., 2002. **149**(5): p. A627-A634.
23. Ban, C., et al., *Nanostructured Fe_3O_4/SWNT Electrode: Binder-Free and High-Rate Li-Ion Anode*. Adv. Mater., 2010. **22**(20): p. E145-E149.
24. Lee, E.S., et al., *High-Voltage, High-Energy Layered-Spinel Composite Cathodes with Superior Cycle Life for Lithium-Ion Batteries*. Chem. Mater., 2012. **24**(3): p. 600-612.
25. Hong, J., et al., *Structural evolution of layered $Li_{1.2}Ni_{0.2}Mn_{0.6}O_2$ upon electrochemical cycling in a Li rechargeable battery*. J. Mater. Chem., 2010. **20**(45): p. 10179-10186.
26. Cabana, J., et al., *Structural and Electrochemical Characterization of Composite Layered-Spinel Electrodes Containing Ni and Mn for Li-Ion Batteries*. J. Electrochem. Soc., 2009. **156**(9): p. A730-A736.
27. Kim, J.M., S. Tsuruta, and N. Kumagai, *Electrochemical properties of $Li(Li_{(1-x)/3}Co_xMn_{(2-x)/3})O_2$ ($0 \leq x \leq 1$) solid solutions prepared by poly-vinyl alcohol (PVA) method*. Electrochem. Commun., 2007. **9**(1): p. 103-108.
28. Yu, S.-H., et al., *Continuous activation of Li_2MnO_3 component upon cycling in $Li_{1.167}Ni_{0.233}Co_{0.100}Mn_{0.467}Mo_{0.033}O_2$ cathode material for lithium ion batteries*. J. Mater. Chem. A, 2013. **1**(8): p. 2833-2839.
29. Perdew, J.P., K. Burke, and M. Ernzerhof, *Generalized gradient approximation made simple*. Phys. Rev. Lett., 1996. **77**(18): p. 3865-3868.
30. Blöchl, P.E., *Projector augmented-wave method*. Phys. Rev. B, 1994. **50**(24): p. 17953.
31. Kresse, G. and D. Joubert, *From ultrasoft pseudopotentials to the projector augmented-wave method*. Phys. Rev. B, 1999. **59**(3): p. 1758.
32. Anisimov, V.I., J. Zaanen, and O.K. Andersen, *Band theory and Mott insulators: Hubbard U instead of Stoner I*. Phys. Rev. B, 1991. **44**(3): p. 943.
33. Chevrier, V.L., et al., *Hybrid density functional calculations of redox potentials and formation energies of transition metal compounds*. Phys. Rev. B, 2010. **82**(7): p. 075122.

34. Hinuma, Y., et al., *Phase transitions in the $LiNi_{0.5}Mn_{0.5}O_2$ system with temperature*. Chem. Mater., 2007. **19**(7): p. 1790-1800.
35. Bréger, J., et al., *High-resolution X-ray diffraction, DIFFaX, NMR and first principles study of disorder in the Li_2MnO_3-$Li[Ni_{1/2}Mn_{1/2}]O_2$ solid solution*. J. Solid State Chem., 2005. **178**(9): p. 2575-2585.
36. Jarvis, K.A., et al., *Atomic Structure of a Lithium-Rich Layered Oxide Material for Lithium-Ion Batteries: Evidence of a Solid Solution*. Chem. Mater., 2011. **23**(16): p. 3614-3621.
37. T OHZUKU, A.U., et al., *Comparative study of $LiCoO_2$, $LiNi_{1/2}Co_{1/2}$ and $LiNiO_2$ for 4 volt secondary lithium cells [J]*. Electrochim. Acta, 1993. **38**(191): p. 1159-1167.
38. Li, Y., et al., *Electrochemical performance of nanocrystalline $Li_3V_2(PO_4)_3$/carbon composite material synthesized by a novel sol-gel method*. Electrochim. Acta, 2006. **51**(28): p. 6498-6502.
39. Deng, Z. and A. Manthiram, *Influence of cationic substitutions on the oxygen loss and reversible capacity of lithium-rich layered oxide cathodes*. J. Phys. Chem. C, 2011. **115**(14): p. 7097-7103.
40. Park, S.-H., et al., *Lithium-manganese-nickel-oxide electrodes with integrated layered-spinel structures for lithium batteries*. Electrochem. Commun., 2007. **9**(2): p. 262-268.
41. Gualtieri, A.F., *Accuracy of XRPD QPA using the combined Rietveld-RIR method*. J. Appl. Crystallogr., 2000. **33**(2): p. 267-278.
42. Martha, S.K., et al., *Electrochemical and rate performance study of high-voltage lithium-rich composition: $Li_{1.2}Mn_{0.525}Ni_{0.175}Co_{0.1}O_2$*. J. Power Sources, 2012. **199**: p. 220-226.
43. Yabuuchi, N., et al., *Detailed Studies of a High-Capacity Electrode Material for Rechargeable Batteries, Li_2MnO_3-$LiCo_{1/3}Ni_{1/3}Mn_{1/3}O_2$*. J. Am. Chem. Soc., 2011. **133**(12): p. 4404-4419.
44. Xiao, R., H. Li, and L. Chen, *Density functional investigation on Li_2MnO_3*. Chem. Mater., 2012. **24**(21): p. 4242-4251.
45. Gu, M., et al., *Formation of the Spinel Phase in the Layered Composite Cathode Used in Li-Ion Batteries*. ACS nano, 2012.
46. Kim, D., et al., *High-energy and high-power Li-rich nickel manganese oxide electrode materials*. Electrochem. Commun., 2010. **12**(11): p. 1618-1621.
47. Park, Y.J., et al., *Synthesis and Electrochemical Characteristics of $Li[Co_xLi_{(1/3-x/3)}Mn_{(2/3-2x/3)}]O_2$ Compounds*. J. Electrochem. Soc., 2004. **151**(5): p. A720-A727.
48. Bareno, J., et al., *Local Structure of Layered Oxide Electrode Materials for Lithium-Ion Batteries*. Adv. Mater., 2010. **22**(10): p. 1122-1127.

49. Yu, H., et al., *Direct Atomic-Resolution Observation of Two Phases in the $Li_{1.2}Mn_{0.567}Ni_{0.166}Co_{0.067}O_2$ Cathode Material for Lithium-Ion Batteries*. Angew. Chem., Int. Ed., 2013.
50. Xu, B., et al., *Identifying surface structural changes in layered Li-excess nickel manganese oxides in high voltage lithium ion batteries: A joint experimental and theoretical study*. Energy Environ. Sci., 2011. **4**(6): p. 2223-2233.
51. Boulineau, A., et al., *First evidence of manganese-nickel segregation and densification upon cycling in Li-rich layered oxides for lithium batteries*. Nano lett., 2013.
52. Gu, M., et al., *Nanoscale Phase Separation, Cation Ordering, and Surface Chemistry in Pristine $Li_{1.2}Ni_{0.2}Mn_{0.6}O_2$ for Li-Ion Batteries*. Chem. Mater., 2013.
53. Lanz, P., C. Villevieille, and P. Novák, *Electrochemical activation of Li_2MnO_3 at elevated temperature investigated by in situ Raman microscopy*. Electrochim. Acta, 2013. **109**: p. 426-432.
54. Li, N., et al., *The role of yttrium content in improving electrochemical performance of layered lithium-rich cathode materials for Li-ion batteries*. J. Mater. Chem. A, 2013. **1**(34): p. 9760-9767.
55. Denis, Y., et al., *Electrochemical activities in Li_2MnO_3*. J. Electrochem. Soc., 2009. **156**(6): p. A417-A424.
56. Koyama, Y., et al., *First-principles study on lithium removal from Li_2MnO_3*. J. Power Sources, 2009. **189**(1): p. 798-801.
57. Okamoto, Y., *Ambivalent Effect of Oxygen Vacancies on Li_2MnO_3: A First-Principles Study*. J. Electrochem. Soc., 2011. **159**(2): p. A152-A157.
58. Xiao, P., et al., *Calculations of Oxygen Stability in Lithium-Rich Layered Cathodes*. J. Phys. Chem. C, 2012. **116**(44): p. 23201-23204.
59. Chebiam, R., et al., *Comparison of the chemical stability of the high energy density cathodes of lithium-ion batteries*. Electrochem. Commun., 2001. **3**(11): p. 624-627.
60. Venkatraman, S., Y. Shin, and A. Manthiram, *Phase Relationships and Structural and Chemical Stabilities of Charged $Li_{1-x}CoO_{2-\delta}$ and $Li_{1-x}Ni_{0.85}Co_{0.15}O_{2-\delta}$ Cathodes*. Electrochem. Solid-State Lett., 2003. **6**(1): p. A9-A12.
61. Kumagai, N., et al., *Structural modification of $Li[Li_{0.27}Co_{0.20}Mn_{0.53}]O_2$ by lithium extraction and its electrochemical property as the positive electrode for Li-ion batteries*. Electrochim. Acta, 2008. **53**(16): p. 5287-5293.

62. Wei, Y., et al., *Electrochemical kinetics and cycling performance of nano* $Li[Li_{0.23}Co_{0.3}Mn_{0.47}]O_2$ *cathode material for lithium ion batteries*. Electrochem. Commun., 2009. **11**(10): p. 2008-2011.
63. Lee, Y., M.G. Kim, and J. Cho, *Layered* $Li_{0.88}[Li_{0.18}Co_{0.33}Mn_{0.49}]O_2$ *nanowires for fast and high capacity Li-ion storage material*. Nano lett., 2008. **8**(3): p. 957-961.
64. Li, Z., et al., *Low temperature properties of the Li* $[Li_{0.2}Co_{0.4}Mn_{0.4}]O_2$ *cathode material for Li-ion batteries*. Electrochem. Commun., 2011. **13**(9): p. 1016-1019.

5.7 Supporting Information

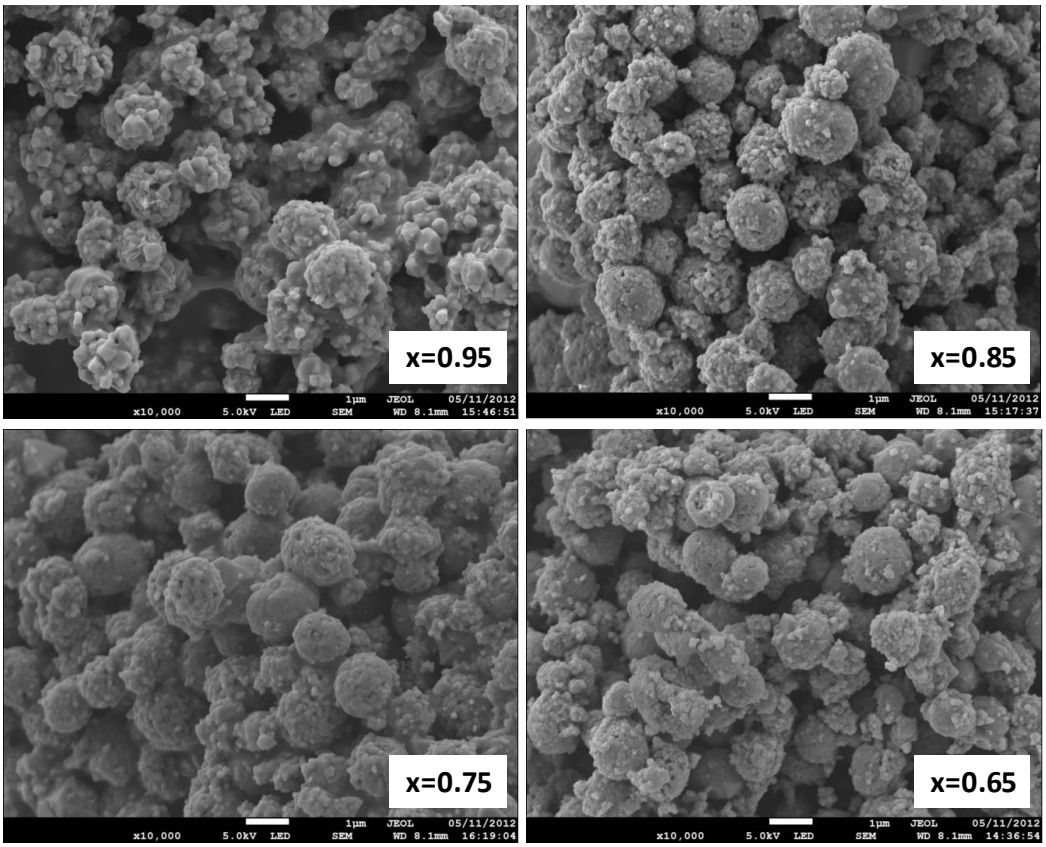

Figure S5.1 SEM images of the $xLi_2[Mn_{0.857}Co_{0.143}]O_3$-(1-x)$Li[Mn_{1.714}Co_{0.286}]O_4$ (x = 0.95, 0.85, 0.75 and 0.65) compounds.

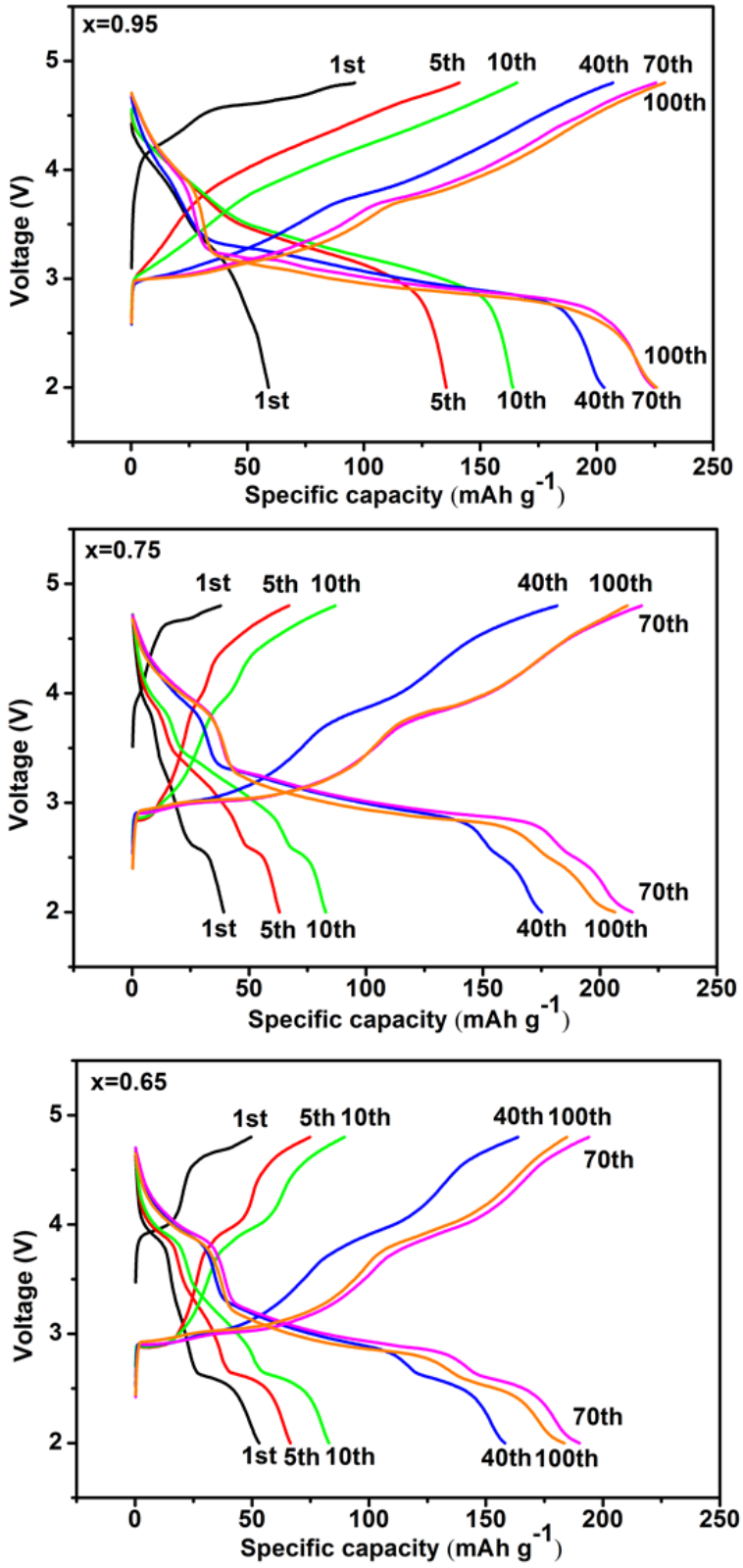

Figure S5.2 Charge/discharge profiles of the $xLi_2[Mn_{0.857}Co_{0.143}]O_3$-(1-x)$Li[Mn_{1.714}Co_{0.286}]O_4$ (x = 0.95, 0.75 and 0.65) composite cathodes in the 1st, 5th, 10th, 40th, 70th and 100th cycles measured in the potential range of 2-4.8 V at the current density of 30 mA g^{-1}.

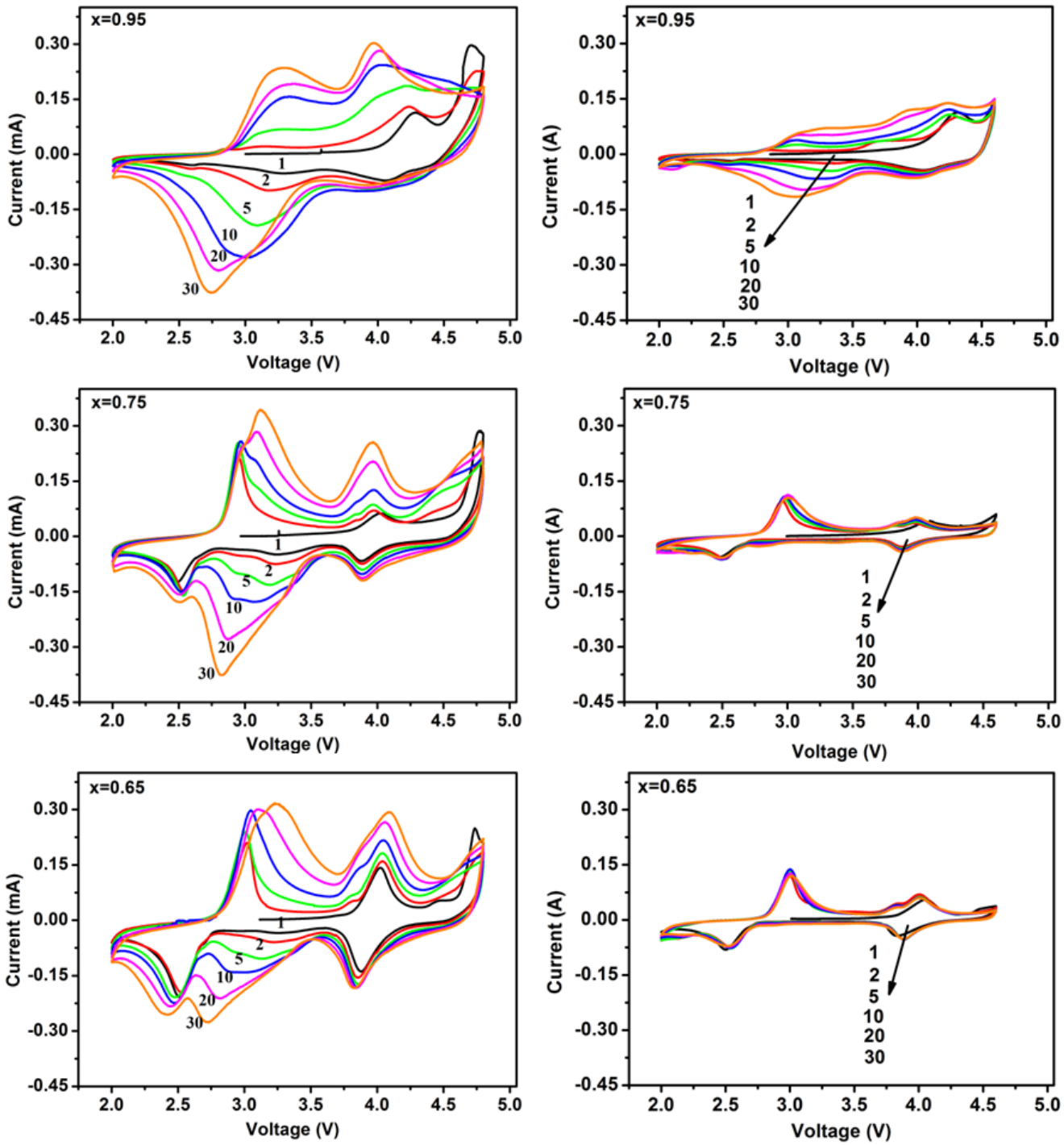

Figure S5.3 Cyclic voltammogram loops of the $xLi_2[Mn_{0.857}Co_{0.143}]O_3$-(1-x)$Li[Mn_{1.714}Co_{0.286}]O_4$ (x = 0.95, 0.75 and 0.65) composite cathodes at the 1st, 2nd, 5th, 10th, 20th and 30th cycles at a scan rate of 0.2 mV s^{-1} within 2-4.8 V or 2-4.6 V.

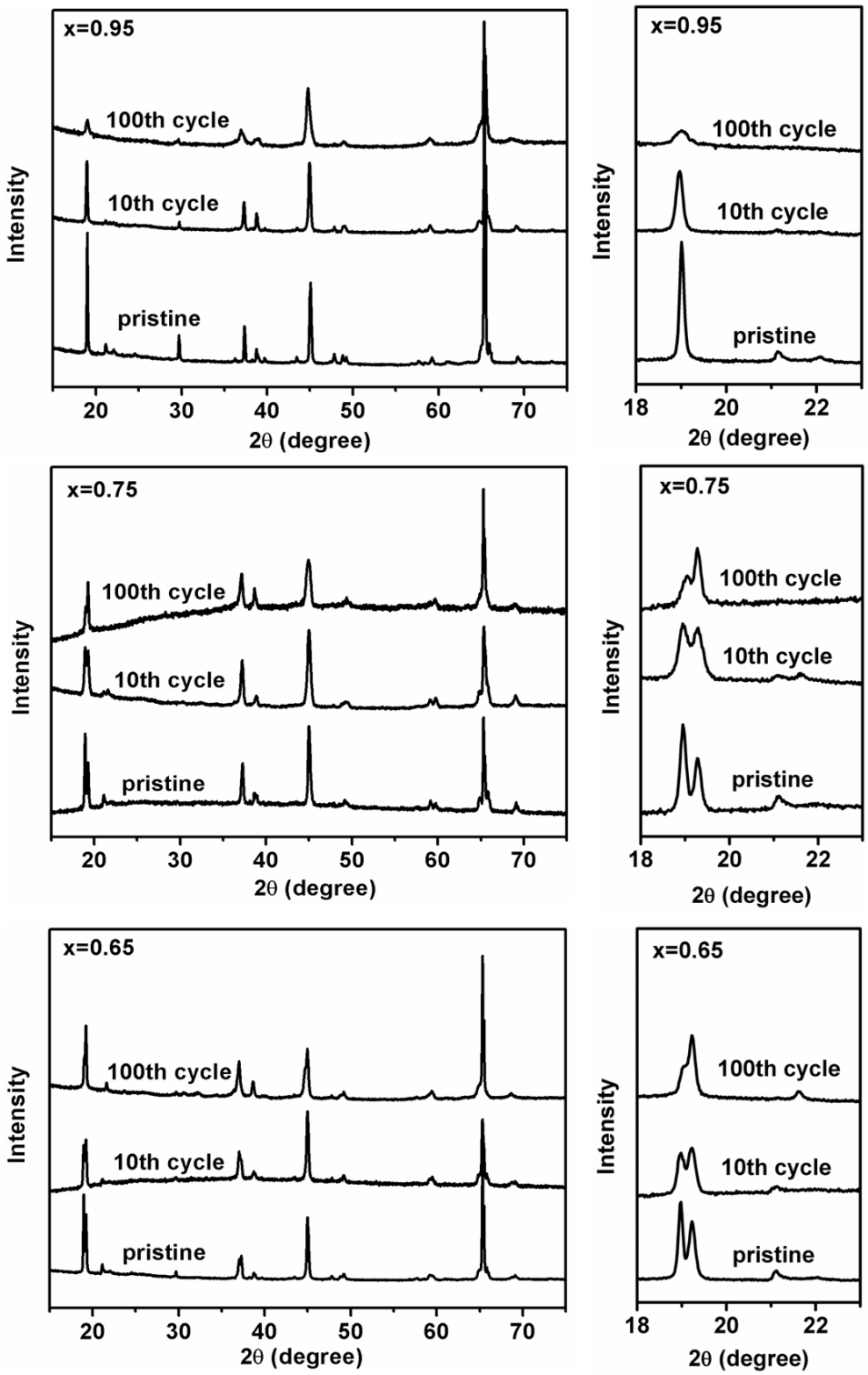

Figure S5.4 XRD patterns of the $xLi_2[Mn_{0.857}Co_{0.143}]O_3$-(1-x)$Li[Mn_{1.714}Co_{0.286}]O_4$ (x = 0.95, 0.75 and 0.65) composite cathodes before cycling and after the 1st, 20th and 100th cycle at 2-4.8 V.

Table S5.1 Weigh percentage of the layered phase in the $xLi_2[Mn_{0.857}Co_{0.143}]O_3$-(1-x)$Li[Mn_{1.714}Co_{0.286}]O_4$ (x = 0.95, 0.75 and 0.65) composite cathodes after different cycles.

cycles	0.85	0.75	0.65
0	94.2%	78.7%	74.8%
10	43.4%	51.1%	49.8%
100	26.4%	23.2%	28.3%

6. Understanding the stepwise capacity-increase of high energy low-Co Li-rich cathode materials for lithium ion batteries

6.1 Abstract

Li-rich layered materials as a promising high-energy cathode candidate have attracted much attention in recent years for next generation lithium ion batteries. However, the fundamental mechanism of the high specific capacity in these cathode materials has not been fully revealed so far. In this work, we report a new class of Li-rich cathode materials $Li[Co_xLi_{1/3-x/3}Mn_{2/3-2x/3}]O_2$ (x=0.087, 0.1, 0.118) with a very low level of Co doping, which exhibit impressive stepwise capacity increase over dozens of cycles from less than 50 mAh g^{-1} to around 250 mAh g^{-1}. A systematic study on their composition, crystal structure and electrochemical performance revealed that the small change of Co content has negligible effect to the crystal structure and morphology, but plays an important role in enhancing the activation rate of the Li_2MnO_3 phase. In addition, optimized cycling potential window and current rate were proven to be critically important for effective Li_2MnO_3 activation and better long-term cycling stability.

6.2 Introduction

Lithium ion batteries (LIBs) have become the dominant power source for portable electronics in recent years due to their high energy densities [1, 2]. The massive consumption of fossil fuels and the corresponding derived environment problems have triggered the rapid development of electric vehicles, which are highly dependent on large-scale applications of high performance LIBs [3]. Currently, a large number of new anode materials have been developed with concurrent superior high specific capacity of up to 1000 mAh g^{-1} and good power density [4-7]; however, the specific capacities of the major cathode materials such as $LiCoO_2$, $LiFePO_4$ and $LiMn_2O_4$ are still too low (less than 170 mAh g^{-1}) to match the anode side [8]. Therefore, searching new cathode materials with high capacity is critical for the future development of LIBs and even the electric vehicle industry.

Li-rich Mn-based layered compounds are a new series of high energy cathode materials that have attracted significant recent attention. Generally, they are composed of two highly integrated layered phases and can be formulated as xLi_2MnO_3 $(1–x)LiMO_2$ ($0 < x < 1$, M = Mn, Co, Ni or their mixture) [9, 10]. Typically, the Li-rich Li_2MnO_3 phase can be activated at a high charging voltage above 4.5 V. During the activation process, the oxygen ions of the crystal lattice will be extracted in the form of oxygen with concurrent deintercalation of Li^+ from the transition metal (TM) layers and diffusion of TM ions to the Li layers. The activation of Li_2MnO_3 phase has been demonstrated to provide extra specific capacity to the Li-rich cathode materials, which can deliver a specific capacity of more than 250 mAh g^{-1} at room temperature [11, 12]. However, there are still a few serious challenging issues that the Li-rich cathode materials have to address before practical application including the low initial columbic efficiency, poor cycling stability, low rate capability and long term working voltage decline [13]. To solve these problems, it is essential to fundamentally understand the lithium storage mechanisms and the origin of these problems from the aspects of chemical composition and crystal structure [14]. Most Li-rich cathode materials in the Li-Mn-Co-O system have been reported with a Co/Mn mole ratio equal or more than 1/3 while the materials with a Co/Mn ratio less than 1/3 are rarely investigated [15-17].In fact, it is much advantageous if the content of Co in Li-rich cathode materials can be significantly suppressed in regards to the cost and toxicity of Co. Therefore, we studied a series of Li-rich Co-doped materials recently with a fixed Co/Mn mole ratio of as less as 1/6 and a variable ratio of Li/(Mn+Co) [18, 19].It was found that the specific capacities of these materials increased upon cycling in the first cycles and such a small amount of Co doping can effectively promote the Li_2MnO_3 activation.

In this work, we report a systematic study on a new class of low-Co Li-rich layered cathode materials $Li[Co_xLi_{1/3-x/3}Mn_{2/3-2x/3}]O_2$ (x=0.087, 0.1, 0.118) which exhibit remarkable capacity increase in the first dozens of cycles. This unique phenomenon of stepwise capacity increase was revealed to be associated with gradual activation of the Li-rich Li_2MnO_3 phase, which is highly dependent on a few key parameters including the cycling potential window, the amount of Co doping and the cycling current rate. The morphology, crystal structure and electrochemical performance of these materials were also investigated in details. This work will not only help to understand the origin of the superior high specific capacity of Li-rich cathode materials, but also shed light on the design of cost-effective and scalable high performance cathode materials for LIBs.

6.3 Experimental

Materials synthesis: All the chemicals are purchased from Aldrich Sigma. The $Li[Co_xLi_{1/3-x/3}Mn_{2/3-2x/3}]O_2$ (x=0, 0.087, 0.1, 0.118) composites were synthesized by two steps. Firstly, stoichiometric amount of $Mn(NO_3)_2$ $4H_2O$ and $Co(NO_3)_2$ $6H_2O$ were dissolved in distilled water and then slowly dropped to equal volume of 0.2 M sodium carbonate solution under vigorous stirring. After 20 h aging at room temperature, the metal ions were fully co-precipitated as carbonates. In the second step, the collected carbonates were pre-treated at 500 ℃ for 5 h in air and then calcined with stoichiometric amount of LiOH H_2O at 900 ℃ for another 12 h in air to produce the final cathode materials. A 3 wt % excess of LiOH H_2O was applied for the calcination process to compensate for Li volatilization at elevated temperature.

Structural and morphological characterization: The composition of each sample was determined by a Varian 725-ES Inductively Coupled Plasma Atomic Emission Spectroscopy (ICP-AES). X-ray diffraction (XRD) was conducted on a Bruker Advanced X-Ray Diffractometer (40 kV, 30 mA) with Cu Kα (λ=0.15406 nm) radiation to detect crystalline structures of the powder samples and electrodes at a scanning rate of 1^o min^{-1}. X-ray photoelectron spectrometry (XPS) analysis was performed by a Kratos Axis Ultra X-ray Photoelectron Spectrometer using $Al_{K\alpha}$ (1253.6 eV) X-ray. Field-emission scanning electron microscopy (SEM, JEOL 7800) and transmission electron microscopy (TEM, Philips FEI Tecnai F20 operated at 200 kV) were applied to collect the morphological and local structure information of the samples.

Electrochemical measurements: All the electrochemical measurements of the materials were conducted on CR2032 coin cells. The working electrodes were prepared by doctor-blade method to coat slurries containing 70 wt % of the active materials, 20 wt % of acetylene black and 10 wt% of

polyvinylidene fluoride (dissolved in N-methyl-2-pyrrolidone with a concentration of 5 wt %) onto aluminum foils (0.7 cm^2). After drying under vacuum at 120 °C for 12 h, these working electrodes were then assembled into coin cells in an argon-filled glove box with lithium foil as the negative electrode and 1 M $LiPF_6$ in a mixture of ethylene carbonate (EC) and dimethyl carbonate (DMC) (1:1) as the electrolyte. Galvanostatic charge/discharge test was performed on a multi-channel Land CT2001A battery testing system. Cyclic voltammetry (CV) measurements were conducted on a CHI660E electrochemistry workstation at a scan rate of 0.2 mV s^{-1} between 2-4.8 V. The electrochemical impedance spectroscopy (EIS) was tested on the same electrochemistry workstation at open-circuit voltage between 100 kHz and 10 mHz. All the electrochemical tests were performed at room temperature.

6.4 Results and discussion

The compositions of all the Co-doped samples are confirmed by ICP-AES analysis as shown in **Table 6.1**. Both the Mn/Co and Li/(Mn+Co) ratios are in good agreement to the nominal values.

Table 6.1 ICP-AES analysis results of the $Li[Co_xLi_{1/3-x/3}Mn_{2/3-2x/3}]O_2$ (x = 0.087, 0.1 and 0.118) composites.

	Mn : Co		Li : (Mn+Co)	
x	Nominal	Experimental	Nominal	Experimental
0.087	7	6.88	1.87	1.92
0.1	6	5.89	1.86	1.88
0.118	5	4.96	1.83	1.81

XRD patterns of all the powder samples are displayed in **Figure 6.1a**. All major diffraction peaks can be well indexed to the R-3m space group (JCPDS No. 84-1634) as a typical layered phase, and some minor peaks between 20 ° and 25 ° are due to the localized $LiMn_6$ superlattice that belongs to the monoclinic Li_2MnO_3-like phase [20-22].It is worth noting that a higher (003) peak can be observed over the (104) peak in each sample. This indicates a low degree of transition metals (TM) existed in the Li layers, which is also supported by the well split pairs of (006)/(012) and (018)/(110) peaks [23].All the samples show sharp diffraction peaks, especially the two main peaks of (003) and (114) which have apparently narrow full-

width at half maximum (FWHM) of around 0.12 ° and 0.23 °, respectively, indicating a high degree of crystallinity for the samples (**Table 6.2**). In addition, they are highly identical among these materials, suggesting that a small amount of Co-doping does not change the crystal structure or cause impurity phases. However, taking a careful look of the enlarged (003) main diffraction peak in **Figure 6.1b**, it can be found that this peak actually shifts slightly to a higher angle with the increase of Co amount (18.645 ° for the x=0 sample, and 18.704 ° for the x=0.118 sample). Such a gradual increase of the diffraction peak position indicates the decrease of lattice parameters, which can be well explained by the smaller ionic size of Co^{3+} (0.545 Å) as guest species than the ionic size of 2/3 of Mn^{4+} (0.53 Å) ions and 1/3 of Li^{+} (0.76 Å), indicating the homogeneous distribution of the Co doping in the whole crystal structure [15, 16].

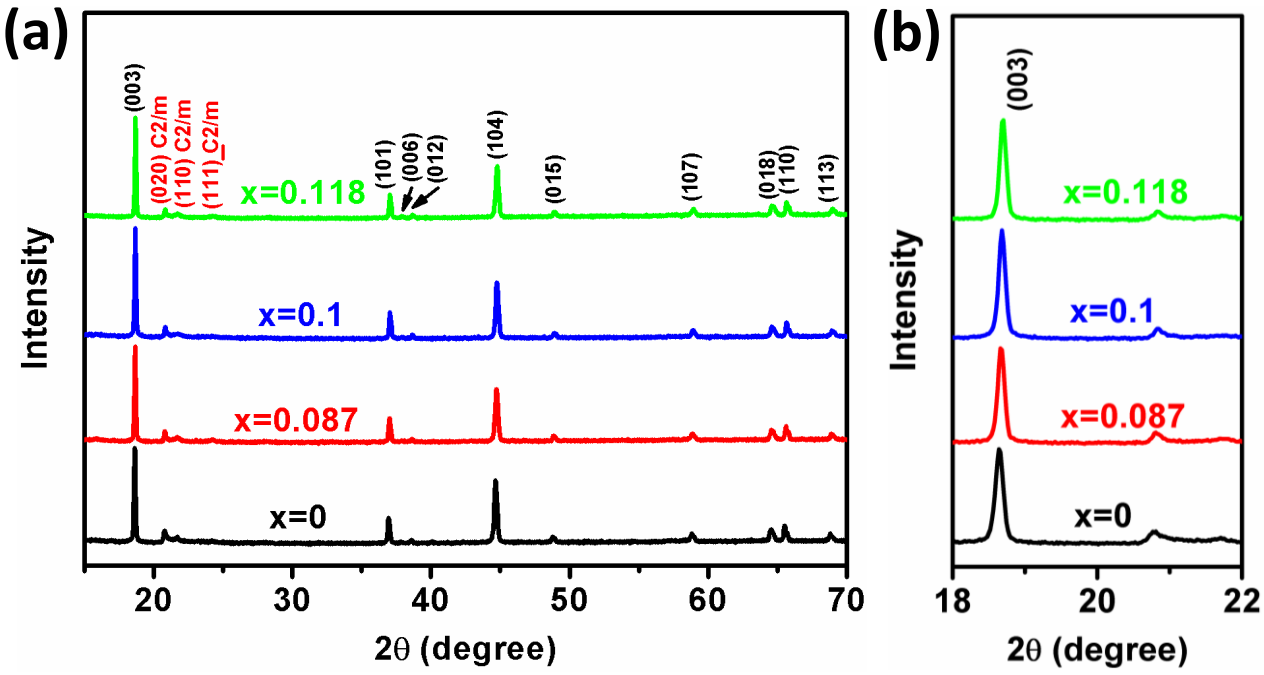

Figure 6.1 (a) Powder XRD patterns of the original $Li[Co_xLi_{1/3-x/3}Mn_{2/3-2x/3}]O_2$ (x=0, 0.087, 0.1, 0.118) compounds; and their enlargement between 20 ° and 25 °.

Table 6.2 Full-width at half maximum (FWHM) of the typical XRD diffraction peaks of the $Li[Co_xLi_{1/3-x/3}Mn_{2/3-2x/3}]O_2$ (x=0.087, 0.1, 0.118) composites.

	FWHM	
x	(003)	(104)
0	0.136 °	0.226 °
0.087	0.119 °	0.235 °
0.1	0.117 °	0.225 °
0.118	0.109 °	0.233 °

Figure 6.2 presents the SEM images of the samples. Basically, 2-3 μm microspheres can be found in each sample. From the high-resolution SEM images of the typical x=0.087 and 0.1 samples (**Fig. 6.2e and 6.2f**), it is clearly revealed that these microspheres are composed of nano-sized sub-units to form aggregated hierarchical structure. This microstructure could be advantageous for the cathode materials in two aspects. The primary nanoparticles might provide short Li^+ diffusion channels and concurrently increase the surface area for the electrode-electrolyte contact [24, 25]; the lattice strain and volume change of the materials during long term Li^+ intercalation/deintercalation may be effectively accommodated by the porous aggregate structure.

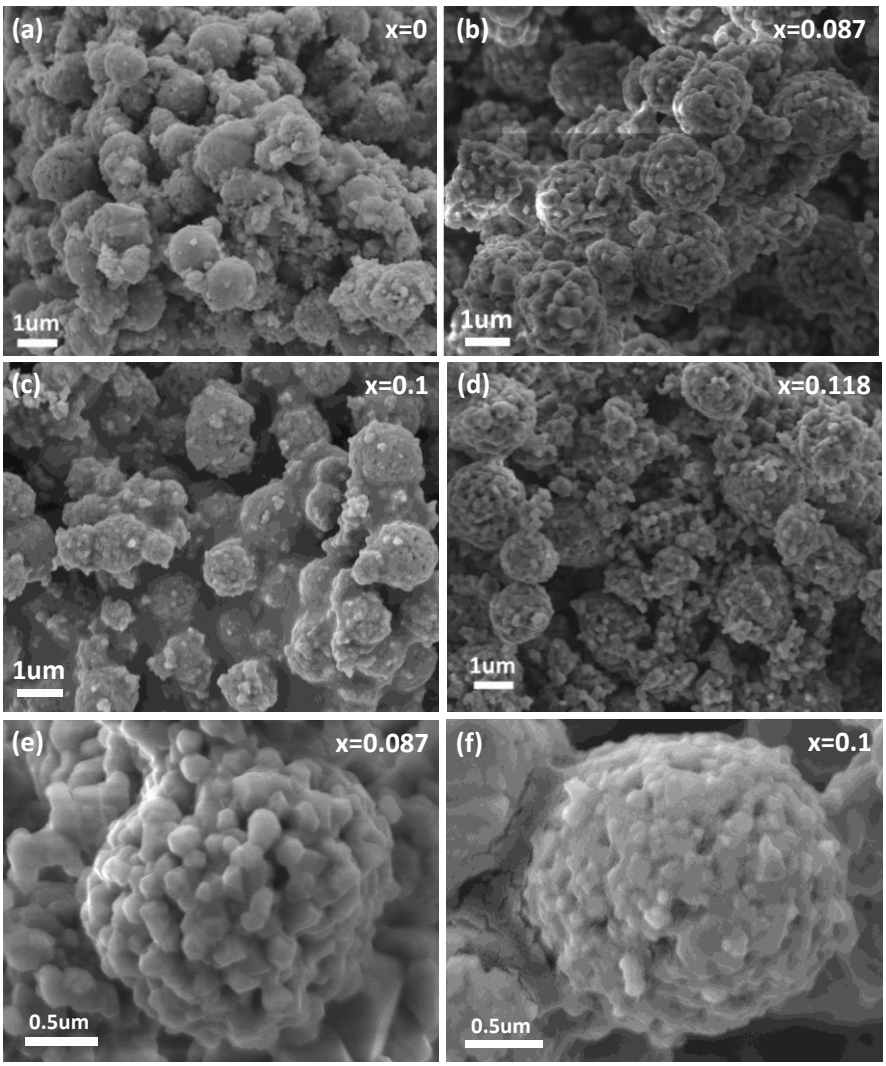

Figure 6.2 (a) to (d) SEM images of the $Li[Co_xLi_{1/3-x/3}Mn_{2/3-2x/3}]O_2$ (x=0, 0.087, 0.1, 0.118) compounds; (e) and (f) high-resolution SEM images of the typical x=0.087 and 0.1 samples.

TEM images and selected area electron diffraction (SAED) patterns revealed similar morphologies and crystalline structure in all the samples. Note that because of the large particle size as revealed by SEM in Fig. 2, it's difficult for the electron beam to passing through the particle; as a result, most parts of the particle image are in dark in TEM images. Nevertheless, the nano-scale smaller secondary nanoparticles around the large spherical particle edges can be seen (**Figure 6.3a, 6.3b**) for the typical x=0.087 sample. Additionally, HRTEM images of a selected primary nanoparticle domain oriented along $[1\text{-}10]_{mon}$ and $[010]_{mon}$ clearly reveal the perfect layered structure along the [001] zone axis [12]. Sharp and bright SAED patterns were also acquired along the corresponding directions. Both patterns point to a high crystallized layered structure; however, the SAED pattern along the $[1\text{-}10]_{mon}$ presents diffuse streaks besides the sharp and bright spot reflections. These streaks are

characteristic of the monoclinic structure and can be well explained by the random overlap of well α–sublattice ordered TM layers along the c-axis, further confirming the existence of monoclinic unit cells [12, 26, 27].

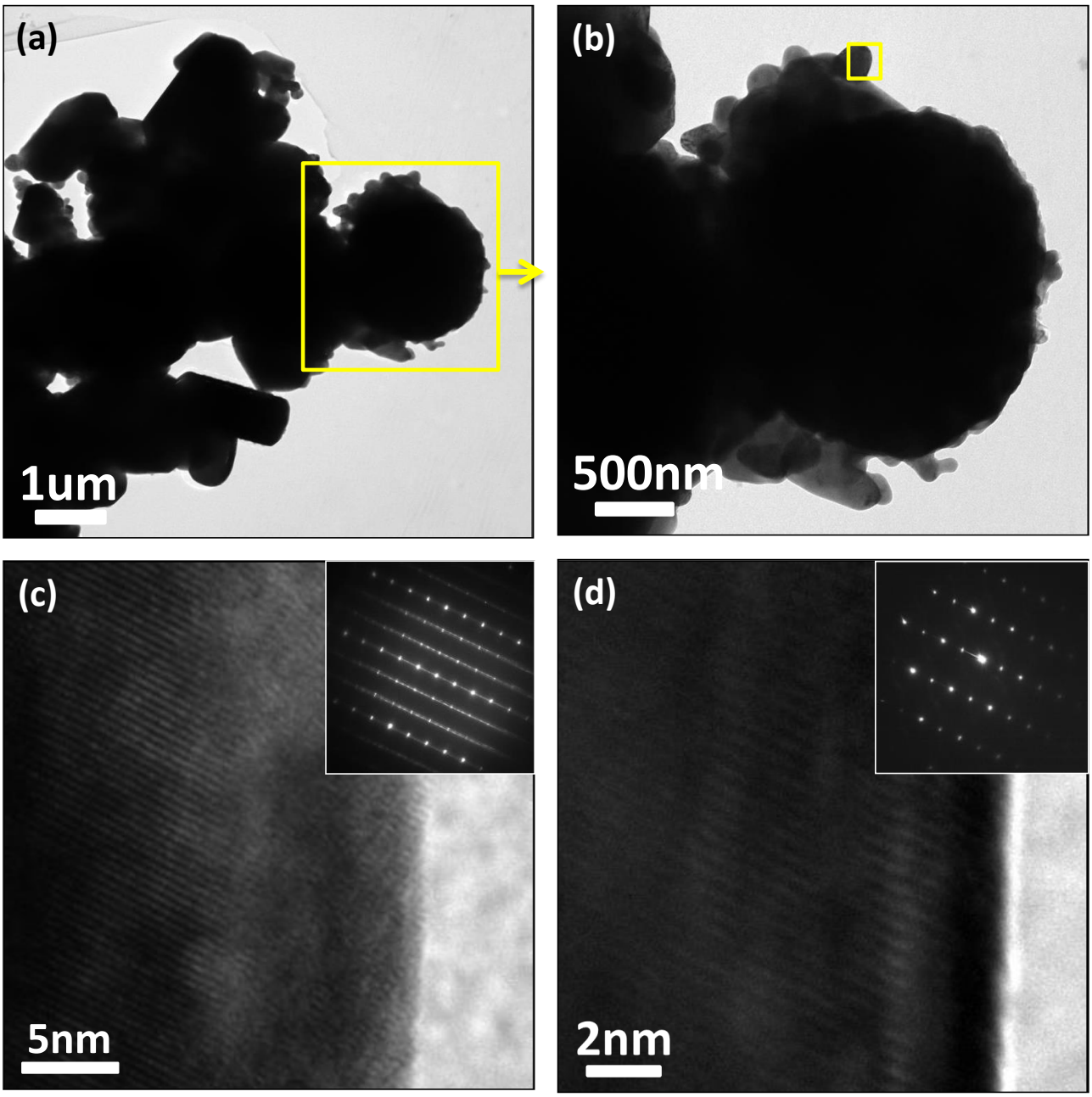

Figure 6.3 (a) TEM images of the x=0.087 sample; (b) Enlargement of the yellow frame in (a); (c, d) HRTEM images of the yellow frame area in (b) along two different zone axis of $[1\text{-}10]_{mon}$ and $[010]_{mon}$. Right-top inset images in (c) and (d) are the corresponding SAED patterns.

XPS of Mn 2p and Co 2p of the Co-doped pristine materials are shown in **Figure 6.4**. It can be found that the binding energies of both the Mn and Co are very similar in these samples, implying that Mn

and Co keep a stable valence state in our samples when the Mn/Co is slightly changed. Specifically, for the Mn $2p_{3/2}$ and $2p_{1/2}$, the binding energies are about 642.1 eV and 653.6 eV, respectively, with an energy split of 11.5 eV. This is highly consistent with those reported of Mn^{4+}, indicating the valence of Mn in these composites is mainly 4+ [28, 29]. On the other side, the spectrum of Co appears almost the same as the reported $LiCoO_2$ [30], suggesting the 3+ oxidation state of Co in our samples.

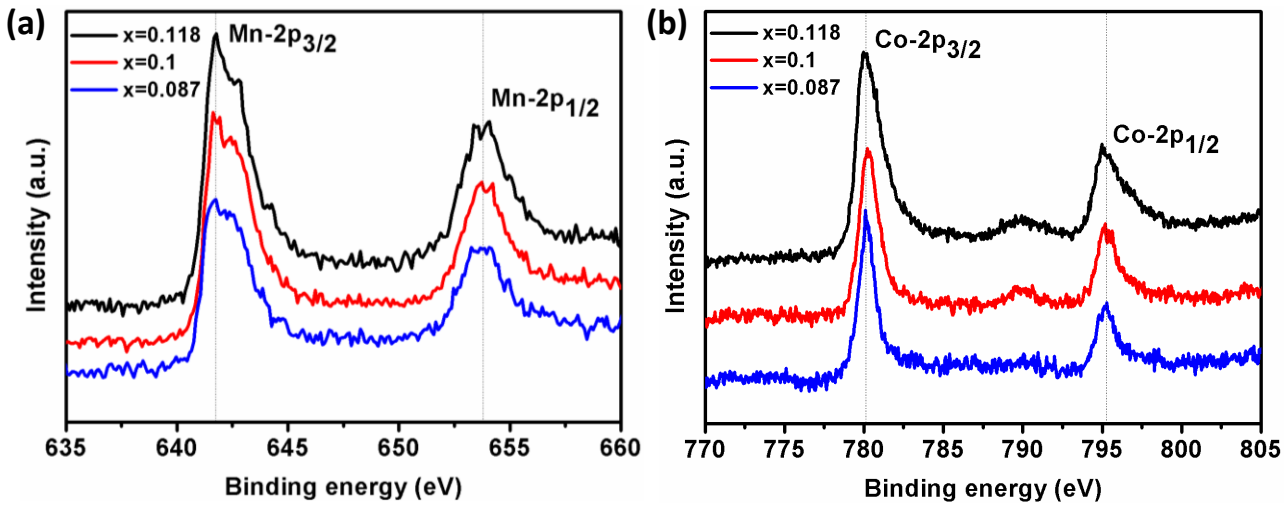

Figure 6.4 The XPS patterns of (a): Mn and (b): Co elements in the original $Li[Co_xLi_{1/3-x/3}Mn_{2/3-2x/3}]O_2$ (x = 0.087, 0.1 and 0.118) compounds.

The cycling performance of the $Li[Co_xLi_{1/3-x/3}Mn_{2/3-2x/3}]O_2$ (x=0, 0.087, 0.1, 0.118) composites at the first 120 charging-discharging cycles at three potential windows of 2-4.6 V, 2-4.8 V and 2-5 V is shown in **Figure 6.5**. It is interesting to find that the specific discharge capacities of these samples are increased upon cycles, and such an increase is particularly prominent at 2-4.8 V and 2-5 V. This phenomenon is different from the general capacity decay in traditional cathode materials during cycling and can be attributed to the continuous activation of the Li_2MnO_3 phase. This continuous activation phenomenon has been proposed to be promoted by Co doping, which can remarkably decrease the energy barrier of the oxygen extraction from the crystal lattice [18, 19]. The effect of Co doping can be further supported here by the fact that all the Co-doped samples deliver a much higher capacity than the pure Li_2MnO_3 sample over cycles, particularly at 2-4.8 V and 2-5 V, and a slight change of the Co content can make a significant difference to the electrochemical performances of these materials. For example, the discharge capacities of the x=0.118, x=0.1 and x=0.087 samples after 120 cycles at 2-4.8 V are 213 mAh g^{-1}, 223 mAh g^{-1} and 234 mAh g^{-1}, respectively, while it is only 50 mAh g^{-1} for the pure Li_2MnO_3 sample at the same condition.

Note that the capacity increase is also highly related to the cycling voltage range. For each sample, it is apparent that the higher the upper cut-off voltage, the faster the capacity increases. As the Li_2MnO_3 activation process involves a high potential O_2-release reaction, a higher cut-off potential is supposed to facilitate deeper Li_2MnO_3 activation and Li extraction, thus leading to the faster capacity increase [31, 32]. However, it is also found that the long term cycling stability of these Co-doped samples was poor at 2-5 V, where the discharge capacities climbed to the peak value in only a few cycles and then declined quickly. In contrast, the discharge capacities of these samples took more cycles to maximize but then kept stable in the consequent cycles at 2-4.8 V. Such a poor cycling stability at 2-5 V could be ascribed to the instability of the electrolyte and possible side reactions of the samples on the electrode-electrolyte interface at high potential [33]. Therefore, 2-4.8 V is used in the following work as an optimized voltage range to effectively activate the Li_2MnO_3 phase of the samples and concurrently maintain good long term cycling stability.

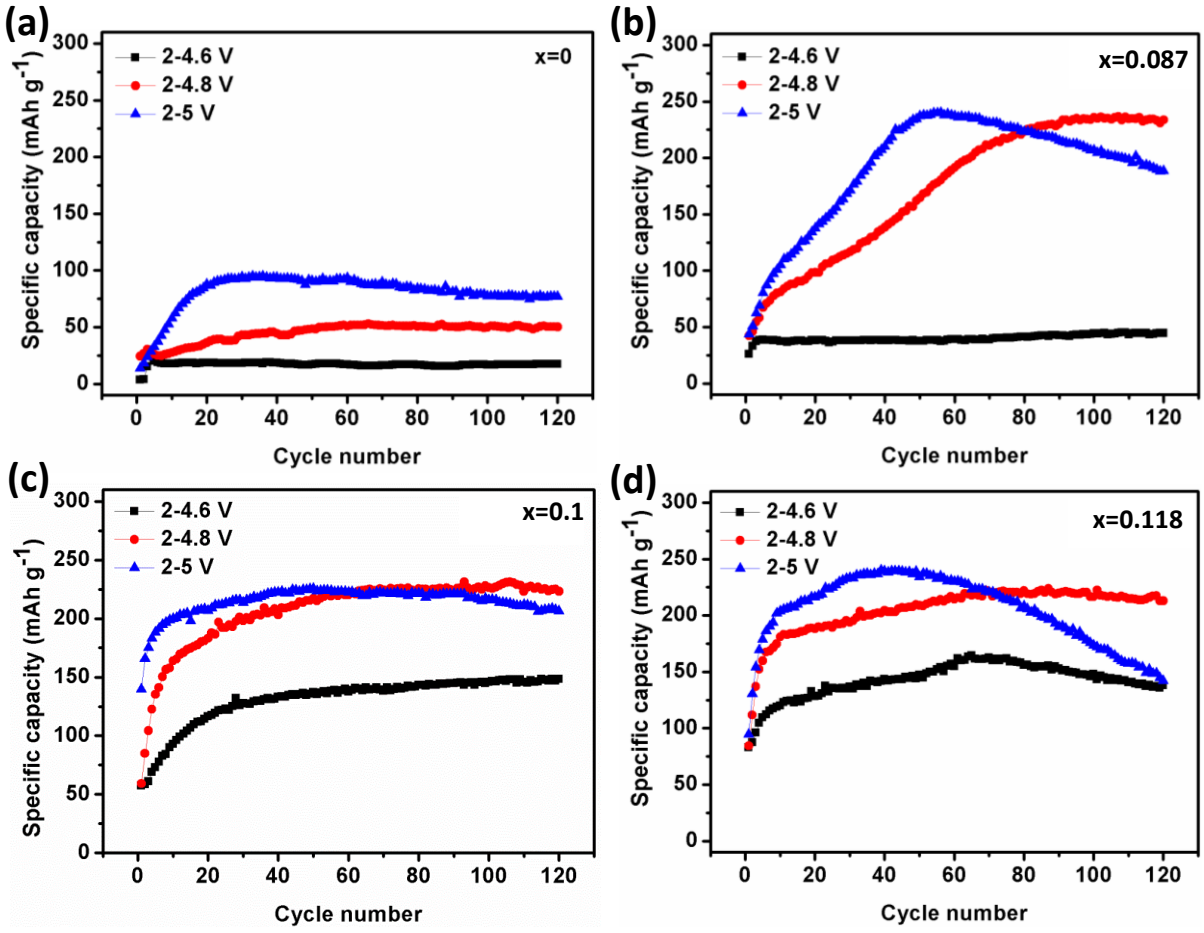

Figure 6.5 Specific discharge capacities of the $Li[Co_xLi_{1/3-x/3}Mn_{2/3-2x/3}]O_2$ (x = 0, 0.087, 0.1 and 0.118) composites in the first 120 cycles at three potential windows of 2-4.6 V, 2-4.8 V and 2-5 V. The current density is 30 mA g^{-1}.

To further explore the effect of Co doping to the electrochemical performance, the specific discharge capacities of all samples in the first 120 cycles at 2-4.8 V are compared in **Figure S6.1**. It can be found that the capacity rapidly increased upon cycles in the Co-doped samples while the Li_2MnO_3 sample, although increased as well, maintained a low capacity of less than 50 mAh g^{-1}. In addition, as the content of Co grows, the capacity increases faster in the first a few cycles, suggesting that Co can facilitate the capacity increase. This is further supported by the cycling performance of the x=0.143 and 0.182 samples under the same testing condition (**Figure S6.2**). With higher Co/Mn mole ratio of 4 and 3, the activation of the Li_2MnO_3 was completed much faster. As a result, the capacity of these two samples increased for only 2 and 4 cycles, respectively and then gradually decreased. On the other side, it is noted that the x=0.087 sample delivered the highest peak capacity of 234 mAh g^{-1} after 120 cycles while the x=0.118 sample achieved the smallest of 213 mAh g^{-1}. This is probably because the increase of Co is at the cost of the Li_2MnO_3 phase, which is the main contributor to the fully activated capacity. On the other side, it can be found from **Figure 6.6** that the columbic efficiency of the sample at 2-4.8 V potential window are similar in the first 120 cycles. In the first 4 or 5 cycles, all of them exhibited quite low columbic efficiency. After the initial 4 or 5 cycles, the efficiency increased quickly from around 60% in the first cycle to over 95% and then became stabilized for the following cycles. This indicates that all these samples experienced the capacity loss mainly in the first 4 or 5 cycles, but retained the extra capacity in the following cycles with negligible electrolyte decomposition during the relatively mild activation process.

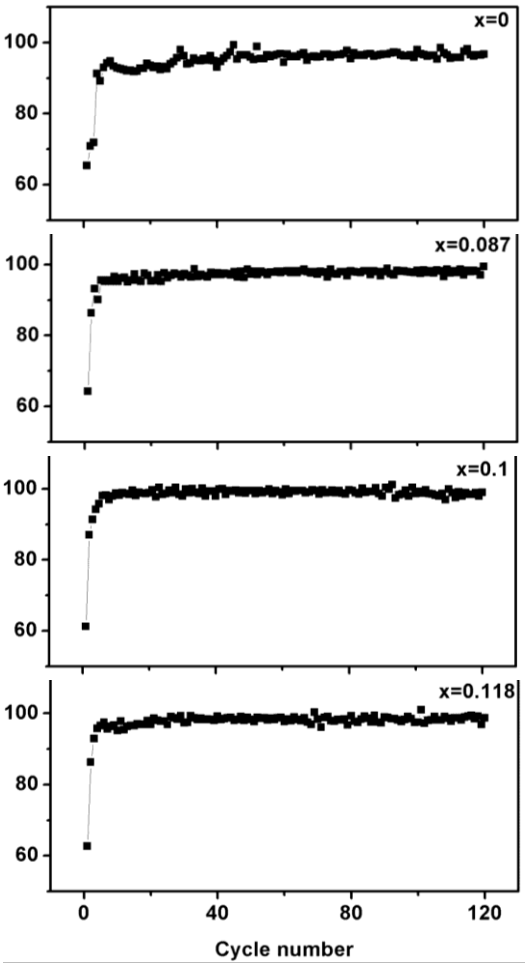

Figure 6.6 Columbic efficiencies of the $Li[Co_xLi_{1/3-x/3}Mn_{2/3-2x/3}]O_2$ (x=0, 0.087, 0.1, 0.118) composites between 2-4.8 V potential window in the first 120 charging-discharging cycles.

Detailed charging-discharging curves of each sample are presented in **Figure 6.7**. For the first charge, a short plateau between 4 V and 4.5 V appeared in all Co-doped samples. This can be ascribed to the oxidation of Co^{3+} to Co^{4+} [19, 34]. More importantly, a long first charge plateau above 4.5 V was developed in the Co-doped samples and grew longer as the Co content increased. This plateau is associated with the Li_2MnO_3 activation process, which involves a few sub-reactions including a further Li extraction from the TM layers, TM rearrangement and O_2 generation from the crystal structure [9, 11, 35]. Therefore, it can be deduced that a slightly higher content of Co-doping can effectively promote the Li_2MnO_3 activation from the very beginning. Compared with the Li_2MnO_3 sample, another impressive feature in the Co-doped samples is the evolution of the 3 V discharge plateau which was invisible in the first discharge but dominated the discharge curve after just a few cycles. This plateau is well accepted to be from a newly formed defect spinel phase embedded on the parent layered structure [18, 36, 37].

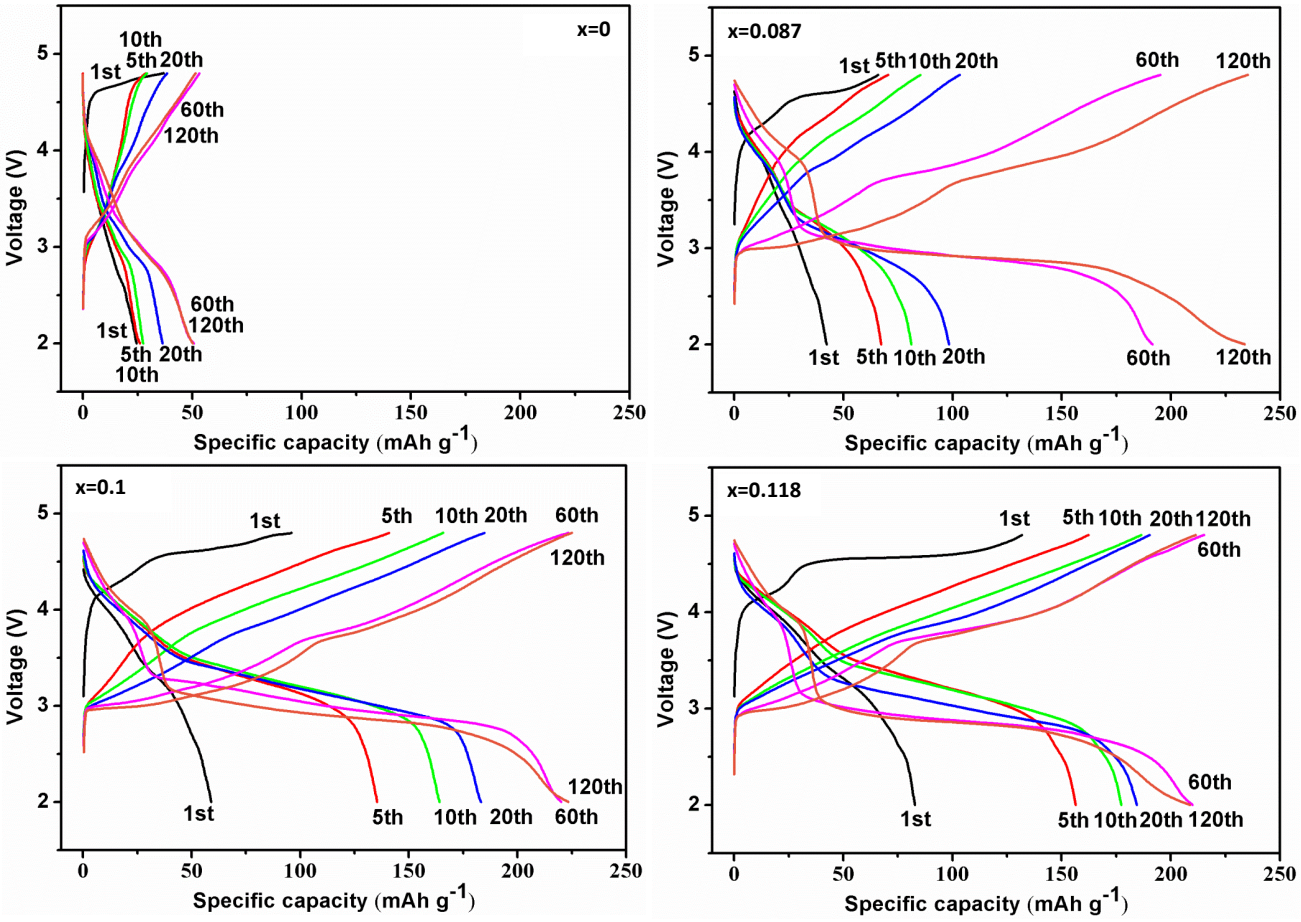

Figure 6.7 Charge/discharge curves of the $Li[Co_xLi_{1/3-x/3}Mn_{2/3-2x/3}]O_2$ (x = 0, 0.087, 0.1 and 0.118) composites at different cycles between 2-4.8 V.

CV measurements were also conducted to further understand the redox reactions of the Co-doped materials upon cycling and the CV curves in the first 10 cycles at 2-4.8 V and a scan rate of 0.2 mV s^{-1} are shown in **Figure 6.8**. In general, a sharp and high oxidation peak at around 4.6 V appeared in the first charge and then faded in the second charge and almost disappeared after 5 cycles. This feature is well consistent with the behavior of the charge plateau above 4.6 V as shown in **Figure 6.7**, suggesting majority of the Li_2MnO_3 phase was activated in the first few cycles. In addition, a pair of redox peaks centered at around 3.2 V was gradually developed in all samples and became the largest after 10 cycles. Such a pair of peaks can be ascribed to the redox reaction of the Mn^{3+}/Mn^{4+} in a spinel environment, suggesting that the layered structure of these Co-doped materials was gradually transformed to a new spinel phase during cycling [38]. As the Co content increased, it is noted that a pair of 4.1 V redox peaks was also enlarged, which can be ascribed to the Co^{3+}/Co^{4+} redox pair [19], indicating more Co involved in the electrochemical reactions. In addition, it can be clearly seen that the area of the CV loops, which is proportional to the charge/discharge capacity, was growing

obviously upon cycles in each sample; on the other hand, the CV loops expanded apparently faster in the sample with higher Co content. All these features are well consistent with the above cycling results in **Figure 6.6**, further supporting the fact that the capacities of the samples gradually increase upon cycling and a slight increase of Co in the samples can drastically facilitate the capacity increment.

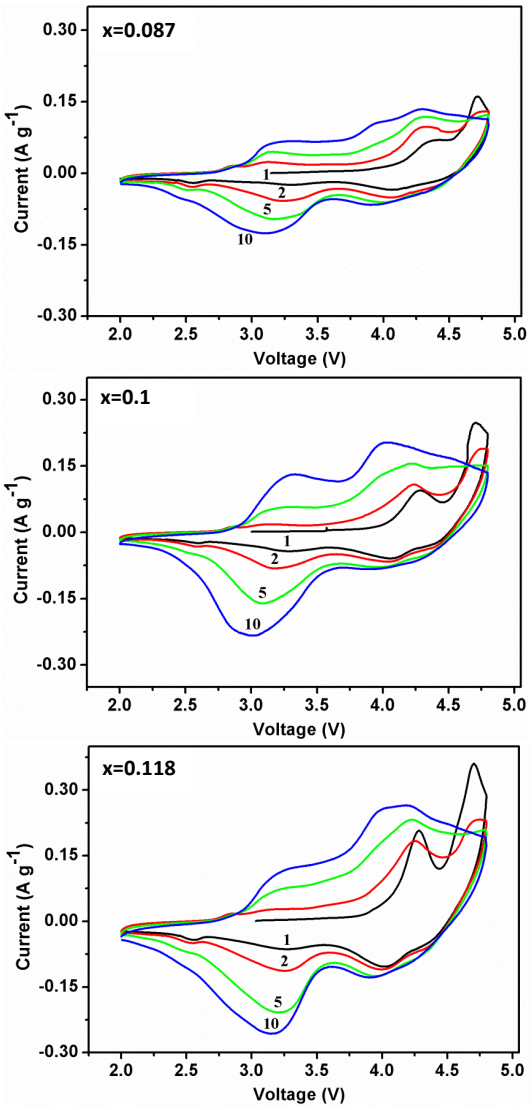

Figure 6.8 CV curves of the $Li[Co_xLi_{1/3-x/3}Mn_{2/3-2x/3}]O_2$ (x = 0.087, 0.1 and 0.118) composites at 2-4.8 V in the first 10 cycles.

The cycling performance of the Co-doped samples was also compared at different current rates of 0.1 C, 0.2 C and 0.5 C and the results of the first 120 cycles are shown in **Figure 6.9**. It is obvious that the capacity-increase was remarkably retarded at 0.2 C and almost vanished at 0.5 C. Considering the complex structure arrangement and diffusion of the heavy transition metals and oxygen ions during the Li_2MnO_3 activation process, a poor kinetics could be expected to account for such a small

capacity increase at high rates [39]. On the other side, it can be found that the capacity-increase at 0.2 C also follows the trend that the more the Co doping, the faster the capacity increases. It has been reported that the Li_2MnO_3 had very poor rate capability while the doped Co featured fast reaction kinetics [39]. While in our Co-doped samples, the Co can not only improve the rate capability, but also help to activate the Li_2MnO_3 phase, therefore, a better rate performance was observed in samples with more Co. Note that the high rate performances of these samples after several activating cycles at low rate of 0.1 C were also measured; however, the results are not competitive to the traditional high-Co Li-rich cathode materials. For instance, the x=0.118 sample after 50 activation cycles at 0.1 C rate delivered a specific discharge capacity of ~ 170 mAh g^{-1} at 0.2 C rate and only ~ 110 mAh g^{-1} at 1 C rate. The capacity has subsequently dropped to ~100 mAh g^{-1} after 10 cycles at 1 C rate. To improve the rate performance, we are now investigating the reasons for poor rate performance and trying to improve it by surface modification methods, for instance, AlF_3 coating. The results will be reported in a future work.

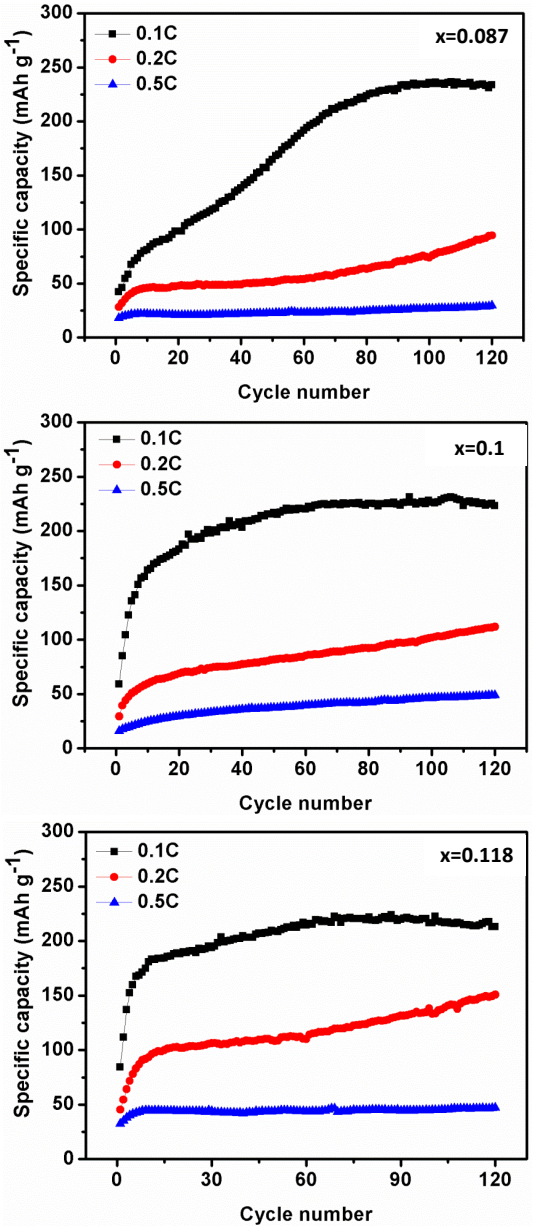

Figure 6.9 Cycling performance of the $Li[Co_xLi_{1/3-x/3}Mn_{2/3-2x/3}]O_2$ (x = 0.087, 0.1 and 0.118) composites at three current densities of 30, 60 and 150 mA g^{-1} between 2-4.8 V.

To investigate the kinetic properties of the Co-doped materials, EIS measurement was conducted on the assembled samples before and after 1 and 5 charging-discharging cycles at 2-4.8 V. The typical Nyquist plots and the corresponding equivalent circuit are shown in **Figure 6.10** and the fitting results based on this equivalent circuit are summarized in **Table S6.1**. Here R_1 is associated with the ohmic resistance between the working electrode and the reference electrode. In a general Nyquist plot, the high frequency intercept corresponds to the ohmic resistance of electrolyte solution and refers to R_2 in our model; the semicircle at medium frequency is related to the charge transfer resistance (R_3) on the electrode particle surface; and the sloping line at low frequency reflects the Li

ion diffusion resistance in the crystal structure of the layered materials [40]. It can be found that the R_3 of all the samples decreased gradually during cycling. For example, from **Table S6.1**, R_3 of the x=0.1 sample reduced from 499 Ω to 221.7 Ω after the first cycle and further decreased to 193.2 Ω after 5 cycles, which is attributable to step-wise Li_2MnO_3 phase activation [41,42]. On the other hand, after 1 or 5 cycles, it is found that the more the Co doping, the shorter the radius of the semicircle and the lower the charge transfer resistance on the particle surface. For example, after 1st cycle, the values of R_3 were 443.6 Ω, 221.7 Ω and 142.8 Ω for the x=0.087, 0.1 and 0.118 samples, respectively, and they further decreases to 305.1 Ω, 193.2 Ω and 169.1 Ω after 5 cycles. Therefore, it is reasonable to conclude that the faster decrease of R_3 in samples with higher Co doping is due to a faster activation rate of the Li_2MnO_3 phase. It worth noting that, to better understand the EIS results and the kinetic mechanism of the activation process, the use of a 3-electrode cell under protective atmosphere can be very useful in our future investigations.

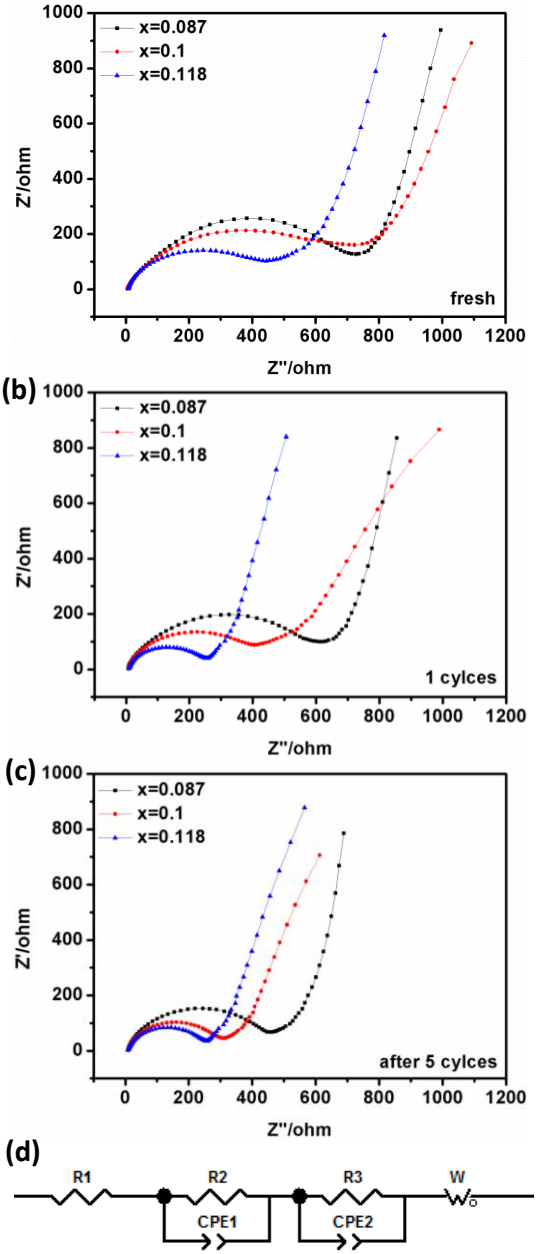

Figure 6.10 Typical Nyquist plots of the Co-doped samples (a) before and after (b) 1 and (c) 5 charging-discharging cycles.

The electrodes of Co-doped samples after 120 charging-discharging cycles at 0.1 C between 2-4.8 V were collected and characterized by *ex-situ* XRD (**Figure 6.11**). The C2/m featured minor peaks between 20° and 25° disappeared in all samples after 120 cycles of deep Li^+ intercalation/deintercalation, indicating the thorough consumption of the Li_2MnO_3 phase [43]. In addition, the XRD patterns of the cycled samples are similar to the reported $LiMnO_2$ (R-3m) structure, suggesting the structure evolution of the parent C2/m to the R-3m that could be induced by the irreversible 2b site Li^+ extraction to accommodate the crystal distortion [19]. Note that the phase

transformation of Li_2MnO_3 during cycling has been a research focus [43]. During the activation process, it can be firstly transformed to a layered-like phase in the initial a few cycles during deep charging at high voltage, and the new phase could be further activated to provide the extra capacity in the following cycles.

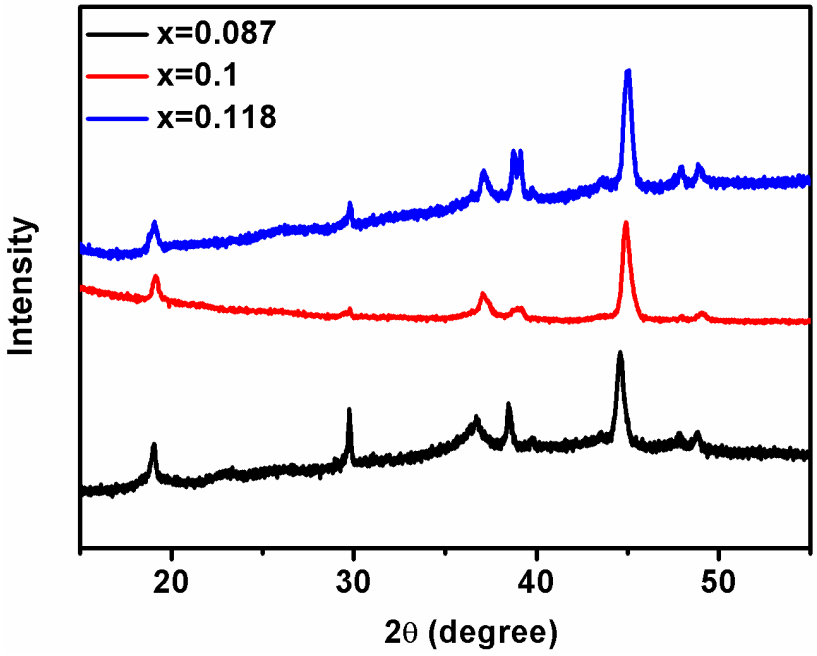

Figure 6.11 *Ex-situ* X-ray diffraction patterns of the x = 0.087, x = 0.1 and x = 0.118electrodes after 120 cycles at 0.1C between 2-4.8 V.

6.5 Conclusions

A serial of low-Co Li-rich cathode materials $Li[Co_xLi_{1/3-x/3}Mn_{2/3-2x/3}]O_2$ (x=0.087, 0.1, 0.118) have been prepared by a simple co-precipitation method. Although these cathode materials showed similar crystal structure, morphology and microstructure, the low Co-doped ones exhibited prominent capacity increase gradually over tens of cycles which rarely occurred in the pure Li_2MnO_3 sample. This large stepwise capacity increase from less than 50 mAh g^{-1} in the first cycle to up to 250 mAh g^{-1} in a few dozens of cycles has been demonstrated as the result of the gradual activation of the Li_2MnO_3 phase which is promoted by the Co-doping [18]. The systematic study on this unique phenomenon of capacity increase revealed that the capacity increase was highly dependent on a few factors including the amount of Co-doping, cycling potential window and the current rate. All the low Co-doped samples can efficiently activate the Li_2MnO_3 phase and a minor change of the Co content can make a significant impact on the rate of the activation process. In addition, an

appropriate cycling potential window of 2-4.8 V was proved to be effective in facilitating the Li_2MnO_3 activation and delivering excellent long-term cycling stability. These findings provide a deep understanding of the origin of superior high specific capacities of Li-rich cathode materials, which can be important to guide the rational design of cheap and high performance cathode materials for lithium ion batteries.

6.6 References

1. Dunn, B., H. Kamath, and J.-M. Tarascon, *Electrical energy storage for the grid: A battery of choices*. Science, 2011. **334**(6058): p. 928-935.
2. Armand, M. and J.-M. Tarascon, *Building better batteries*. Nature, 2008. **451**(7179): p. 652-657.
3. Liu, J., *Addressing the grand challenges in energy storage*. Adv. Funct. Mater., 2013. **23**(8): p. 924-928.
4. Wang, H., et al., *Mn_3O_4-graphene hybrid as a high-capacity anode material for lithium ion batteries*. J. Am. Chem. Soc., 2010. **132**(40): p. 13978-13980.
5. Luo, B., et al., *Reduced Graphene Oxide-Mediated Growth of Uniform Tin-Core/Carbon-Sheath Coaxial Nanocables with Enhanced Lithium Ion Storage Properties*. Adv. Mater., 2012. **24**(11): p. 1405-1409.
6. Jeong, G., et al., *Core-Shell Structured Silicon Nanoparticles@TiO_{2-x}/Carbon Mesoporous Microfiber Composite as a Safe and High-Performance Lithium-Ion Battery Anode*. ACS nano, 2014. **8**(3): p. 2977-2985.
7. Chan, C.K., et al., *Solution-grown silicon nanowires for lithium-ion battery anodes*. ACS nano, 2010. **4**(3): p. 1443-1450.
8. Goodenough, J.B. and K.-S. Park, *The Li-ion rechargeable battery: a perspective*. J. Am. Chem. Soc., 2013. **135**(4): p. 1167-1176.
9. Thackeray, M.M., et al., *Li_2MnO_3-stabilized $LiMO_2$ (M = Mn, Ni, Co) electrodes for lithium-ion batteries*. J. Mater. Chem., 2007. **17**(30): p. 3112-3125.
10. Thackeray, M.M., et al., *Advances in manganese-oxide 'composite' electrodes for lithium-ion batteries*. J. Mater. Chem., 2005. **15**(23): p. 2257-2267.
11. Armstrong, A.R., et al., *Demonstrating oxygen loss and associated structural reorganization in the lithium battery cathode $Li[Ni_{0.2}Li_{0.2}Mn_{0.6}]O_2$*. J. Am. Chem. Soc., 2006. **128**(26): p. 8694-8698.

12. Yu, H., et al., *Direct Atomic-Resolution Observation of Two Phases in the $Li_{1.2}Mn_{0.567}Ni_{0.166}Co_{0.067}O_2$ Cathode Material for Lithium-Ion Batteries*. Angew. Chem., Int. Ed., 2013. **52**(23): p. 5969-5973.
13. Yu, H. and H. Zhou, *High-Energy Cathode Materials (Li_2MnO_3-$LiMO_2$) for Lithium-Ion Batteries*. J. Phys. Chem. Lett., 2013. **4**(8): p. 1268-1280.
14. Jarvis, K.A., et al., *The role of composition in the atomic structure, oxygen loss, and capacity of layered Li-Mn-Ni oxide cathodes. J. Mater. Chem. A*, 2014. **2**(5): p. 1353-1362.
15. Park, Y.J., et al., *Synthesis and Electrochemical Characteristics of $Li[Co_xLi_{(1/3-x/3)}Mn_{(2/3-2x/3)}]O_2$ Compounds*. J. Electrochem. Soc., 2004. **151**(5): p. A720-A727.
16. Kim, J.-M., S. Tsuruta, and N. Kumagai, *Electrochemical properties of $Li(Li_{(1-x)/3}Co_xMn_{(2-2x)/3})O_2$ ($0 \leq x \leq 1$) solid solutions prepared by poly-vinyl alcohol (PVA) method*. Electrochem. Commun., 2007. **9**(1): p. 103-108.
17. Kumagai, N., et al., *Structural modification of $Li[Li_{0.27}Co_{0.20}Mn_{0.53}]O_2$ by lithium extraction and its electrochemical property as the positive electrode for Li-ion batteries*. Electrochim. Acta, 2008. **53**(16): p. 5287-5293.
18. Ye, D., et al., *Capacity-controllable Li-rich cathode materials for lithium-ion batteries*. Nano Energy, 2014. **6**: p. 92-102.
19. Ozawa, K., et al., *Electrochemical characteristics of layered $Li_{1.95}Mn_{0.9}Co_{0.15}O_3$ (C2/m) as a lithium-battery cathode*. J. Electrochem. Soc., 2012. **159**(3): p. A300-A304.
20. Kang, S.-H., et al., *Interpreting the structural and electrochemical complexity of 0.5 Li_2MnO_3 0.5$LiMO_2$ electrodes for lithium batteries ($M = Mn_{0.5-x}Ni_{0.5-x}Co_{2x}$, $0 \leq x \leq 0.5$)*. J. Mater. Chem., 2007. **17**(20): p. 2069-2077.
21. Bréger, J., et al., *High-resolution X-ray diffraction, DIFFaX, NMR and first principles study of disorder in the Li_2MnO_3-$Li[Ni_{1/2}Mn_{1/2}]O_2$ solid solution*. J. Solid State Chem., 2005. **178**(9): p. 2575-2585.
22. Jarvis, K.A., et al., *Atomic Structure of a Lithium-Rich Layered Oxide Material for Lithium-Ion Batteries: Evidence of a Solid Solution*. Chem. Mater., 2011. **23**(16): p. 3614-3621.
23. Li, Y., et al., *Electrochemical performance of nanocrystalline $Li_3V_2(PO_4)_3$/carbon composite material synthesized by a novel sol-gel method*. Electrochim. Acta, 2006. **51**(28): p. 6498-6502.
24. Zhou, L., Zhao, D. and Lou, X.D., *$LiNi_{0.5}Mn_{1.5}O_4$ Hollow Structures as High-Performance Cathodes for Lithium-Ion Batteries.* Angew. Chem., 2012. **124**(1): p. 243-245.
25. Jiang, Y., et al., *Hollow 0.3Li_2MnO_3 0.7$LiNi_{0.5}Mn_{0.5}O_2$ microspheres as a high-performance cathode material for lithium–ion batteries.* Chem. Chem. Phys., 2013. **15**(8): p. 2954-2960.

26. Bareno, J., et al., *Local Structure of Layered Oxide Electrode Materials for Lithium-Ion Batteries*. Adv. Mater., 2010. **22**(10): p. 1122-1127.
27. Boulineau, A., et al., *Reinvestigation of Li_2MnO_3 Structure: Electron Diffraction and High Resolution TEM*. Chem. Mater., 2009. **21**(18): p. 4216-4222.
28. Regan, E., et al., *Surface and bulk composition of lithium manganese oxides*. Surf. Interface Anal., 1999. **27**(12): p. 1064-1068.
29. Li, Z., et al., *Synthesis of hydrothermally reduced graphene/MnO_2 composites and their electrochemical properties as supercapacitors*. J. Power Sources, 2011. **196**(19): p. 8160-8165.
30. Madhavi, S., et al., *Synthesis and Cathodic Properties of $LiCo_{1-y}Rh_yO_2$ ($0 \leq y \leq 0.2$) and $LiRhO_2$*. J. Electrochem. Soc., 2001. **148**(11): p. A1279-A1286.
31. van Bommel, A., L. Krause, and J. Dahn, *Investigation of the irreversible capacity loss in the lithium-rich oxide $Li[Li_{1/5}Ni_{1/5}Mn_{3/5}]O_2$*. J. Electrochem. Soc., 2011. **158**(6): p. A731-A735.
32. Ito, A., et al., *Cyclic deterioration and its improvement for Li-rich layered cathode material $Li[Ni_{0.17}Li_{0.2}Co_{0.07}Mn_{0.56}]O_2$*. J. Power Sources, 2010. **195**(2): p. 567-573.
33. Lee, K.T., S. Jeong, and J. Cho, *Roles of surface chemistry on safety and electrochemistry in lithium ion batteries*. Acc. Chem. Res., 2012. **46**(5): p. 1161-1170.
34. Yabuuchi, N., et al., *Detailed Studies of a High-Capacity Electrode Material for Rechargeable Batteries, Li_2MnO_3-$LiCo_{1/3}Ni_{1/3}Mn_{1/3}O_2$*. J. Am. Chem. Soc., 2011. **133**(12): p. 4404-4419.
35. Xu, B., et al., *Identifying surface structural changes in layered Li-excess nickel manganese oxides in high voltage lithium ion batteries: A joint experimental and theoretical study*. Energy Environ. Sci., 2011. **4**(6): p. 2223-2233.
36. Gu, M., et al., *Formation of the spinel phase in the layered composite cathode used in Li-ion batteries*. Acs Nano, 2012. **7**(1): p. 760-767.
37. Song, B., et al., *Structural evolution and the capacity fade mechanism upon long-term cycling in Li-rich cathode material*. Phys. Chem. Chem. Phys., 2012. **14**(37): p. 12875-12883.
38. Croy, J.R., et al., *Countering the Voltage Decay in High Capacity xLi_2MnO_3 $(1-x)LiMO_2$ Electrodes (M = Mn, Ni, Co) for Li^+ Ion Batteries*. J. Electrochem. Soc., 2012. **159**(6): p. A781-A790.
39. Yu, X., et al., *Understanding the Rate Capability of High-Energy-Density Li-Rich Layered $Li_{1.2}Ni_{0.15}Co_{0.1}Mn_{0.55}O_2$ Cathode Materials*. Adv. Energy Mater., 2013.
40. Toprakci, O., et al., *Synthesis and characterization of xLi_2MnO_3 $(1-x)LiMn_{1/3}Ni_{1/3}Co_{1/3}O_2$ composite cathode materials for rechargeable lithium-ion batteries*. J. Power Sources, 2013. **241**: p. 522-528.

41. Du, K., et al., *Sodium additive to improve rate performance of $Li[Li_{0.2}Mn_{0.54}Ni_{0.13}Co_{0.13}]O_2$ material for Li-ion batteries*. J. Power Sources, 2013. **244**: p. 29-34.
42. Dong, X., et al., *Sodium substitution for partial lithium to significantly enhance the cycling stability of Li_2MnO_3 cathode material*. J. Power Sources, 2013. **243**: p. 78-87.
43. Lee, E.-S., et al., *High-Voltage, high-energy layered-spinel composite cathodes with superior cycle life for lithium-ion batteries*. Chem. Mater., 2012. **24**(3): p. 600-612.

5.7 Supporting Information

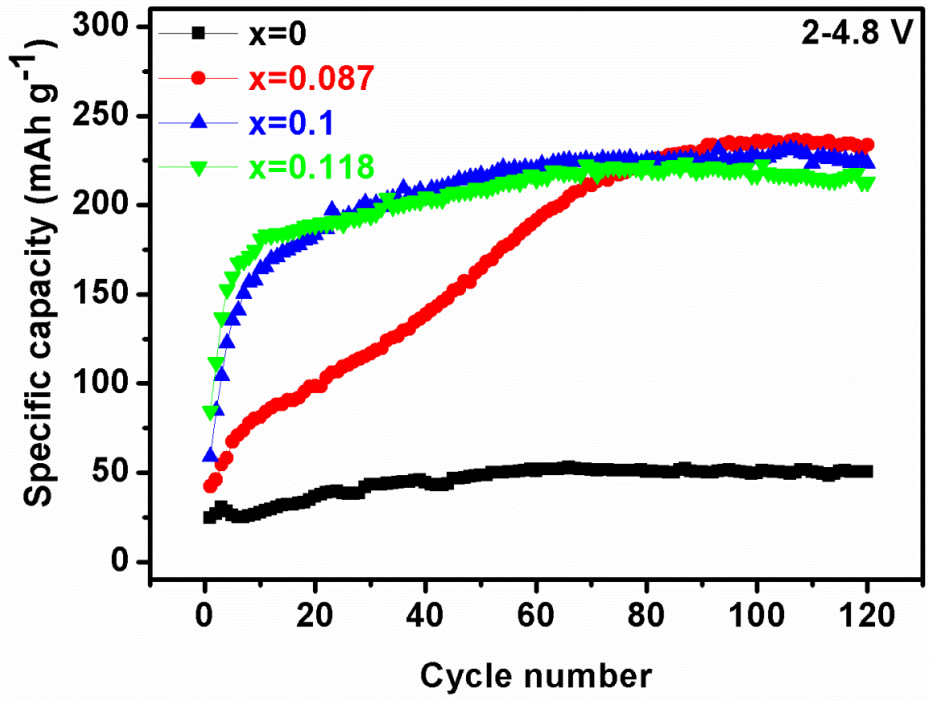

Figure S6.1 Comparison of the cycling performance of the $Li[Co_xLi_{1/3-x/3}Mn_{2/3-2x/3}]O_2$ (x=0, 0.087, 0.1, 0.118) composites between 2-4.8 V potential window in the first 120 charging-discharging cycles.

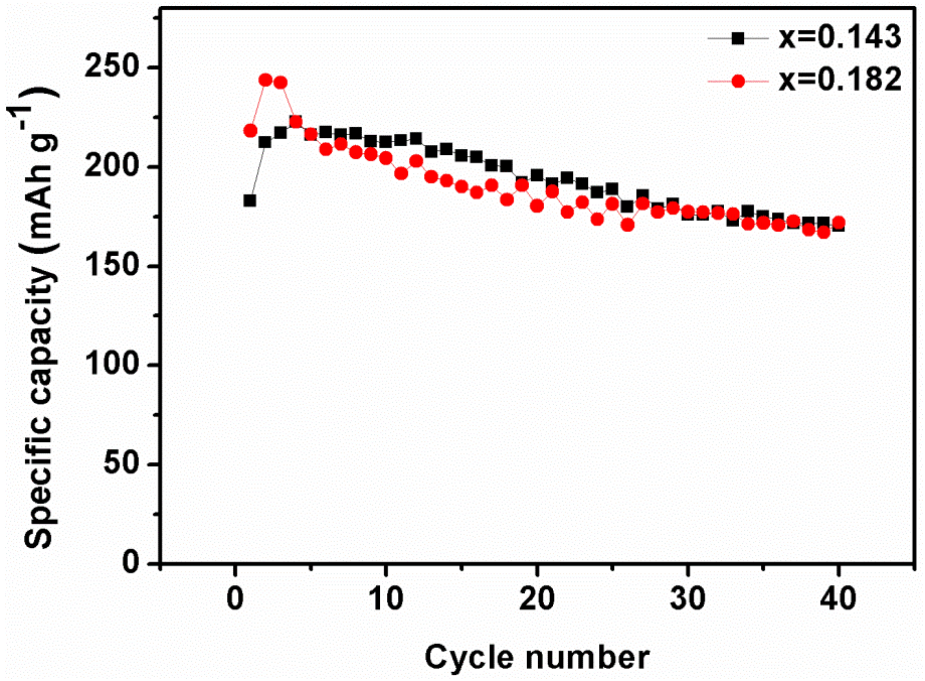

Figure S6.2 Cycling performance of the x=0.143 and 0.182 samples at 30 mA g^{-1} between 2-4.8 V.

Table S6.1 Resistance values of the $Li[Co_xLi_{1/3-x/3}Mn_{2/3-2x/3}]O_2$ (x=0.087, 0.1, 0.118) composites before cycling and after the 1st and 5th cycle.

Sample	Before cycle			After 1st cycle			After 5th cycle		
X	R1(Ω)	R2(Ω)	R3(Ω)	R1(Ω)	R2(Ω)	R3(Ω)	R1(Ω)	R2(Ω)	R3(Ω)
0.087	5.7	58.6	554.6	5.7	66.6	443.6	7.6	79.1	305.1
0.1	2.8	34.1	499	3.0	56.8	221.7	7.5	55.5	193.2
0.118	5.5	57.9	295.5	6.5	53.6	142.8	5.9	39.3	169.1

7. Ni-induced stepwise capacity increase in Ni-less Li-rich cathode materials for high performance lithium ion batteries

7.1 Abstract

Li-rich cathode materials have been considered as promising candidates for high-energy lithium ion batteries (LIBs). In this study, we report a new series of Li-rich materials ($Li[Li_{1/3-2x/3}Mn_{2/3-x/3}Ni_x]O_2$ ($0.09 \leq x \leq 0.2$)) doped with small amounts of Ni as cathode materials in LIBs, which exhibited unusual phenomenon of capacity increase up to tens of cycles due to the continuous activation of the Li_2MnO_3 phase. Both experimental and computational results indicate that unlike commonly studied Ni-doped Li-rich cathode materials, smaller amounts of Ni doping can promote the stepwise Li_2MnO_3 activation to obtain increased specific capacity and better cycling capability. In contrast, excessive Ni will over-activate the Li_2MnO_3 and result in a large capacity loss in the first cycle. The $Li_{1.25}Mn_{0.625}Ni_{0.125}O_2$ material with an optimized content of Ni delivered a superior high capacity of ~280 mAh g^{-1} and good cycling stability at room temperature.

7.2 Introduction

Due to the high demands of electric vehicles and large-scale energy storage systems, rechargeable lithium ion batteries (LIBs) have received increasing attention as one of the best potential power sources for these applications [1–3]. Many new types of anode materials, such as Si [4] and some metal oxides [5, 6] have been developed as potential replacements for the conventional anode—graphite, and the newly introduced super-conductive graphene and its complexes with metal or metal oxides have demonstrated a superior high capacity of more than 1000 mAh g^{-1} with excellent rate performance [7–10]. However, the current commercial cathode materials for LIBs, such as $LiCoO_2$ (140 mAh g^{-1}), $LiMn_2O_4$ (120 mAh g^{-1}) and $LiFePO_4$ (160 mAh g^{-1}) are still far from satisfactory in terms of their low energy density and high cost [11–14], which has led to intensive efforts devoted to the exploration of new alternatives.

Li-rich layered oxides are a family of high energy cathode materials, which have been studied in recent years following the pioneering work by Thackeray [15, 16]. Generally, they are complex composites consisting of two highly integrated layered structures with the composition of Li_2MnO_3 ($C2/m$) and $LiMO_2$ ($R\bar{3}m$) and can deliver a high specific capacity of more than 250 mAh g^{-1} (M = Ni, Co, Mn or their combination) [16–19]. Within this category of materials, a series of composites with the composition of $Li[Li_{1/3-2x/3}Mn_{2/3-x/3}Ni_x]O_2$ are of particular interest due to the absence of expensive and toxic Co. Much effort has been committed to revealing the relationships between the composition, atomic structure and the corresponding electrochemistry performance [20–29].

It has been generally accepted that Ni-doping can concurrently provide high voltage and improve the thermal stability of the layered cathode materials. On the other hand, in the case of the Li-rich materials, the high capacities arise mainly from the activation of the Li_2MnO_3 component, so the content of Ni should be limited in order to achieve high specific capacity. In addition, as the increased Ni content may substitute Li in the Li layer and lower the Li^+ mobility, minimizing the Ni content also favors improved rate performance [28, 30–32]. Considering all the above factors, particularly the working voltage and specific capacity, it is essential to maintain a balanced level of Ni in the Li-rich cathode materials to maximize the energy density. However, only the Ni/Mn ratios between 1/3 and 1/1 have been extensively studied in Li–Mn–Ni–O system to date [20, 21, 23–29, 32–34] while the performances of such composites with Ni/Mn ratios less than 1/3 have not been systematically explored so far.

Herein we report a series of intentionally designed Ni-poor Li-rich cathode materials $Li[Li_{1/3-2x/3}Mn_{2/3-x/3}Ni_x]O_2$ ($0.09 \leq x \leq 0.2$) where the Ni/Mn ratios are specified to be 1/7, 1/6, 1/5, 1/4 and 1/3, respectively (abbreviated as Ni/7, Ni/6, Ni/5, Ni/4 and Ni/3). Very interestingly, unlike the previously reported highly Ni-doped Li-rich materials with gradually declining capacities, the capacities of our materials were relatively small in the first cycle but continuously increased in the following tens of cycles to reach a maximum value of up to 280 mAh g^{-1}. Detailed structure characterization confirmed that the continuous capacity increase is due to the gradual evolution of the Li_2MnO_3 phase, which is very different from the commonly studied Ni-doped Li-rich materials. More importantly, the substantial capacity loss in the first cycle that is commonly observed in Li-rich materials was significantly retarded in our optimized Ni/5 samples, leading to a remarkably high capacity. In addition, the undesirable large oxygen release in conventional Li-rich materials in the first cycle can also be substantially suppressed in our Ni-poor materials.

7.3 Experimental section

Materials synthesis: All reagents were obtained from Sigma Aldrich. The $Li[Ni_xLi_{1/3-2x/3}Mn_{2/3-x/3}]O_2$ (x = 0.091, 0.105, 0.125, 0.154, 0.2) cathode materials were synthesized in two steps. In a typical synthesis, stoichiometric amounts of $Mn(NO_3)_2$ and $Ni(NO_3)_2$ were dissolved in distilled water and then co-precipitated with an equal volume of 0.2 M sodium carbonate solution. After stirring for 20 h at room temperature, the light brown precipitate was filtered, washed and dried at 100 ℃. In the next step, the collected precipitate was pre-heated at 500 ℃ in air for 5 h and then calcined with a stoichiometric amount of $LiOH·H_2O$ at 900 ℃ in air for another 12 h to obtain the final products.

Materials characterization: The mole ratio of the metal elements in each sample was determined by a Varian 725-ES inductively coupled plasma atomic emission spectrometer (ICP-AES). Crystalline structures of powder samples and electrodes were measured by X-ray diffraction (XRD) on a Bruker ADVANCE X-ray diffractometer (40 kV, 30 mA) with Cu Kα (λ = 0.15406 nm) radiation at a scanning rate of 1^o min^{-1}. Morphological characteristics of the samples were investigated using a field-emission scanning electron microscope (FE-SEM, JEOL 7800). Transmission electron microscopy (TEM) investigations were conducted on a Philips FEI Tecnai F20 microscope operated at 200 kV.

Electrochemical test: All the electrochemical tests were conducted in CR2032 coin cells at room temperature. Firstly, a working electrode was prepared by the doctor blade process. The active

materials, acetylene black and polyvinylidene fluoride were mechanically mixed in the weight ratio of 7:2:1 with an appropriate amount of *N*-methyl-2-pyrrolidone. After that, the slurry was coated onto an aluminum foil (0.7 cm^2) and then dried in a vacuum oven at 120 °C for 12 h. The prepared working electrode was fabricated into CR2032 coin cells in an argon-filled glove box. Lithium foil and 1 M $LiPF_6$ in a mixture of ethylene carbonate (EC) and dimethyl carbonate (DMC) (1:1) were used as the negative electrode and electrolyte, respectively. The galvanostatic charge/discharge tests were performed using a multi-channel battery tester (Land CT2001A). The cyclic voltammetry (CV) measurements were conducted on a CHI660E electrochemical workstation.

Computational Method: The Perdew–Burke–Ernzerhof functional embedded in the Vienna ab initio simulation package (VASP) was employed for the periodic density functional theory (DFT) calculations, and the projector augmented wave method with a cutoff energy of 380 eV was adopted to describe the electron–ion interactions [35–37]. The k-space was sampled by the gamma point. As it is associated with oxygen vacancies (OV), on-site electron correlation is essential and the DFT plus Hubbard model (DFT + U) was consequently employed in this work with the U valued at 5.0 eV for Mn and Co atoms [38–40]. A 2 × 1 × 2 supercell was built to model Li_2MnO_3 with the dimensions of 9.87 Å × 8.53 Å × 10.06 Å and formula of $Li_{32}Mn_{16}O_{48}$. OVs were represented by extracting one O-atom from the lattice while nickel doping involves replacing an Mn-atom with another transition metal (TM) atom. The OV formation energy was calculated by $E_f = E(Li_xMn_{16-\delta}TM_\delta O_{48}) - E(Li_xMn_{16-\delta}TM_\delta O_{47}) - {}^1/_2E(O_2)$. A negative value of E_f means that the formation of OV is endothermic.

7.4 Results and discussion

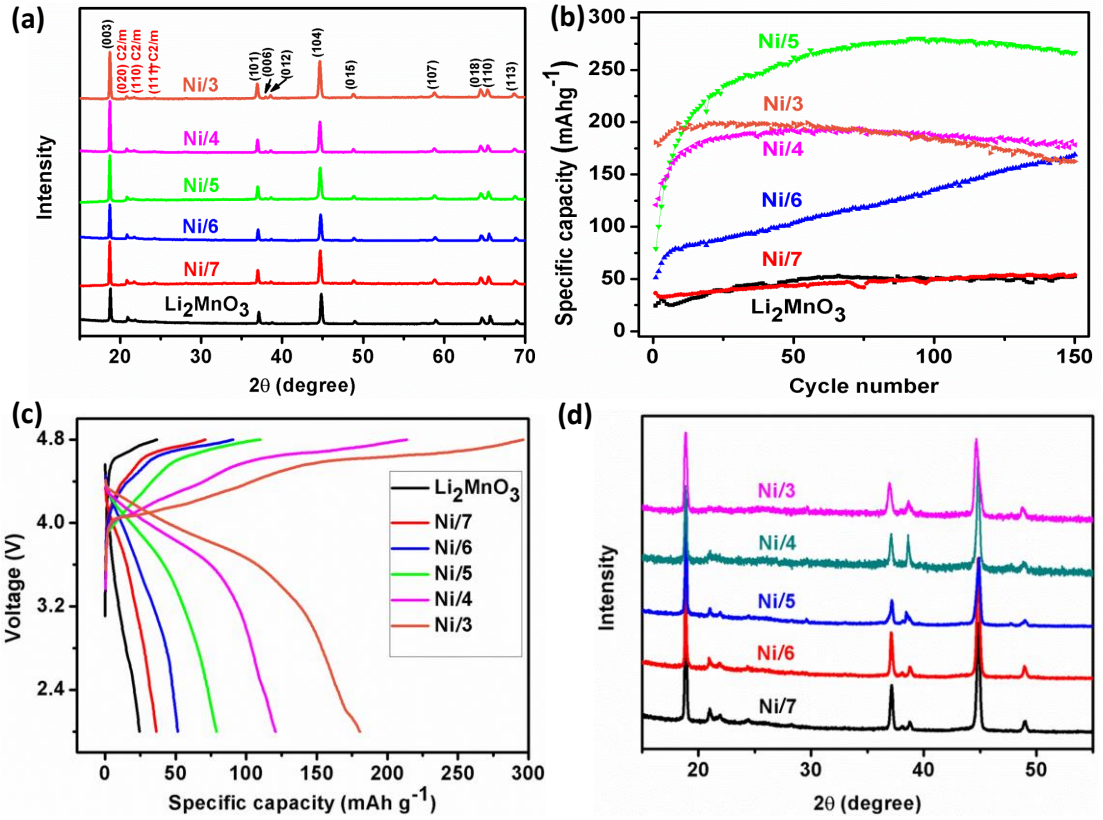

Figure 7.1 a) XRD patterns of pristine cathode materials with different Ni-doping content; b) Cycling performance of the cathode materials in the first 150 cycles at 30 mA g^{-1} between 2-4.8 V; c) The relevant 1st charge and discharge curves of Ni-doped cathode materials at 30 mA g^{-1} between 2-4.8 V; d) XRD patterns of the electrodes after the 1st cycle.

The mole ratios of Mn/Ni and Li/(Mn+Ni) for the $Li[Ni_xLi_{1/3-2x/3}Mn_{2/3-x/3}]O_2$ materials determined by ICP analysis are shown in Table S1 (in the Electronic Supplementary Material (ESM)). As indicated, the Ni/Mn ratios are consistent with the nominal values, indicating that the stoichiometry of the final products is close to the expected composition. XRD patterns of all the pristine samples (**Fig. 7.1a**) showed that all the Ni-doped cathode materials are highly crystalline and the structures are nearly identical to each other. The main diffraction peaks can be well indexed to the $R\bar{3}m$ space group (JCPDS No. 84-1634) with a typical layered phase. Some minor peaks appeared between 20 ° and 25 °, which can be indexed to be the localized $LiMn_6$ superlattice in the monoclinic Li_2MnO_3-like regions [41–43]. In addition, a much higher intensity of the (003) peak relative to that of the (104) peak was observed, indicating a low degree of cation mixing in the Li layers. This phenomenon was also demonstrated by the well split pairs of (006)/(012) and (018)/(110) peaks [30]. These Ni-doped

Li-rich cathode materials exhibited very similar microstructure and morphology as observed by the FE-SEM (**Fig. S7.1** (in the ESM)). Particles having spherical morphology and a diameter of 2–3 μm were detected, with a hierarchical porous structure formed by the assembly of nano-sized sub-units homogeneously distributed over the whole microparticles. Such a hierarchical microstructure is very favorable for cathode materials because the primary nanoparticles can concurrently offer a large surface area for electrode–electrolyte contact and shorten the path for Li^+ diffusion [44–46]. Meanwhile, such a porous structure can effectively release the lattice strain and volume variation caused by the long period Li^+ intercalation/deintercalation reaction during the charge–discharge process.

To compare the electrochemical performance of these Ni-doped materials, they were initially cycled at 30 mA g^{-1} (0.1C) between 2 and 4.8 V for 150 cycles. As shown in **Figure 7.1b**, the discharge capacities increase in the first few cycles. However, the rate and extent of the capacity increase are significantly different from each other. Ni/3, Ni/4 and Ni/5 samples become fully activated and reach their maximum capacity in the 9^{th}, 35^{th} and 92^{th} cycle, respectively. For the Ni/6 sample, the capacity increased almost linearly in the first 150 cycles and reached 169 mAh g^{-1}. In contrast, for the samples of Ni/7 and the pure Li_2MnO_3, the capacities were almost unchanged and remained below 60 mAh g^{-1}, similar to the values reported under the same conditions [47, 48]. Apparently, higher amounts of Ni-doping can lead to a faster capacity increase. More interestingly, the best performance was observed in the Ni/5 composite with a medium-low level of Ni doping. A specific discharge capacity of 279.6 mAh g^{-1} could be achieved in the 100^{th} cycle and well retained (>95%) after 150 cycles. Such a high discharge capacity and cycling stability is competitive with—or even better than—those reported for materials with higher content of Ni-doping and extra surface coating [49, 50], offering the possibility of designing high energy Li-rich cathode materials with less Ni using uncomplicated procedures.

Figure 7.1c shows the first charge/discharge curves of all samples. Both the first charge and discharge capacities increased with increasing content of Ni doping. Specifically, it can be found that the charge curves were composed of two plateaus—one at 4.0–4.6 V and the other at 4.6–4.8 V, both of which are extended as the Ni content increases. The first one at 4.0–4.6 V can be attributed to the oxidation reaction of the Ni^{2+} and Ni^{3+} ions to Ni^{4+} (possibly also to minor amounts of residual Mn^{3+} ions), and extended as a result of increasing Ni content [29]. The second one above 4.6 V corresponds to the activation process of the Li_2MnO_3 phase that is generally considered to involve simultaneous O extraction from the crystal lattice, further Li^+ extraction and rearrangement of the

TM ions [16, 28, 29]. As the Ni content increased, this plateau was significantly stretched, indicating that more Li_2MnO_3 was activated in the first charging process. In addition, it is noted that as the Ni content increased, the capacity loss in the first cycle also increased. The Ni/3 sample showed the most serious capacity loss of 116 mAh g^{-1} in the first cycle, which is 23 mAh g^{-1} and 85 mAh g^{-1} higher than the values for the Ni/4 and Ni/5 sample, respectively. Such a high capacity loss can be attributed to the major structural evolution—including lattice O removal and TM ion rearrangement– during the Li_2MnO_3 activation of materials with large content of dopants [18, 29, 34, 48]. By checking the columbic efficiency of these materials in the first 150 cycles (**Fig. S7.2**, in the ESM), it can be seen that the efficiencies increased markedly in the 2^{nd} cycle and quickly reached ~100%, indicating that the extra capacity generated from the Li_2MnO_3 activation is almost 100% reversible from the 2^{nd} cycle onwards. It has been reported that a higher capacity can be achieved if the upper voltage limit for Li_2MnO_3 activation is reached in a stepwise manner over a few cycles, and the capacity loss is caused by the diffusion of TM ions into the Li^+ vacancies during the activation process [51]. Our results are consistent with these earlier results. The high efficiency from the 2^{nd} cycle onwards in our materials could be explained by the much smaller extent of Li_2MnO_3 activation in the subsequent cycles, which can significantly decrease the chance of Li^+ vacancies being occupied by the diffused TM ions.

XRD patterns of these materials after the first cycle are shown in **Figure 7.1d**. The weak diffraction peaks located between 20–25 ° that reflect the Li–Mn ordering in the TM ion layers become gradually weaker in the more highly Ni-doped materials and almost disappear for the Ni/3 electrode, further confirming the effect of Ni doping in promoting the Li_2MnO_3 activation.

From the above discussion, it can be deduced that the electrochemical behavior of these Li-rich materials is closely related to their Ni content. Therefore, simulation studies were conducted to compare Ni and a variety of neighboring TM ions in terms of their influence on the energy barriers of TM ion diffusion and the formation of O vacancies (**Fig. 7.2**). In most Li-rich cathode materials, the first charge can be generally divided into two regions [16, 49]. When the voltage is below 4.5 V, all the TM ions like Co^{3+}, Ni^{2+} are oxidized, with Li ions being simultaneously removed from the Li layers, leaving local empty octahedral sites. As the charging voltage is continuously raised over 4.5 V, the Li_2MnO_3 phase will be gradually activated. This complex high voltage process involves a few sub-reactions, including the diffusing of Li and TM ions from the TM ion layers to the Li layers, the removal of lattice O ions and further Li extraction. As the aim of this work is to study the effect of Ni on the Li_2MnO_3 activation process that only happens in the high voltage region with some local Li

vacancies in the Li layers, it is assumed in our simulation that the octahedral sites in the Li layers are empty [52].

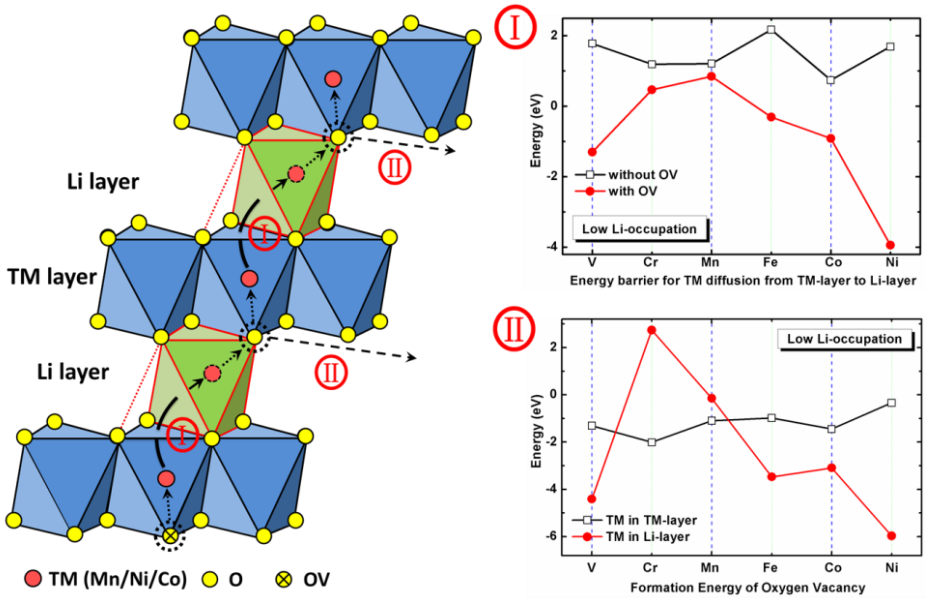

Figure 7.2 Schematic illustration of TM diffusion and formation of oxygen vacancies in Li-rich materials and the relevant energy barriers as the function of different TM ions.

In ideal pristine materials, no oxygen vacancies exist and TM ions only reside in their own layers. The energy barriers for the two sub-reactions of Li_2MnO_3 activation in this condition can be reflected by the white squares of the right hand side figures in **Figure 7.2**. Diffusion of both the Mn and Ni is very restricted and they have a very limited effect on the promotion of the formation of oxygen vacancies. This can explain why the un-doped Li_2MnO_3 sample and Ni/7 sample both had very small capacity. As it has been reported that the amount of Ni in the Li layer drops significantly as the total Ni content decreases [27, 31, 32], it is reasonable to infer that the Ni/7 and Li_2MnO_3 samples are close to the ideal model that has no TM ions in the Li layers, and therefore, only very limited capacity could be achieved in these two materials since almost no Li_2MnO_3 phase is being activated.

As the Ni content gradually increases, more Ni may exist in the Li layer. In this case, the energy barrier for the formation of oxygen vacancies drops significantly (from the white squares to the red spheres in **Fig. 7.2**) with a difference of about 6 eV. This is a huge change that will significantly promote oxygen removal. Like a chain reaction, the newly formed oxygen vacancies will in return help more Ni diffuse into the Li layers. As this process continues, a small increase in the Ni content may result into the activation of a large part of the Li_2MnO_3 phase. This assumption is in good agreement with the electrochemical performance of our Ni-doped materials. Although the

Ni/(Mn+Ni) ratio was varied within a narrow range between 12.5% (Ni/7) and 25% (Ni/3), the extent of activation of the Li_2MnO_3 was significantly enhanced from nearly zero (Ni/7) to almost fully complete in the first cycle (Ni/3). In addition, it should be mentioned here that no capacity increase with increasing number of cycles has been observed for most reported Ni-doped material systems [20, 25, 53], which—based on our results—could be explained by the high Ni/Mn ratio (equal to, or larger than, 1/3) in these cases, which enabled the Li_2MnO_3 phase to be activated mainly in the first charge.

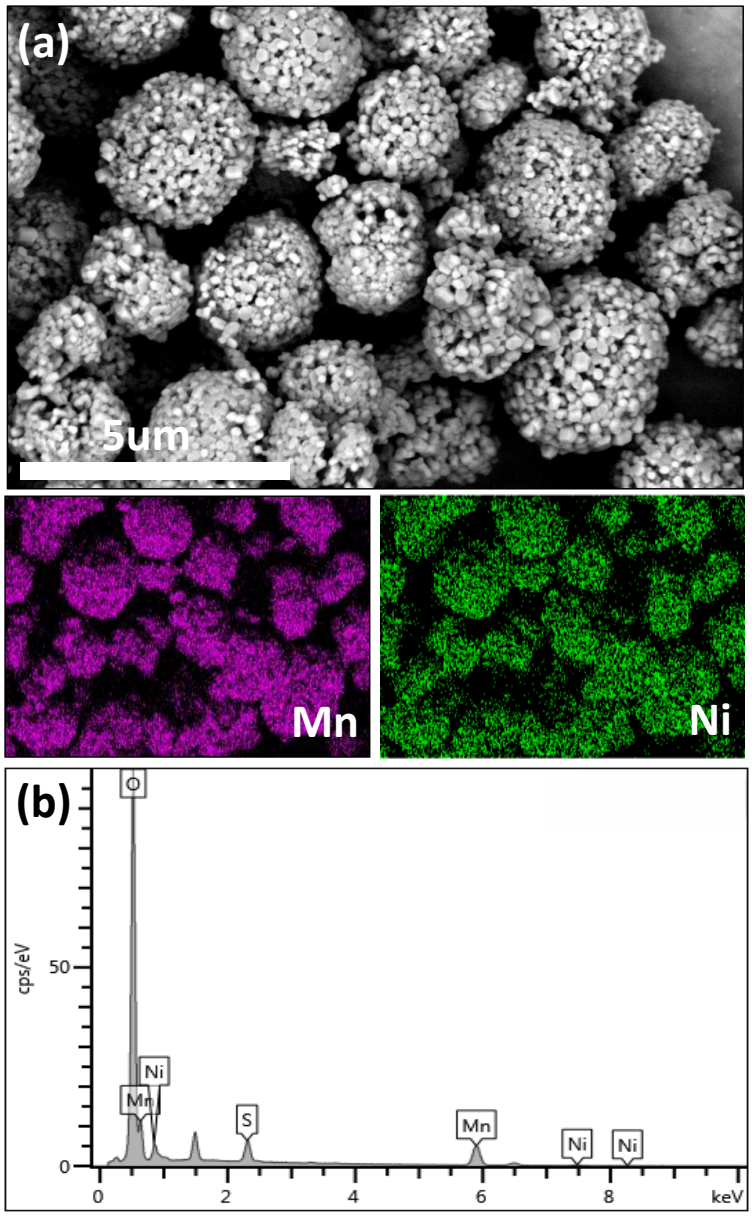

Figure 7.3 a) SEM image and corresponding EDS- mapping of Mn and Ni; b) and the related EDS spectra of the Ni/5 sample.

To further reveal sources of the superior electrochemical performance of the Ni/5 sample, more detailed analysis was conducted. Firstly, it can be found from the EDS-mapping (**Fig. 7.3**) that Ni and Mn elements are homogeneously distributed over the whole spherical matrix, demonstrating the uniform doping of Ni into the Li-rich material. A well-crystallized layered structure with typical layer distance of around 0.47 nm was revealed by the high resolution TEM image (**Fig. 7.4a**). The related electron diffraction pattern along the [010] axis confirms the clear monoclinic structure of the Ni/5 sample (**Fig. 7.4b**).

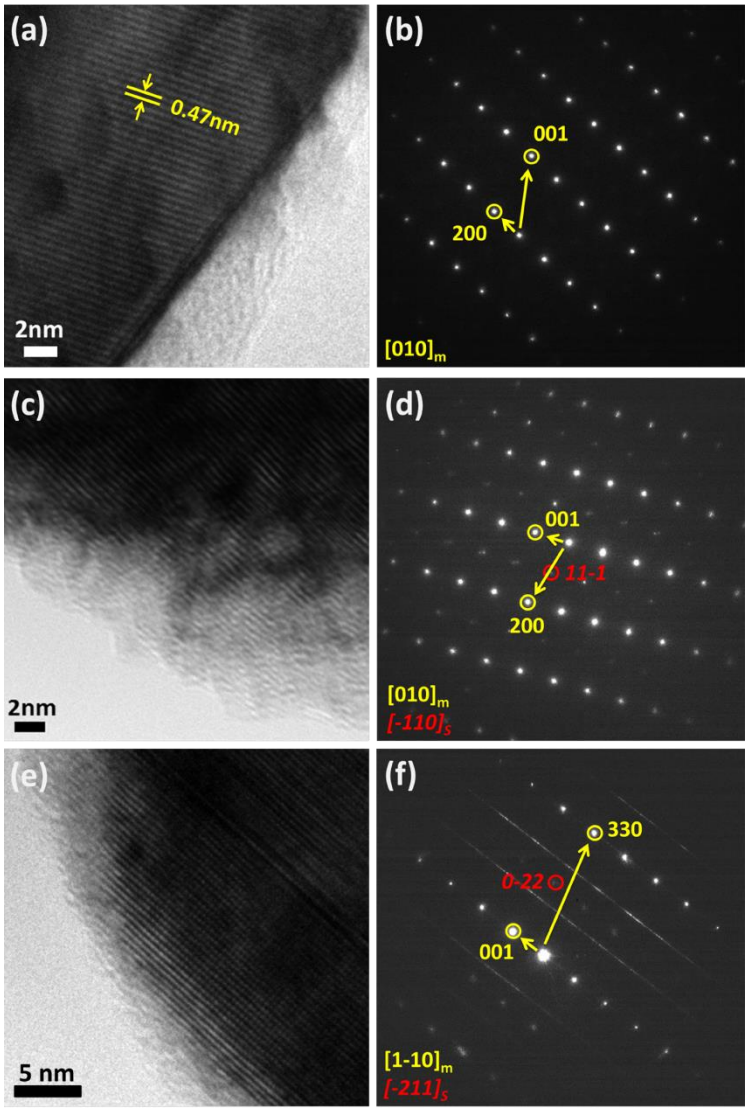

Figure 7.4 (a, b) HR-TEM image and the corresponding electron diffraction pattern along the $[010]_{mon}$ axis of the pristine Ni/5 sample; (c, d, e, f) HR-TEM images and the corresponding electron diffraction patterns along the $[010]_{mon}$ axis and $[1\text{-}10]_{mon}$ axis of the Ni/5 electrode after 100 electrochemical cycles.

As the Ni/5 sample was cycled for about 100 times to reach its maximum specific discharge capacity, the first 200 cycles of this sample are presented in **Figure 7.5a**, and demonstrate its good cycling stability. It is found that a high discharge capacity of more than 240 mAh g^{-1} was delivered by the Ni/5 sample in the 200th cycle. This value is about 86% of the peak capacity of 279.6 mAh g^{-1}, demonstrating the high rate of capacity retention of this material. Such a capacity retention ratio compares very favorably with those for most reported Li-rich cathode materials with Ni doping under similar testing conditions [25, 45, 54]. It should be mentioned that the long activation time of around 100 cycles may not be advantageous for practical application, although the activation period could be controlled by further modifying the activation parameters. For example, a broad cycling potential window or a changed current density can speed up the Li_2MnO_3 activation process [55]. Fortunately, these parameters can be altered manually during the electrochemical reactions to enhance the activation process and shorten the activation time. In addition, intentionally extending the high voltage charging period in the initial cycles, as shown below, could also be an effective way to tackle this problem.

Detailed charge/discharge plots of Ni/5 in different cycles are displayed in **Figure 7.5b**. It can be clearly seen that the 4.6–4.8 V charging plateau quickly faded after the first cycle and then quickly integrated with a long slope starting from around 3.6 V in the following cycles. This means a relatively high content of the Li_2MnO_3 phase was activated in the first cycle while the rest was gradually activated in a much reduced manner. The fast decline of the redox peaks located at around 4.8 V in the CV curves (**Fig. 7.5c**) further supports this varied manner of Li_2MnO_3 activation. In addition, a pair of flat charge and discharge plateaus centered at 3 V gradually evolved and finally became major feature in the first 150 cycles. This is also well reflected by the enlargement of the CV redox pairs at around 3 V, indicating that more Mn ions were involved in the electrochemical redox reactions and the structure was gradually transformed to the spinel phase [55–57]. Note that the discharge voltage plateau gradually declined over long term cycling of the Ni/5 sample (**Figs. 7.5b** and **7.5c**). This phenomenon of voltage drop has also been observed in other Li-rich cathode materials [58, 59] and has generally been attributed to the diffusion of the TM ions into the Li layers, which may alter the crystallographic site energy for Li^+ occupation and enhance the phase transformation of the original layered phase to the spinel-like phase. This problematic voltage decay is of interest and can possibly be addressed by further optimizing the composition and surface modification, which is currently under detailed investigation. Good rate performance of the Ni/5 sample after the initial activation process has also been demonstrated, as shown **in Figure S7.3** (in the ESM). High specific discharge capacities of about 260 mAh g^{-1}, 222 mAh g^{-1} and 182 mAh g^{-1}

were delivered at current densities of 60 mA g^{-1}, 150 mA g^{-1} and 300 mA g^{-1} respectively, which are competitive with other Li-rich cathode materials with higher contents of Ni [54, 57].

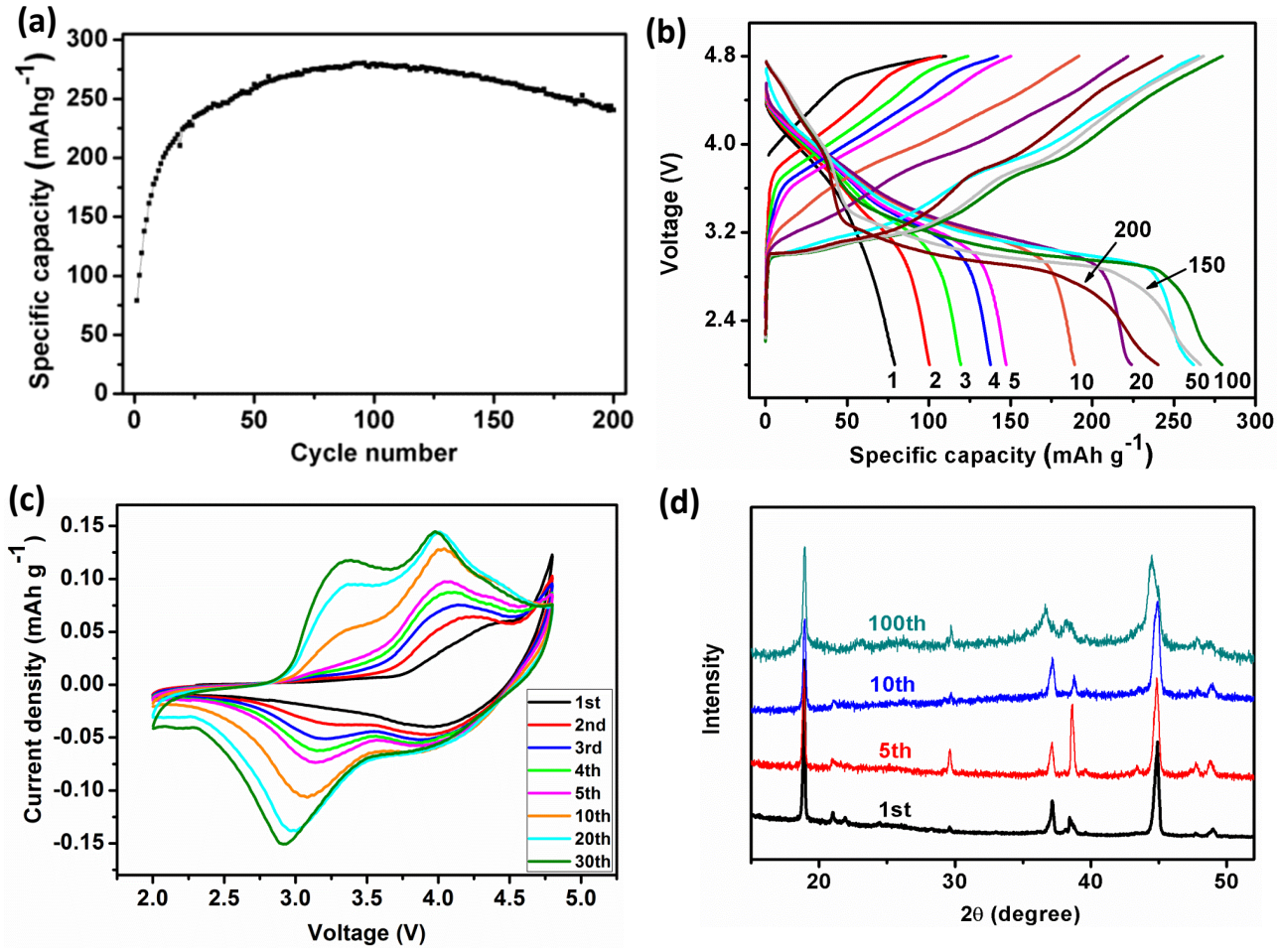

Figure 7.5 (a) Cycling performance of the Ni/5 material in the first 200 cycles at 30 mA g^{-1} between 2-4.8 V; (b) and the corresponding charge/discharge curves of typical cycles; (c) CV curves of Ni/5 in different cycles at a scan rate of 0.02 mV s^{-1}; (d) XRD patterns of the Ni/5 electrodes after different cycles.

Ex situ XRD patterns of the Ni/5 electrodes after different cycles are shown in **Figure 7.5d**. It can be seen that the intensities of the characteristic peaks of Li_2MnO_3 at around 20–25 °gradually decreased upon cycling and the peaks totally disappeared after 100 cycles, further confirming the gradual consumption of the Li_2MnO_3 component. In addition, comparing the HR-TEM images and related electron diffractions of the pristine Ni/5 sample and the electrode after 100 cycles (**Fig. 7.4**), reticulate patterns embedded on the pristine parallel lattice and new spots associated with the spinel phase were observed in the cycled samples along both the $[010]_{mon}$ and $[1\bar{1}0]_{mon}$ axes, strongly indicating that a new spinel phase, based on the parent layered structure, had been generated. This is

consistent with the long 3 V discharge plateau and 3 V CV peak, which were also observed in other reported Li-rich materials as characteristic features of a defect spinel phase [15, 40, 50, 60]. The Electrochemical impedance spectroscopy (EIS) measurements of the Ni/5 material were also conducted (**Fig. S7.4**, in the ESM). It was found that the charge transfer resistance, that is related to the charge transfer on the electrode/electrolyte interface, gradually decreased during the activation process [61, 62]. This trend is in good agreement with the fact that more Li^+ is involved in the electrochemical reactions as the capacity increases during the activation process.

It is worth mentioning that the first charge plateau at 4.6–4.8 V in Ni/5 is much shorter than that for the Ni/3 and Ni/4 materials. This plateau quickly declined and vanished after the 5^{th} cycle. It is well-known that this plateau indicates an oxygen-releasing reaction in Li-rich cathode materials, and the length is in proportion to the amount of O_2 generation [16, 27, 29, 63]. Therefore, it can be inferred that the O_2 generated in the Ni/5 material is much less than that for the Ni/3 and Ni/4 materials. As O_2 accumulation in batteries may bring safety concerns, some techniques such as surface coating or incorporating additives in the electrolyte have been adopted to eliminate the O_2 release [64, 65]. However, these complex approaches are time-consuming and expensive, which severely restricts their practical applications. Since our Ni/5 sample has the intrinsic property of producing much less O_2, it may bring us one step closer to a safer and cheaper Li-rich battery system.

Based on the above discussion, the fact that Ni/5 shows the highest capacity has two possible origins. On the one hand, sufficient content of Ni doping is critical to fully activate the Li-rich phase in the first few cycles. On the other hand, too much Ni-doping may lead to excessive activation and consequently, a big capacity loss in the first cycle. Therefore, the optimized Ni/5 sample may benefit from its balanced level of Ni-doping and make maximum use of the capacity originating from the Li_2MnO_3 activation.

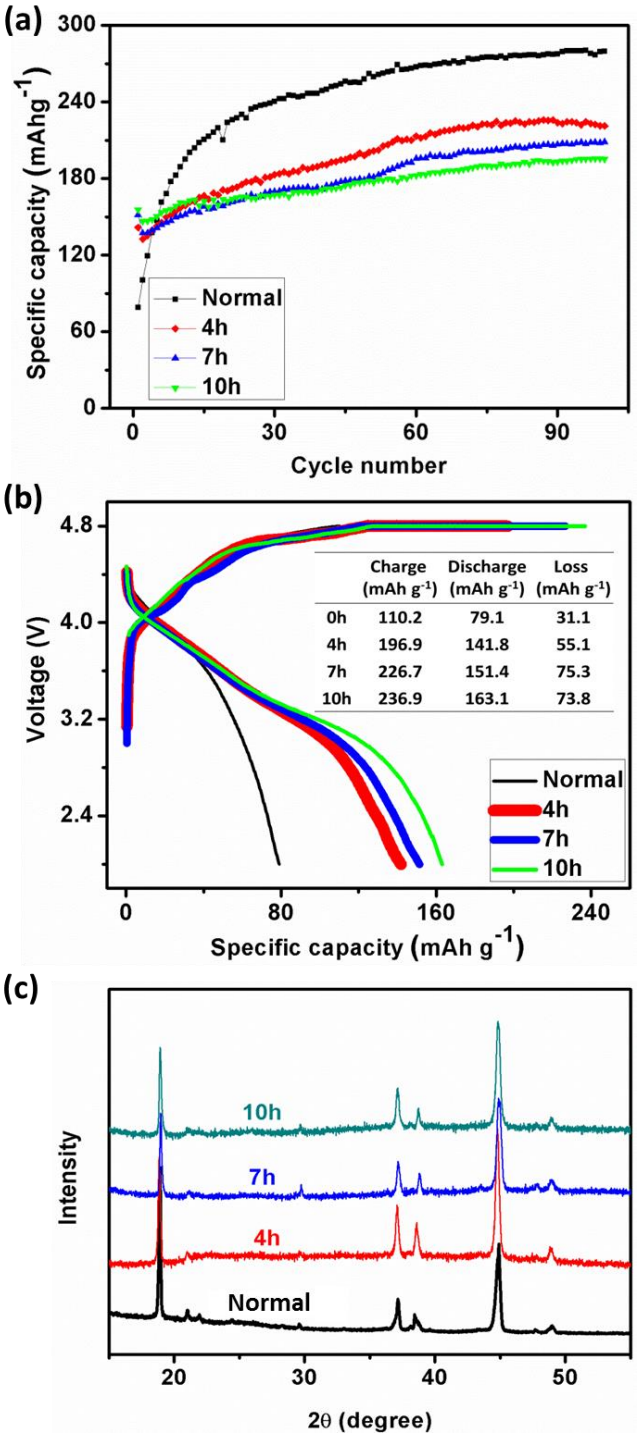

Figure 7.6 a) Cycling performance and b) first charge/discharge curves of the Ni/5 electrode and its c) XRD patterns after the first cycle without or with extended 4, 7 or 10h of 4.8 V constant-voltage charging in the first cycle, respectively.

We hypothesize that excessive activation of Li_2MnO_3 in the first cycle may lead to large capacity loss due to the large-scale structure change and TM ion rearrangement. To test this hypothesis, we intentionally extended the activation time of the Ni/5 sample in the first cycle. That is, after the

normal constant current charge to 4.8 V, the samples were continuously charged at 4.8 V for 4 h, 7 h and 10 h respectively, followed by normal cycles. Initially, it can be clearly seen from **Figure 7.6a** that the maximum capacity of the Ni/5 sample was significantly reduced after 4 h constant high-voltage charging in the first cycle. Then, it further decreased as the holding time lasted even longer. In addition, although all these over-charged electrodes still experienced a capacity increase in the subsequent cycles, the trend was much less marked than for the normal one. On the other hand, comparing the first charge and discharge curves only (**Fig. 7.6b**), it is found that both the charge and discharge capacities increased with prolonged 4.8 V charging. Meanwhile, the capacity loss in the first cycle was simultaneously enlarged as well.

All these observations support our hypothesis: during the extended 4.8 V charging process in the first cycle, much more Li_2MnO_3 phase was activated and consumed, leading to larger first charge/discharge capacity; meanwhile, as the Li_2MnO_3 activation becomes greater, more TM ions may diffuse and occupy the Li vacancies, resulting in a larger capacity loss. The accumulated lattice strain and extensive lattice O extraction associated with the large-scale Li_2MnO_3 activation process may increase the capacity loss even further. Therefore, in order to obtain a high specific capacity and suppress the capacity loss, aggressive activation of the Li_2MnO_3 phase in the first charge should be avoided in these materials.

The electrodes of the Ni/5 sample after the first cycle with different durations of 4.8 V charging were characterized by XRD (**Fig. 7.6c**). The intensity of the *C*2/*m* peaks at 20–25 °significantly decreased after holding the sample at 4.8 V charging for a few hours, providing structural evidence of the continuous activation of Li_2MnO_3 during this period. It should be noted that the intensity of these small peaks are not greatly further changed or disappeared when the 4.8 V charging of the Ni/5 electrode was further prolonged from 4 h to 7 h or 10 h. From **Figure 7.6b**, it can also be found that the increase in charge capacity from 4 h to 10 h was very small and less than half of that from 0 h to 4 h. This implies that 4 h charging at 4.8 V may be long enough to consume the majority of the Li_2MnO_3 phase.

Based on the above discussion, the relationship between the electrochemical behavior, Ni content and structure evolution of these Li-rich cathode materials can be summarized, as shown in Scheme 1. In high content Ni-doped materials (Condition I), the majority of the Li_2MnO_3 phase will be used in the first cycle, leading to large scale structure change and associated atomic rearrangement. As a result, much of the capacity obtained from the Li_2MnO_3 activation then becomes irreversible. Conversely, in Li-rich materials with very low content of Ni or even no Ni (Condition III), the

Li_2MnO_3 cannot be activated effectively and the specific capacity will stay low. Here in our series of Ni-doped Li-rich composites, in terms of the specific capacity, a material with a medium-low level of Ni-doping (Condition II) is favorable to kinetically activate the Li_2MnO_3 at a reasonable rate and—more importantly—limit the large capacity loss in the first cycle.

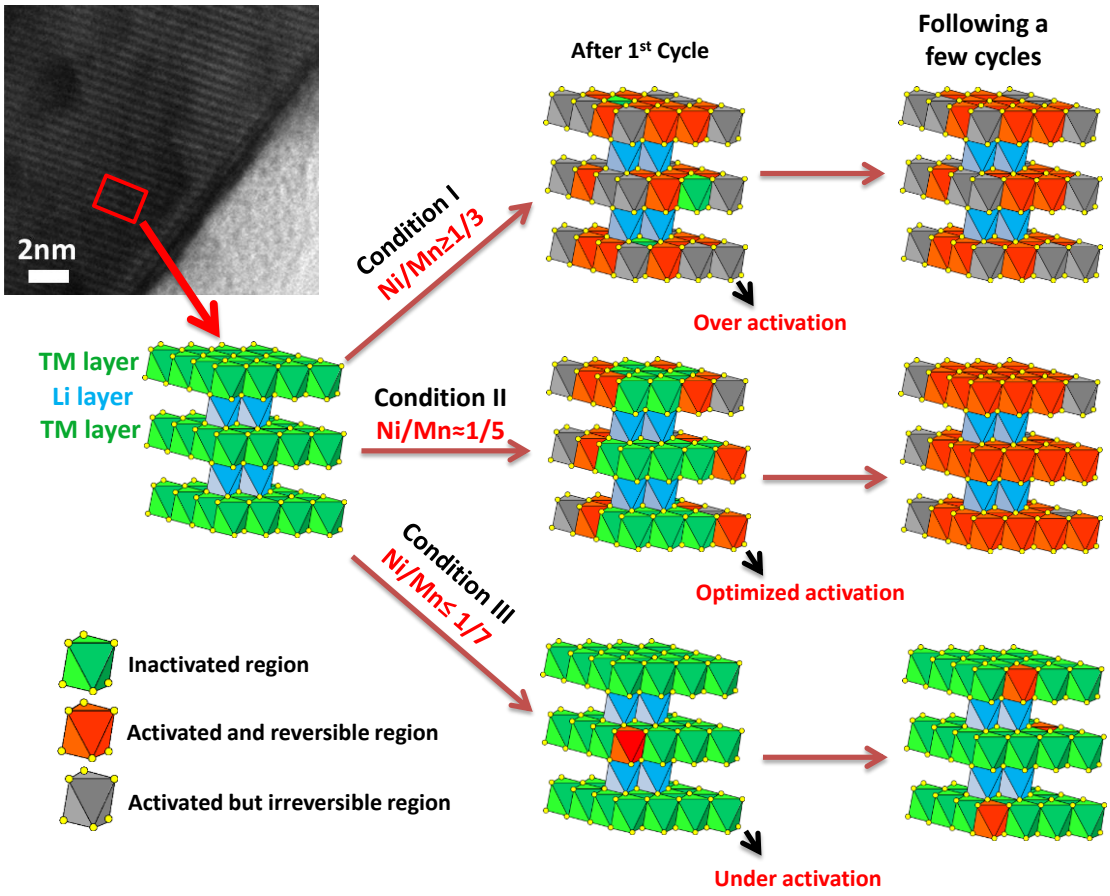

Figure 7.7 Effect of over activation, optimized activation and under activation of the Li_2MnO_3 phase on the structure evolution and electrochemical behaviours of layered Li-rich materials depending on the content of Ni.

7.5 Conclusions

The composition, microstructure and electrochemical properties of a series of Ni-poor Li-rich cathode materials with the composition $Li[Li_{1/3-2\ x/3}Mn_{2/3-x/3}Ni_x]O_2$ ($0.09 \leq x \leq 0.2$) have been systematically investigated in an attempt to obtain high performance Li-rich cathode materials for LIBs. Compared to traditional Li-rich Li–Mn–Ni–O material systems with high Ni-doping content, our Li-rich cathode materials with optimized low content of Ni exhibited an unusual specific

capacity increase in the first dozens of cycles due to the continuous activation of the Li_2MnO_3 phase upon cycling. Combining our experimental and computational results revealed that the Ni-doping can significantly promote the Li_2MnO_3 activation and provide extra specific capacity. However, excessive Ni-doping can lead to the undesirable excessive activation of the Li_2MnO_3 phase, with an associated substantial capacity loss, in the first cycle. As a result, the content of Ni in our low Ni Li-rich material systems was optimized in order to achieve a superior specific capacity (~280 mAh g^{-1}) and good cycling stability at room temperature. This work can not only provide new insights into the fundamental understanding of the reaction mechanisms for Li-rich Li–Mn–Ni–O material systems, but also shed light on the design of cheaper and safer high-energy cathode materials for new generation LIBs.

7.6 References

1. Armand, M. and J.-M. Tarascon, *Building better batteries*. Nature, 2008. **451**(7179): p. 652-657.
2. Dunn, B., H. Kamath, and J.-M. Tarascon, *Electrical energy storage for the grid: A battery of choices*. Science, 2011. **334**(6058): p. 928-935.
3. Liu, J., *Addressing the grand challenges in energy storage*. Adv. Funct. Mater., 2013. **23**(8): p. 924-928.
4. Chan, C.K., et al., *Solution-grown silicon nanowires for lithium-ion battery anodes*. ACS nano, 2010. **4**(3): p. 1443-1450.
5. Jeong, G., et al., *Core-Shell Structured Silicon Nanoparticles@TiO_{2-x}/Carbon Mesoporous Microfiber Composite as a Safe and High-Performance Lithium-Ion Battery Anode*. ACS nano, 2014. **8**(3): p. 2977-2985.
6. Kim, J.-G., et al., *Controlled Ag-driven superior rate-capability of $Li_4Ti_5O_{12}$ anodes for lithium rechargeable batteries*. Nano Res., 2013. **6**(5): p. 365-372.
7. Luo, B., et al., *Graphene-Confined Sn Nanosheets with Enhanced Lithium Storage Capability*. Adv. Mater., 2012. **24**(26): p. 3538-3543.
8. Luo, B., et al., *Reduced Graphene Oxide-Mediated Growth of Uniform Tin-Core/Carbon-Sheath Coaxial Nanocables with Enhanced Lithium Ion Storage Properties*. Adv. Mater., 2012. **24**(11): p. 1405-1409.
9. Wang, H., et al., *Mn_3O_4-graphene hybrid as a high-capacity anode material for lithium ion batteries*. J. Am. Chem. Soc., 2010. **132**(40): p. 13978-13980.

10. Wang, D., et al., *Self-assembled TiO_2-graphene hybrid nanostructures for enhanced Li-ion insertion*. ACS nano, 2009. **3**(4): p. 907-914.
11. Goodenough, J.B., *Electrochemical energy storage in a sustainable modern society*. Energy Environ. Sci., 2014. **7**(1): p. 14-18.
12. Aricò, A.S., et al., *Nanostructured materials for advanced energy conversion and storage devices*. Nat. Mater., 2005. **4**(5): p. 366-377.
13. Xiao, X., J. Lu, and Y. Li, *$LiMn_2O_4$ microspheres: Synthesis, characterization and use as a cathode in lithium ion batteries*. Nano Res., 2010. **3**(10): p. 733-737.
14. Armstrong, M.J., et al., *Evaluating the performance of nanostructured materials as lithium-ion battery electrodes*. Nano Res., 2014. **7**(1): p. 1-62.
15. Johnson, C., et al., *Lithium-manganese oxide electrodes with layered-spinel composite structures xLi_2MnO_3 $(1-x)Li_{1+y}Mn_{2-y}O_4$ $(0< x< 1,\ 0\leq y\leq 0.33)$ for lithium batteries*. Electrochem. Commun., 2005. **7**(5): p. 528-536.
16. Thackeray, M.M., et al., *Li_2MnO_3-stabilized $LiMO_2$ (M = Mn, Ni, Co) electrodes for lithium-ion batteries*. J. Mater. Chem., 2007. **17**(30): p. 3112-3125.
17. Bareno, J., et al., *Local Structure of Layered Oxide Electrode Materials for Lithium-Ion Batteries*. Adv. Mater., 2010. **22**(10): p. 1122-1127.
18. Boulineau, A., et al., *Evolutions of $Li_{1.2}Mn_{0.61}Ni_{0.18}Mg_{0.01}O_2$ during the Initial Charge/Discharge Cycle Studied by Advanced Electron Microscopy*. Chem. Mater., 2012. **24**(18): p. 3558-3566.
19. Yu, H., et al., *Direct Atomic-Resolution Observation of Two Phases in the $Li_{1.2}Mn_{0.567}Ni_{0.166}Co_{0.067}O_2$ Cathode Material for Lithium-Ion Batteries*. Angew. Chem., Int. Ed., 2013. **52**(23): p. 5969-5973.
20. Lu, Z., et al., *Synthesis, Structure, and Electrochemical Behavior of $Li[Ni_xLi_{1/3-2x/3}Mn_{2/3-x/3}]O_2$*. J. Electrochem. Soc., 2002. **149**(6): p. A778-A791.
21. Yoon, W.-S., et al., *Local structure and cation ordering in O_3 lithium nickel manganese oxides with stoichiometry $Li[Ni_xMn_{(2-x)/3}Li_{(1-2x)/3}]O_2$ NMR studies and first principles calculations*. Electrochem. Solid-State Lett., 2004. **7**(7): p. A167-A171.
22. Bréger, J., et al., *High-resolution X-ray diffraction, DIFFaX, NMR and first principles study of disorder in the Li_2MnO_3-$Li[Ni_{1/2}Mn_{1/2}]O_2$ solid solution*. J. Solid State Chem., 2005. **178**(9): p. 2575-2585.
23. Park, S.-H., et al., *Lithium-manganese-nickel-oxide electrodes with integrated layered-spinel structures for lithium batteries*. Electrochem. Commun., 2007. **9**(2): p. 262-268.

24. Lei, C., et al., *Local structure and composition studies of $Li_{1.2}Ni_{0.2}Mn_{0.6}O_2$ by analytical electron microscopy*. J. Power Sources, 2008. **178**(1): p. 422-433.
25. Fell, C.R., et al., *Synthesis-Structure-Property Relations in Layered, "Li-excess" Oxides Electrode Materials $Li[Li_{1/3-2x/3}Ni_xMn_{2/3-x/3}]O_2$ (x = 1/3, 1/4, and 1/5)*. J. Electrochem. Soc., 2010. **157**(11): p. A1202-A1211.
26. Gao, M., et al., *Synthesis and electrochemical performance of long lifespan Li-rich $Li_{1+x}(Ni_{0.37}Mn_{0.63})_{1-x}O_2$ cathode materials for lithium-ion batteries*. Electrochim. Acta, 2013. **95**(Complete): p. 87-94.
27. Jarvis, K.A., et al., *The role of composition in the atomic structure, oxygen loss, and capacity of layered Li-Mn-Ni oxide cathodes*. J. Mater. Chem. A, 2014. **2**(5): p. 1353-1362.
28. Xu, B., et al., *Identifying surface structural changes in layered Li-excess nickel manganese oxides in high voltage lithium ion batteries: A joint experimental and theoretical study*. Energy Environ. Sci., 2011. **4**(6): p. 2223-2233.
29. Armstrong, A.R., et al., *Demonstrating oxygen loss and associated structural reorganization in the lithium battery cathode $Li[Ni_{0.2}Li_{0.2}Mn_{0.6}]O_2$*. J. Am. Chem. Soc., 2006. **128**(26): p. 8694-8698.
30. Schougaard, S.B., et al., *$LiNi_{0.5+\delta}Mn_{0.5-\delta}O_2$ A High-Rate, High-Capacity Cathode for Lithium Rechargeable Batteries*. Adv. Mater., 2006. **18**(7): p. 905-909.
31. Lu, Z., Z. Chen, and J. Dahn, *Lack of Cation Clustering in $Li[Ni_xLi_{1/3-2x/3}Mn_{2/3-x/3}]O_2$ ($0< x\leq 1/2$) and $Li[Cr_xLi_{(1-x)/3}Mn_{(2-2x)/3}]O_2$ ($0< x< 1$)*. Chem. Mater., 2003. **15**(16): p. 3214-3220.
32. Meng, Y., et al., *Cation Ordering in Layered O_3 $Li[Ni_xLi_{1/3-2x/3}Mn_{2/3-x/3}]O_2$ ($0\leq x\leq 1/2$) Compounds*. Chem. Mater., 2005. **17**(9): p. 2386-2394.
33. Lu, Z., D. MacNeil, and J. Dahn, *Layered cathode materials $Li[Ni_xLi_{(1/3-2x/3)}Mn_{(2/3-x/3)}]O_2$ for lithium-ion batteries*. Electrochemical and Solid-State Letters, 2001. **4**(11): p. A191-A194.
34. Lu, Z. and J.R. Dahn, *Understanding the anomalous capacity of $Li/Li[Ni_xLi_{(1/3-2x/3)}Mn_{(2/3-x/3)}]O_2$ cells using in situ X-ray diffraction and electrochemical studies*. J. Electrochem. Soc., 2002. **149**(7): p. A815-A822.
35. Perdew, J.P., K. Burke, and M. Ernzerhof, *Generalized gradient approximation made simple*. Phys. Rev. Lett., 1996. **77**(18): p. 3865-3868.
36. Blöchl, P.E., *Projector augmented-wave method*. Phys. Rev. B, 1994. **50**(24): p. 17953.
37. Kresse, G. and D. Joubert, *From ultrasoft pseudopotentials to the projector augmented-wave method*. Phys. Rev. B, 1999. **59**(3): p. 1758.

38. Anisimov, V.I., J. Zaanen, and O.K. Andersen, *Band theory and Mott insulators: Hubbard U instead of Stoner I*. Phys. Rev. B, 1991. **44**(3): p. 943.
39. Chevrier, V.L., et al., *Hybrid density functional calculations of redox potentials and formation energies of transition metal compounds*. Phys. Rev. B, 2010. **82**(7): p. 075122.
40. Hinuma, Y., et al., *Phase transitions in the $LiNi_{0.5}Mn_{0.5}O_2$ system with temperature*. Chem. Mater., 2007. **19**(7): p. 1790-1800.
41. Kang, S.-H., et al., *Interpreting the structural and electrochemical complexity of $0.5Li_2MnO_3$ $0.5LiMO_2$ electrodes for lithium batteries ($M = Mn_{0.5-x}Ni_{0.5-x}Co_{2x}$, $0 \leq x \leq 0.5$).* J. Mater. Chem. 2007. **17**(20): p. 2069-2077.
42. Bréger, J., et al., *High-resolution X-ray diffraction, DIFFaX, NMR and first principles study of disorder in the Li_2MnO_3–$Li[Ni_{1/2}Mn_{1/2}]O_2$ solid solution.* J. Solid State Chem., 2005. **178**(9): p. 2575-2585.
43. Jarvis, K.A., et al., *Atomic Structure of a Lithium-Rich Layered Oxide Material for Lithium-Ion Batteries: Evidence of a Solid Solution*. Chem. Mater., 2011. **23**(16): p. 3614-3621.
44. He, X., et al., *Enhanced electrochemical performance in lithium ion batteries of a hollow spherical lithium-rich cathode material synthesized by a molten salt method*. Nano Res., 2014. **7**(1): p. 110-118.
45. Denis, Y., et al., *Electrochemical activities in Li_2MnO_3*. J. Electrochem. Soc., 2009. **156**(6): p. A417-A424.
46. Shi, S., et al., *Hollow $Li_{1.2}Mn_{0.5}Co_{0.25}Ni_{0.05}O_2$ microcube prepared by binary template as a cathode material for lithium ion batteries.* J. Power Sources, 2014. **257**: p. 198-204.
47. Denis, Y., et al., *Electrochemical activities in Li_2MnO_3.* J. Electrochem. Soc., 2009. **156**(6): p. A417-A424.
48. Robertson, A.D. and P.G. Bruce, *Mechanism of electrochemical activity in Li_2MnO_3*. Chem. Mater., 2003. **15**(10): p. 1984-1992.
49. Wang, R., et al., *Atomic Structure of Li_2MnO_3 after Partial Delithiation and Re-Lithiation*. Adv. Energy Mater., 2013. **3**(10): p. 1358-1367.
50. Sun, Y.K., et al., *The Role of AlF_3 Coatings in Improving Electrochemical Cycling of Li-Enriched Nickel-Manganese Oxide Electrodes for Li-Ion Batteries*. Adv. Mater., 2012. **24**(9): p. 1192-1196.
51. van Bommel, A., L. Krause, and J. Dahn, *Investigation of the irreversible capacity loss in the lithium-rich oxide $Li[Li_{1/5}Ni_{1/5}Mn_{3/5}]O_2$*. J. Electrochem. Soc., 2011. **158**(6): p. A731-A735.

52. Lee, J., et al., *Unlocking the Potential of Cation-Disordered Oxides for Rechargeable Lithium Batteries*. Science, 2014. **343**(6170): p. 519-522.
53. Ohzuku, T., et al., *High-capacity lithium insertion materials of lithium nickel manganese oxides for advanced lithium-ion batteries: toward rechargeable capacity more than 300 mAh* g^{-1}. J. Mater. Chem., 2011. **21**(27): p. 10179-10188.
54. Lee, H.J. and Y.J. Park, *Synthesis of Li* $[Ni_{0.2}Li_{0.2}Mn_{0.6}]O_2$ *nano-particles and their surface modification using a polydopamine layer*. J. Power Sources, 2013. **244**: p. 222-233.
55. Ye, D., et al., *Capacity-controllable Li-rich cathode materials for lithium-ion batteries*. Nano Energy, 2014. **6**: p. 92-102.
56. Croy, J.R., et al., *Countering the Voltage Decay in High Capacity* xLi_2MnO_3 *(1-x)*$LiMO_2$ *Electrodes (M = Mn,Ni, Co) for* Li^+ *Ion Batteries*. J. Electrochem. Soc., 2012. **159**(6): p. A781-A790.
57. Martha, S.K., et al., *Electrochemical and rate performance study of high-voltage lithium-rich composition:* $Li_{1.2}Mn_{0.525}Ni_{0.175}Co_{0.1}O_2$. J. Power Sources, 2012. **199**: p. 220-226.
58. Lee, E.-S. and A. Manthiram, *Smart design of lithium-rich layered oxide cathode compositions with suppressed voltage decay*. J. Mater. Chem. A, 2014. **2**(11): p. 3932-3939.
59. Croy, J.R., et al., *Examining Hysteresis in Composite* xLi_2MnO_3 *(1–x)*$LiMO_2$ *Cathode Structures.* J. Phys. Chem. C, 2013. **117**(13): p. 6525-6536.
60. Gu, M., et al., *Formation of the spinel phase in the layered composite cathode used in Li-ion batteries*. Acs Nano, 2012. **7**(1): p. 760-767.
61. Toprakci, O., et al., *Synthesis and characterization of* xLi_2MnO_3 *(1-x)* $LiMn_{1/3}Ni_{1/3}Co_{1/3}O_2$ *composite cathode materials for rechargeable lithium-ion batteries.* J. power sources, 2013. **241**: p. 522-528.
62. Dong, X., et al., *Sodium substitution for partial lithium to significantly enhance the cycling stability of* Li_2MnO_3 *cathode material.* J. power sources, 2013. **243**: p. 78-87.
63. Rana, J., et al., *Structural Changes in* Li_2MnO_3 *Cathode Material for Li-Ion Batteries.* Adv. Energy Mater., 2014. **4**(5).
64. Lee, K.T., S. Jeong, and J. Cho, *Roles of surface chemistry on safety and electrochemistry in lithium ion batteries*. Acc. Chem. Res., 2012. **46**(5): p. 1161-1170.
65. Park, K.-S., et al., *Suppression of* O_2 *evolution from oxide cathode for lithium-ion batteries:* VO_x*-impregnated* $0.5Li_2MnO_3$-$0.5LiNi_{0.4}Co_{0.2}Mn_{0.4}O_2$ *cathode*. Chem. Commun., 2010. **46**(23): p. 4190-4192.

7.7 Supporting Information

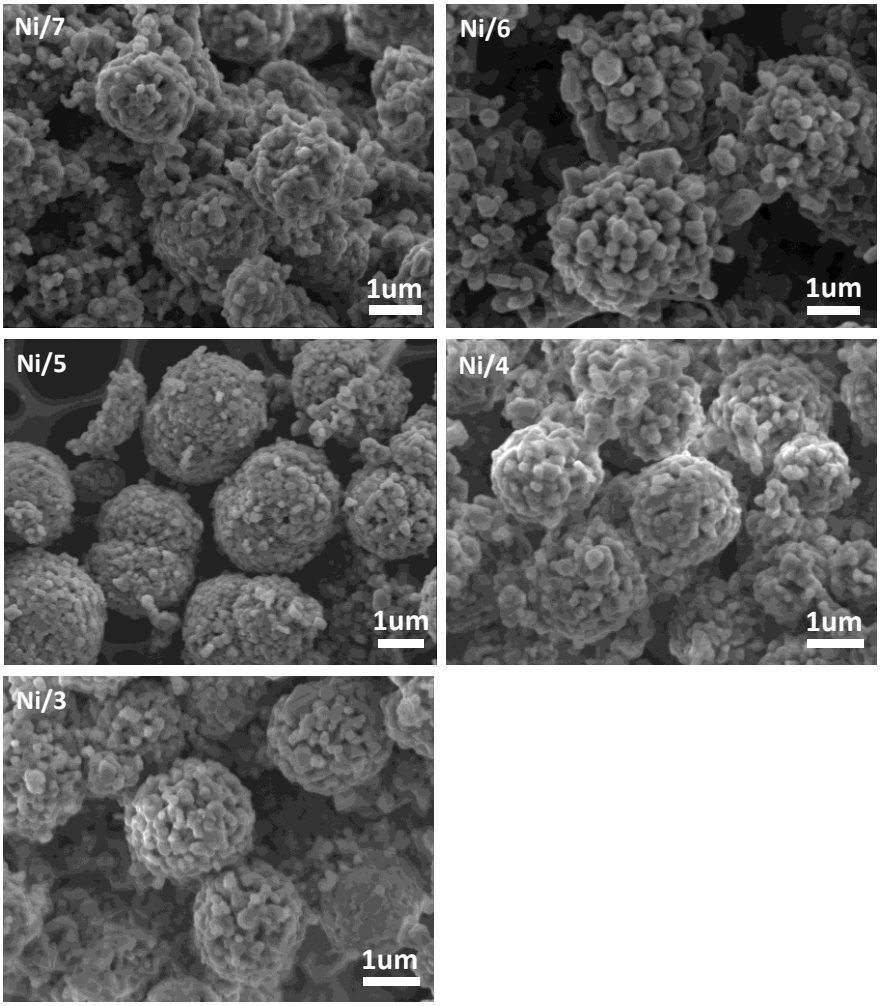

Figure S7.1 FE-SEM of all the Ni-doped cathode materials

Table S7.1 The nominal and experimental mole ratios of Mn/Ni and Li/(Mn+Ni) of the $Li[Ni_xLi_{1/3-2x/3}Mn_{2/3-x/3}]O_2$ materials

sample	Mn : Ni		Li : (Mn+Ni)	
	Nominal	experimental	Nominal	experimental
Ni/7	7	6.81	1.75	1.66
Ni/6	6	5.92	1.7	1.62
Ni/5	5	4.93	1.65	1.62
Ni/4	4	4.02	1.61	1.56
Ni/3	3	2.95	1.5	1.48

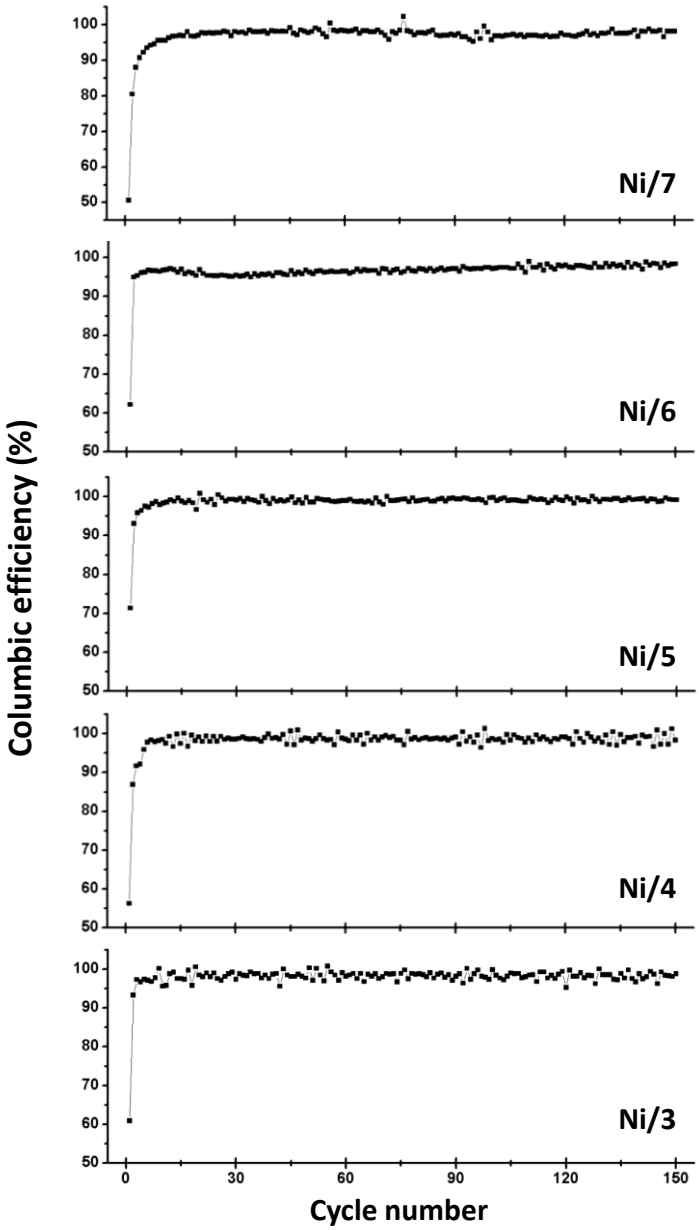

Figure S7.2 Columbic efficiencies of all the Ni-doped samples in the first 150 cycles

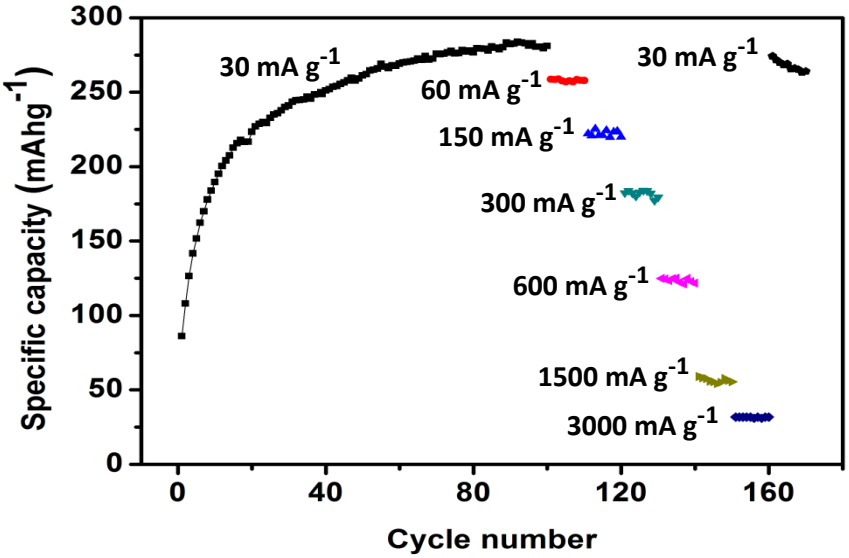

Figure S7.3 Rate performance of the Ni/5 sample after activation at 30 mA g^{-1} for 100 cycles

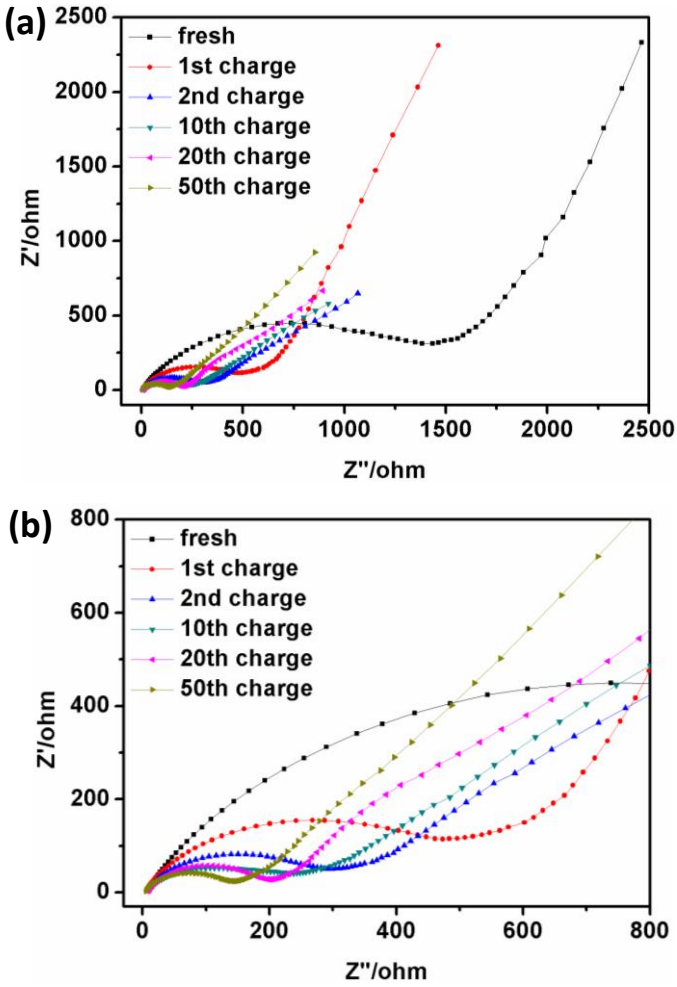

Figure S7.4 (a) Nyquist plots of the Ni/5 sample and (b) its enlargement before and after different activation cycles at the charge state of 4.5 V.

8. Revealing the migration consequence of O and Mn in artificially retarded Li_2MnO_3 activation

8.1 Abstract

Li-rich layered cathode materials have been considered as a family of promising high-energy density cathode materials for next generation LIBs. In this work, we report an interesting Ni-less Li-rich cathode material $Li_{1.87}Mn_{0.94}Ni_{0.19}O_3$ showing continuous capacity increase over cycles. It is due to a retarded Li_2MnO_3 phase activation process induced by the content of Ni doping and offers a unique platform to investigate the intermediate state of the Li_2MnO_3 activation process. Combining the powerful synchrotron in-situ X-ray diffraction analysis and advanced scanning transmission electron microscopy observation with a high angle annular dark field detector, it has been revealed that during the Li_2MnO_3 activation process, the O_2 generation sub-reaction may possess a much faster kinetics over the transition metal diffusion sub-reaction, as a result, the latter plays a key role in finalising the Li_2MnO_3 activation process and leads to the gradual phase transformation of the parent layered monoclinic phase to a 3 V defect cubic spinel phase and the step-wise capacity increase over cycles.

8.2 Introduction

In the past decade, electric vehicles (EVs) have made significant progress and been commercialized successfully as a response to the global fossil energy crisis of the 21th century and the corresponding serious environmental problems. However, the price of EVs is still a large barrier to replace the traditional internal-combustion engine based cars mainly due to the lack of a cheap and high-energy battery. LIBs are the most popular power sources for portable electronics and have been generally considered as the most potential one to power EVs [1-3]. Currently, numerous novel anode materials with superior specific capacity of more than 1000 mAh g^{-1} and high power density have been developed for LIBs [4-6] ; however, the specific capacities of the traditional cathode materials such as $LiCoO_2$, $LiFePO_4$ and $LiMn_2O_4$ are rather limited to match the anode [7].

Li-rich layered cathode materials have attracted much recent attention due to their extraordinary high specific capacity of more than 250 mAh g^{-1} at room temperature. Generally, they are described as $xLi_2MnO_3 \cdot (1-x)LiMO_2$ (M = Mn, Ni, Co or their mixture), in which the Li_2MnO_3 can be activated by high voltage charging to provide the extra capacity [8]. To meet the demand of practical applications, there are still significant challenges for the Li-rich cathode materials including the poor long-term cycling stability, low power density and voltage decline; and more importantly, the fundamental understandings of the electrochemical reactions and the corresponding crystal structure evolutions are still not fully revealed due to the complexity of compositions and structures [9, 10].

Li-rich materials within the Li-Ni-Mn-O system are favourable because of the absence of expensive and toxic Co. Among them, the $Li_{1.2}Mn_{0.6}Ni_{0.2}O_2$ material has been well studied as a representative composition [11, 12]. It is featured with a flat and long charging plateau from around 4.5 V to 4.8 V in the first charge. Activation of the Li_2MnO_3 phase has been demonstrated as the intrinsic reason for such a long plateau which involves a few sub reactions including Li extraction from both the Li and the TM layers, oxygen release from the crystal lattice and the TM ions diffusion [12-14]. However, as the Li_2MnO_3 phase is often completely activated in the first cycle, it is difficult to investigate these sub-reactions independently. In most cases, they are basically considered to occur simultaneously as a whole [15]. In our recent work, some Li-Ni-Mn-O Li-rich materials with unusual low-content of Ni showed interesting phenomenon of gradual capacity increase over cycling due to the retarded and continuous activation of the Li_2MnO_3 phase [16, 17]. Therefore, the Li_2MnO_3 activation process was incomplete in the initial cycles, providing an excellent platform to study the intermediate phase and sub reactions of the Li-rich cathode materials.

Here we report a systematic study on the sub-reactions of the Li_2MnO_3 activation process in the Ni-less Li-rich cathode material by detailed electrochemical and structural characterization technics. A prominent oxygen-generation plateau was observed in the first charge above 4.6 V; however, no obvious change of the Li-TM ordering was detected in the *in-situ* XRD pattern during this period while the c-lattice kept increasing, strongly indicating that the oxygen release reaction was accompanied by the Li extraction only from the Li layers. Based on a combined sectional charge/discharge capacity investigation and HAADF-STEM observation, it was revealed that although the oxygen release plateau disappeared within the first 5 cycles, the Li_2MnO_3 activation process continued for up to 70 cycles with gradual capacity increase, crystal structure evolution and consequent voltage decline, strongly indicating that the two sub reactions of oxygen release and TM rearrangement may not necessarily occur concurrently, and the latter is the key kinetic step to finalize the Li_2MnO_3 activation and result into the gradual capacity increase.

8.3 Experimental section

Materials synthesis: All the chemicals are from Aldrich Sigma. The $Li_{1.87}Mn_{0.94}Ni_{0.19}O_3$ cathode material synthesis was completed in two steps. Firstly, stoichiometric $Mn(NO_3)_2$ and $Ni(NO_3)_2$ were dissolved in distilled water and then co-precipitated with equal volume of 0.2 M sodium carbonate. The immediate light brown precipitate was aged at room temperature for 20 h, collected and then dried at 100 ℃. After that, the precipitate was pre-heated at 500 ℃ in air for 5 h and then calcined with stoichiometric $LiOH \cdot H_2O$ at 900 ℃ in air for another 12 h to obtain the final product. An excess of 3 wt % $LiOH \cdot H_2O$ was used to compensate for Li volatilization at this temperature.

Materials characterization: The mole ratio of the metal elements was determined by a Varian 725-ES Inductively Coupled Plasma Atomic Emission Spectroscopy (ICP-AES). *Ex-situ* powder X-ray diffraction (XRD) characterization for the pristine powder sample was conducted on a Bruker Advanced X-Ray Diffractometer (40 kV, 30 mA) with Cu Kα (λ= 0.15406 nm) radiation at a scanning rate of 1^o min^{-1}. High resolution synchrotron *in-situ* X-ray diffraction patterns were collected in transmission mode on Beamline 10-BM-1 of Australian Synchrotron using the MY THEN micro-strip detector and a Si(111) monochromators with the wavelength of 0.8265 Å. Corresponding cycling test of the cell was conducted on a Solartron SB1210 galvanostat/potentiostat under a constant current density of 30 mAh g^{-1} [18]. Field-emission scanning electron microscope for all the samples was performed on FE-SEM, JEOL 7800 to investigate their morphological characteristics. Scanning transmission electron microscopy (STEM) observation was conducted on JEM-ARM200F at 200kV with a high angle annular dark field (HAADF) detector. X-ray

photoelectron spectrometry (XPS) analysis was carried out on a Kratos Axis Ultra X-ray Photoelectron Spectrometer with AlKα (1253.6 eV) X-ray.

Electrochemical test: All the electrochemical measurements were carried out in CR2032 coin cells at room temperature. Firstly, a mixture of the active materials, acetylene black and polyvinylidene fluoride were mechanical grounded in a mortar with the weight ratio of 7:2:1 and then coated as slurry with appropriate amount of N-methyl-2-pyrrolidone onto aluminium foil using the doctor blade method. After that, the slurry was dried in vacuum oven at 120 °C for 12 h and then cut into working electrodes with an area of 0.7 cm^2. The whole process of CR2032 coin cell fabrication was completed in an argon-filled glove box. The as-prepared electrode was assembled as the cathode. Lithium foil and 1 M $LiPF_6$ in a mixture of ethylene carbonate (EC) and dimethyl carbonate (DMC) (1:1) were used as the negative electrode and electrolyte, respectively. The galvanostatic charge/discharge measurement was performed in a multi-channel battery tester (Land CT2001A) while the cyclic voltammetry (CV) tests were conducted in a CHI660E Electrochemical Workstation.

8.4 Results and discussion

Figure 8.1 shows the XRD pattern of the material. All the main diffraction peaks are sharp and clear, and highly fitted with the typical layered R-3m space group (JCPDS No. 84-1634) except a few minor peaks located between 20 ° and 25 °, which are due to the localized $LiMn_6$ super-lattice in the Li_2MnO_3-like monoclinic structure [8, 19, 20]. On the other side, a high (003)/(104) peak intensity ratio (>1.2) can be clearly observed with well split of (006)/(012) and (018)/(110) peaks pairs, suggesting a low degree of TM ions in the Li layers [21]. All these observations demonstrate a highly crystallized material with a typical layered monoclinic structure.

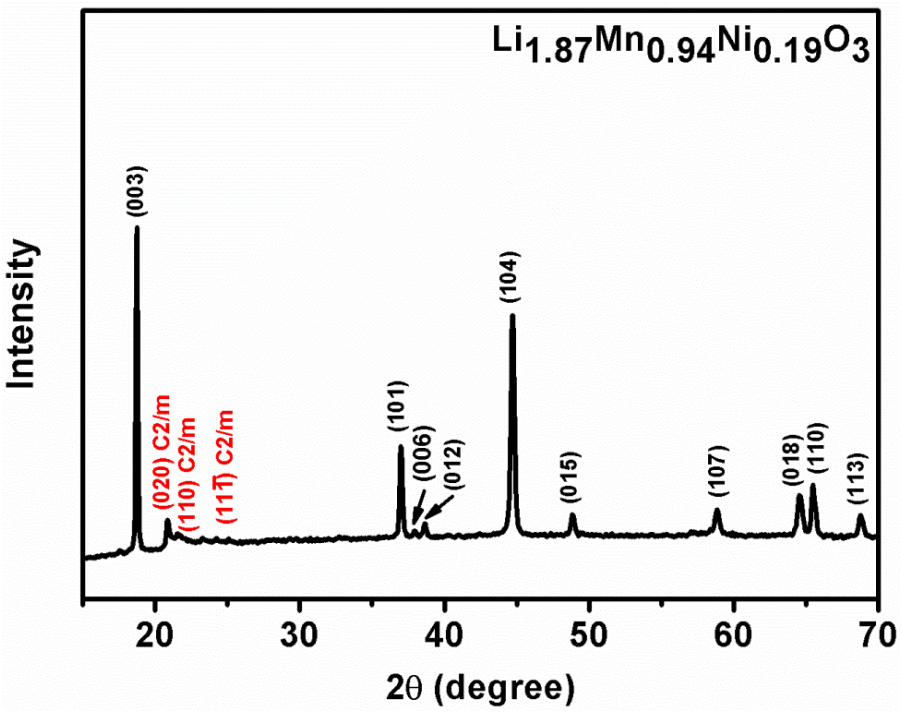

Figure 8.1 Powder X-ray diffraction pattern of the pristine $Li_{1.87}Mn_{0.94}Ni_{0.19}O_3$ composite

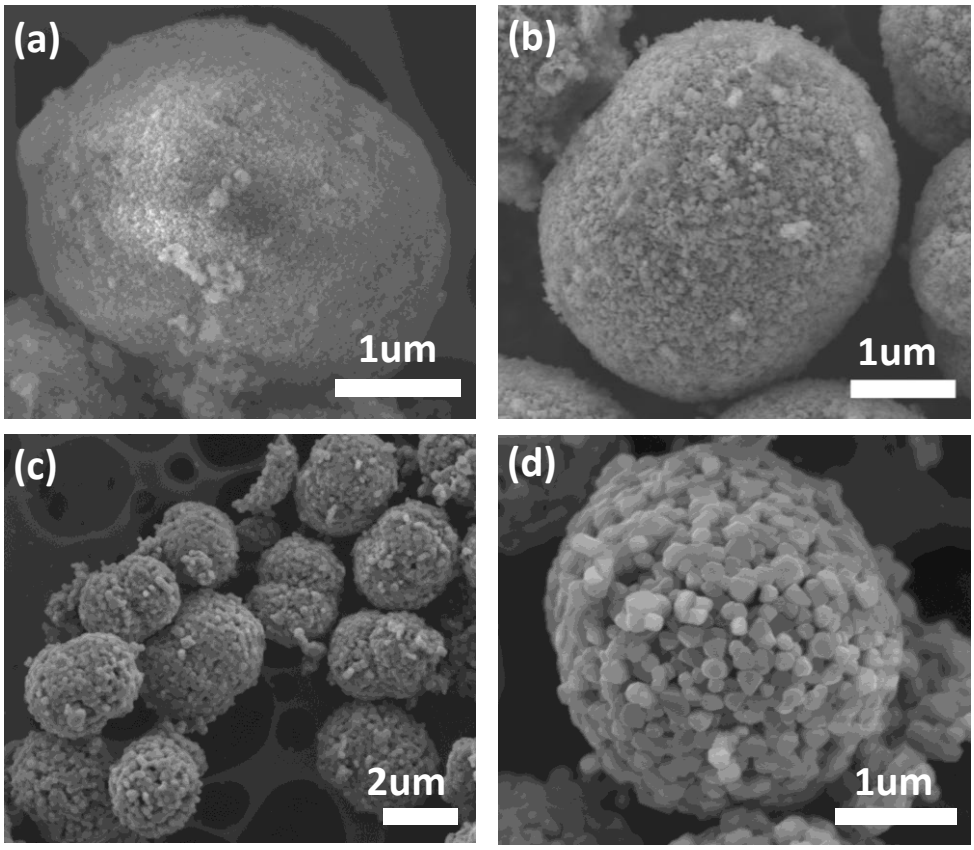

Figure 8.2 FE-SEM images of the (a) carbonate precursor (b) 500 ℃ pre-heated oxide precursor and (c, d) final $Li_{1.87}Mn_{0.94}Ni_{0.19}O_3$ composite

The morphology and microstructure of the precursors and final product were observed by FE-SEM as shown in **Figure 8.2**. The spherical shape of the carbonate precursor (**Fig. 8.2a**) is well inherited by the final $Li_{1.87}Mn_{0.94}Ni_{0.19}O3$ product (**Fig. 8.2c** and **8.2d**) on a large scale with almost the same diameter of around 2 to 3 nm. However, the surface of these carbonate microspheres became much rougher and porous ((**Fig. 8.2b**) after the 500 ℃ heat-treatment, and were then well crystallized with the LiOH during the calcination process to form homogeneous 100 nm sized nanocrystals over the whole microspheres as clearly revealed in (**Fig. 8.2d**). This hierarchical microstructure is advantageous for cathode materials because it may accommodate the lattice strain of the crystal structures during long term cycling and concurrently provide sufficient surface area for electrode-electrolyte contact [22, 23].

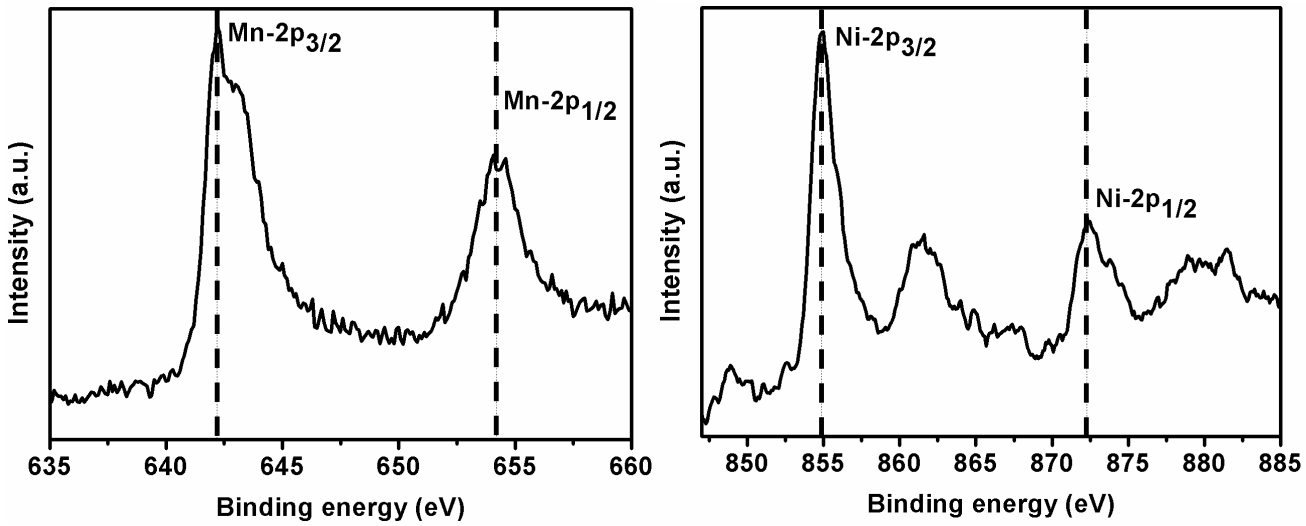

Figure 8.3 The XPS spectra of (a) Mn_{2p} and (b) Ni_{2p} for the pristine $Li_{1.87}Mn_{0.94}Ni_{0.19}O_3$ composite powder

To identify the valence state of Mn and Ni in the pristine $Li_{1.87}Mn_{0.94}Ni_{0.19}O_3$ composite, XPS was performed and the spectra of Mn- and Ni-2p is shown in **Figure 8.3**. The Mn $2p_{3/2}$ binding energy is around 642.2 eV, which is highly consistent with that of Mn^{4+} [24, 25]. The Ni $2p_{3/2}$ energy locates at 854.9 eV. This is very close to that of Ni^{3+} in $LiNiO_2$, indicating most of the Ni ions are in the oxidation state of 3+ [26].

Cycling performance of the $Li_{1.87}Mn_{0.94}Ni_{0.19}O_3$ material was tested at 30 mA g^{-1} (0.1C) at room temperature between 2 V and 4.8 V (**Fig. 8.4**). Interestingly, both the specific charge and discharge capacities of this material continuously increased from roughly 100 mAh g^{-1} in the first cycle to almost 270 mAh g^{-1} in the 60th cycle, and then kept rising smoothly until the 100^{th} cycle with an end of about 280 mAh g^{-1}. Such a phenomenon of prominent capacity increase over cycles has also been

reported recently by another group in a Ni-doped Li-rich cathode material system with the same Ni/Mn mole ratio and also my previous work in a low Co Li-rich material system [17, 27]. A less Ni or Co content has been proposed to slow down the Li_2MnO_3 activation process and result into the gradual capacity increase, which is probably highly related to the gradual phase transformation from the parent layered structure to a new spinel phase over cycles. It should be highlighted here that the columbic efficiency of this material didn't follow the trend of gradual increase over cycles, but more like most of the Li-rich materials, it was remarkably low in the first cycle but then jumped drastically to more than 90% in the 2^{nd} cycle and rapidly got stabilized at almost 100% after the 5^{th} cycle. The low first-cycle efficiency has been well demonstrated to originate from the simultaneous release of oxygen and extraction of lithium during the high-voltage long-plateau charging process, which is partially irreversible and results into the capacity loss on the first cycle [8, 12]. Consequently, it can be assumed in the material that the high voltage oxygen-release reaction mainly occurred in the first charge and became much weaker from the 2^{nd} charge and basically disappeared after the 5^{th} cycle.

The charge/discharge curves of some typical cycles are presented (**Fig. 8.4 inset)** to investigate the details of the capacity increase. Firstly, looking at the first charging curves, it can be divided into two parts depending on the voltage ranges. In the first range from 2-4.6 V, a specific charge capacity of 55.1 mAh g^{-1} was achieved. This is reasonable considering the fact that if all the Ni ions are 3+ and can be oxidized to 4+, it will result into a specific charge capacity of 41.2 mAh g^{-1}, and the small portion of Ni^{2+} as shown by XPS and possibly minor residual of Mn^{3+} will contribute a small part of extra capacity. For the second range from 4.6-4.8 V, a representative high-voltage (>4.6 V) charging plateau of Li-rich cathode materials is very clear in the $Li_{1.87}Mn_{0.94}Ni_{0.19}O_3$ material; however, it faded significantly in the 2^{nd} cycle and disappeared after the 5^{th} cycle. As this high-voltage charging plateau has been well known to be strongly associated with an irreversible oxygen extraction process from the Li-rich cathode materials [8, 12, 13], the claim is further supported here that the oxygen release reaction focused on the first cycle and became negligible after the 5^{th} cycle in this Li-rich composite.

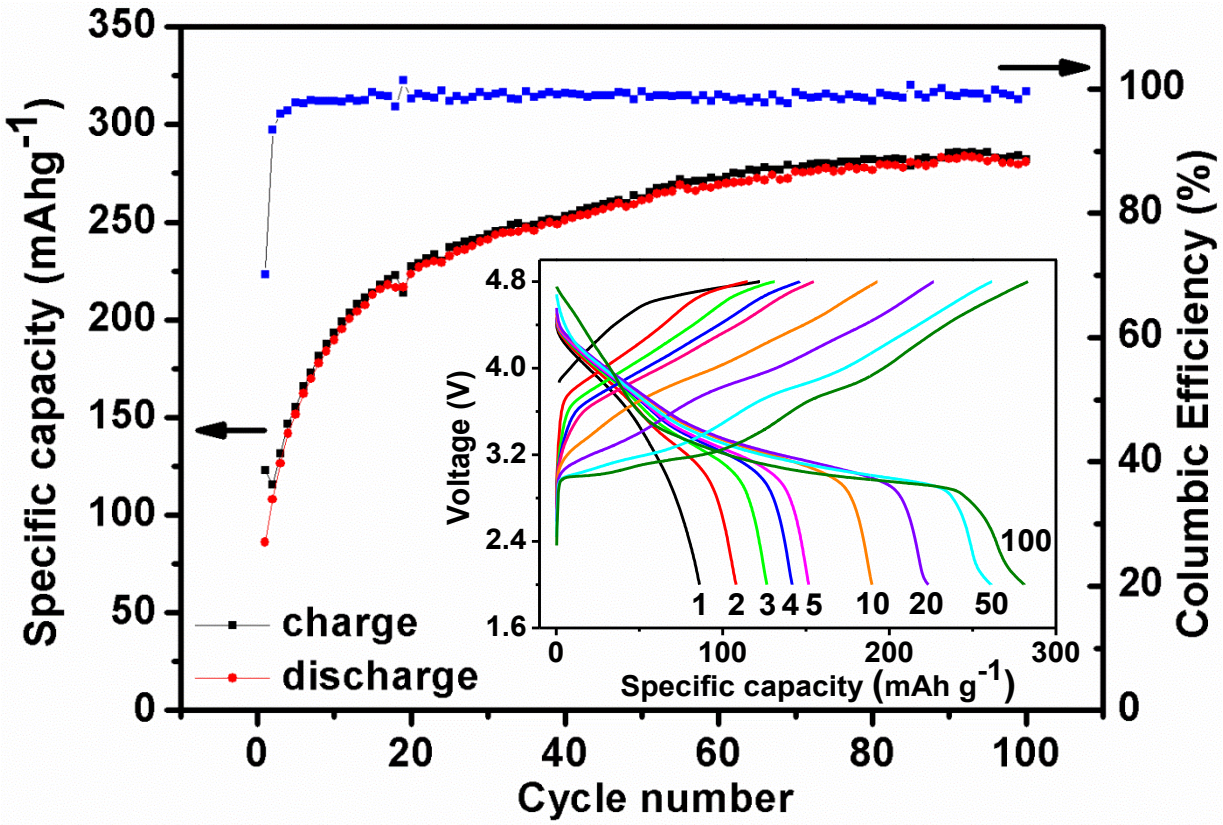

Figure 8.4 Charge and discharge capacities and the corresponding columbic efficiency of the $Li_{1.87}Mn_{0.94}Ni_{0.19}O_3$ material in the first 100 cycles at 30 mA g-1 between 2 V and 4.8 V. Inset are the detailed charge/discharge curves of this material in some typical cycles.

On the other side, the charge curves gradually evolved into two slopes with one from 2.9 V to 3.6 V and the other from 3.6 V to 4.8 V. The former regularly grew from nothing to about 141.4 mAh g^{-1} in the end of the first 100 cycles and contributed majority of the charge capacity increase (the total charge capacity increase in the first 100 cycles is 159.1 mAh g^{-1}). The latter had just a minor increase in length, but experienced a significantly change in shape. The initial two plateaus were integrated into a smooth one in just 5 cycles and then maintained afterwards. Similarly, the discharge curves also continually elongated over cycles. The growth mainly happened on the 3 V region and finally formed a dominating 3 V plateau. Overall, both the gradually reinforced 3.2 V charge slope and 3 V discharge plateau are well consistent with cathode materials with spinel phase features, indicating a gradual phase transformation during cycling [28, 29]. In addition, a decrease in the discharge voltage between 3 V and 3.8 V during cycling may be noted. Such a voltage drop has been proposed to be related to a hysteresis phenomenon that also signifies an irreversible phase transformation in Li-rich cathode materials [30, 31].

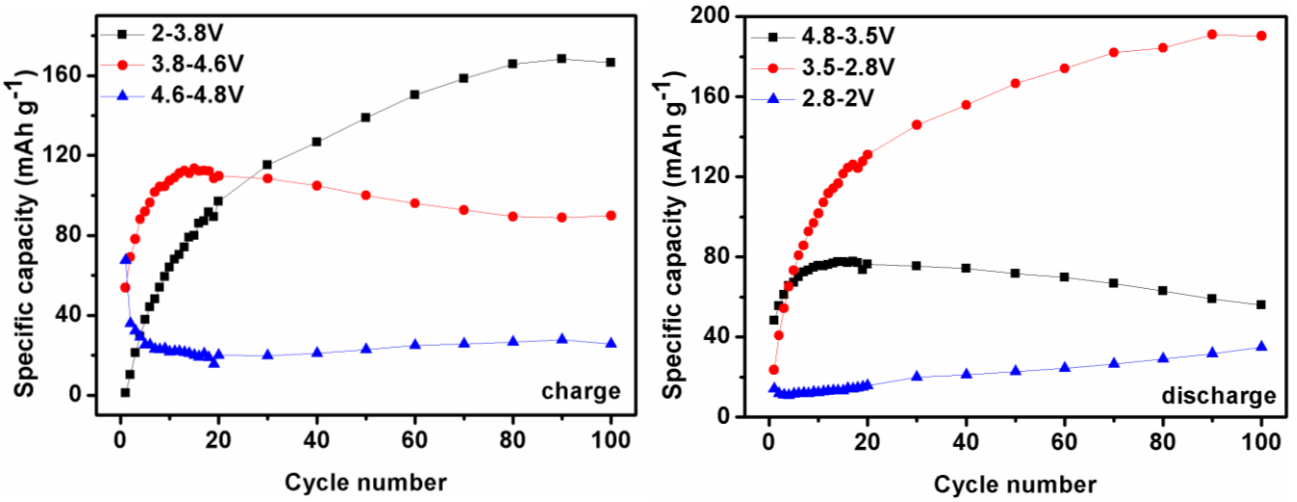

Figure 8.5 (a) Net specific charge capacities of the $Li_{1.87}Mn_{0.94}Ni_{0.19}O_3$ cathode material in the voltage ranges of 2-3.8 V, 3.8-4.6 V and 4.6-4.8 V in the first 100 cycle; (b) net discharge capacities in the voltage ranges of 4.8-3.5 V, 3.5-2.8 V and 2.8-2 V in the first 100 cycle

To have a clearer vision on the origin of the capacity increase, both the charge and discharge process are split into three voltage regions. The varying tendency of the specific capacity in each region during cycling has been plotted and shown in **Figure 8.5**. For the charge process, the capacity in the region between 4.6 V and 4.8 V decreased significantly in the first 5 cycles and then kept stable for the rest of cycles. This is in accordance to the charge profile (**Fig. 8.5**), further supporting the deduction that the oxygen extraction mainly happened in the very beginning. For the other two charge regions at 2 V-3.8 V and 3.8 V-4.6 V, both of the capacity curves present very similar trend as the two discharge curves at 3.5 V-2.8 V and 4.8 V-3.5 V, respectively. The similarity of the charge and discharge capacity curves in high and medium voltage ranges indicates the corresponding redox reactions are reversible. On the other side, although both the two pairs of curves showed apparent increase in the beginning, the high voltage pair stopped growing in the 13th cycle and then declined smoothly for the rest of cycles while the medium voltage pair continued the increase until the end of the test. It should be highlighted here that the oxygen extraction appeared to occur mainly on the first charge and finish in the first 5 cycles, but the structure evolution continued through all the cycling period and resulted into the gradual growth of the spinel-featured medium-voltage capacity curves.

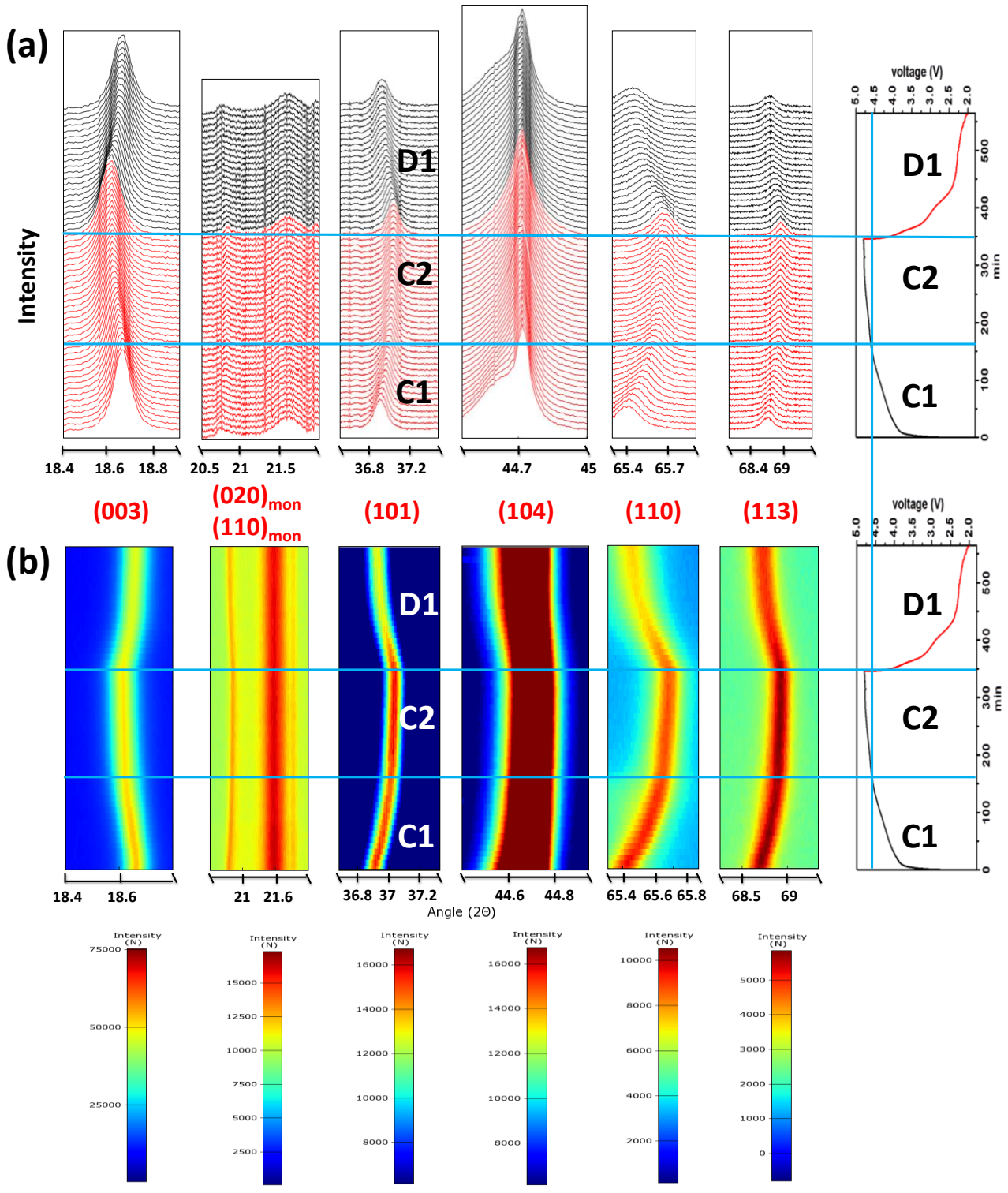

Figure 8.6 Selected area *in-situ* XRD patterns and corresponding first cycle charge/discharge profile versus time of the $Li_{1.87}Mn_{0.94}Ni_{0.19}O_3$ composite. (a) is the stacked *in-situ* XRD patterns and (b) is the colourful time resolved intensity distribution plots with reference colour bar underneath

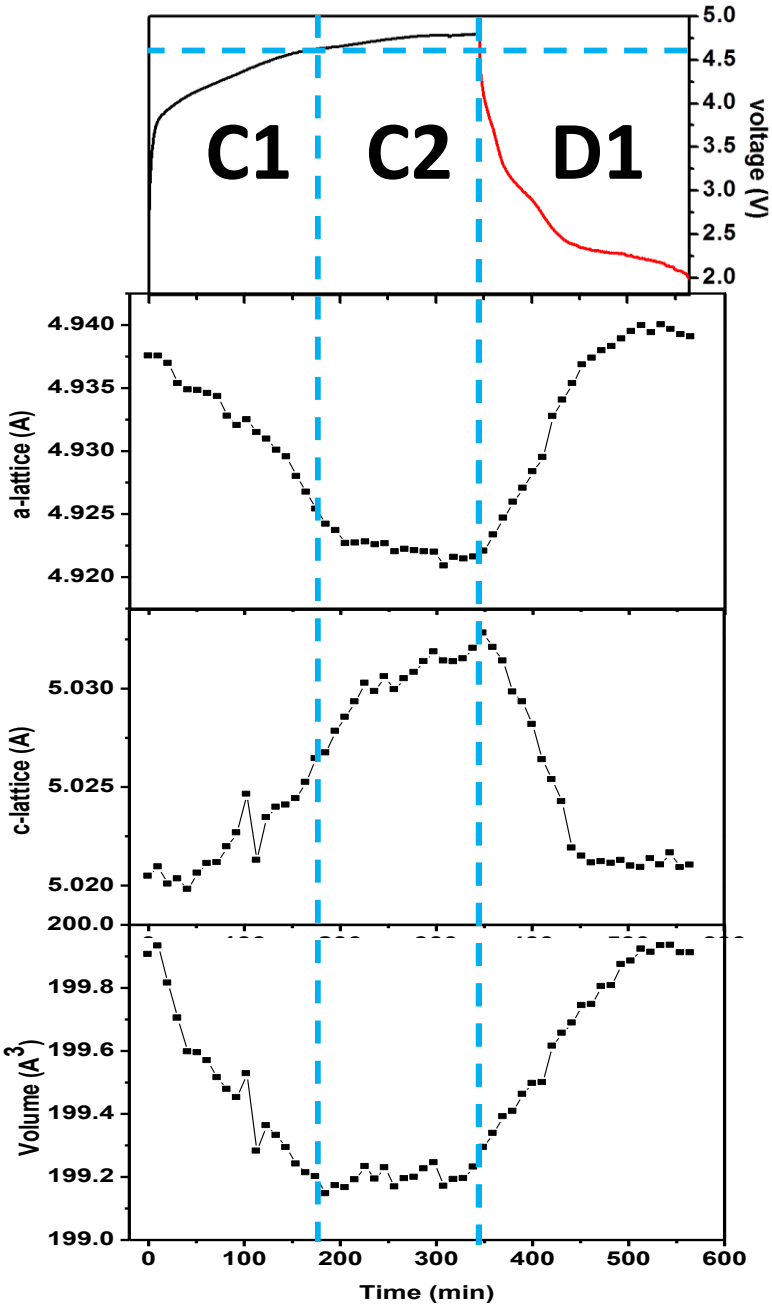

Figure 8.7 Change of the Rietveld refined a and c-lattice parameters and corresponding unit cell volume during the first cycle

In situ X-ray diffraction (XRD) has been proved to be a powerful technique to monitor the real-time structural transformation and lattice change of inorganic cathode materials during long term electrochemical reactions. To further understand the crystal structure changes of the $Li_{1.87}Mn_{0.94}Ni_{0.19}O_3$ material, *in-situ* XRD measurement was conducted during the first cycle at 30 mA g^{-1} between 2-4.8 V (**Fig. 8.6**). For the convenience of comparison, the first cycle was divided into three sections including C1 for charging between open-circuit voltage to 4.6 V, C2 between 4.6

V and 4.8 V and D1 for the whole discharge. For a clearer observation, only the characteristic diffraction peaks of the cathode material including (003), $(020)_{mon}$, $(110)_{mon}$, (101), (104), (110) and (113) are presented here. **Figure 8.6a** is the stacked *in-situ* XRD patterns and the red and black colours represent the corresponding charge and discharge process. **Figure 8.6b** is the colourful time resolved intensity plots in which a more straightforward detection on the evolution of the diffraction peaks in both intensity and position can be realized by direct visual observation of the colour distribution versus time with a reference colour bar located underneath. In addition, the a and c lattice parameters of the monoclinic unit cell and the related cell volume were calculated from Rietveld refinement and displayed in **Figure 8.7**.

In the first C1 region, the (003) peak shifted prominently to the lower 2θ range while the (104) and (113) peaks moved towards the higher range. The shift of these peaks indicates a higher d-spacing of the Li layers in the unit cell, which is evidently supported by the steep increase of the c-lattice. All these results demonstrated a simple Li extraction process from the Li layers, which results into stronger electrostatic repulsion of the neighbouring oxygen layers and consequently, the expansion of the c-lattice [13, 32]. On the other side, the a-lattice dropped in C1 region due to the oxidation of the Ni^{2+} (0.69Å) to Ni^{4+}(0.56Å) [32].

After C1, a long-plateau charging region C2 was started from around 4.6 V. The (003), (104) and (113) peaks followed the trend in region C1, though not that obvious. This is well consistent with the continuous growing of the c-parameter in this region. It should be highlighted here that the c-parameter in C2 region behaved totally differently from those reported in which the c-lattice jumped down significantly near 4.8 V due to the proposed Li extraction from the TM layers [13, 32], strongly implying a Li extraction also from the Li layers in the $Li_{1.87}Mn_{0.94}Ni_{0.19}O_3$ material during the first cycle high-voltage charging period. In addition, from both the stacked linear diffraction pattern and the colourful intensity plots in **Figure 8.6**, it can be found that the height and intensity of the $(010)_{mon}$ and $(110)_{mon}$ peaks were basically unchanged for both the C1 and C2 regions. As mentioned previously, these diffraction peaks are characteristic of $LiMn_6$ ordering in the TM layers of Li-rich cathode materials. In most of these materials, a large portion of the lithium ions in the TM layers will be extracted during the high voltage charging process in the first cycle, leading to the breakup of the $LiMn_6$ ordering and consequently, the decay of the $(010)_{mon}$ and $(110)_{mon}$ diffraction peaks [13, 33]. Therefore, the preservation of them provides strong evidence to a stable $LiMn_6$ ordering in the TM layers during the first charge. For the a-parameter, it stopped the rapid decrease and became almost constant within this region. This means the average radii of the TM ions

remained in C2 region. As a result, the well-known oxygen release reaction became the only source to compensate the high voltage (4.6-4.8 V) charge balance with Li extraction [32].

For the D2 discharge region, an opposite shift of the (003) (104) and (113) peaks can be observed, however, all of them slightly deviated from the original position in the end of the discharge. Also, the c-parameter decreased at this region and ended slightly higher than the pristine value. These observations are in accordance to the Li re-intercalation process into the Li layers, indicating that the Li extraction in the charge process was not fully reversible. Meanwhile, the a-parameter increased in D2 region and became a little larger than the pristine state. This is because of the reduction of the TM ions during discharge, and the net increase of the a-parameter on the whole cycle is probably due to the partial reduction of the Mn^{4+} ions during discharge [34].

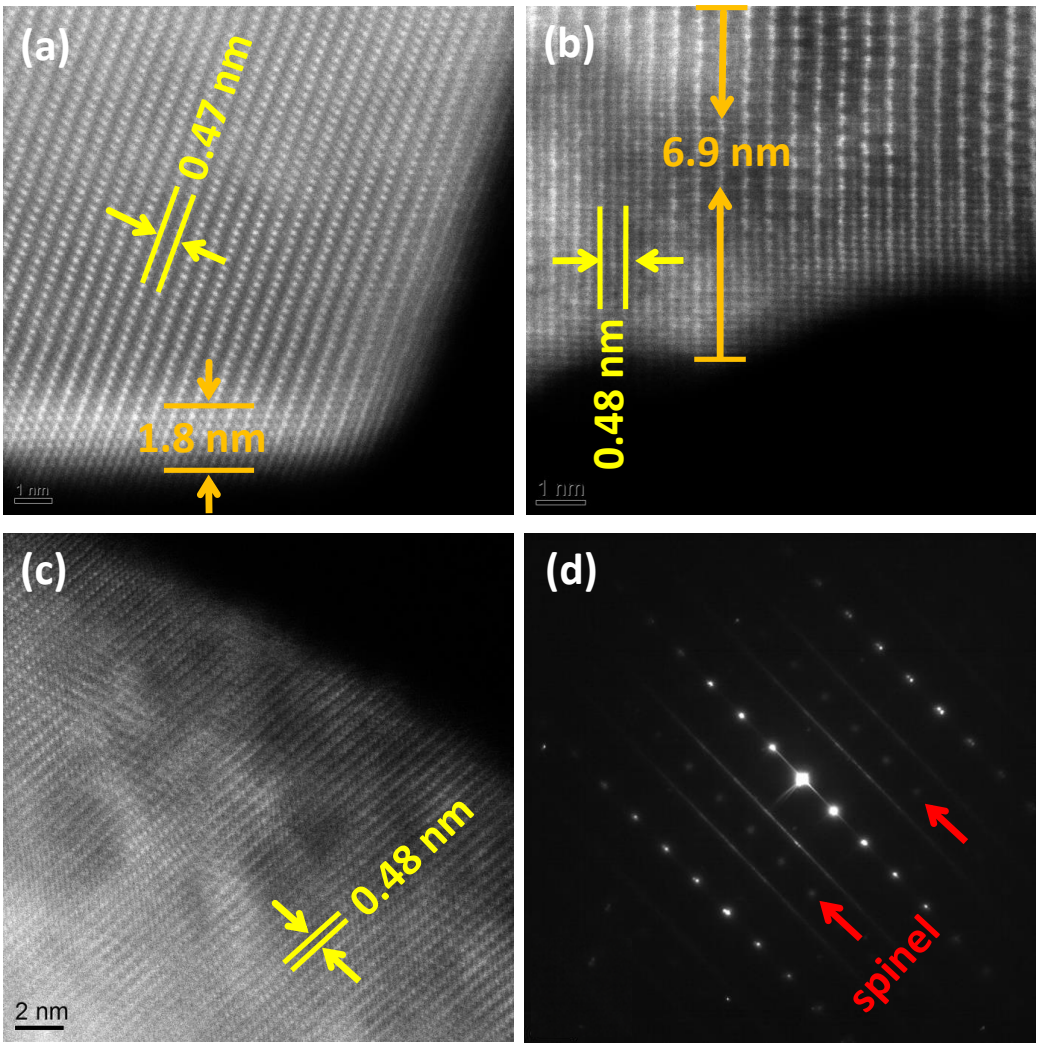

Figure 8.8 HAADF-STEM images of (a) pristine, (b) 10 times cycled and (c) 50 times cycled $Li_{1.87}Mn_{0.94}Ni_{0.19}O_3$ composite and (d) the corresponding SAED pattern of (c) along $[100]_{mon}$

To further investigate the crystal structure evolution of the $Li_{1.87}Mn_{0.94}Ni_{0.19}O_3$ composite during cycling, aberration-corrected high-angle annular-dark-field scanning transmission electron microscopy (HAADF-STEM) characterization was performed (**Fig. 8.8**). It should be noted here that only heavy elements like Mn and Ni can be observed in HAADF-STEM images as white spots while light elements such as Li or O are invisible [35]. A highly crystallized layered structure with a layer distance of 0.47 nm of the pristine sample can be clearly detected from **Figure 8.8a**. It may be noted that there are some while spots between the TM layers on the surface with a thickness of around 2 nm, indicating a spinel surface which is possibly due to the insufficiency of Li source during high temperature calcination. After 10 electrochemical cycles, although the layered feature was still distinguishable, a significantly larger amount of white spots can be found on the Li layers in **Figure 8.8b**, indicating a prominent TM diffusion from the TM layers to the Li layers. In addition, the white spots in the Li layers appear to gradually fade from the surface to the bulk, implying a surface-to-bulk reaction path. It is also found that the layered distance was slightly larger than the pristine one. This is in accordance to the *in-situ* XRD results and possibly due to the irreversible loss of Li and O in the initial cycle from the Li layers. After 50 cycles, some local reticulate patterns can be clearly observed on the original parallel lines over the whole crystal framework (**Fig. 8.8c**). This has been demonstrated the characteristics of the spinel phase [36], which indicates a large scale TM diffusion to the Li layers during the long-term cycling. In addition, the SAED pattern of the 50 times cycled sample displayed extra spots as marked in **Figure 8.8d** between the diffuse scattering lines. This spots can be well explained by a spinel phase evolved from the parent layered structure, further confirming the gradual structure evolution and TM diffusion during long term electrochemical cycling [36, 37].

Based on the above results, the reaction process of the $Li_{1.87}Mn_{0.94}Ni_{0.19}O_3$ material during the first cycle can be described as follow: for the charge below 4.6 V, Li was extracted from the Li layers accompanied by oxidation of the TM cations to their highest oxidation state; for the high-voltage charge between 4.6 V and 4.8 V, the Li was continuously extracted from the Li layers with simultaneous oxygen generation to compensate the charge balance. During the discharge, Li was re-inserted into the Li layers, accompanied with the reduction of the Ni ions and probably a small part of Mn^{4+}, but some of the capacity was lost due to the irreversible oxygen release. It should be highlighted here that, in contrast to most Li-rich cathode materials [11, 12, 33], basically no Li or TM were extracted from the TM layers in the $Li_{1.87}Mn_{0.94}Ni_{0.19}O_3$ material during the first high-voltage charge. This is interesting because it strongly indicates that the oxygen release and TM

rearrangement processes may not necessarily occur at the same time, and the former probably feature much faster reaction kinetics.

8.5 Conclusions

Li-rich layered $Li_{1.87}Mn_{0.94}Ni_{0.19}O_3$ microspheres were synthesized and tested as a cathode material for LIBs in this report. Due to an uncommonly low content of Ni, the Li_2MnO_3 activation process in the $Li_{1.87}Mn_{0.94}Ni_{0.19}O_3$ material was artificially retarded and split into dozens of cycles, resulting into the interesting phenomenon of gradual capacity increase over cycles in this material. More importantly, due to the low-Ni induced slow kinetics of the Li_2MnO_3 activation process, it was revealed by a combination of electrochemistry measurements and advanced *in-situ* XRD and HAADF-STEM characterization that the Li extracted in the first charge was mainly from the Li layers, even at high voltage range with simultaneous oxygen generation, and the cation ordering in the TM layers was basically stable during this period; in addition, the oxygen generation mainly occurred in the first 5 cycles and disappeared afterwards while the structure transformation from the layered phase to the spinel took dozens of cycles to complete, which is highly related to the gradual capacity increase of the material. Based on these results, it can be deducted that the oxygen release reaction features a much faster kinetics than that of the phase transformation which involves the diffusion of both Li and TM from the TM layers, and the latter may play a key role in determining the capacity of the Li-rich cathode materials. This work can not only provide clues in design and synthesis of low-cost and high energy Li-rich cathode materials, but more importantly, give some insights in ultimately understanding the fundamental electrochemical reaction mechanisms and the corresponding structure evolution.

8.6 References

1. Park, O.K., et al., *Who will drive electric vehicles, olivine or spinel?* Energy Environ. Sci., 2011. **4**(5): p. 1621-1633.
2. Dunn, B., H. Kamath, and J.-M. Tarascon, *Electrical energy storage for the grid: A battery of choices.* Science, 2011. **334**(6058): p. 928-935.
3. Van Noorden, R., *The rechargeable revolution: A better battery.* Nature, 2014. **507**(7490): p. 26-28.
4. Luo, B., et al., *Graphene-Confined Sn Nanosheets with Enhanced Lithium Storage Capability.* Adv. Mater., 2012. **24**(26): p. 3538-3543.

5. Wang, H., et al., *Mn_3O_4-graphene hybrid as a high-capacity anode material for lithium ion batteries.* J. Am. Chem. Soc., 2010. **132**(40): p. 13978-13980.
6. Chan, C.K., et al., *High-performance lithium battery anodes using silicon nanowires.* Nat. Nanotechnol., 2007. **3**(1): p. 31-35.
7. Yu, H., et al., *Direct Atomic-Resolution Observation of Two Phases in the $Li_{1.2}Mn_{0.567}Ni_{0.166}Co_{0.067}O_2$ Cathode Material for Lithium-Ion Batteries.* Angew. Chem., Int. Ed., 2013. **52**(23): p. 5969-5973.
8. Thackeray, M.M., et al., *Li_2MnO_3-stabilized $LiMO_2$ (M = Mn, Ni, Co) electrodes for lithium-ion batteries.* J. Mater. Chem., 2007. **17**(30): p. 3112-3125.
9. Yu, H. and H. Zhou, *High-Energy Cathode Materials (Li_2MnO_3-$LiMO_2$) for Lithium-Ion Batteries.* J. Phys. Chem. Lett., 2013. **4**(8): p. 1268-1280.
10. Park, S.-H., et al., *Lithium-manganese-nickel-oxide electrodes with integrated layered-spinel structures for lithium batteries.* Electrochem. Commun., 2007. **9**(2): p. 262-268.
11. Xu, B., et al., *Identifying surface structural changes in layered Li-excess nickel manganese oxides in high voltage lithium ion batteries: A joint experimental and theoretical study.* Energy Environ. Sci., 2011. **4**(6): p. 2223-2233.
12. Armstrong, A.R., et al., *Demonstrating oxygen loss and associated structural reorganization in the lithium battery cathode $Li[Ni_{0.2}Li_{0.2}Mn_{0.6}]O_2$.* J. Am. Chem. Soc., 2006. **128**(26): p. 8694-8698.
13. Lu, Z. and J. Dahn, *Understanding the Anomalous Capacity of $Li/Li[Ni_xLi_{(1/3-2x/3)}Mn_{(2/3-x/3)}]O_2$ Cells Using In Situ X-Ray Diffraction and Electrochemical Studies.* J. Electrochem. Soc., 2002. **149**(7): p. A815-A822.
14. Robertson, A.D. and P.G. Bruce, *Mechanism of electrochemical activity in Li_2MnO_3.* Chem. Mater., 2003. **15**(10): p. 1984-1992.
15. Hy, S., et al., *Direct In situ Observation of Li_2O Evolution on Li-Rich High-Capacity Cathode Material, $Li[Ni_xLi_{(1-2x)/3}Mn_{(2-x)/3}]O_2$ ($0 \leq x \leq 0.5$).* J. Am. Chem. Soc., 2014. **136**(3): p. 999-1007.
16. Ozawa, K., et al., *Electrochemical Characteristics of Layered $Li_{1.95}Mn_{0.9}Co_{0.15}O_3$ (C2/m) as a Lithium-Battery Cathode.* J. Electrochem. Soc., 2012. **159**(3): p. A300-A304.
17. Ye, D., et al., *Capacity-controllable Li-rich cathode materials for lithium-ion batteries.* Nano Energy, 2014. **6**: p. 92-102.
18. Brant, W.R., et al., *A simple electrochemical cell for in-situ fundamental structural analysis using synchrotron X-ray powder diffraction.* J. Power Sources, 2013. **244**: p. 109-114.

19. Bréger, J., et al., *High-resolution X-ray diffraction, DIFFaX, NMR and first principles study of disorder in the Li_2MnO_3–$Li[Ni_{1/2}Mn_{1/2}]O_2$ solid solution.* J. Solid State Chem., 2005. **178**(9): p. 2575-2585.
20. Jarvis, K.A., et al., *Atomic Structure of a Lithium-Rich Layered Oxide Material for Lithium-Ion Batteries: Evidence of a Solid Solution.* Chem. Mater., 2011. **23**(16): p. 3614-3621.
21. Li, Y., et al., *Electrochemical performance of nanocrystalline $Li_3V_2(PO_4)_3$/carbon composite material synthesized by a novel sol-gel method.* Electrochim. Acta, 2006. **51**(28): p. 6498-6502.
22. Lou, X.W.D., L.A. Archer, and Z. Yang, *Hollow Micro-/Nanostructures: Synthesis and Applications.* Adv. Mater., 2008. **20**(21): p. 3987-4019.
23. Jiang, Y., et al., *Hollow $0.3Li_2MnO_3 \cdot 0.7LiNi_{0.5}Mn_{0.5}O_2$ microspheres as a high-performance cathode material for lithium-ion batteries.* Phys. Chem. Chem. Phys., 2013. **15**(8): p. 2954-2960.
24. Regan, E., et al., *Surface and bulk composition of lithium manganese oxides.* Surf. Interface Anal., 1999. **27**(12): p. 1064-1068.
25. Li, Z., et al., *Synthesis of hydrothermally reduced graphene/MnO_2 composites and their electrochemical properties as supercapacitors.* J. Power Sources, 2011. **196**(19): p. 8160-8165.
26. Spahr, M.E., et al., *Characterization of layered lithium nickel manganese oxides synthesized by a novel oxidative coprecipitation method and their electrochemical performance as lithium insertion electrode materials.* J. Electrochem. Soc., 1998. **145**(4): p. 1113-1121.
27. Rowe, A.W. and J. Dahn, *Positive Electrode Materials in the Li-Mn-Ni-O System Exhibiting Anomalous Capacity Growth during Extended Cycling.* J. Electrochem. Soc., 2014. **161**(3): p. A308-A317.
28. Gu, M., et al., *Formation of the spinel phase in the layered composite cathode used in Li-ion batteries.* Acs Nano, 2012. **7**(1): p. 760-767.
29. Song, B., et al., *Structural evolution and the capacity fade mechanism upon long-term cycling in Li-rich cathode material.* Phys. Chem. Chem. Phys., 2012. **14**(37): p. 12875-12883.
30. Croy, J.R., et al., *Examining Hysteresis in Composite $xLi_2MnO_3 \cdot (1-x)LiMO_2$ Cathode Structures.* J. Phys. Chem. C, 2013. **117**(13): p. 6525-6536.
31. Gallagher, K.G., et al., *Correlating hysteresis and voltage fade in lithium-and manganese-rich layered transition-metal oxide electrodes.* Electrochem. Commun., 2013. **33**: p. 96-98.
32. Mohanty, D., et al., *Structural transformation of a lithium-rich $Li_{1.2}Co_{0.1}Mn_{0.55}Ni_{0.15}O_2$ cathode during high voltage cycling resolved by in situ X-ray diffraction.* J. Power Sources, 2013. **229**: p. 239-248.

33. Wang, R., et al., *Atomic Structure of Li_2MnO_3 after Partial Delithiation and Re-Lithiation.* Adv. Energy Mater., 2013. **3**(10): p. 1358-1367.
34. Mohanty, D., et al., *Structural transformation in a $Li_{1.2}Co_{0.1}Mn_{0.55}Ni_{0.15}O_2$ lithium-ion battery cathode during high-voltage hold.* RSC Advances, 2013. **3**(20): p. 7479-7485.
35. Bareno, J., et al., *Local Structure of Layered Oxide Electrode Materials for Lithium-Ion Batteries.* Adv. Mater., 2010. **22**(10): p. 1122-1127.
36. Boulineau, A., et al., *Evolutions of $Li_{1.2}Mn_{0.61}Ni_{0.18}Mg_{0.01}O_2$ during the Initial Charge/Discharge Cycle Studied by Advanced Electron Microscopy.* Chem. Mater., 2012. **24**(18): p. 3558-3566.
37. Boulineau, A., et al., *Reinvestigation of Li_2MnO_3 Structure: Electron Diffraction and High Resolution TEM.* Chem. Mater., 2009. **21**(18): p. 4216-4222.

9. Conclusions and recommendations

9.1 Conclusions

The key challenge for EVs battery is the lack of a high energy and reliable lithium ion cathode material. The objective of this thesis is to develop high energy Li-rich cathode materials for LIBs and investigate the corresponding electrochemistry reaction mechanisms. Several key contributions this thesis work has made to the Li-rich cathode material field are summarized as follows:

(1) In Li-Mn-Co-O system, the composition, structure and electrochemistry performance of a series of Li-rich layered-spinel integrated cathode materials with variable Li/(Mn+Co) mole ratio have been studied systematically. Unlike the conventional Li-rich cathode materials, these new Li-rich composite materials exhibited continuous capacity increase in the first tens of cycles from less than 50 mAh g^{-1} in the first cycle to up to 250 mAh g^{-1} at potential window of 2-4.8 V. The regular capacity increase has been demonstrated due to the continuous activation of the initial Li-rich layered phase on the surface of the composite particles, which is significantly promoted by the small content of Co doping. Based on the electrochemistry behaviours of these materials at different potential windows, cathode materials with controllable specific discharge capacity were designed by deliberately partially activating the composite materials to certain degrees.

(2) In Li-Mn-Co-O system, a serials of low-Co Li-rich cathode materials $Li[Co_xLi_{1/3-x/3}Mn_{2/3-2x/3}]O_2$ (x = 0.087, 0.1 and 0.118) with variable Co content and prominent gradual capacity increase over cycles have been systematically investigated. It has been revealed that the capacity increase was highly dependent on a few factors including the amount of Co-doping, cycling potential window and the current rate. All the low Co-doped samples can efficiently activate the Li_2MnO_3 phase and a minor change of the Co content can make a significant impact on the rate of the activation process. In addition, optimized cycling potential window and current rate have been demonstrated significantly to ensure the effective Li_2MnO_3 activation and good long-term cycling stability.

(3) In Li-Mn-Ni-O system, the composition, microstructure and electrochemical properties of a new series of Ni-less Li-rich cathode materials in the composition of $Li[Li_{1/3-2\ x/3}Mn_{2/3-x/3}Ni_x]O_2$ ($0.09 \leq x \leq 0.2$) have been systematically investigated to develop high performance Li-rich cathode materials for LIBs. They exhibit unusual specific capacity increase in the first dozens of cycles due to the continuous activation of the Li_2MnO_3 phase upon cycles. It has been demonstrated that the Ni-doping can significantly promote the Li_2MnO_3 activation to provide extra specific capacity, but

excessive Ni-doping can lead to undesirable excessive activation of the Li_2MnO_3 phase associated with substantial capacity loss in the first cycle. As a result, an optimized content of Ni has been demonstrated in the Li-Mn-Ni-O material systems to achieve a superior specific capacity (~280 mAh g^{-1}) and good cycling stability at room temperature.

(4) In Li-Mn-Ni-O system, the material with optimized Ni content and best specific capacity has been further investigated by advanced characterization including HAADF-STEM and *in-situ* XRD to have a deep understanding of the reaction mechanisms. Based on the gradual activation process of the Li_2MnO_3 phase induced by the low content of Ni doping in this material, it becomes possible to investigate the intermediate state of the Li_2MnO_3 activation process. It has been revealed that, compared with the O_2 generation reaction, the phase transformation of the parent layered monoclinic phase to a 3 V defect cubic spinel phase is the main limit factor to finalize the Li_2MnO_3 activation process and capacity increase.

9.2 Recommendations

Based on the research progress and outcome of this thesis on the field of layered Li-rich cathode materials, the following issues are strongly recommended for further research efforts to develop better high-energy LIBs:

Further understanding on the reaction mechanisms and kinetics: As discussed in chapter 2, there are still significant debates on the fundamental understanding of the reaction mechanisms and kinetics of Li-rich cathode materials. Based on the results in chapter 8, a new reaction mechanism of the Li_2MnO_3 phase activation process has been proposed, in which different kinetics of the sub-reactions are suggested to account for the fast oxygen release and low TMs diffusion. Therefore, more detailed research and more precise characterization on the materials, particularly on the quantitative analysis of the *in-situ* oxygen release during electrochemical cycling, are highly recommended to obtain more convinced information and conclusion.

Surface coating for better long-term cycling stability and rate performance: As shown in chapter 5 to 8, most of these Li-rich materials can sustain around 90% of the maximum specific capacities for 50 cycles at 2-4.8 V, however, the cyclibility declined quickly after that and even worse at 2-5 V. Such capacity decay has been demonstrated from the Mn dissolution on the surface into the electrolyte and the corresponding irreversible side reactions. Besides, we also found apparent capacity drop at higher rates, which is probably due to low electric conductivity on the surface. To

address these drawbacks, surface coating with a conductive yet inert coating layer, such as AlF_3, AlO_2, MnO_2 or even carbon deserve a try for better electrochemical performance.

Optimized Co and Ni co-doping for balanced high-voltage and cycling stability: According to the discussion and comparison of the results as shown in chapter 6 and 8, it can be noted that the materials doped with Co favoured a better cycling stability while the others doped with Ni featured a high working voltage on average. Considering the content of Co or Ni applied on the thesis work was small, a slightly higher amount of Co and Ni co-doping with variable Co/Ni mole ratio may concurrently possess the advantages of good long-term cycling stability and high working voltage.

Beyond this thesis work, there are still some significant problems for layered Li-rich cathode materials to solve, such as the voltage decline during cycling, low initial cycle columbic efficiency and poor rate performance, all of which largely correspond to the surface deterioration and the internal crystal structure transformation over cycling. Although many research efforts have been committed to improving the surface condition and enhancing the crystallinity, it is still challenging to completely prevent the phase transformation and the related voltage decay. Thus, how to ultimately avoid or minimize the long-term structure evolution and voltage decay should be substantially emphasized. In addition, the lack of a stable high-voltage electrolyte is another barrier to go across and that deserves more research interests. Finally, a cross-border research in chemistry, physics and materials engineering with advanced nano-technology and materials characterization methodology is highly desired to brace a bright prospect of the new generation high-energy Li-rich cathode materials.